

# A Modal Approach to Precision Motion Control

by

Pradeep Kumar Subrahmanyam

B.S., Institution of Engineers, India (1991)

M.Tech., Indian Institute of Technology, Bombay (1993)

M.S., University of Minnesota, Minneapolis (1995)

Submitted to the Department of Mechanical Engineering  
in partial fulfillment of the requirements for the degree of

Doctor of Philosophy in Mechanical Engineering

at the

MASSACHUSETTS INSTITUTE OF TECHNOLOGY

September 1999

© Massachusetts Institute of Technology 1999. All rights reserved.

Author .....

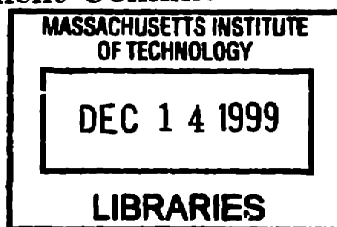
Department of Mechanical Engineering  
August 31, 1999

Certified by .....

Professor David L. Trumper  
Department of Mechanical Engineering  
Thesis Supervisor

Accepted by .....

Ain A. Sonin  
Chairman, Department Committee on Graduate Students



ARCHIVES

the settling times on the prototype wafer stepper is demonstrated.

**Thesis Committee :**

<b>Prof. David L. Trumper</b>	<b>Associate Professor of Mechanical Engineering</b>
<b>Prof. Jean-Jacques Slotine</b>	<b>Professor of Mechanical Engineering</b>
<b>Prof. Jeffrey H. Lang</b>	<b>Professor of Electrical Engineering</b>
<b>Prof. George C. Verghese</b>	<b>Professor of Electrical Engineering</b>
<b>Prof. Samir A. Nayfeh</b>	<b>Assistant Professor of Mechanical Engineering</b>

## Acknowledgments

I would like to thank my advisor Prof. David Trumper for his advice over the course of this thesis. Working with him has been a learning experience which went far beyond just issues related to this thesis. I would also like to thank Prof. Jeffrey Lang. In addition to his inputs on my thesis, Prof. Lang has contributed significantly to my interest in electromechanics. My interest in control theory has to a large extent been shaped by the courses on linear systems and non-linear control that I took with Prof. George Verghese and Prof. Jean-Jacques Slotine respectively. It has been a great experience learning from them and discussing my thesis with them. I have also benefited a lot from my consultations with Prof. Samir Nayfeh about structural design.

Next, I would like to thank Dr. Mark Williams at Ultratech Stepper. Mark has been a great person to work with - a person with lots of ideas, drive and initiative and I consider it a privilege having worked with him on the design of the active isolation system. At Integrated Solutions (now Ultratech Stepper) I have had the assistance of some wonderfully talented and dedicated engineers - Paul Bischoff, now the Director of Engineering who was instrumental in clearing many hurdles in procurement of parts, and Peter Faill, the DSP guru who helped me immensely with the programming of the 'C40 DSPs for the control of the stepper. I also would like to acknowledge the financial support received from Integrated Solutions Inc., and later Ultratech Stepper during most of my time at MIT.

In the lab at MIT, it has been fun interacting with my lab mates. Specific mention should be made of Steve Ludwick and Michael Liebman. It was fun to talk about design and control issues with Steve. I have also had a lot of fun discussing electric machinery with Mike. Robert Ritter, Ming-Chih Weng, David Ma, Paul Konkola, Dave Chargin and Yuka Miyake have also made the precision motion control lab a great place to work. Working at MIT has been made a lot more enjoyable thanks to my friends - John and Peter Madden. The many hours we spent hiking, playing tennis and just chatting about our research are some of the best I've ever had. I should also

not forget to mention the great amount of support I received from Maureen Lynch and David Rodriguera in handling administrative tasks and Fred Cote at the LMP shop.

It is almost impossible to complete a Ph.D. thesis without strong family support. My family has been a great source of strength and inspiration to me - especially my mom, and to her and my dad this thesis is respectfully dedicated. My brother and sister have also been instrumental in supporting me through the pressures of a Ph.D. at MIT, and their support is gratefully acknowledged. Last but not least, my wife Kimberly has been a source of strength when my morale was down and especially during the writing of this thesis taken care of almost everything possible so I could concentrate on my thesis. I am ever so grateful for her support.

# Contents

<b>1</b>	<b>Introduction</b>	<b>22</b>
1.1	Background . . . . .	22
1.2	Overview . . . . .	26
1.2.1	Vibration Isolation . . . . .	26
1.2.2	Structural Resonance . . . . .	31
1.3	Why a Modal Approach? . . . . .	33
1.3.1	Choice of Control Law . . . . .	35
1.3.2	Eigenstructure Assignment . . . . .	37
1.4	Summary of Contributions . . . . .	38
<b>2</b>	<b>Disturbance Mechanisms - Seismic Vibrations</b>	<b>41</b>
2.1	Introduction . . . . .	41
2.2	Vibration Sources and Propagation . . . . .	43
2.3	Spectral Analysis and Bandwidth Issues . . . . .	46
2.4	Review of Current Vibration Requirements . . . . .	52
2.4.1	Nikon . . . . .	52
2.4.2	Canon . . . . .	53
2.4.3	SVG Lithography . . . . .	53
2.4.4	ASM Lithography . . . . .	54
2.5	BBN Criteria . . . . .	56
2.5.1	FHA Criteria . . . . .	57
2.6	Need for Low Frequency Vibration Isolation . . . . .	59
2.7	Summary of Chapter 2 . . . . .	65

<b>3</b>	<b>Passive Vibration Isolation</b>	<b>66</b>
3.1	Introduction . . . . .	66
3.2	Passive Isolation . . . . .	68
3.3	Pneumatic Mounts . . . . .	70
3.4	Negative Stiffness Mechanisms . . . . .	74
3.5	Fundamental limits to Passive Vibration Isolation . . . . .	75
3.6	A Kalman filter approach to the synthesis of passive mounts . . . . .	81
3.6.1	The Kalman Filter . . . . .	82
3.6.2	Optimal Passive mount synthesis . . . . .	87
3.7	Summary of Chapter 3 . . . . .	88
<b>4</b>	<b>Active Isolation Design</b>	<b>90</b>
4.1	Introduction . . . . .	90
4.2	Relevant Literature . . . . .	91
4.2.1	Commercial Devices . . . . .	92
4.3	Active Isolation Architecture . . . . .	95
4.4	The Active Isolation Design Paradigm . . . . .	97
4.5	Feedback Control Design for Active Isolation . . . . .	99
4.6	Single Degree of Freedom Example . . . . .	101
4.7	Frequency Weighting . . . . .	107
4.8	Passive <i>vs.</i> Active Isolation . . . . .	111
4.9	Summary of Chapter 4 . . . . .	113
<b>5</b>	<b>Mechanical Design and Kinematics of the Isolation System</b>	<b>114</b>
5.1	Introduction . . . . .	114
5.2	Mechanical Design . . . . .	115
5.3	Passive Mount Selection . . . . .	120
5.3.1	Analysis of passive mounts . . . . .	120
5.3.2	Passive mount characteristics and location . . . . .	124
5.4	Actuator Design . . . . .	128
5.4.1	Transformations to Compute Actuator Forces . . . . .	136

5.5	Feedback Linearization and the Measurement of Actuator Gaps . . . .	138
5.5.1	Transformations for Gap Computation . . . . .	141
5.6	Measurement of Acceleration . . . . .	144
5.6.1	Anti-Aliasing Filters . . . . .	147
5.6.2	Transformations for Computation of Acceleration of Stepper .	149
5.7	Summary of Chapter 5 . . . . .	153
<b>6</b>	<b>Rigid Body Modeling and Control</b>	<b>154</b>
6.1	Introduction . . . . .	154
6.2	Rigid Body Modeling . . . . .	155
6.2.1	Equations of Motion . . . . .	157
6.2.2	Modal Coordinates . . . . .	159
6.3	Coordinate Frames . . . . .	161
6.4	System Identification . . . . .	163
6.5	Control . . . . .	171
6.5.1	Fine Motion Stage . . . . .	171
6.5.2	Coarse Motion Stages . . . . .	174
6.6	Feedback Control Design for Active Isolation . . . . .	177
6.6.1	Feedforward Control . . . . .	178
6.7	Implementation . . . . .	179
6.8	Experimental Results . . . . .	183
6.9	Summary of Chapter 6 . . . . .	186
<b>7</b>	<b>Flexibility Effects</b>	<b>187</b>
7.1	Introduction . . . . .	187
7.2	Modeling Undamped Mechanical Structures . . . . .	189
7.3	Distributed Feedback Control . . . . .	194
7.3.1	Independent Modal Space Control (IMSC) . . . . .	194
7.3.2	Approximations to Distributed Feedback Control . . . . .	195
7.4	Control and Observation Spillover . . . . .	196
7.4.1	Modal Control . . . . .	198

7.5	Modal analysis of the GCA XLS 7000 series stepper . . . . .	200
7.6	Modeling Flexibility Effects on the Prototype Stepper . . . . .	202
7.7	Summary of Chapter 7 . . . . .	206
<b>8</b>	<b>Eigenstructure Assignment</b>	<b>208</b>
8.1	Introduction . . . . .	208
8.2	Preliminaries and Problem Statement . . . . .	213
8.3	Structural Systems . . . . .	216
8.4	Review of Literature . . . . .	219
8.5	Eigenvalue Assignment for State-Space Systems . . . . .	222
8.5.1	Partial Specification of Eigenvectors . . . . .	225
8.5.2	A Caveat . . . . .	226
8.5.3	Eigenvalue Assignment for Structural Systems . . . . .	227
8.6	Eigenvector Assignment for State-Space Systems . . . . .	228
8.6.1	Selection of the Optimum Eigenvalue . . . . .	234
8.7	A Special Case of Eigenvector Assignment . . . . .	236
8.8	Example of a State Space System . . . . .	237
8.8.1	Eigenvalue Assignment . . . . .	238
8.8.2	Eigenvector Assignment . . . . .	239
8.9	Example of a Structural Problem . . . . .	241
8.10	Application to the Wafer Stepper . . . . .	244
8.11	Summary of Chapter 8 . . . . .	247
<b>9</b>	<b>Conclusion and Future Work</b>	<b>249</b>
9.1	Summary . . . . .	249
9.2	Recommendations for future work . . . . .	252
<b>A</b>	<b>Hardware Interconnections for Active Isolation</b>	<b>254</b>



# List of Figures

1-1	Schematic of the prototype photolithographic wafer stepper illustrating disturbance mechanisms . . . . .	23
1-2	Single degree of freedom system retrofitted with an actuator, a sensor and an active controller. Note the two conflicting disturbance mechanisms $\ddot{z}_0$ and $f_d$ . . . . .	28
1-3	Trade-off between base and payload disturbance rejection. Note that the sensitivity $P(j\omega)$ and the complementary sensitivity $Q(j\omega)$ follow traditional control system practice and sum up to unity. . . . .	28
1-4	The Active isolation design paradigm. . . . .	29
1-5	Isolation performance during stage motions . . . . .	31
1-6	Schematic of a precision machine. . . . .	32
2-1	Effect of Isolation Break in Slab on a Rayleigh wave. Reproduced from Gordon [27]. . . . .	45
2-2	Practical <i>vs.</i> ideal filter characteristics . . . . .	47
2-3	Bandwidth computations for narrow band analysis illustrated for a 400-line FFT over a 0-100 Hz range. The passband is $100/400 = 0.25$ Hz and the bandwidth with a Hanning window is $1.5 \times 0.25 = 0.375$ Hz. . . . .	48
2-4	Frequency Response Functions of two different one-third octave filters ( $f_0$ denotes the center frequency). Note the proportional bandwidth of the two filters (appears to be a constant bandwidth in a logarithmic plot). . . . .	49

2-5	Allowable floor vibration level for the Nikon NSR-S203 Series steppers. One-third octave band spectrum, values are 0-to-peak acceleration. The horizontal specification applies both to front-back and left-right directions [52]. . . . .	53
2-6	Allowable floor vibration level for the Canon FPA-3000i5 Series steppers. Power spectrum amplitude is measured 0-peak and a Hanning window used to prevent spectral leakage [18]. . . . .	54
2-7	Allowable floor vibration level for the ASML PAS 5500/500 Series steppers [3]. . . . .	55
2-8	BBN floor vibration criteria (VC) curves for precision equipment installation showing also ISO guidelines [26]. The curves limit the RMS velocity output of one-third octave filters centered along the frequency range illustrated. . . . .	56
2-9	FHA floor vibration criteria. Reproduced from Owen <i>et al.</i> [54]. . . . .	57
2-10	Two degree of freedom model representing the first longitudinal mode of vibration of the prototype stepper in the vertical(Z) direction . . . . .	60
2-11	Comparison of the first-order Markov process to VC-E requirements . . . . .	62
2-12	Comparison of the three different transfer functions corresponding to a) Hard mount, b) Passive Isolation, and c) Active Isolation. . . . .	63
3-1	Schematic of prototype stepper showing disturbance mechanisms and Cartesian coordinate frame fixed to the center of gravity . . . . .	67
3-2	Single degree of freedom passive vibration isolation system illustrating seismic disturbances . . . . .	68
3-3	Transmissibility of a single degree of freedom passive vibration isolation system for various values of damping ratio . . . . .	69
3-4	Zener or "sprung-damped" model for a pneumatic isolation system. $V_s$ and $V_d$ are the volumes of the spring chamber and damping chamber respectively. $N$ is the spring ratio. . . . .	71

3-5	Transmissibility of a pneumatic vibration isolation system for various values of damping ratio . . . . .	72
3-6	Illustration of the negative spring stiffness mechanism used to obtain sub-hertz isolation. Net isolator stiffness can be made to approach 0, $K = K_s - K_n$ . Illustration reproduced from Platus [56] . . . . .	75
3-7	Single degree of freedom passive vibration isolation system illustrating both seismic and payload disturbances . . . . .	76
3-8	Multi-degree of freedom passive vibration isolation problem cast as a feedback control design problem . . . . .	78
3-9	Trade-off between base and payload disturbance rejection as the natural frequency of the mount $\bar{\omega}_n$ is changed from 1 to 2. Note that the sensitivity $P(j\omega)$ and the complementary sensitivity $Q(j\omega)$ follow traditional control system practice. . . . .	80
3-10	Illustration of the stochastic dynamics of the plant and its Kalman filter for the passive isolation problem. . . . .	85
4-1	Schematic representation of a single axis hardmount reproduced from Beard <i>et al.</i> [12]. $M_P$ is the payload to be isolated, $M_i$ the intermediate mass, $K_p$ the stiffness of the elastomeric mount and $K_a$ the finite stiffness of the piezoelectric actuator. . . . .	93
4-2	Comparison of Parallel and Series Isolation Architectures . . . . .	95
4-3	Influence of active control on a passive mount. Active isolation design paradigm. . . . .	98
4-4	The general feedback system description. . . . .	100
4-5	Single degree of freedom system retrofitted with an actuator, a sensor and an active controller. Note the explicit negative feedback employed. . . . .	101
4-6	LQG compensator transfer function that provides isolation over two decades. . . . .	103
4-7	Plant and LQG loop transfer functions with $\rho$ and $\Theta$ chosen to set bandwidth to a decade above and below mount resonance. . . . .	104

4-8	Nyquist plot of the LQG loop transfer functions illustrated in Figure 4-7 along with the unit circle. Note the 60 degree phase margin at both crossover points. . . . .	105
4-9	Sensitivity plot for the active mount. Note active isolation provides isolation over a decade above and a decade below the open-loop resonance. . . . .	105
4-10	Transmissibility plot for active (closed-loop) and passive (open-loop) mounts. Note active isolation provides isolation over a decade above and a decade below the open-loop resonance. . . . .	106
4-11	Payload disturbance rejection for the active and passive mounts. Note the improved rejection of the active mount one decade above and one decade below the open-loop resonance. We are no longer governed by the fundamental tradeoff of (3.16). . . . .	107
4-12	Frequency shaping cost functions $W_z(j\omega)$ and $W_u(j\omega)$ to obtain narrowband and broadband improvement in isolation performance. . . .	110
4-13	Frequency shaping of the sensitivity function to obtain a notch in the transmissibility around the passive mount resonance. Note the decreased magnitude of the sensitivity function at the mount resonance as compared to 4-9. . . . .	111
4-14	Frequency shaping of the sensitivity function to illustrate a notch in the transmissibility around the passive mount resonance. . . . .	112
5-1	Schematic of prototype stepper showing disturbance mechanisms and Cartesian coordinate frame fixed to the center of gravity . . . . .	115
5-2	Cutaway view of one leg of the system . . . . .	118
5-3	Picture of the passive components and actuators of a single leg. A 12-inch ruler and a nickel are also shown to give a sense of scale. . . .	119

5-4	Free acceleration profile of the stepper due to a step motion of 20 mm of the X-coarse stage. The time-domain plot of the acceleration profile as well as a 1024 point FFT are illustrated. The FFT clearly shows the higher-order harmonics as well as the fundamental disturbance at 5 Hz. . . . .	121
5-5	Power spectral density (PSD) plots of the payload disturbance and seismic vibrations. The payload disturbance is found to be modeled by a first-order Markov process and both the PSD and its fit are illustrated. Seismic vibrations are also modeled by a first-order Markov process along the lines of Chapter 2. . . . .	122
5-6	Power spectral density (PSD) plots of the payload error motion due to payload force disturbance and seismic vibrations. Note that the chief contributor to error motions is the payload force disturbance. . . . .	123
5-7	Experimental setup to determine Mount Parameters : The Mass of the casting is separately determined to be 296.8 Kg. . . . .	124
5-8	Acceleration of Base Casting in the Z direction when subjected to an impulse . . . . .	125
5-9	Location of Passive Mounts. The Cartesian coordinate frame is fixed to the center of gravity of the stepper. . . . .	127
5-10	Cross section of a variable reluctance actuator . . . . .	130
5-11	Calibration curves for the variable reluctance actuators . . . . .	131
5-12	Forces provided at each leg location . . . . .	132
5-13	Assembly of actuators to leg. A 12-inch ruler as well as a nickel on the top of the mount are shown for scale. . . . .	133
5-14	Layout of the Actuators for Active Isolation : Note that the plane of actuation (in the Z direction) coincides with the plane of support defined in Figure 5-9. . . . .	134
5-15	Four legs, each turned around by 90 degrees showing the actuator locations . . . . .	135
5-16	Connection of Actuator Pairs to Power Amplifier . . . . .	136

5-17	A leg during assembly showing the capacitance gauge positions. Three legs are instrumented with capacitance probes as shown. . . . .	140
5-18	The components of a single instrumented leg showing the actuators, targets, capacitance gauges and accelerometers in place. The top plate is bolted to the post to complete the assembly. . . . .	145
5-19	Overall accelerometer FRF showing electrical and mechanical error regions as well as working region . . . . .	146
5-20	Experimentally determined FRF of Vibrametrics accelerometer (serial # 831) showing the gradual phase loss over the working region . . . .	148
5-21	Unity-gain, low pass Sallen-Key Anti-Aliasing filter. Note the 500 K $\Omega$ impedance across the output of the accelerometer amplifier to prevent saturation. . . . .	148
5-22	Frequency response of anti-aliasing filter. Experimental response is plotted using solid lines and predicted response using dashed lines. . .	149
5-23	Layout of the sensors and actuators for the active isolation system. Capacitance probes are shown mounted away from legs for clarity . .	151
5-24	Photograph of the four active legs assembled to the prototype wafer stepper . . . . .	152
6-1	Schematic illustrating the sequence of events that take place each sample interval. All the computations illustrated are implemented on a parallel DSP system comprising 8 'C40 DSPs on a VME bus. A total of 14 degrees of freedom are controlled to position the wafer precisely under the optical column. . . . .	155
6-2	Displaced three degree of freedom rigid body model in the X-Z plane. The dampers are assumed to be in parallel with the springs and are not shown. . . . .	157
6-3	Displaced rotational system in the X-Y plane. The dampers are assumed to be in parallel with the springs and are not shown. . . . .	158

6-4	System identification setup. Both forces and acceleration are in the Cartesian coordinate frame to obtain the transfer functions listed in (6.12). . . . .	164
6-5	Transfer function $\ddot{x}/F_x$ . . . . .	165
6-6	Transfer function $\ddot{\theta}_y/F_x$ . . . . .	166
6-7	Transfer function $\ddot{y}/F_y$ . . . . .	166
6-8	Transfer function $\ddot{\theta}_x/F_y$ . . . . .	167
6-9	Transfer function $\ddot{z}/F_z$ . . . . .	167
6-10	Transfer function $\ddot{\theta}_x/\tau_x$ . . . . .	168
6-11	Transfer function $\ddot{y}/\tau_x$ . . . . .	168
6-12	Transfer function $\ddot{\theta}_y/\tau_y$ . . . . .	169
6-13	Transfer function $\ddot{x}/\tau_y$ . . . . .	169
6-14	Transfer function $\ddot{\theta}_z/\tau_z$ . . . . .	170
6-15	Time domain simulation of the transfer function $\ddot{x}/F_x$ compared to measured acceleration of the stepper when the X Coarse stage motion is profiled according to a triangular velocity law. . . . .	171
6-16	Loop transmission for the fine stage using a lead-lag compensation law. Note the crossover frequency of 100 Hz. . . . .	172
6-17	Error function for the fine motion stage. . . . .	173
6-18	Comparison of experimental and predicted step responses. Note the close match in between the two. The small phase delay is attributed to a one sample interval delay. . . . .	174
6-19	Loop transmission for the Y coarse motion stage using a lead-lag compensation law. Note the crossover frequency of 50 Hz. . . . .	175
6-20	Error function for the Y coarse motion stage. . . . .	175
6-21	Comparison of experimental and predicted transient responses of the Y Coarse stage. The stage motion is profiled according to a triangular velocity law. Note the close match in between the simulation and experiment. . . . .	176

6-22	Vibration transmissibility of the active controller illustrating broad-band and narrowband improvements over passive isolation. . . . .	177
6-23	DSP Architecture used for the ISIS/Active isolation project. The dashed lines represent the fast serial port connections in between the Hydra card and the Commio cards. Note HP1-3 represents the 3 <sup>rd</sup> comm port of the HP 1 'C40 processor and so on. . . . .	180
6-24	Active Isolation Control algorithm . . . . .	180
6-25	Frequency response of band-pass filter. Filter is implemented in assembly as a second order IIR Biquad. . . . .	182
6-26	Experimental setup to measure Z-axis transmissibility. Note that the accelerometer on the bridge of the stepper represents the Z-axis acceleration computed by the DSP according to (5.21) . . . . .	184
6-27	Measured Z axis Transmissibility . . . . .	184
6-28	Isolation performance during stage motions . . . . .	186
7-1	Discretized model of a precision machine. Note that the performance motion is affected by the flexibility of the machine components. . . .	188
7-2	Control and Observation Spillover [8]. . . . .	199
7-3	Six degree of freedom lumped parameter model of the stepper, coarse stage and fine stage in the XZ plane. Note the bending mode of the lens column at 84.3 Hz is modeled by the mass $M_r$ . . . . .	203
7-4	FFT of error motions in the X direction. Note the first five peaks, all below 100 Hz. These are due to control spillover which causes these modes to be continuously excited. . . . .	205
8-1	Characterization of the space of attainable eigenvectors. Projecting the desired eigenvector $\phi_i^d$ onto this space results in minimum 2-norm of the error $\ \epsilon_i\ _2$ . . . . .	224
8-2	Characterization of the space of attainable eigenvectors. . . . .	230
8-3	Multi-input electric circuit [40]. . . . .	237
8-4	Step response from eigenvalue assignment. . . . .	239



<b>8-5</b>	<b>Surface plot of error norm . . . . .</b>	<b>240</b>
<b>8-6</b>	<b>Step response from eigenvector assignment . . . . .</b>	<b>241</b>
<b>8-7</b>	<b>Four degree of freedom structural system . . . . .</b>	<b>242</b>
<b>8-8</b>	<b>FFT of error motions in the <math>X</math> direction. Note the clear attenuation of the flexible bending mode at 84.3 Hz. Also due to the lack of an integrator in the fine stage control law, low frequency performance of the modal controller is worse than the LQG controller. . . . .</b>	<b>245</b>

# List of Tables

1.1	Product critical level lithography requirements (Excerpts from Table 24 of the National technology roadmap [4]) . . . . .	24
1.2	Settling times on the prototype wafer stepper for the various cases of isolation/control. Settling time in this thesis is defined as the time it takes for error motions in between the stage and the lens column to be less than 50 nm following a 20 mm step. The 20 mm step is the result of a triangular velocity profile over 250 ms. . . . .	25
1.3	Comparison of the performance of active and passive isolation. Note that the transmissibility of the passive mount is the sensitivity function times the passive transmissibility for both disturbance mechanisms. .	30
2.1	Application and interpretation of the BBN criterion curves shown in Figure 2-8. Amplitude limits are RMS values. Table reproduced from [26]. . . . .	58
2.2	Application and interpretation of the FHA criterion curves shown in Figure 2-9. Amplitude limits are RMS values [54]. . . . .	59
2.3	Product critical level lithography requirements (Excerpts from Table 24 of the National technology roadmap [4]) . . . . .	60
2.4	Comparison of standard deviation of error motions for the two degree of freedom model . . . . .	64
4.1	Comparison of the performance of active and passive isolation. Note that the transmissibility of the passive mount is the sensitivity function times the passive transmissibility for both disturbance mechanisms. .	99

5.1	Inertial Parameters of Prototype Wafer Stepper with the coarse stages positioned at the center of their stroke. Note negligible Products of Inertia . . . . .	116
5.2	Inertial Parameters of the coarse and fine motion stages. Products of Inertia of the fine stage are negligible and not mentioned . . . . .	117
5.3	Passive Mount Parameters. The parameters in the vertical direction $K_z$ and $C_z$ are measured using the logarithmic decrement method, while the lateral stiffness and damping parameters $K_x$ and $C_x$ are set to equal the values in the vertical direction. . . . .	126
5.4	Passive Mount Location : Note that the plane of support/actuation is offset from the center of gravity of the stepper leading to coupled rotational and translational motion . . . . .	128
5.5	Actuator Parameters . . . . .	130
5.6	Actuator Locations from Center of Gravity of Stepper . . . . .	132
5.7	Capacitance Gauge Locations from Center of Gravity of Stepper . . . . .	139
5.8	Accelerometer Locations from Center of Gravity of Stepper . . . . .	147
6.1	Coarse stage force vector stage location in the Cartesian coordinate frame. Note that $y_{fcx}$ changes in real time with the movement of the stage. . . . .	178
6.2	Arrangement of DSPs on the VME bus and their functions . . . . .	181
7.1	GCA XLS 7000 Series machine rigid body modal parameters. Reproduced from the Sandia report [65]. . . . .	201
7.2	Generalized coordinates for the six degree of freedom model of the prototype stepper illustrated in Figure 7-3 . . . . .	204
7.3	Identification of flexible modes in the error motions between the fine stage and the lens. . . . .	205

8.1	Settling times on the prototype wafer stepper for the various cases of isolation/control. Settling time in this thesis is defined as the time it takes for error motions in between the stage and the lens column to be less than 50 nm following a 20 mm step. The 20 mm step is the result of a triangular velocity profile over 250 ms. . . . .	246
A.1	Actuator Pairs, D/A Channels : The 8 actuator pairs are driven by power amplifiers which are connected to the Digital to Analog Converters on Industry Pack 2 (8 channels) on COMM/I0 3 . . . . .	254
A.2	Capacitance Gauges, A/D Channels : All the capacitance gauge signals are connected to the Analog to Digital Converters on Industry Pack 0 (8 channels) on COMM/I0 3 . . . . .	255
A.3	Accelerometer Gains, A/D Channels : All the accelerometer signals are connected to the Analog to Digital Converters on Industry Packs 0 (4 channels) and 1 (2 channels) on COMM/I0 4 . . . . .	255

# Chapter 1

## Introduction

### 1.1 Background

This thesis investigates the motion control requirements of modern-day precision machines and presents mechanical and control design solutions to enable precise and rapid motions. A prototype wafer stepper<sup>1</sup> illustrated in Figure 1-1 is the platform for the developments throughout this thesis. The stepper comprises a pair of stacked X and Y coarse stages and a 6-degree of freedom MAGLEV fine stage to position the wafer accurately in all 6-degrees of freedom under the optical column. To obtain an idea about the accuracy of motions demanded by the photolithography process, we reproduce an excerpt from the national technology roadmap for semiconductors sponsored by the Semiconductor Industry Association (SIA) and published by Sematech [4] in Table 1.1. The parameter of interest to us is the overlay which determines the accuracy to which one layer of the semiconductor integrated circuit being processed needs to be positioned over the previous one. At the nanometric levels of overlay required as illustrated in Table 1.1, significant demands are made on the mechanical and control design of the wafer stepper. The increased accuracy in positioning the wafer must also be weighed against the increased dynamic range of motions required due to increasing wafer diameter. The design of the motion control scheme (both

---

<sup>1</sup>ISIS series of steppers made by Ultratech Stepper, Tewksbury, MA

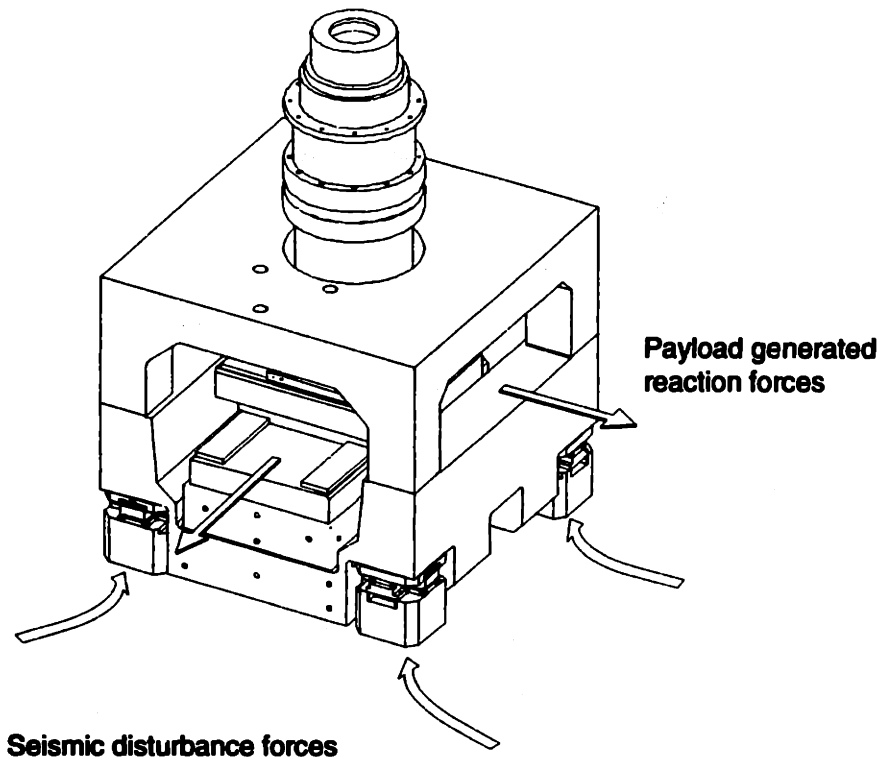


**Figure 1-1: Schematic of the prototype photolithographic wafer stepper illustrating disturbance mechanisms**

structural as well as control design) must be able to balance the rather large dynamic range ( $\approx 10^6$ ) against the stringent positioning requirements.

Two of the biggest impediments towards realizing the performance goals are due to

- **Environmental Disturbance :** At nanometric levels of positioning accuracy, environmental effects become significant. These could be due to thermal effects, windage, turbulence in the ducts etc. According to Gordon [27], the most significant environmental disturbance in a micro-electronics fabrication facility is due to seismic vibrations.
- **Structural Resonance :** The wafer stepper is a rather large machine due to the size of the wafers that need to be handled, the range of motion required and the need for various subsystems such as optical systems, handling systems

---

<sup>2</sup>For isolated lines (MPU Gates)

<sup>3</sup>Mean +  $3\sigma$

Year	1997	1999	2001	2003	2006	2009	2012
Technology	250 nm	180 nm	150 nm	130 nm	100 nm	70 nm	50 nm
Min. Feature Size <sup>2</sup> [nm]	200	140	120	100	70	50	35
Product Overlay <sup>3</sup> [nm]	85	65	55	45	35	25	20
Wafer Diameter [mm]	200	300	300	300	300	450	450

**Table 1.1: Product critical level lithography requirements (Excerpts from Table 24 of the National technology roadmap [4])**

etc. Resonant frequencies scale inversely with size and complexity and as such their effects are unavoidable on a wafer stepper although close attention is paid to the design of the machine. Seismic vibrations and disturbances due to the motion of other components on the stepper excite the structural resonances on the machine and cause error motions.

From a motion control standpoint, these are two conflicting phenomena - the presence of structural resonance reduces the attainable loop gain and environmental disturbances require high gain control. This is a fundamental limitation of feedback control [5] where the need for performance needs to be balanced against the need for robustness. Given the above, it becomes important to address both environmental disturbances as well as structural resonance carefully. This thesis addresses these issues in a phased manner.

Table 1.2 highlights the key results from this thesis while illustrating the performance benefits obtained by careful structural and control design. Three different cases are presented in Table 1.2. All three correspond to a 20 mm step motion of the X-coarse stage of the wafer stepper. This motion is profiled according to a triangular velocity profile which is tapered off at the end with a spline to produce jerk-free motion. The velocity profile is spread over a period of approximately 250 ms. The settling time is measured by the amount of time it takes for the relative motion between the lens column and the mirror on the fine stage to settle below a peak of 50 nm

Description	Settling Time [ms]
Passive Isolation	2500
Active Isolation (LQG + IMSC)	550
Active Isolation (Modal)	350

Table 1.2: Settling times on the prototype wafer stepper for the various cases of isolation/control. Settling time in this thesis is defined as the time it takes for error motions in between the stage and the lens column to be less than 50 nm following a 20 mm step. The 20 mm step is the result of a triangular velocity profile over 250 ms.

in all 6 axes<sup>4</sup>.

The first case corresponds to current industry practice where the stepper is placed on passive mounts which are either pneumatic or elastomeric. For the data obtained in this thesis, the stepper is placed on elastomeric mounts that result in a natural frequency of around 15-20 Hz. The passive isolation helps reject seismic vibrations, but the settling time is seen to be about ten times the period of the motion profile and hence not an optimal solution. Later, in this thesis, passive isolation is shown to suffer from a fundamental tradeoff which explains the long settling times required. The second case corresponds to an active isolator for the stepper. Active isolation is shown to attenuate both seismic vibrations and payload disturbances (due to stage motions) in this thesis and does not suffer from the tradeoff due to passive isolation. Thus active isolation is an optimal means of obtaining rapid settling and good attenuation of error motions. The active isolation scheme for the second case is designed using a combination of Linear Quadratic (LQG) techniques and Independent Modal Space Control (IMSC) and does not consider the flexibility of the wafer stepper. Addressing the structural resonance of the wafer stepper using a modal control law proposed in this thesis leads to further performance improvements where the stepper takes only 100 ms more than the motion profile to reach a settled state.

Table 1.2 thus provides a motivation for the work described in this thesis. Performance improvements through isolation of the machine from environmental disturbances are demonstrated followed by a further improvement in performance obtained

---

<sup>4</sup>In its current implementation, only five axes are considered, the auto-focus mechanism for the Z-axis is not in place yet.



by considering the flexural dynamics of the machine. Although we focus on the prototype wafer stepper of Figure 1-1, the developments in this thesis can also be applied to other machines or instruments which exhibit similar characteristics and requirements. Examples of such precision machines include photolithographic steppers, diamond turning machines, coordinate measuring machines, precision grinders and hard disk drives.

## **1.2 Overview**

The motion control specifications for the stepper illustrated in Figure 1-1 are given for the optical length and the alignment of the wafer with the reticle. The speed and accuracy of the desired motions require innovative approaches not only to the feedback control problem, but also to sensing, actuation, design, modeling and disturbance attenuation. A review of literature does not show how to design a controller for such a machine, let alone integrate the mechanical and control design. In this thesis, we address the problems of disturbance attenuation and structural resonance simultaneously to realize optimal performance of the machine.

### **1.2.1 Vibration Isolation**

Chapter 2 presents a review of the disturbance mechanisms encountered by such a machine. The primary disturbance mechanisms are seismic disturbances which are stochastic, and inertial forces due to stage motion which are deterministic as illustrated in Figure 1-1. In addition, Chapter 2 reviews propagation of seismic vibrations and discusses ways and means to attenuate vibration through proper design of the environment. A review of the requirements imposed by leading stepper vendors on the vibration environments is presented followed by a review of generic vibration criteria and a tutorial on representation of vibration spectra in the frequency domain. We then demonstrate the need for low frequency vibration isolation by creating a simple two degree of freedom model that represents the first flexible mode of the stepper and use a simple power spectral density representation of floor vibrations to excite

this model. This simulation along with the technology roadmap from the national semiconductor association [4] clearly establishes the need for vibration isolation in wafer steppers.

It has long been known that payload and seismic disturbances impose conflicting requirements on the isolation system calling for hard and soft mounts respectively. However, an analytical treatment of this fundamental tradeoff is not available in literature. Chapter 3 derives this fundamental tradeoff by posing the passive isolation problem in a control system design framework. Considering a rigid body (with all six degrees of freedom) subject to seismic vibrations and supported by discrete isolators, we have the following :

$$\begin{aligned}
 \ddot{\mathbf{X}}(s) &= (\mathbf{M}s^2 + \mathbf{C}s + \mathbf{K})^{-1} \mathbf{M}s^2 (\mathbf{M}^{-1}\mathbf{F}_d(s)) + \\
 &\quad (\mathbf{M}s^2 + \mathbf{C}s + \mathbf{K})^{-1} (\mathbf{C}s + \mathbf{K}) \ddot{\mathbf{X}}_0(s) \\
 &= \mathbf{P}(s) (\mathbf{M}^{-1}\mathbf{F}_d(s)) + \mathbf{Q}(s)\ddot{\mathbf{X}}_0(s)
 \end{aligned} \tag{1.1}$$

where  $\mathbf{X}(s)$  is a six dimensional vector comprising the Laplace transforms of the six rigid body degrees of freedom,  $\mathbf{M}$  the mass/inertia matrix,  $\mathbf{C}$  the damping matrix and  $\mathbf{K}$  the stiffness matrix.  $\mathbf{X}_0$  is a six dimensional vector of seismic vibrations and  $\mathbf{f}_d$  is a six dimensional vector of payload disturbance forces. Equations (1.1) illustrate the sensitivity and complementary sensitivity functions for a multi-degree of freedom system. We observe from (1.1) that

$$\mathbf{P}(s) + \mathbf{Q}(s) = \mathbf{I} \tag{1.2}$$

This establishes the fundamental tradeoff for a passive device in analytical terms. Payload accelerations are related to payload disturbance forces through the sensitivity function and to seismic disturbances through the complementary sensitivity function. Thus, the passive design problem is shown to be subject to the same fundamental tradeoff that exists in control systems design, *i.e.*, the sensitivity and complementary sensitivity functions sum up to unity. The single degree of freedom

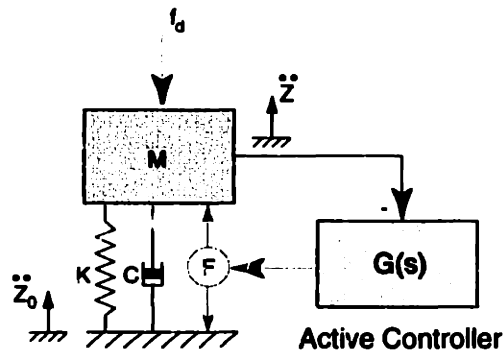


Figure 1-2: Single degree of freedom system retrofitted with an actuator, a sensor and an active controller. Note the two conflicting disturbance mechanisms  $\ddot{z}_0$  and  $f_d$ .

example in Figure 1-2 is used to illustrate this fundamental tradeoff. A dimensionless

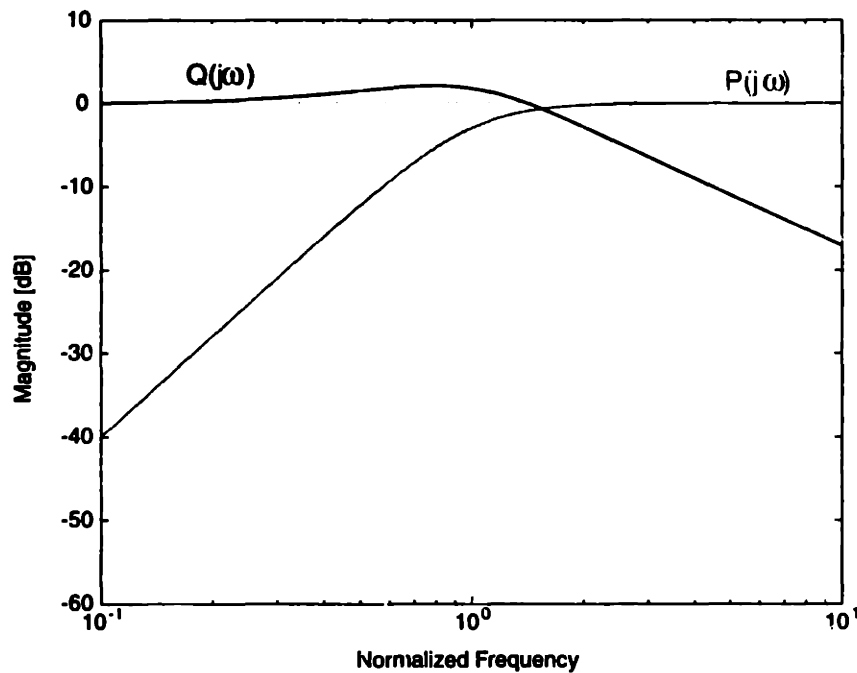


Figure 1-3: Trade-off between base and payload disturbance rejection. Note that the sensitivity  $P(j\omega)$  and the complementary sensitivity  $Q(j\omega)$  follow traditional control system practice and sum up to unity.

plot of (1.1) for a damping ratio of 0.707 is illustrated in Figure 1-3 as a function of normalized frequency. Improved vibration isolation comes at the expense of payload disturbance rejection and vice-versa. The sensitivity and complementary sensitivity functions always sum up to unity.

We carry our investigations on passive isolation further by posing the design of an

optimal mount (mount stiffness and damping) as a Kalman filtering problem. This is motivated by the fact that in a control system, process disturbances are related to the output through the sensitivity function and sensor noise through the complementary sensitivity function. A Kalman filter is an optimal filter that minimizes the state estimation errors in the presence of these conflicting noise sources, and the passive isolation design problem can be cast into the form of a filter design problem. Chapter 3 also details the low frequency isolation options - these are either due to pneumatic mounts or negative stiffness mechanisms. An expository overview of these mechanisms is presented.

Passive and active vibration isolation schemes are compared in Chapter 4. Commercially available active isolation systems are discussed and the differences between their approach and the approach in this thesis highlighted. Active isolation architectures and their implications on actuation are discussed. We also demonstrate that an active mount is not subject to the same fundamental tradeoff as a passive mount. To observe this, consider the active control paradigm illustrated in Figure 1-4. The

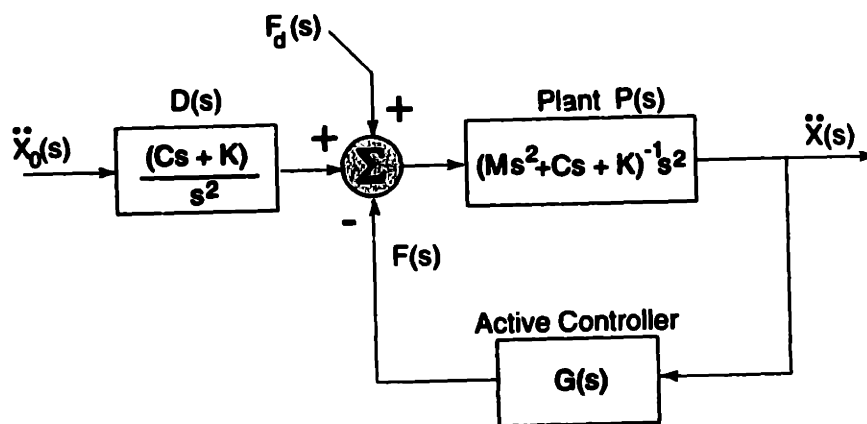


Figure 1-4: The Active isolation design paradigm.

sensitivity function of the loop is given by

$$S(s) = (I + PG)^{-1} \quad (1.3)$$

By manipulation of the block diagram in Figure 1-4, we obtain the results in Table 1.2.1. We see that the sensitivity function of the loop has the same effect on

Disturbance	Passive	Active
Seismic	$\mathbf{PD}\ddot{\mathbf{x}}_0$	$\mathbf{SPD}\ddot{\mathbf{x}}_0$
Payload	$\mathbf{P}\mathbf{f}_d$	$\mathbf{SP}\mathbf{f}_d$

Table 1.3: Comparison of the performance of active and passive isolation. Note that the transmissibility of the passive mount is the sensitivity function times the passive transmissibility for both disturbance mechanisms.

both the conflicting disturbance sources. Thus, through the application of active compensation, performance improvements can be realized in both seismic transmissibility as well as payload disturbance rejection. We obtain performance improvement over the passive case when the sensitivity function is less than unity. The sensitivity function is shaped by a LQG approach. This  $\mathcal{H}_2$  approach is chosen since most performance specifications are RMS values. A simple application of a LQG compensator is demonstrated for a single degree of freedom system. This sets the roll-up and roll-off crossover frequencies. Frequency weighting is presented as a technique to design and implement higher order compensators and provide narrow-band attenuation in addition to broad-band attenuation.

The mechanical design of a parallel active/passive isolation system developed in this thesis is outlined next. The isolation hardware is discussed in detail, specifically, the mounts, actuators and sensors. An analytical study of the resulting error motions from the passive mount is presented. Constitutive relations for the mounts, actuators, sensors and amplifiers are developed. The location of the mounts, actuators and sensors is discussed and used to derive the kinematic relations of the wafer stepper. For this purpose, a Cartesian coordinate frame is set up and linear transformations derived to relate the quantities in this frame to the actuator forces and sensor measurements. The actuators selected are non-linear, but are chosen nevertheless for their small footprint. Feedback linearization is used as a tool to linearize the actuators. Various issues with the sensors and actuators are discussed.

A rigid-body model is set up for the machine and used to derive the equations of motion in Chapter 6. These equations are used to derive a natural or modal coordinate

frame. The relationship between this coordinate frame and the Cartesian coordinate frame in Chapter 5 is derived. This is followed by the experimental determination of various key transfer functions using a swept-sine system identification procedure. These transfer functions are found to match well with those predicted by the model. The application of the compensator design techniques from Chapter 4 to the wafer stepper is demonstrated. Specifications on the shape of the sensitivity function are derived based on our knowledge of the disturbance phenomena as well as the passive mount parameters. The feedback control law is derived using a frequency weighted LQG approach [29]. The implementation of the control law for the isolation system as well as the stages of the stepper on the parallel 8-processor 'C40 DSP system is then described. Experimental results on transient response during stage motion and transmissibility of the isolation system are also presented. The performance of the

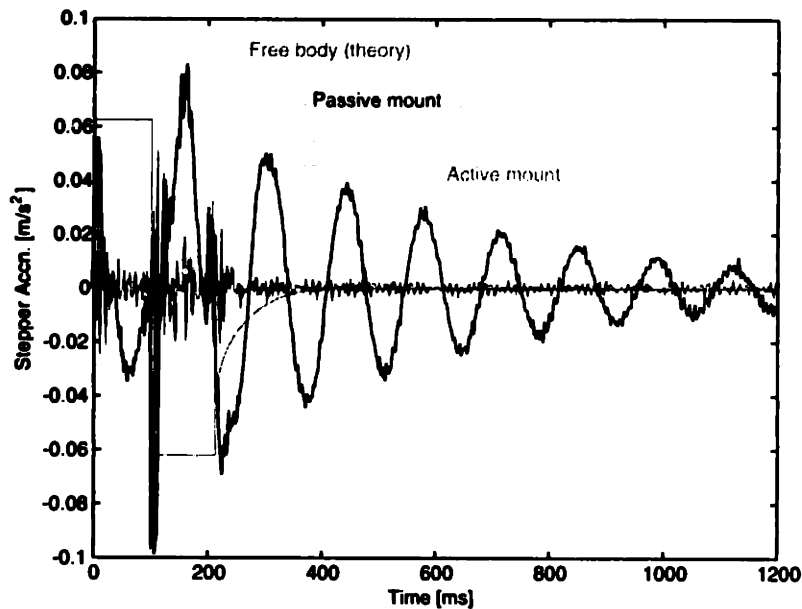


Figure 1-5: Isolation performance during stage motions

active and passive isolation schemes is compared in Figure 1-5.

## 1.2.2 Structural Resonance

So far in the development of the isolation system, the variable of interest was the motion of the base of the stepper in determining the efficiency of the isolator. How-

ever the real performance measure is the optical length in between the reticle and the wafer. The fundamental resonance of the optical column falls within the active bandwidth of both the isolation system and the stage control loops. As such, it is important to model the effects of this resonance to ensure stability of the loop as well as improve performance. Figure 1-6 illustrates a generic precision machine that has

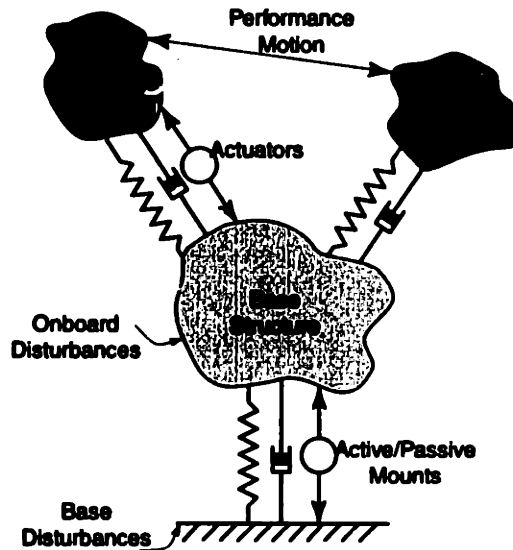


Figure 1-6: Schematic of a precision machine.

such a resonance.

Motion control requirements for such machines typically involve the following :

- Stable motions and controlled transient behavior
- Fast, precise positioning and settling
- Good rejection of both environmental and onboard disturbances

The design engineer meets these specifications by mounting actuators and other compliant springs in between the various masses. The traditional approach has been to make the machine as stiff as possible such that the flexible modes of both the static and moving elements are above the control bandwidth. With increasing bandwidth requirements and limited specific stiffness of structural materials, it is difficult to design machines that are much stiffer. This leads to compromises in attainable performance. We propose the engineering of these flexible modes, *i.e.*, we acknowledge

the presence of flexible modes in the control bandwidth and circumvent it by proper design of the control scheme.

Canonical models along the lines of Figure 7-1 for precision machines are presented in Chapter 7. The effect of structural resonance on control performance is discussed. The work of Balas [8] is reviewed to introduce the concept of control and observation spillover and their detrimental effects on the stability and performance of the wafer stepper. The flexural dynamics of the prototype wafer stepper is derived using the results of a modal analysis on a similar wafer platform by Sandia National Labs [65]. Higher order models are created to consider the flexural dynamics. These are used along with the mode shape assignment procedure derived in Chapter 8 to compute the feedback gain matrix for the prototype wafer stepper. The resulting controller is implemented on the prototype stepper and the error motions are compared to those from Chapter 6. We conclude by demonstrating that there is considerable improvement in performance through experimental evaluations on the prototype stepper.

### **1.3 Why a Modal Approach?**

A significant effort is spent on the design and modeling of precision machines. This can be used to set up detailed higher order models over the desired frequency span. True models of the machine structure are infinite-dimensional, but to be useful from a controls perspective, we need to consider only a finite number of modes within the frequency span of interest. Thus, the model itself is usually discretized by a consideration of the modal properties of the machine and it seems natural to follow a similar approach to the control problem. In most cases, these models are obtained by experimental means through modal testing and can be used to assign values to the masses and springs shown in Figure 1-6. Instead of using this modeling effort to form an unstructured uncertainty bound as is done in modern  $H_\infty$  control techniques, we retain the structure of the uncertainty to design controllers to obtain improved performance. Our approach to the control problem is in a modal sense. Specifically, we attempt to assign closed-loop natural frequencies and mode shapes to the machine



structure. This modal approach relates the flexible modes of the machine structure to the attainable closed-loop modes. This permits us to engineer structural resonance rather than following the age old engineering paradigm of making the machine as stiff as possible. This has implications on the mechanical design and therefore, the cost of the machine. Our modal approach to the control problem is based on the premise that this is the most natural way to manipulate the dynamics of a structure. This is made evident by the following discussion.

The forced response, disturbance response and initial condition response of the machine can all be expressed as linear combinations of the various modes of the machine. Following standard state variable notation we have

$$\begin{aligned}\dot{\mathbf{x}}(t) &= \mathbf{A}_c \mathbf{x}(t) + \mathbf{B}_r \mathbf{r}(t) + \mathbf{E} \mathbf{d}(t) \\ \mathbf{z}(t) &= \mathbf{C}_p \mathbf{x}(t)\end{aligned}\tag{1.4}$$

where  $\mathbf{x}(t) \in \mathfrak{R}^n$  is the state vector,  $\mathbf{z}(t) \in \mathfrak{R}^p$  the performance measure (that we would like to keep as small as possible),  $\mathbf{r}(t) \in \mathfrak{R}^m$  the reference,  $\mathbf{d}(t) \in \mathfrak{R}^r$  the disturbance,  $\mathbf{A}_c$  the closed-loop state matrix,  $\mathbf{B}_r$  the reference coupling matrix,  $\mathbf{E}$  the disturbance coupling matrix and  $\mathbf{C}_p$  the performance matrix. Now, the zero state response of the performance measure is given by the integral,

$$\mathbf{z}(t) = \mathbf{C}_p \int_0^t e^{\mathbf{A}_c(t-\tau)} [\mathbf{B}_r \mathbf{r}(\tau) + \mathbf{E} \mathbf{d}(\tau)] d\tau\tag{1.5}$$

Substituting the spectral decomposition of  $\mathbf{A}_c = \Phi \Lambda \Psi^T$  in the above,

$$\mathbf{z}(t) = \mathbf{C}_p \Phi \int_0^t e^{\Lambda(t-\tau)} [\Psi^T \mathbf{B}_r \mathbf{r}(\tau) + \Psi^T \mathbf{E} \mathbf{d}(\tau)] d\tau\tag{1.6}$$

we observe that the shape of the response to both reference signals and disturbance inputs is significantly influenced by the left  $\Phi$  and right modal matrices  $\Psi$ .  $\Lambda$  is the matrix of eigenvalues.

We initially make the assumption that the matrix  $\mathbf{A}_c$  is diagonalizable. Under this assumption, we can rewrite the spectral decomposition of the closed loop matrix

as :

$$\mathbf{A}_c = \Phi \Lambda \Psi^T = \sum_{i=1}^n \lambda_i \phi_i \psi_i^T \quad (1.7)$$

The performance measure  $\mathbf{z}(t)$  is then given by

$$\begin{aligned} \mathbf{z}(t) &= \mathbf{C}_p \sum_{i=1}^n \mathbf{z}_i(t) \\ &= \sum_{i=1}^n \int_0^t e^{\lambda_i(t-\tau)} \mathbf{C}_p \phi_i \psi_i^T \mathbf{B}_r \mathbf{r}(\tau) d\tau + \sum_{i=1}^n \int_0^t e^{\lambda_i(t-\tau)} \mathbf{C}_p \phi_i \psi_i^T \mathbf{E} \mathbf{d}(\tau) d\tau \end{aligned} \quad (1.8)$$

Equation (1.8) shows the effects of the exogenous signals *i.e.*, the reference and disturbance signals on the performance measure  $\mathbf{z}(t)$ . The performance measure is shown to be a linear combination of the individual modes, and by suitably altering the modes of the machine, better tracking and disturbance attenuation is achieved. We also note from (1.8) that the eigenvectors affect the shape of the transient behavior of the system while the eigenvalues affect the speed and stability. For very rapid motions it is required that the transients also be controlled and propagated through the machine in a prescribed manner. Besides, if the closed-loop modes can be explicitly related to the open-loop modes, it would be possible to obtain optimal mechanical design criteria from a controls standpoint. We do exactly this using our choice of control law.

### 1.3.1 Choice of Control Law

Feedback control design for precision machines is usually performed using classical single input-single output (SISO) techniques. SISO strategies for control may not address the coupling between the various parts of the machine. The control performance is hence restricted in terms of bandwidth. Good control performance requires that the dynamics of the machine be controlled as a whole rather than by closing SISO loops around various parts of the machine. This is done by application of multi-input multi-output (MIMO) control strategies. MIMO control design is traditionally done

using one of the following techniques :

- **$\mathcal{H}_2$  control**

This is the application of linear quadratic techniques to the design of both the controller and the observer and results in the so called Linear Quadratic Gaussian (LQG) controller. Process disturbances, sensor noise and control effort are weighted to synthesize an optimum controller. Heuristic rules exist for the selection of these weighting matrices in the time domain. Frequency weighting can be performed using a simple application of Parseval's theorem [29] to synthesize the controller. This is an elegant approach to control system synthesis. Very high-order controllers may result from the weighting procedure used and become important issues with real-time implementation. Besides, the approach is not well adapted to dealing with model uncertainty.

- **$\mathcal{H}_\infty$  control**

This is an extension of LQG control which takes into account the worst case disturbances that act on the system. A minimax optimization problem is set up as a differential game and a similar optimization is carried out as with the LQG case [5]. It has the advantage that a numerical measure of stability and performance robustness is obtained. However, high order controllers result and the intuition into the physical process may be lost.

- **Eigenstructure assignment**

This has been the traditional approach to control and goes by the name of pole placement. This has lately been replaced by modern control techniques such as  $\mathcal{H}_2$  and  $\mathcal{H}_\infty$  methods. It is heavily model based and it is hard to make statements on performance and stability robustness.

Real-time implementation emphasizes the need to design low order controllers. Modern approaches to control use either  $\mathcal{H}_2$  or  $\mathcal{H}_\infty$  techniques to generate controllers of rather high order and follow this effort with an order reduction algorithm. All this mathematical manipulation causes the underlying physical phenomena and intuition

to be lost. We choose the eigenstructure assignment technique and develop a unique algorithm to obtain the state feedback gain matrix. Our choice of control law is justified by the fact that great attention is paid to the mechanical design of precision machines and their environment. This permits the use of model-based controller design procedures that allow us to achieve increased performance. This is in contrast to robust control techniques where uncertainty is treated as being unstructured and the requirement for stability robustness causes loss in performance.

### **1.3.2 Eigenstructure Assignment**

Eigenstructure assignment facilitates the direct design of the closed-loop eigenvalues and eigenvectors rather than through quadratic indices. We take the approach that the specification of the mode shapes (or the eigenvectors) is the natural way to specify the desired dynamics of the machine and focus on eigenstructure assignment with an emphasis on the assignment of eigenvectors. Specifically, we consider the problem of mode-shape assignment in underactuated systems. This is because we live in an elastic world, and such flexible systems (with infinite degrees of freedom) are always underactuated (finite number of actuators).

Typically, eigenstructure assignment is carried out by placing the eigenvalues of the closed loop system at some desired locations. For SISO problems, this is a well-defined problem and goes by the name of pole-placement. It becomes more interesting in the case of MIMO problems where the problem of obtaining the feedback gains is underconstrained and does not have a unique solution. This additional freedom is used to improve robustness [35] of the closed-loop system or to specify the closed-loop eigenvectors [48]. Complete specification of the closed-loop eigenvectors makes the problem overconstrained and only the best fit eigenvectors (usually according to a least squares error criterion) are obtained. In the algorithms available in literature, the closed-loop eigenvalues are held fixed and this restricts the closed-loop eigenvectors to lie in a fixed subspace corresponding to the choice of eigenvalue [48]. There is no information on the sensitivity of this subspace to changes in eigenvalue. There exists no premise for holding the closed-loop eigenvalue fixed, especially in a MIMO control

problem. We acknowledge this and look for an explicit solution relating the behavior of the closed-loop eigenvector with the eigenvalue. This additional degree of freedom can be used to reduce if not eliminate the error between the desired and attainable eigenvectors while allowing the eigenvalue to move around in a small region about the desired eigenvalue. The parametrization that leads us to this solution is also found to relate the open-loop flexible modes to the closed-loop modes of the linear system and thus can be used to optimize the mechanical design of the system.

The process of eigenstructure assignment for general linear systems is derived in Chapter 8. A survey of literature reveals that there are no solutions for the explicit variation of the attainable closed-loop eigenvector with the closed-loop eigenvalue. We first derive the conditions for the exact assignability of eigenvectors. A closed-form expression for the resulting eigenvalue in such a case is derived, and its stability investigated. In the absence of exact assignability, the error in eigenvectors can be minimized by allowing the eigenvalue to move around in a small area about the desired value in the complex plane. An explicit relation is developed to demonstrate the behavior of the eigenvector as a function of the eigenvalue and its use demonstrated in reducing if not eliminating the error in the desired eigenvector completely for small changes in the desired eigenvalue. This solution is then extended to the natural frequency/mode shape assignment for discrete structural systems with negligible damping. Conditions under which a mode may be assigned exactly to underactuated systems are derived. The parametrization of the desired closed-loop modes reveals an interesting relationship between the attainable closed-loop and flexible open-loop modes. This can be used to *engineer* the structural resonance of the machine. Pursuit of the repercussions of this parametrization on the mechanical design of such precision machines is left for future work.

## 1.4 Summary of Contributions

- An analytical study of passive mounts is presented by casting them into the feedback framework. The fundamental tradeoff of a passive mount in attenuating

both seismic vibrations and payload disturbances is related to the fundamental tradeoff between sensitivity and complementary sensitivity functions in control literature.

- A novel approach to the design of optimal passive mounts is derived through the application of Kalman filtering techniques. The optimal mount minimizes the 2-norm of the payload motions.
- Active isolation is shown to have a simultaneous beneficial effect on both the seismic vibration transmissibility as well as payload disturbance rejection. The sensitivity of the control loop is shown to attenuate the transmissibilities from both disturbance phenomena to the payload motions. Frequency-weighting is introduced as a technique to shape the sensitivity and thus the transmissibilities.
- An active isolation system is designed and implemented on a prototype wafer stepper ready for commercial deployment. This isolation scheme is extremely power efficient and has a small footprint due to the nonlinear variable reluctance actuators used.
- Simultaneous control of the vibrations of the stepper and the coarse and fine motion stages is demonstrated. This leads to an order of magnitude reduction in settling times.
- Eigenvector assignment for linear systems is developed. Conditions for the exact assignability of eigenvectors is derived. A closed-form expression for the resulting eigenvalue in such a case is derived. In the absence of exact assignability, the error in eigenvectors can be minimized by allowing the eigenvalue to move around in a small area about the desired value in the complex plane. An explicit relation is developed to demonstrate the behavior of the eigenvector as a function of the eigenvalue.
- The parametrization used to explicitly relate the closed-loop eigenvalue and the achievable closed-loop eigenvector reveals an interesting relationship between

the closed-loop and flexible open-loop modes. For structural systems, it is demonstrated that a choice of certain closed-loop modes leads to singular solutions due to the zero dynamics. The explicit relationship between the open-loop and closed-loop modes also has implications on structural design for control.

# **Chapter 2**

## **Disturbance Mechanisms - Seismic Vibrations**

### **2.1 Introduction**

As the requirements on precision and speed of motion in precision machines increase, it becomes increasingly important to study disturbance mechanisms, their propagation and attenuation. Two types of disturbances exist on machine tools - those associated with the process, and those associated with the environment. Process disturbances usually arise out of inertial forces due to the movement of the various parts of the machine and through cutting forces. While the inertial forces are deterministic, the cutting forces are mostly unknown. In this thesis, we consider a class of machines such as wafer steppers where tool/workpiece interaction forces are negligible if not completely absent. Here, the process disturbance forces are those associated with the movement of the various parts of the machine, and thus deterministic. Environmental disturbances in such machines are usually seismic or acoustic. These are invariably modeled as broadband stochastic processes even though they originate from some deterministic source such as other machinery, personnel movement, acoustic coupling, vehicular traffic, and material handling equipment.

Precision machines are usually most sensitive to low-frequency disturbances. Energy content of the disturbances goes down with increasing frequency and is usually



negligible over the audible range in precision machine environments such as wafer fabs<sup>1</sup>. This is because wafer steppers are always operated in enclosures with thermal, particulate and acoustic control. Hence, we focus on ground vibrations rather than acoustic coupling as the primary disturbance mechanism. Ground vibrations disrupt the operation of precision equipment in various ways. They disturb the metrology loop due to elastic motions of the machine structure, joint pressure oscillations, frictional force variations and relaxation of elastic strains. This leads to imprecise motions in addition to longer settling times, thus, leading to loss of productivity. The study of these seismic disturbances, their propagation and attenuation is the focus of this chapter.

Rivin [63],[64] has published isolation requirements for precision machines such as grinders, jig borers, and lathes. Additionally, he documents the vibrations of various shop floors ranging from machine shop facilities to micro-electronic fabs. Data from various plants throughout the U.S. and the former Soviet Union is presented. A generic two-mass model is set up to simulate the first elastic mode of most machines. Various scaling factors are presented to illustrate the application of transmissibility of this two-mass model to different geometries. From this exhaustive documentation, it is found that the first natural frequency of most machines lies between 30 and 80 Hz. The second natural frequency is also found to lie consistently between 100 and 150 Hz. This observation is found to be consistent with the modal tests performed by Sandia National labs on the XLS 7000 wafer stepper [65]. Our approach to the modeling and control of precision machines draws heavily on these results as will be seen in Chapter 7.

In this thesis, we focus on photolithography as our main application, although our results are applicable to other precision machines/equipment. According to Gordon [27], vibration is one of the several “contaminants” that can affect the “yield” of the micro-electronics fabrication process. He cites the reasons as being the following :

- The per-unit-area power consumption of a fab exceeds that of a normal building

---

<sup>1</sup>A wafer fabrication facility or fab is the factory within which semiconductor processing takes place.

(such as an office) by a factor of 100 or more. This is due to the presence of (vibration producing) equipment such as chillers, pumps, handling equipment etc.

- The vibration sensitivity of the most critical metrology and photolithography tools commonly used in fabrication can exceed human sensitivity to vibration by a factor of 100 or more.

To be able to attenuate the effects of ground vibrations on photolithographic tools such as wafer steppers, we first need to study vibration sources and their propagation in semiconductor fabs. We then review some of the fundamental issues behind spectral representation of ground vibrations. Following this, we review the requirements that various stepper manufacturers place on the vibration environment to guarantee proper operation of their tools. These requirements are either in the time domain or the frequency domain and are found to vary considerably between manufacturers. This has prompted researchers to identify generic vibration criteria which could be used to guide the design of fabs. Two different sets of generic vibration criteria are discussed. One set of criteria has been adopted by the Institute for Environmental Science (IES) and is used in the rest of the developments in this thesis. Finally, we demonstrate the need for vibration isolation by referring to the semiconductor technology roadmap published by the Semiconductor Industry Association [4]. We use a two degree of freedom model along the lines of Rivin [63] along with simple models of floor vibration to demonstrate the need for low frequency vibration isolation on photolithographic tools.

## **2.2 Vibration Sources and Propagation**

Vibration control design of high technology facilities has been discussed in a classic paper by Ungar *et al* [80]. They classify the sources of vibration to be either external or internal sources. External sources include vehicular traffic, railroads etc., while internal sources include personnel and equipment movement, and service machinery

such as compressors, chilling plant equipment etc. They discuss ways and means to attenuate the effects of such disturbances and draw some guidelines for the location and design of such micro-electronics facilities.

Based on a large number of measurements and experience, Gordon [27] has found vibrations in micro-electronics facilities to be broadband. He attributes it among other things to the turbulent flow of fluids. Except for a small fraction that is propagated through acoustic coupling, most of the vibrational energy is propagated through the ground. Therefore, it is of interest to study the mechanism for propagation. The type of ground wave that characterizes the propagation of vibrational energy through the ground is called the Rayleigh wave and is described by the equation :

$$V_2 = V_1 \sqrt{\frac{R_1}{R_2}} e^{-\alpha(R_2 - R_1)} \quad (2.1)$$

where  $V_1$  and  $V_2$  are the wave amplitudes at distances  $R_1$  and  $R_2$  from the vibration source and  $\alpha$  is the material damping coefficient of the soil. Values of  $\alpha$  typically range from 0.003 to 0.016 per meter according to Gordon [27]. The Rayleigh wave is a surface wave that spreads out from a point source in the form of a symmetrical annular wave as shown in Figure 2-1. Most of its energy is contained within a depth of one to one-and-a-half wavelengths from the surface. Since typical Rayleigh wave speeds lie in the range 122 to 305 m/sec, the depth of the wave varies from 18 to 46 m at 10 Hz to 4 to 9 m at 50 Hz.

A number of methods are suggested in the literature [27] for attenuating the ground-borne path of vibration. Possible methods include digging a trench deeper than the depth of the Rayleigh wave or using a pile depth greater than that of the Rayleigh wave. These methods are impractical since most of the environmental vibration on a site from both near and distant sources lies around 10 Hz (requiring a pile/trench depth of 18 to 46 m). One preferred method is to support the building on stiff rock close to the surface (depending of course, on the composition of the site). Wave amplitudes in the stiff rock layer are much lower and help in attenuating vibrations transmitted to the lab floor.

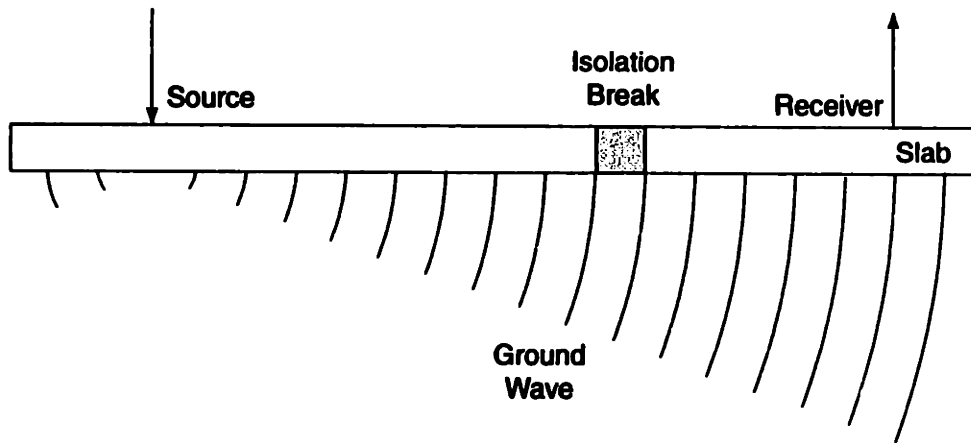


Figure 2-1: Effect of Isolation Break in Slab on a Rayleigh wave. Reproduced from Gordon [27].

Gordon[27] concludes that it is impossible to isolate buildings from one another using separate footings or isolation breaks as shown in Figure 2-1 based on exhaustive measurements. He claims the ground is too efficient a path of vibration propagation for such techniques to be effective. His studies on the spectral composition of disturbances also reveals a number of low frequency components (due to the speeds of human motion, traffic etc.). This makes the design of vibration isolators to isolate sensitive equipment in the fab extremely important. Our simple computations on wave speeds and depths also establish the difficulty in designing micro-electronics facilities to reject low frequency ( $\leq 10$  Hz) vibrations. Besides, the low-pass filtering effect of the ground also makes the study and attenuation of low-frequency ground vibrations extremely important.

The other medium for propagation of ground vibrations is the fab structure itself. The fab structure is infinite dimensional and there have been attempts to model certain fab structures using finite element studies. However, this is still ongoing work and no known classical models exist. Photolithographic steppers are usually mounted on rigid columns off the fab floor itself which is usually slab-on-grade. We initially make a rigid floor assumption and later discuss the relaxation of this assumption to include flexible modes of the floor. This affects our controller design as shown in Chapter 7.

Before proceeding further, we review some issues related to the measurement of

vibrations and their representation in the frequency domain. This review helps clarify the specifications on the vibration environments required by various stepper vendors and also the generic criteria presented later in this chapter.

## 2.3 Spectral Analysis and Bandwidth Issues

Vibrations are commonly characterized in the frequency domain using the amplitude spectrum<sup>2</sup>. The use of a frequency spectrum offers the following advantages over time history.

- It allows actual amplitudes to be correlated with known frequency-dependent sensitivity of the equipment.
- It averages the time history over an integration time period, thus removing instantaneous peaks (which have very little energy) which may have no effect on sensitive equipment.
- It excludes from consideration the frequency components that are of little consequence. For example, these frequency components could be at transmission zeros of the structure (dynamic vibration absorbers).
- It allows some identification of the nature of the source. Harmonics of the line frequency are typically due to pumps, motors, etc.

Each point on the spectrum represents an amplitude that passes a certain frequency band. This amplitude is measured by passing the signal through a bandpass filter. It is important to take into account the size of this frequency band or bandwidth when comparing different vibration spectra. Figure 2-2 illustrates both ideal and practical bandpass filters. The so-called *effective noise bandwidth* of a filter is defined as the width of a filter which, with an identical reference-amplitude gain would transmit the same power from a white-noise source. Another bandwidth associated with a filter is its 3 dB *bandwidth*. This is the difference between the half-power points of

---

<sup>2</sup>Note that this is not a spectral density.

the amplitude characteristic of the filter *i.e.*, the points where the filter gain is 3 dB below the reference amplitude level.

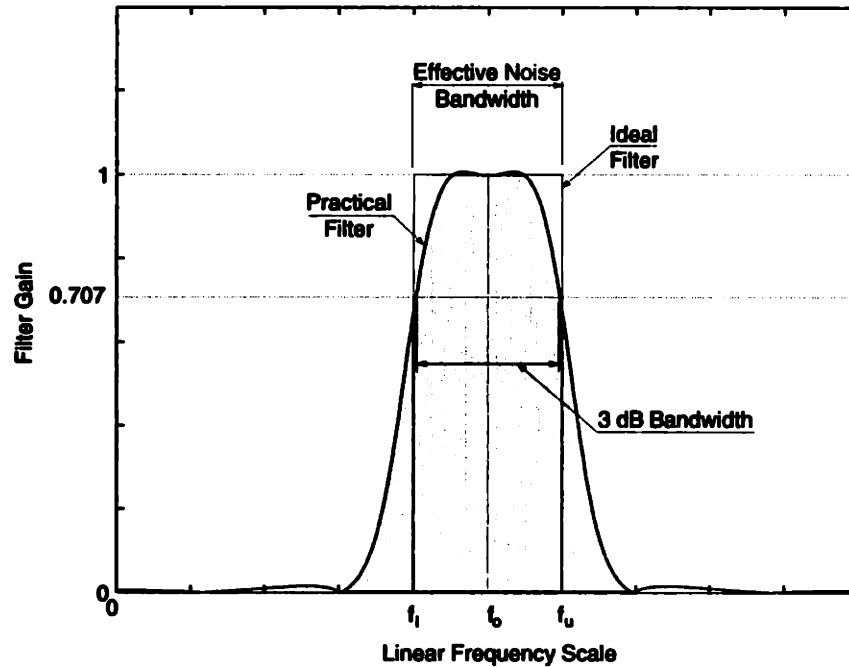


Figure 2-2: Practical *vs.* ideal filter characteristics

In most practical filters, the difference between the 3 dB bandwidth and the effective noise bandwidth is relatively small and can be ignored. We choose the term bandwidth to refer to the 3 dB bandwidth unless otherwise specified, since this can be easily measured experimentally. The concept of bandwidth is of central importance in spectral analysis and there exist three distinct spectral representations based on bandwidth. They are as follows :

- **Narrow (Constant) Band Analysis**

In recent times, this is proving to be the most popular approach due to the *real-time* computation afforded by the use of the Fast Fourier Transform (FFT). Modern equipment for frequency analysis uses FFT algorithms in which the frequency domain of interest is segmented into narrow frequency bands of constant width. The FFT algorithm determines the rms signal amplitude corresponding to the center of each band. For example, a narrow band analysis commonly used in vibration studies is illustrated in Figure 2-3. The bandwidth illustrated

is 0.375 Hz which is typical for a 400-line FFT over the range 0-100 Hz. To

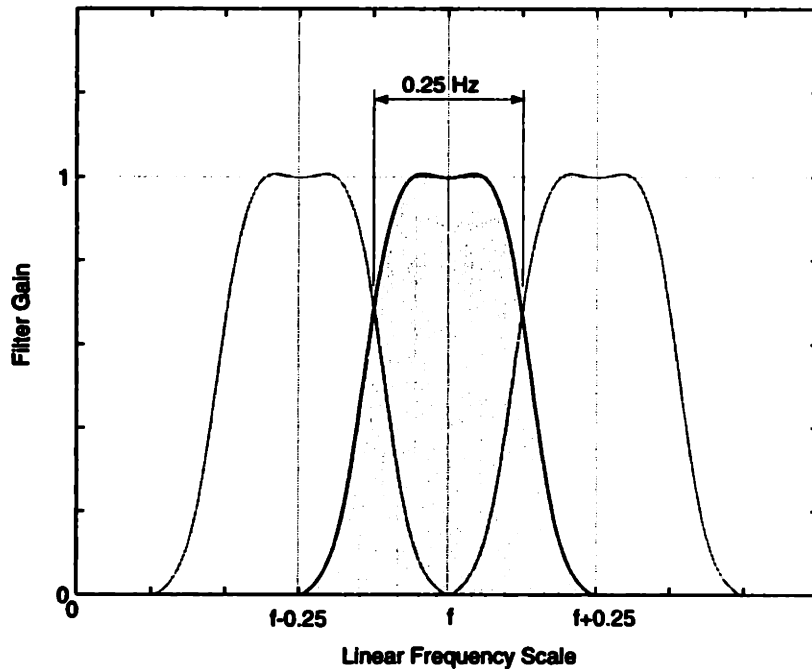


Figure 2-3: Bandwidth computations for narrow band analysis illustrated for a 400-line FFT over a 0-100 Hz range. The passband is  $100/400 = 0.25$  Hz and the bandwidth with a Hanning window is  $1.5 \times 0.25 = 0.375$  Hz.

understand this computation, we first define the passband as the band in between the crossover points of the filter with its two adjacent filters as illustrated in Figure 2-3. The passband is obtained by dividing the range by the number of lines in the FFT. For the example considered, this is the ratio  $100/400$  and equals 0.25 Hz. Most digital frequency analyzers employ window functions to prevent spectral leakage. One common window used in vibration analysis is the Hanning window whose noise bandwidth is defined to be 1.5 times the passband [43]. With the Hanning windowing function, the bandwidth for the 400-line FFT over the range 0-100 Hz illustrated in Figure 2-3 can be computed to be 0.375 Hz.

- **Proportional (Broad) Band Analysis**

Older techniques of frequency domain analysis used proportional bandwidth. In fact, this is still popular in acoustic measurements. Analysis using proportional bandwidth is usually referred to as broad-band analysis. Standard industry

practice is to use one-third octave filters, in which the difference between the upper and lower limiting frequencies is 23.1 % of the nominal center frequency and three adjacent bands represent an octave or doubling of frequency. Established standards define the conventional center frequencies. The one-third octave filter is illustrated in Figure 2-4.

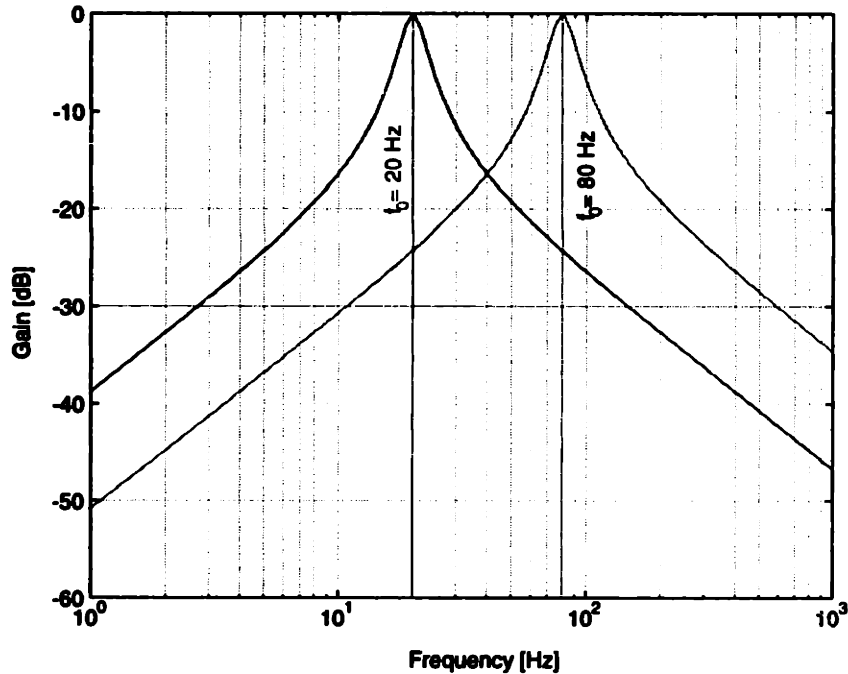


Figure 2-4: Frequency Response Functions of two different one-third octave filters ( $f_0$  denotes the center frequency). Note the proportional bandwidth of the two filters (appears to be a constant bandwidth in a logarithmic plot).

It is interesting to note that ISO<sup>3</sup> 2631 recommends that one-third octave band filters be used where many closely-spaced frequencies or broadband energy is involved. Broadband vibrations that are relatively constant with frequency can be converted from one spectral representation to another using (2.2)

$$V_{NB1} = V_{NB2} \sqrt{\frac{BW_2}{BW_1}} \quad (2.2)$$

where  $V_{NB1}$  and  $V_{NB2}$  are the amplitudes using the two different constant-bandwidth analyzers, and  $BW_1$  and  $BW_2$  are the two bandwidths respectively.

<sup>3</sup>International Standards Organization.



Following a similar approach, (2.3) can be used to convert from a constant narrow bandwidth ( $BW_{NB}$ ) to the one-third octave band with center frequency  $f_0$ .

$$V_{1/3} = V_{NB} \sqrt{\frac{0.23 f_0}{BW_{NB}}} \quad (2.3)$$

The broadband assumption is a key to the use of the above conversion formulas. This approach can be used to synthesize larger bands from smaller bands, but not vice-versa.

- **Power Spectral Density**

This approach is gaining more favor in recent times since it is absolute in its representation of broadband data. This is because the amplitude is normalized by the square root of the measurement bandwidth and measurements of a broadband signal will give the same density spectrum irrespective of the bandwidth used. However, this is not ideally suited for representing tonal data. A single tone measured using a one-third octave band and divided by the square-root of the measurement bandwidth will give a completely different result from that obtained by measuring the same tone with a constant (but different) bandwidth. For example, consider a pure tone at 20 Hz with an energy of 1 Volt RMS. The PSD computed by the narrow band analysis illustrated earlier (400 line FFT, 0.375 Hz bandwidth) will be  $1.633 \text{ VRMS}/\sqrt{\text{Hz}}$ . On the contrary, the PSD computed by broadband analysis (one-third octave bandwidth of  $0.23 \times 20 = 4.6 \text{ Hz}$ ) will be  $0.4663 \text{ VRMS}/\sqrt{\text{Hz}}$ . Besides, the PSD level of a tone in one proportional band will be completely different from that of a tone of the same amplitude but occurring in a different band since the bandwidths vary with frequency in such an analysis.

Amick [1] reviews the various spectral representations with data from different fab floors and emphasizes the advantages of the one-third octave representation. Ungar [79] states that the one-third octave bands tend to approximate the response bandwidths of equipment and hence using them adequately takes into account the

effects of closely spaced excitation frequency components. Gordon [26] presents the following argument in support :

A resonator will respond with equal energy to a pure tone and to a band of broadband energy when each is set to the same amplitude if the broadband energy is applied with a bandwidth given by

$$\Delta f = \frac{\pi}{2}\eta f_0 \quad (2.4)$$

where  $f_0$  is the resonant frequency and  $\eta$  is the loss factor of the resonator. Equation (2.4) makes two important points :

- The higher the damping of the structure, the wider is the range of frequencies to which the resonator will respond and therefore, the greater is the bandwidth of broadband energy that should be used in evaluating the adequacy of the floor.
- Assuming constant damping, the measurement bandwidth should increase in proportion to the frequency.

Typical loss factors  $\eta$  encountered in engineering structures range from about 0.01 to 0.1 [49]. Substituting this into (2.4) we obtain the proportional bandwidth to be 16 % for  $\eta = 0.1$ .

$$\Delta f = 0.16f_0 \quad (2.5)$$

The bandwidth of the one-third octave is 23.1 % of the center frequency which provides a fairly conservative measure of broadband energy insofar as its effect on a resonator (or series of resonators) is concerned.

These arguments have led to the adoption of the one-third octave band filters for spectral representation of the vibration environment. These have been made a standard by the Institute of Environmental Sciences (IES). Before discussing this standard however, it is worthwhile to review the demands on the vibration environment imposed by various stepper vendors.

## 2.4 Review of Current Vibration Requirements

The key manufacturers of step and repeat, and step and scan machines are Nikon, Canon, ASM Lithography and SVG Lithography. These vendors send out site preparation manuals to customers before the machine is shipped. Excerpts from these manuals are reproduced in this section. Both time domain and frequency domain criteria are usually specified. The time domain criteria place a restriction on the total floor energy while the frequency domain criteria detail the spectral distribution of this energy.

### 2.4.1 Nikon

Nikon Lithography is presently the largest supplier of step and repeat tools to the semiconductor industry. We consider the Nikon NSR-S203 Series step-and-repeat scanning system and reproduce portions from the site preparation guide [52]. There are three conditions (two specifications and one target value) :

- **Time Domain Vibration Specification**

The vibration signal should be filtered by a low pass (4<sup>th</sup> order Butterworth filter or similar) filter having a cutoff frequency of 100 Hz (-3 dB at 100 Hz). The vertical vibration signal should not exceed 3.18 gal<sup>4</sup> RMS and the horizontal vibration signal should not exceed 1.06 gal RMS in both the front/back and right/left directions.

- **Frequency Domain Vibration Specification**

This specification limits excessive vibration energy in certain frequency bands. It is based on 1/3-octave analysis of the time domain acceleration data (without the 100 Hz low pass filtering) and the criteria are shown in Figure 2-5. The horizontal vibration limit is more constraining than the vertical limit and the values are shown zero-to-peak. The range of frequencies considered is between 1.6 Hz and 250 Hz.

---

<sup>4</sup>1 gal = 1 cm/sec<sup>2</sup> = 0.00102 G (≈1 mG)

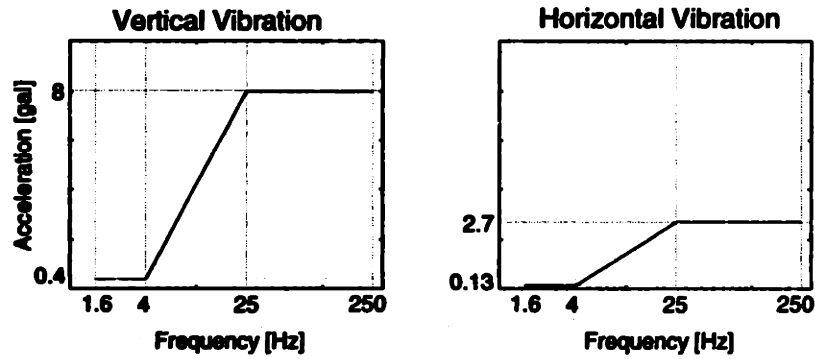


Figure 2-5: Allowable floor vibration level for the Nikon NSR-S203 Series steppers. One-third octave band spectrum, values are 0-to-peak acceleration. The horizontal specification applies both to front-back and left-right directions [52].

- **Facility Dynamic Response Target**

This is a specification on the floor to ensure that the support structure has sufficient strength to resist the dynamic loads forced upon it and is specified as a requirement on acceleration. Note that acceleration is the transfer function from force to acceleration of a structural system. The target requirements on acceleration are more conservative in the step and repeat system than on the scanning system due to the nature of the dynamic forces generated by the stage motions. The specifications are shown in the form of a Bode plot in the Nikon site preparation manual [52] and are not reproduced here.

## 2.4.2 Canon

The requirements for the Canon FPA-3000i5 [18] are set in terms of the peak value of the power spectral density of floor vibrations (both horizontal and vertical) at the four mounting points. The specification on the vibration is given for a frequency range between 0.5 Hz and 300 Hz as illustrated in Figure 2-6.

## 2.4.3 SVG Lithography

SVG Lithography (formerly Perkin-Elmer) is presently the largest supplier of step and scan tools to the semiconductor industry. The site preparation manual for the Micrascan III [74] details the vibration requirements for optimal operation of the

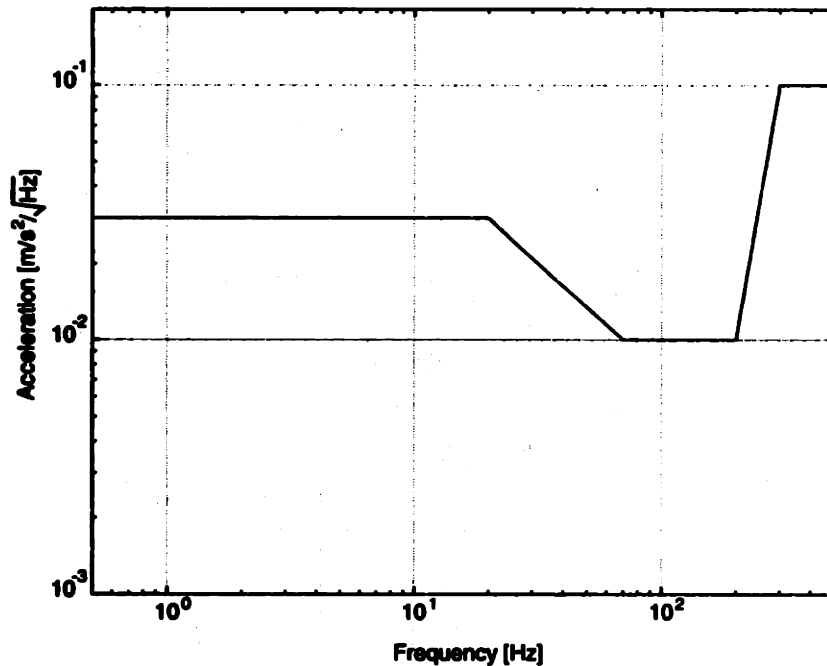


**Figure 2-6: Allowable floor vibration level for the Canon FPA-3000i5 Series steppers. Power spectrum amplitude is measured 0-peak and a Hanning window used to prevent spectral leakage [18].**

stepper. The characterization of the floor involves measurement of the power spectral density of the floor in the three orthogonal Cartesian directions in the frequency range 2 Hz to 252 Hz with about 800 lines of resolution. Although a restriction on the shape of the PSD plot is not mentioned in the manual, the data needs to be approved by SVG Lithography. However, the requirement is that the square root of the area under the PSD plot which is a measure of the standard deviation of the acceleration of the floor be less than 2.5 mG RMS in each of the three orthogonal directions. This limits the total vibration energy of the floor and is in fact a time-domain specification although it is required that the power spectral density be measured (Parseval's formula relates the two).

#### **2.4.4 ASM Lithography**

ASM Lithography outlines the vibration requirements for the PAS 5500/500 series of steppers. The requirements on the shape of the power spectral density between 1 Hz and 200 Hz are given. The requirements are the same in both the horizontal

and vertical directions. Two different PSD plots are given, one for the exposure unit and the other for the excimer laser unit which is mounted separately (usually in the sub-fab). 1/3-Octave vibration specifications are also given along with the BBN

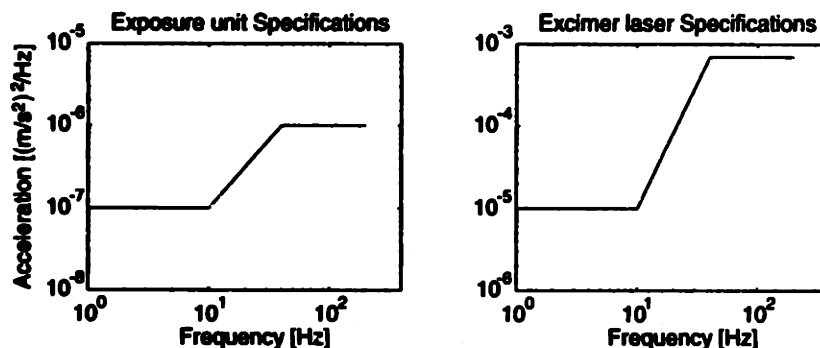


Figure 2-7: Allowable floor vibration level for the ASML PAS 5500/500 Series steppers [3].

criteria (to be discussed in detail later) and shown to be less conservative than BBN level D. The 1/3-octave plot seems to have been obtained using (2.3) and has not been reproduced here. Requirements on static stiffness and flatness of the floor are also given in the site preparation manual [3].

From the above, we see that the environmental vibration specification varies considerably between wafer stepper manufacturers. This leads to difficulties in both fab-floor design and vibration isolation system design. This problem was recognized early on by various researchers. A key development was the organization of a conference on vibration control in micro-electronics, optics and metrology sponsored by the International Society for Optical Engineering (SPIE). In a seminal paper, Gordon [26] traces the origins of vibration sensitivity curves (for the Perkin-Elmer Series 300 Microalign) and relates it to contemporary equipment. He describes the derivation of generic vibration criteria (BBN criteria) which has since been used widely in the design of micro-electronics facilities. These have since been adopted as a standard by the Institute of Environmental Sciences (IES) and are given in Appendix C of IES-RP-CC012.1, "Considerations in Clean Room Design" published by the IES in 1993 [53]. These generic vibration criteria are described in the next section.

## 2.5 BBN Criteria

The Bolt Beranek & Newman Inc. (BBN) criteria are historically the first set of criteria to characterise vibration environments in micro-electronics facilities. In a seminal paper, Gordon [26] traces the origins of vibration sensitivity curves (for the Perkin-Elmer Series 300 Microalign) and relates it to contemporary equipment. These studies were crucial to the development of the BBN vibration criteria.

The BBN curves presented in Figure 2-8 are widely used in the design of micro-electronics facilities. These use proportional (one-third octave) bandwidths for spectral representation of vibrations. The main elements of the criteria are as follows :

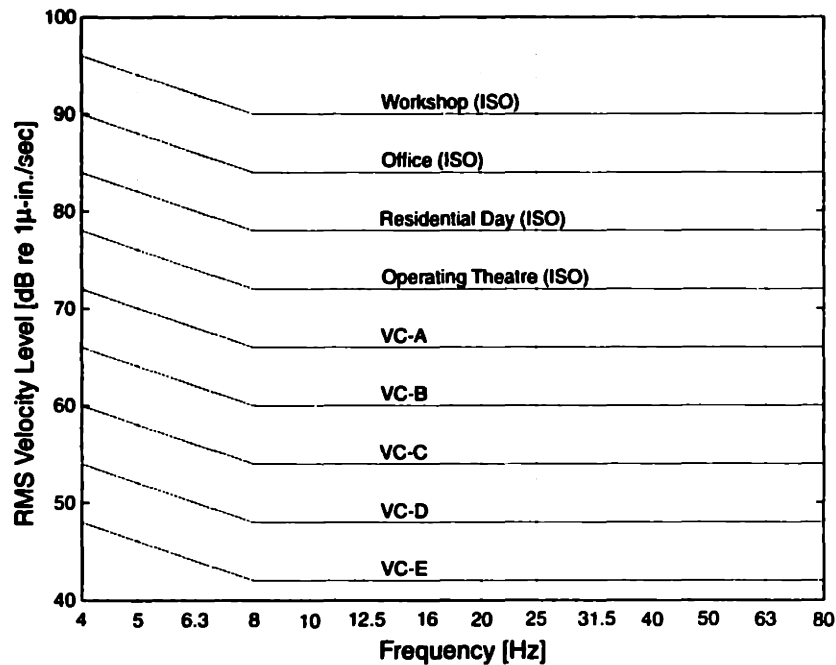


Figure 2-8: BBN floor vibration criteria (VC) curves for precision equipment installation showing also ISO guidelines [26]. The curves limit the RMS velocity output of one-third octave filters centered along the frequency range illustrated.

- The floor vibration is expressed in terms of its root-mean-square (RMS) velocity. Velocity is chosen as the variable of interest. Gordon's reasoning for the choice of velocity as the variable of interest stems from his studies on the sensitivity of the Perkin-Elmer machines to ground vibrations. He observed that the points of maximum sensitivity at different frequencies occurred on curves of constant velocity.

- A proportional bandwidth (one-third octave - 23 % of band center frequency) is used as opposed to fixed bandwidth (narrow band FFT). This stems from a conservative view of the internal damping of typical equipment components as shown by (2.5).
- A greater vibration velocity is allowed under 8 Hz. This corresponds to the fact that the resonant frequency of most machines is above this range.

Table 2.1 illustrates the interpretation of these criterion curves. Table 2.1 is reproduced from Gordon [26] and represents the experience of the author at the time of writing (1991).

### 2.5.1 FHA Criteria

The FHA criteria introduced by Frank Hubach Associates specifies that the vibration signal be analyzed by FFT analysis with a resolution of 0.125 Hz (an effective noise bandwidth of 0.1875 Hz). These criteria define five levels, each corresponding to different types of vibration-sensitive equipment and technology over a frequency range 5-50 Hz. They are described in Table 2.2.

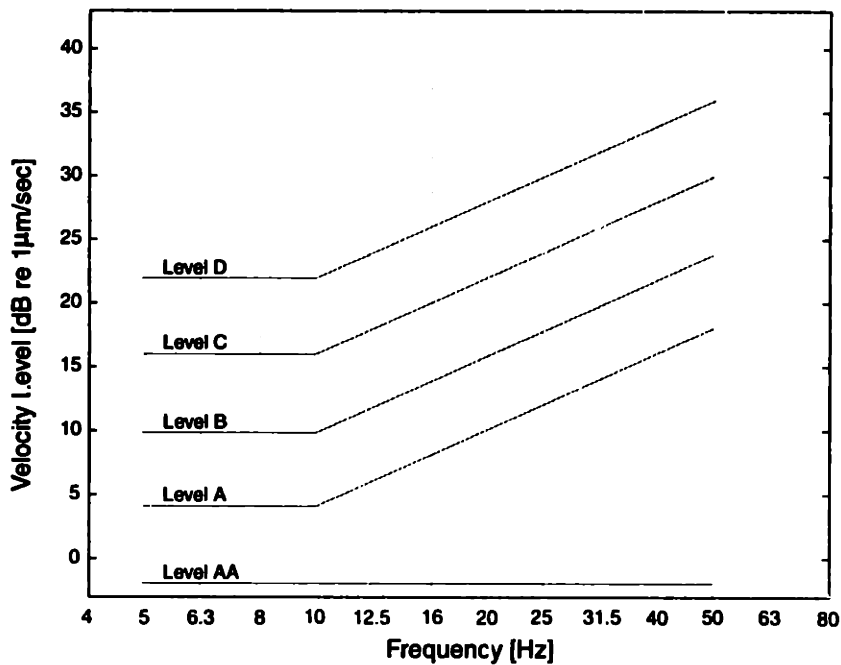


Figure 2-9: FHA floor vibration criteria. Reproduced from Owen *et al.* [54].



Criterion Curve	Maximum Level $\mu$ -in/sec (dB)	Detail Size ( $\mu$ m)	Description of use
Workshop (ISO)	32000 (90)	N/A	Distinctly feelable vibration. Appropriate to workshops and non-sensitive areas
Office (ISO)	16000 (84)	N/A	Feelable vibration. Appropriate to offices and non-sensitive areas
Residential Day (ISO)	8000 (78)	75	Barely feelable vibration. Appropriate to sleep areas in most instances. Probably adequate for computer equipment, probe test equipment and low-power (to 50X) microscopes
Operation Theater (ISO)	4000 (72)	25	Vibration not feelable. Suitable for sensitive sleep areas. Suitable in most instances for microscopes to 100X and for other equipment of low sensitivity
VC-A	2000 (66)	8	Adequate in most instances for optical microscopes to 400X, microbalances, optical balances, proximity and projection aligners, etc.
VC-B	1000 (60)	3	An appropriate standard for optical microscopes to 1000X, inspection and lithography equipment (including steppers) to 3 $\mu$ m line widths
VC-C	500 (54)	1	A good standard for most lithography and inspection equipment (including electron microscopes) to 1 $\mu$ m detail size.
VC-D	250 (48)	0.3	Suitable in most instances for the most demanding equipment including electron microscopes (TEMs and SEMs) and E-Beam systems, operating to the limits of their capability.
VC-E	125 (42)	0.1	A difficult criterion to achieve in most instances. Assumed to be adequate for the most demanding of sensitive systems including long path, laser-based, small target systems and other systems requiring extraordinary dynamic stability

Table 2.1: Application and interpretation of the BBN criterion curves shown in Figure 2-8. Amplitude limits are RMS values. Table reproduced from [26].

FHA Level	Amplitude Limit		Technology or Equipment
	5-10 Hz	10-50 Hz	
AA	0.8 $\mu\text{m}/\text{sec}$	0.8 $\mu\text{m}/\text{sec}$	Ultra sensitive metrology
A	1.6 $\mu\text{m}/\text{sec}$	0.025 $\mu\text{m}$	Silicon at submicron geometries, SEMs, E- beams
B	3.1 $\mu\text{m}/\text{sec}$	0.05 $\mu\text{m}$	Silicon at approximately 1 $\mu\text{m}$ geometries, GaAs at submicron geometries
C	6.3 $\mu\text{m}/\text{sec}$	0.1 $\mu\text{m}$	Silicon at 2+ geometries, 1000x microscopes
D	12.5 $\mu\text{m}/\text{sec}$	0.2 $\mu\text{m}$	100x microscopes

Table 2.2: Application and interpretation of the FHA criterion curves shown in Figure 2-9. Amplitude limits are RMS values [54].

For reasons mentioned in section 2.3, the BBN criteria are more widely used than the FHA criteria and have been adopted amongst other organizations, by the Institute for Environmental Science (IES). The FHA criteria are mentioned here for completeness and will not be used in further developments in this thesis.

Having studied vibration sources, their propagation, representation and generic criteria, we can now set up simple models of floor vibration. These models along with simple models of a wafer stepper are now used to demonstrate the need for low frequency vibration isolation.

## 2.6 Need for Low Frequency Vibration Isolation

We begin by presenting the need for low frequency isolation using a simple, yet practical example. To do this, we study the motion control requirements of photolithography. The national technology roadmap for semiconductors sponsored by the Semiconductor Industry Association (SIA) and published by Sematech [4] is a good guide to determine the isolation requirements of future wafer steppers. An excerpt from the roadmap relevant to motion control requirements is reproduced in Table 2.3. The interesting trends to observe are those of decreasing feature sizes

---

<sup>5</sup>For isolated lines (MPU Gates)

<sup>6</sup>Mean + 3 $\sigma$

Year	1997	1999	2001	2003	2006	2009	2012
Technology	250 nm	180 nm	150 nm	130 nm	100 nm	70 nm	50 nm
Min. Feature Size <sup>5</sup> [nm]	200	140	120	100	70	50	35
Product Overlay <sup>6</sup> [nm]	85	65	55	45	35	25	20
Wafer Diameter [mm]	200	300	300	300	300	450	450

Table 2.3: Product critical level lithography requirements (Excerpts from Table 24 of the National technology roadmap [4])

(and product overlay) while the wafer diameter increases.

We take a very simplistic view of the dynamics of the wafer stepper to determine isolation requirements. Following the approach taken by Rivin [63] to determine isolation requirements for various precision machines, we model the prototype wafer stepper in the Z-direction and represent it by the two-degree-of-freedom system shown in Figure 2-10. Mass  $M_1$  represents the base of the stepper while  $M_2$  represents the

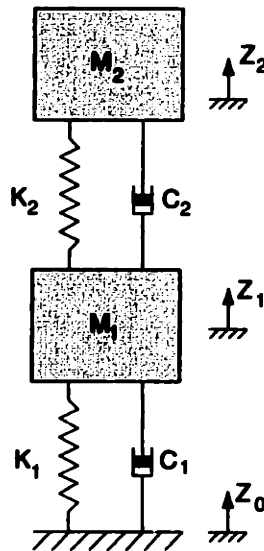


Figure 2-10: Two degree of freedom model representing the first longitudinal mode of vibration of the prototype stepper in the vertical(Z) direction

modal mass of the first resonance of the lens mount. This mode of vibration is at 26 Hz according to the modal analysis conducted by Sandia National Labs on the XLS 7000 series lithography machine [65].

Next, we model the floor vibrations are modeled as a first order Markov process. Such a model although grossly simplified can be chosen to be conservative enough to give us analytical estimates on vibration isolation requirements. The power spectral density (PSD) of the floor vibrations for such a process is given by

$$S_x(\omega) = \frac{2\beta\sigma^2}{\omega^2 + \beta^2} \quad (2.6)$$

We choose the cutoff frequency  $\beta$  to be 10 Hz. This is a reasonably accurate model of a floor which is excited primarily by footfall, turbulent flow of fluids in pipelines and similar low frequency broadband sources [79]. Finally, we select the standard deviation  $\sigma$  for floor vibrations to be 25 nm. This magnitude is selected such that VC-E criterion forms an upper bound to the floor vibrations. To compare the PSD of the floor vibrations to the BBN criterion VC-E, the power spectral density in (2.6) is first converted to an equivalent one-third octave representation using

$$\begin{aligned} V_{1/3@_{\omega_0}} &= \left( \int_{\omega=0.89\omega_0}^{\omega=1.12\omega_0} \frac{2\beta\sigma^2}{\omega^2 + \beta^2} d\omega \right)^{0.5} \\ &= \left[ 2\sigma^2 \left( \tan^{-1} \left( \frac{1.12\omega_0}{\beta} \right) - \tan^{-1} \left( \frac{0.89\omega_0}{\beta} \right) \right) \right]^{0.5} \end{aligned}$$

This equivalent one-third octave output  $V_{1/3}$  is compared to the BBN criterion VC-E in Figure 2-11. The VC-E criterion is found to be an upper bound to the modeled floor vibrations, and hence our model is a reasonably conservative estimate of floor vibrations in a fab satisfying the VC-E criterion.

The PSD of the error motion  $S_y(\omega)$  between the lens and the stage (assumed to be rigidly coupled to the stepper in our simplistic model) is then given by

$$S_y(\omega) = |G(j\omega)|^2 S_x(\omega) \quad (2.7)$$

where  $G(j\omega)$  is the transfer function between the floor vibrations and the relative motion  $z_2 - z_1$ . We consider three different cases of isolation, *i.e.*, hard mount, passive isolation and active isolation in our study. The magnitude plots corresponding

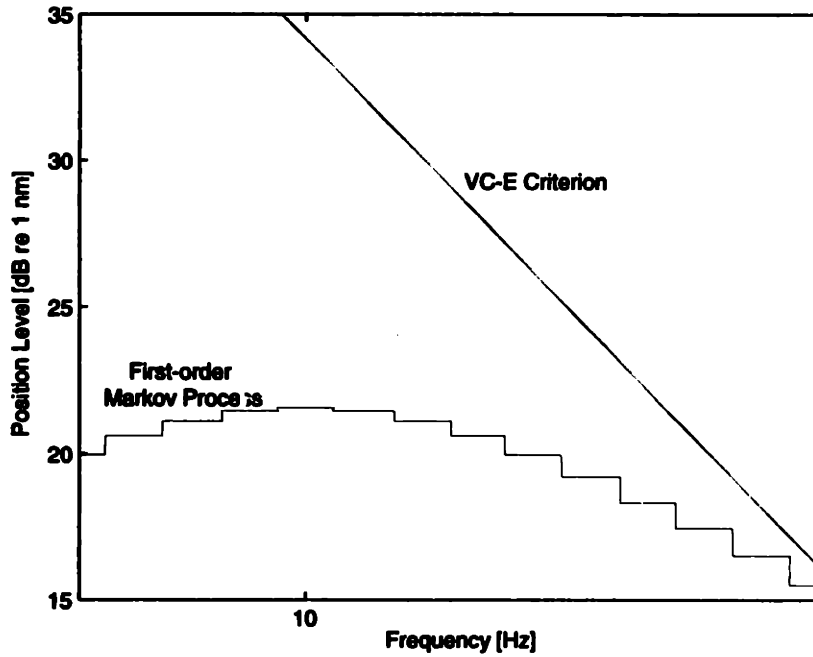


Figure 2-11: Comparison of the first-order Markov process to VC-E requirements

to these three transfer functions are represented pictorially in Figure 2-12.

The variance of the error motion  $S_y(\omega)$  is then simply given by the area under the output PSD curve and can be computed using the integral,

$$\sigma_y^2 = \frac{1}{2\pi} \int_{-\infty}^{\infty} S_y(\omega) d\omega \quad (2.8)$$

The computation of the integral in 2.8 is greatly simplified by using tables of integrals of the general form

$$I_n = \frac{1}{2\pi j} \int_{-j\infty}^{j\infty} H(s)H(-s)ds \quad (2.9)$$

where  $H(s)$  is the transfer function of the shaping filter and  $n$  its order. In our example

$$H(s) = \frac{\sqrt{2\beta}\sigma}{s + \beta} G(s) \quad (2.10)$$

where  $G(s)$  is the transfer function from (2.7). Tables of mean square error integrals appropriate to this task can be found in Appendix E of Newton, Gould and Kaiser [51]. We use these tables to compute the variance corresponding to various

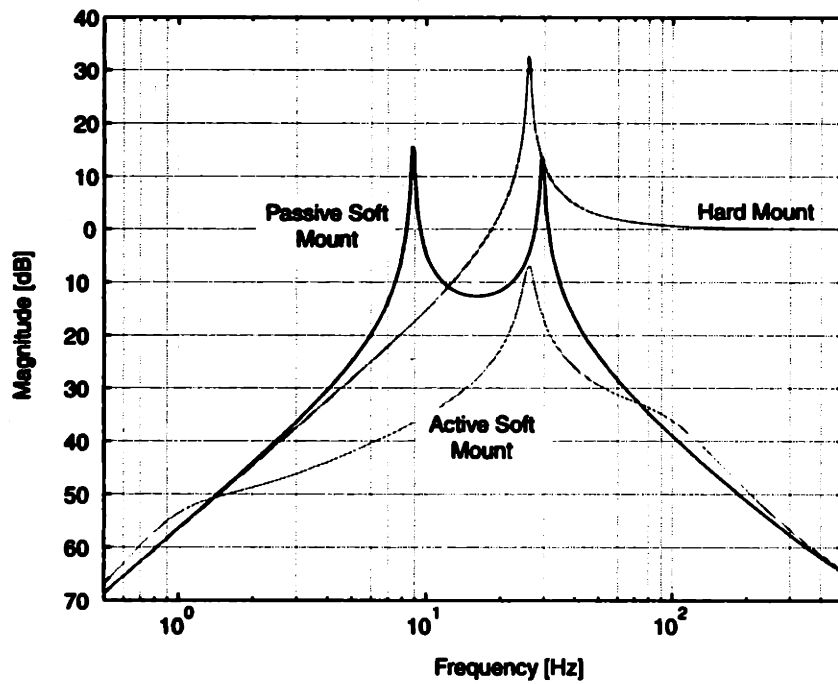


Figure 2-12: Comparison of the three different transfer functions corresponding to a) Hard mount, b) Passive Isolation, and c) Active Isolation.

cases of isolation.

Description	Standard Deviation [nm]
Floor	25
Hard mount	102.38
Passive Mount (10 Hz)	20.46
Passive Mount (1 Hz)	0.1451
Active Mount	0.0276

Table 2.4: Comparison of standard deviation of error motions for the two degree of freedom model

Table (2.4) lists the value of the standard deviation of the error motions  $z_2 - z_1$  under various cases of isolation. It can immediately be seen that some form of isolation is needed since the hardmount (where the stepper base is rigidly bolted to the floor) leads to amplification of the floor motion and thus to a standard deviation that far exceeds the product overlay values given in Table 2.3. Passive isolation with a natural frequency of 10 Hz can be implemented with elastomeric mounts. With this isolation, the standard deviation is reduced slightly below floor levels and does meet requirements on product overlay. However, we should keep in mind that our model does not take into account the coupling present between various modes of the machine and the presence of other significant low frequency modes. There are also usually significant peaks in the floor spectrum and our simple model of floor vibrations ignores these. Finally, the ground vibrations are only one component to the overall error budget and we desire to reduce the effect of ground vibrations to the overall error budget further.

Lowering the natural frequency of the passive mount reduces the standard deviation further. A natural frequency of 1 Hz can be obtained by using either air springs or negative stiffness mechanisms [56] as discussed in Chapter 3. However, it should be noted that the use of such soft mounts makes the stepper susceptible to payload disturbances caused by stage motions. This is a fundamental constitutive limitation of passive mounts and is illustrated in Chapter 3. A simple active isolation scheme (of the kind described in Chapter 4) reduces the error motions further while not being

constrained by the constitutive limitations of passive mounts. Chapter 3 derives the limitations of passive mounts and Chapter 4 illustrates how active mounts are not subject to the same constraints. Various forms of isolation and their pros and cons are also discussed in Chapter 4.

## **2.7 Summary of Chapter 2**

Disturbance sources in precision machine environments are discussed. Ground vibrations are found to be the key contributor to error motions. The propagation of ground vibrations is studied. It is found that although the fab can be designed to reject high frequency vibrations, rejection of low frequency vibrations at the fab level is both expensive and difficult. This makes the design of vibration isolators important. Floor vibrations are characterized using generic criteria. A review of vibration requirements of various vendors is also presented. A simple model of a precision machine is constructed to illustrate the influence of ground vibrations on error motions and demonstrate the importance of low-frequency isolation.



# Chapter 3

## Passive Vibration Isolation

### 3.1 Introduction

Ground vibrations can excite the flexible modes of the machine leading to error motions which in turn cause longer settling times and poor performance. Through a series of studies Rivin [63], [64] has established that most precision machines have their first elastic mode in the vicinity of about 30 to 80 Hz. The presence of this low frequency mode makes vibration isolation very important in such precision machines. The two-degree-of-freedom model considered in Chapter 2 emphasizes this fact and illustrates the relation between ground vibrations and machine error motions due to the elastic modes. It is seen from Table 2.4 that hard mounts amplify the error motions while soft mounts attenuate them. The importance of low natural frequency isolation mounts is also made evident by this example.

Vibration isolation is also important in experiments such as those to detect gravity waves. Debra [21] provides some very interesting applications for vibration isolation which include the gravity wave detection antenna, diamond turning machines and other precision machines and instruments. In this thesis, we consider the problem of isolating precision machines with specific reference to the photolithographic stepper shown in Figure 3-1.

Although isolation becomes truly important only in the presence of flexible modes of the equipment being isolated, traditional approaches to vibration isolation have

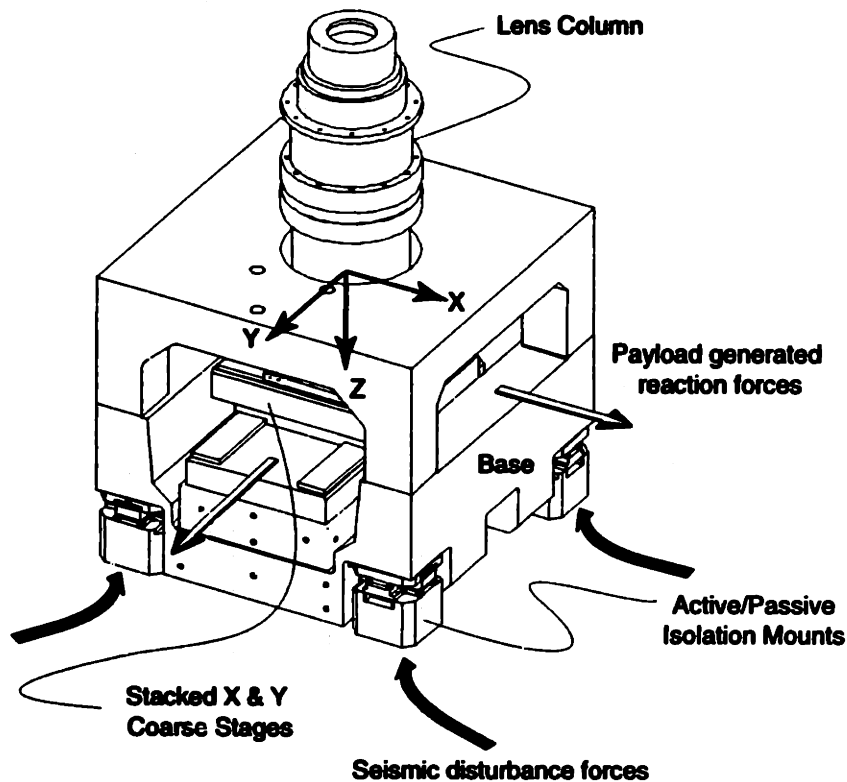


**Figure 3-1: Schematic of prototype stepper showing disturbance mechanisms and Cartesian coordinate frame fixed to the center of gravity**

been to treat both the payload being isolated and the substructure supporting the payload as rigid bodies. Unfortunately, the rigid body assumption leads to poor performance in passive isolation architectures, as well as instability in active schemes. We will consider flexibility in more detail in Chapter 7.

Figure 3-1 shows the disturbance mechanisms acting on the prototype stepper used as the testbed in this thesis. We first note that addressing the two disturbance mechanisms leads to a fundamental conflict. Good vibration isolation requires the stepper to be mounted on very soft springs. This causes the transmissibility of the soft mount to be small across the frequencies of interest and reduces the variance of the error motions as shown in the two degree of freedom example in Chapter 2. However, a soft mount also causes excessive error motions of the stepper during stage motion (payload disturbances); and this in fact is the chief contributor to stepper vibrations in present day devices. Thus, we find that a soft mount is required for good vibration isolation while a hard mount is required for payload disturbance re-

jection. It is impossible to meet these conflicting requirements using a passive device. We demonstrate this tradeoff analytically by treating the passive vibration isolation problem as a control systems paradigm.

In this chapter, we discuss various passive isolation architectures with an emphasis on low natural frequency isolation. We discuss the pros and cons of passive isolation schemes and present some innovative designs that are commercially available. We derive the fundamental limitation of passive isolation in attenuating both seismic and payload disturbance using a single degree of freedom system as an example and extend this to multiple degree of freedom systems. We pose the passive isolation problem as a control systems paradigm and demonstrate the fundamental tradeoff in the context of control systems theory. This tradeoff motivates the application of control system principles towards the design of passive isolation mounts. Specifically an optimal design of the mount parameters is obtained as the solution to a Kalman filtering problem.

## 3.2 Passive Isolation

Passive isolation in its simplest form is a compliance that passes the low frequency forces but attenuates high frequency forces. Figure 3-2 shows a simple structural system that schematically represents a single degree of freedom vibration isolation system. The mass  $M$  represents the payload to be isolated from the base motions  $z_0$  and the spring/damper is the mount to be designed. The ratio  $z/z_0$  is called the

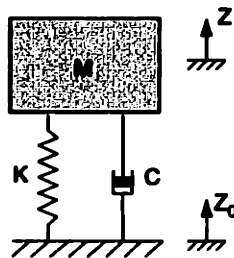


Figure 3-2: Single degree of freedom passive vibration isolation system illustrating seismic disturbances

transmissibility of the mount and can be defined as the improvement in the ratio

of the performance of the isolated case to that of the hardmount as a function of frequency. Blackwood [14] refers to this dimensionless ratio as the passive sensitivity of the mount. The transmissibility in the single degree of freedom case is given by the following transfer function.

$$P(s) = \frac{z(s)}{z_0(s)} = \frac{\ddot{z}(s)}{\ddot{z}_0(s)} = \frac{Cs + K}{Ms^2 + Cs + K} \quad (3.1)$$

By defining the natural frequency and damping ratio of the mount as

$$\omega_n^2 = \frac{K}{M} \quad \zeta = \frac{C}{2M\omega_n} \quad (3.2)$$

we can represent the transmissibility in its modal form as

$$P(s) = \frac{z(s)}{z_0(s)} = \frac{\ddot{z}(s)}{\ddot{z}_0(s)} = \frac{2\zeta\omega_n s + \omega_n^2}{s^2 + 2\zeta\omega_n s + \omega_n^2} \quad (3.3)$$

The magnitude and phase of the transmissibility are plotted in Figure 3-3 as a function of normalized frequency  $\bar{\omega} = \omega/\omega_n$  for different values of the damping ratio  $\zeta$ . It is seen that the transmissibility at  $\bar{\omega} = \sqrt{2}$  is unity regardless of the damping ratio

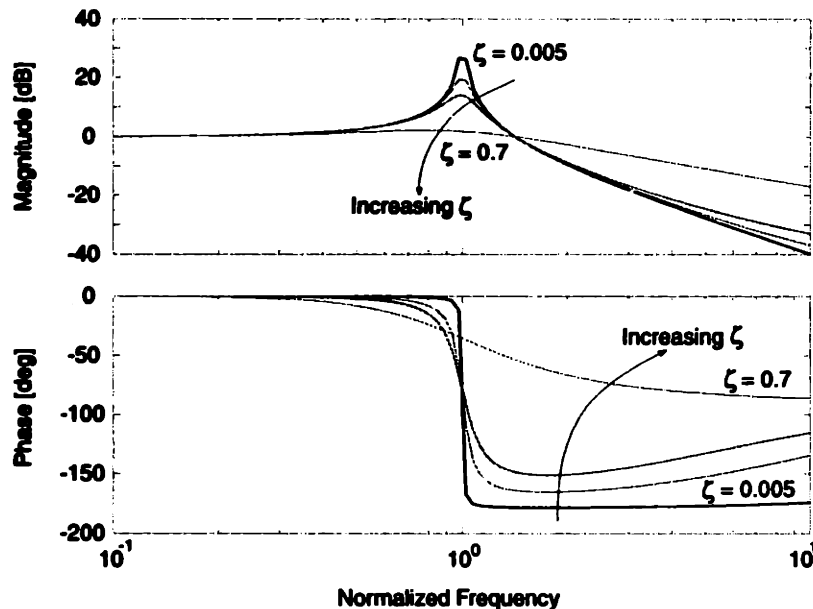


Figure 3-3: Transmissibility of a single degree of freedom passive vibration isolation system for various values of damping ratio

and that the mount attenuates the disturbances at all greater frequencies. At lower frequencies, the mount passes the disturbances through unaffected or amplifies them depending on the damping ratio. The effect of increasing the damping ratio  $\zeta$  is to attenuate the resonance near  $\bar{\omega} = 1$  at the cost of increased transmissibility at high frequencies. For zero damping,  $P(s)$  rolls off with a logarithmic slope of -2; at finite values of damping, a real zero at  $\bar{\omega} = 1/(2\zeta)$  increases the high frequency asymptote to a slope of -1. We observe that a simple viscous damping mechanism as illustrated above is limited in performance either at resonance (due to low damping ratios) or at high frequencies (due to high damping ratios). This limitation can be overcome through the use of elastically coupled damping which is illustrated in the context of pneumatic mounts shortly.

An additional performance metric that is not evident from the normalized frequency plot is the static deflection. It is seen from our discussion in Chapter 2 that, reducing the stiffness and thence the natural frequency of the mount leads to better isolation. However, this comes at the cost of increased static deflection. The gravity-induced static deflection for a spring mount is given by

$$\delta = \frac{Mg}{K} = \frac{g}{\omega_n^2} \quad (3.4)$$

where  $g = 9.81\text{m/s}^2$  is the acceleration due to gravity. For example, for a mount with a corner frequency of 10 Hz, the static deflection is approximately 2.5 mm; at 1 Hz the static deflection is approximately 250 mm. For sub-hertz natural frequencies, the static deflection is in the range of a few meters which makes it impossible to obtain such low-frequency isolation performance with purely passive elastomeric or metallic spring mounts.

### 3.3 Pneumatic Mounts

Problems with static deflection and damping can be addressed through the use of pneumatic mounts which has led to their widespread adoption in passive isolation

systems. We first discuss the damping issue in the context of pneumatic mounts although this discussion is applicable to any elastically coupled damper. An isolator mount with elastically coupled damping is modeled using the Zener model [68] which consists of a spring in series with a parallel spring damper arrangement as shown in Figure 3-4. This is the standard “sprung” damping in a pneumatic isolation system.

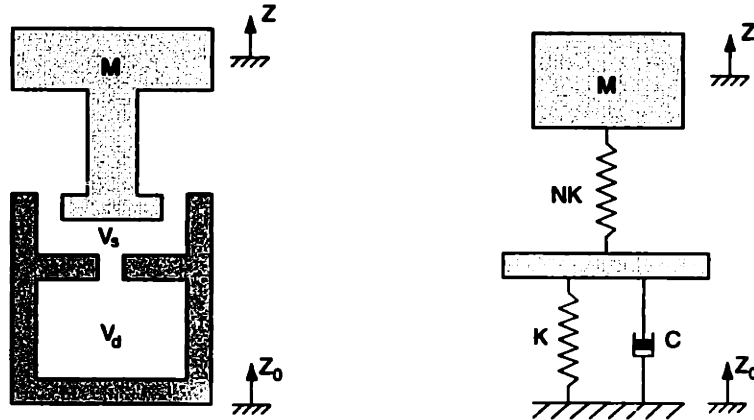


Figure 3-4: Zener or “sprung-damped” model for a pneumatic isolation system.  $V_s$  and  $V_d$  are the volumes of the spring chamber and damping chamber respectively.  $N$  is the spring ratio.

At low frequencies the mount has a spring stiffness  $NK/(N+1)$  while at high frequencies, the damper locks up and the mount stiffness increases to  $NK$ . For an isolation mount with this damping mechanism, the high frequency rolloff of the transmissibility approaches a logarithmic slope of  $-2$  irrespective of the damping ratio. It is also readily seen from the figure that for a zero damping condition  $C = 0$ , the system natural frequency is determined by the mass  $M$  with springs  $NK$  and  $K$  in series. For infinitely high damping  $C = \infty$ , the system natural frequency is determined by the mass  $M$  and spring  $NK$  only and therefore can be higher. The response of a system having a damping ratio in between zero and infinity falls between the corresponding response curves as illustrated in Figure 3-5.

Therefore, an appropriately designed pneumatic isolator can have near critical damping and at the same time retain the vibration isolation rate of an undamped isolator at high frequencies. For a mount described by the Zener model, the trans-

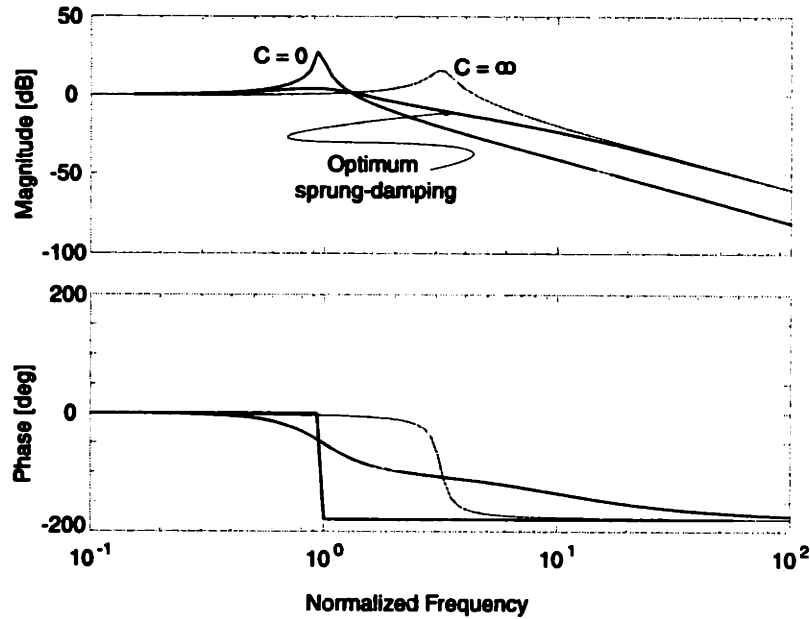


Figure 3-5: Transmissibility of a pneumatic vibration isolation system for various values of damping ratio

missibility can be derived as

$$\begin{aligned}
 P(s) = \frac{z(s)}{z_0(s)} &= \frac{NKC s + NK^2}{MCs^3 + (N+1)MKs^2 + NKCs + NK^2} \\
 &= \frac{N\omega_n^2\zeta s + \frac{N}{2}\omega_n^2}{\zeta s^3 + \frac{N+1}{2}s^2 + N\omega_n^2\zeta s + \frac{N}{2}\omega_n^2}
 \end{aligned} \tag{3.5}$$

where we have again used the definitions for natural frequency and damping ratio from (3.2). Equation (3.5) allows us to clearly observe the limiting characteristics (due to damping) of the Zener model. A good treatment of various damping mechanisms can be found in Ruzicka and Derby [68].

In addition to the favorable damping characteristics, pneumatic isolators can also be designed to provide very low and constant natural frequencies. This is evident from the following discussion. The spring stiffness of a pneumatic isolator is defined by

$$K = \frac{\gamma PA^2}{V} \tag{3.6}$$

where

$$\gamma = C_p/C_v = 1.4 \text{ (for air)}$$

$C_p$  = Specific heat of gas at constant pressure

$C_v$  = Specific heat of gas at constant volume

$P$  = Pressure

$A$  = Effective Area

$V$  = Volume

When the isolator supports a weight  $W = PA$  and the volume can be expressed as  $V = hA$  where  $h$  is the effective air column height, we can obtain an equivalent expression for the isolator stiffness.

$$K = \frac{\gamma W}{h} \quad (3.7)$$

The natural frequency of the isolator is then given by

$$\omega_n = \sqrt{\frac{gK}{W}} = \sqrt{\frac{g\gamma}{h}} \quad (3.8)$$

where  $g$  is the acceleration due to gravity (9.81 m/s<sup>2</sup>). It can be seen from (3.8) that the system natural frequency remains constant independent of the mass supported as long as the effective air column height  $h$  is maintained constant. Rearranging terms in (3.8), we obtain an expression for the effective air column height of a pneumatic isolator can be obtained as

$$h = \frac{g\gamma}{\omega_n^2} \quad (3.9)$$

Comparing (3.9) with (3.4), we see that the “effective air column height” of the isolator is only 40 % greater than the required static deflection  $\delta$  of a linear spring for a given natural frequency  $\omega_n$  [38]. Furthermore, since the effective air column



height is defined by the enclosed air volume divided by the effective piston area, the overall isolator height can be made rather small by making the chamber wider than the piston. Thus a pneumatic isolator can be made to have a compact footprint while providing us with a low natural frequency.

Isolation in the lateral directions in pneumatic systems is usually obtained by a pendulum or rolling diaphragm arrangement. Kunica [38] provides an excellent review of pneumatic isolators and their applications especially for sub-hertz isolation. Typical orifice designs between the two air chambers shown in Figure 3-4 can cause turbulent air flow and hence nonlinearity in system behavior. This causes damping to be completely ineffective at very large or very small amplitudes and can cause deterioration in system performance. Debra [20] identified this problem and proposed porous media to obtain laminar flow in between the two chambers. This has led to trouble free, robust performance and has been adopted commercially in the Newport line of air legs [50].

### 3.4 Negative Stiffness Mechanisms

Low natural frequencies have also been obtained using metallic springs using a novel negative-stiffness mechanism (NSM)<sup>1</sup> designed by Platus [56]. The NSM illustrated in Figure 3-6 consists of two bars hinged at the center, supported at their outer ends on pivots which are free to move horizontally, and loaded in compression by opposing forces  $P$ . The bars are in a state of unstable equilibrium (the center position of the NSM as shown). For small displacements, this “spring” has a negative stiffness  $K_n$  due to the instability. When these compressed bars are used along with a vertical metallic spring of stiffness  $K_s$  that supports the weight  $W$  of the equipment to be isolated, a stable configuration results. The resulting isolator stiffness  $K = K_s - K_n$  can be made to approach zero. The vertical metallic spring  $K_s$  is chosen to provide little static deflection. Horizontally placed flexures are used in place of the hinged bars in practical systems.

---

<sup>1</sup>commercially available as the nano-K product line from Minus K Technology.

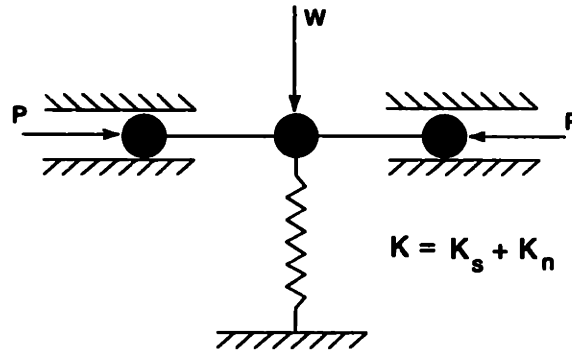


Figure 3-6: Illustration of the negative spring stiffness mechanism used to obtain sub-hertz isolation. Net isolator stiffness can be made to approach 0,  $K = K_s - K_n$ . Illustration reproduced from Platus [56]

Platus [56] reports natural frequencies as low as 0.75 Hz with these mechanisms. Isolation in the lateral directions is achieved by a parallelogram arrangement of flexures. Well designed pneumatic systems are capable of matching the performance of these NSMs, but for some critical applications, especially electron microscopy, NSMs seem to be preferred over pneumatic systems.

We observe that both pneumatic isolators and the negative stiffness mechanisms are capable of providing natural frequencies in the vicinity of 1 Hz. From Table 2.4, this level of isolation is appropriate for wafer steppers and leads to sub-nanometric error motions due to seismic vibrations. In fact, passive isolation is the preferred means of isolation in most precision instruments such as scanning electron microscopes. However, the presence of moving parts and the inertial reaction forces of motion they exert on the payload affects the performance of passive isolation. This is illustrated through an analytical treatment of the fundamental tradeoff of passive vibration isolation in the following section.

### 3.5 Fundamental limits to Passive Vibration Isolation

It is a well known fact that seismic and payload disturbances are conflicting in nature. However, there has not been an analytical description of this phenomenon. We derive

this fundamental tradeoff analytically and relate it to the fundamental tradeoff in control system design. This analytical description along with a spectral characterization of the seismic and payload disturbances helps one make decisions about the feasibility and the amount of passive isolation required (natural frequency and damping of the mount). It also lays the framework for our discussion on active control.

We start our discussion by referring to single degree of freedom systems and extend it to multiple degree of freedom systems. Figure 3-2 is repeated here with payload disturbances represented by the force  $f_d$  acting directly on the payload mass  $M$ . This

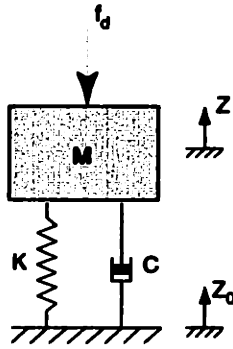


Figure 3-7: Single degree of freedom passive vibration isolation system illustrating both seismic and payload disturbances

may be the resultant of reaction forces from moving parts on the payload. Given that the acceleration of the payload  $\ddot{z}$  is the variable of interest, we compute the transfer functions from the two disturbances  $f_d$  and  $\ddot{z}_0$  to the acceleration of the payload.

$$\frac{\ddot{z}}{f_d(s)} = \frac{s^2}{Ms^2 + Cs + K} = \frac{s^2/M}{s^2 + 2\zeta\omega_n s + \omega_n^2} \quad (3.10)$$

$$\frac{\ddot{z}(s)}{\ddot{z}_0(s)} = \frac{Cs + K}{Ms^2 + Cs + K} = \frac{2\zeta\omega_n s + \omega_n^2}{s^2 + 2\zeta\omega_n s + \omega_n^2} \quad (3.11)$$

While (3.11) is non-dimensional (the ratio of the payload and seismic acceleration), (3.10) is the ratio of the payload acceleration to the disturbance force and has units of 1/Kg. To be able to compare the effects of the two disturbance mechanisms, we normalize the disturbance force  $f_d$  by the payload mass  $M$  to form a payload disturbance acceleration or equivalently we form a non-dimensional quantity by multiplying

(3.10) by the payload mass  $M$ . We term this quantity  $P(s) = M\ddot{z}/f_d(s)$  the *passive sensitivity function* and the ratio  $Q(s) = \ddot{z}(s)/\ddot{z}_0(s)$  the *passive complementary sensitivity function*. Accordingly, we define the passive sensitivity and complementary sensitivity functions to be

$$\begin{aligned} P(s) &= \frac{M\ddot{z}}{f_d(s)} = \frac{Ms^2}{Ms^2 + Cs + K} = \frac{s^2}{s^2 + 2\zeta\omega_n s + \omega_n^2} \\ Q(s) &= \frac{\ddot{z}(s)}{\ddot{z}_0(s)} = \frac{Cs + K}{Ms^2 + Cs + K} = \frac{2\zeta\omega_n s + \omega_n^2}{s^2 + 2\zeta\omega_n s + \omega_n^2} \end{aligned} \quad (3.12)$$

Equations (3.12) demonstrate the effect of the two disturbance mechanisms clearly and reveal some very interesting features. It is evident that the following relationship holds for the single degree of freedom structure under consideration.

$$P(s) + Q(s) = 1 \quad (3.13)$$

This relationship demonstrates the fundamental tradeoff - it is impossible to have good attenuation of both seismic and payload disturbances and is strikingly similar to the concept of sensitivity and complementary sensitivity functions in control literature that determine disturbance and noise rejection of a closed loop system. Blackwood [14] defines the ratio  $Q(s) = \ddot{z}(s)/\ddot{z}_0(s)$  to be the passive sensitivity function. However, we redefine it to be the passive complementary sensitivity function while defining the ratio  $P(s) = M\ddot{z}/f_d(s)$  to be the passive sensitivity function. The reasons for our redefinition will be apparent shortly.

We first generalize the concept of passive sensitivity and complementary sensitivity functions to multiple degree of freedom problems. For this generalization, consider a rigid body (with all six degrees of freedom) subject to seismic vibrations and supported by discrete isolators. The equations of motion for such a system can be written as

$$M\ddot{\mathbf{x}} + C\dot{\mathbf{x}} + K\mathbf{x} = C\dot{\mathbf{x}}_0 + K\mathbf{x}_0 + \mathbf{f}_d \quad (3.14)$$

where  $\mathbf{x}$  is a six dimensional vector comprising the six rigid body degrees of freedom,  $\mathbf{M}$  the mass/inertia matrix,  $\mathbf{C}$  the damping matrix and  $\mathbf{K}$  the stiffness matrix.  $\mathbf{x}_0$  is a six dimensional vector of seismic vibrations and  $\mathbf{f}_d$  is a six dimensional vector of payload disturbance forces. Taking Laplace transforms and performing a few algebraic manipulations, we obtain

$$\begin{aligned}\ddot{\mathbf{X}}(s) &= (\mathbf{M}s^2 + \mathbf{C}s + \mathbf{K})^{-1} \mathbf{M}s^2 (\mathbf{M}^{-1}\mathbf{F}_d(s)) + \\ &\quad (\mathbf{M}s^2 + \mathbf{C}s + \mathbf{K})^{-1} (\mathbf{C}s + \mathbf{K}) \ddot{\mathbf{X}}_0(s) \\ &= \mathbf{P}(s) (\mathbf{M}^{-1}\mathbf{F}_d(s)) + \mathbf{Q}(s)\ddot{\mathbf{X}}_0(s)\end{aligned}\tag{3.15}$$

Equations (3.15) illustrate the sensitivity and complementary sensitivity functions for a multi-degree of freedom system. It is evident that the tradeoff established for the single degree of freedom system in (3.13) also holds good for the multiple degree of freedom system. Indeed, we observe from (3.15) that

$$\mathbf{P}(s) + \mathbf{Q}(s) = \mathbf{I}\tag{3.16}$$

We now put things in a control systems context and cast the vibration isolation problem as a feedback control problem<sup>2</sup> as illustrated in Figure 3-8. We can quickly

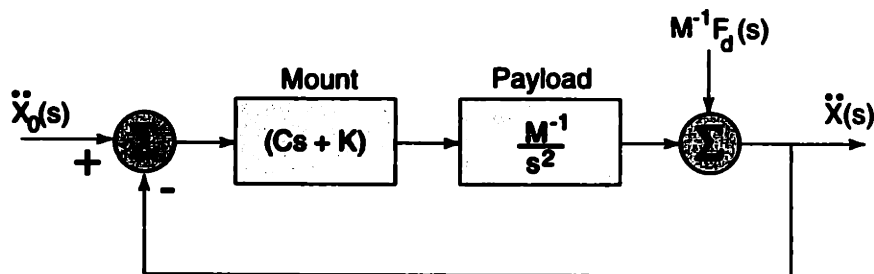


Figure 3-8: Multi-degree of freedom passive vibration isolation problem cast as a feedback control design problem

verify that equations (3.15) hold good for the feedback system illustrated in Figure 3-

<sup>2</sup>We actually pose it later as an optimal filtering problem.

8. This is done as follows :

$$\begin{aligned}\ddot{\mathbf{X}}(s) &= \mathbf{M}^{-1}\mathbf{F}_d(s) + \frac{\mathbf{M}^{-1}}{s^2}(\mathbf{C}s + \mathbf{K})\ddot{\mathbf{X}}_0(s) - \frac{\mathbf{M}^{-1}}{s^2}(\mathbf{C}s + \mathbf{K})\ddot{\mathbf{X}}(s) \\ \Rightarrow \left[ \mathbf{I} + \frac{\mathbf{M}^{-1}}{s^2}(\mathbf{C}s + \mathbf{K}) \right] \ddot{\mathbf{X}}(s) &= \mathbf{M}^{-1}\mathbf{F}_d(s) + \frac{\mathbf{M}^{-1}}{s^2}(\mathbf{C}s + \mathbf{K})\ddot{\mathbf{X}}_0(s)\end{aligned}$$

We now apply the matrix inversion lemma<sup>3</sup> to compute the inverse

$$\begin{aligned}\left[ \mathbf{I} + \frac{\mathbf{M}^{-1}}{s^2}(\mathbf{C}s + \mathbf{K}) \right]^{-1} &= \mathbf{I} - (\mathbf{M}s^2 + \mathbf{C}s + \mathbf{K})^{-1}(\mathbf{C}s + \mathbf{K}) \\ &= (\mathbf{M}s^2 + \mathbf{C}s + \mathbf{K})^{-1}\mathbf{M}s^2\end{aligned}$$

and finally obtain (3.15). Casting the passive isolation problem in a control systems context places a lot of things in perspective. Established control system design practices can now be used to analyze and synthesize the isolation mounts. The practice of adding an isolation mount to a payload is akin to that of lead compensation or proportional-derivative control. Increasing the proportional gain or the stiffness of the mount helps increase the natural (or crossover) frequency of the mount while increasing the derivative gain or the damping helps damp the response. The passive isolation problem can now be posed as an optimal control problem to determine the optimal stiffness and damping of the isolation mounts.

Figure 3-8 demonstrates our reason for differing from Blackwood [14] in our definition of the passive sensitivity function. Our definition allows us to obtain a strictly proper plant (or payload), while the definition in Blackwood [14] would entail working with a strictly improper plant. Also, our definition of the plant as the payload mass is intuitive, since in a vibration isolation design problem, one traditionally starts out with the mass/inertia matrix  $\mathbf{M}$  and designs the mounts. Besides, in control systems literature, the sensitivity function is traditionally zero at low frequencies and tends to unity at higher frequencies while the opposite holds true for the complementary sensitivity function. Our definition of sensitivity and complementary sensitivity permits

---

<sup>3</sup> $(\mathbf{A} + \mathbf{BCD})^{-1} = \mathbf{A}^{-1} - \mathbf{A}^{-1}\mathbf{B}(\mathbf{C}^{-1} + \mathbf{DA}^{-1}\mathbf{B})^{-1}\mathbf{DA}^{-1}$

us to obtain a similar behavior for the vibration isolation problem. This is illustrated for a single degree of freedom system in Figure 3-9.

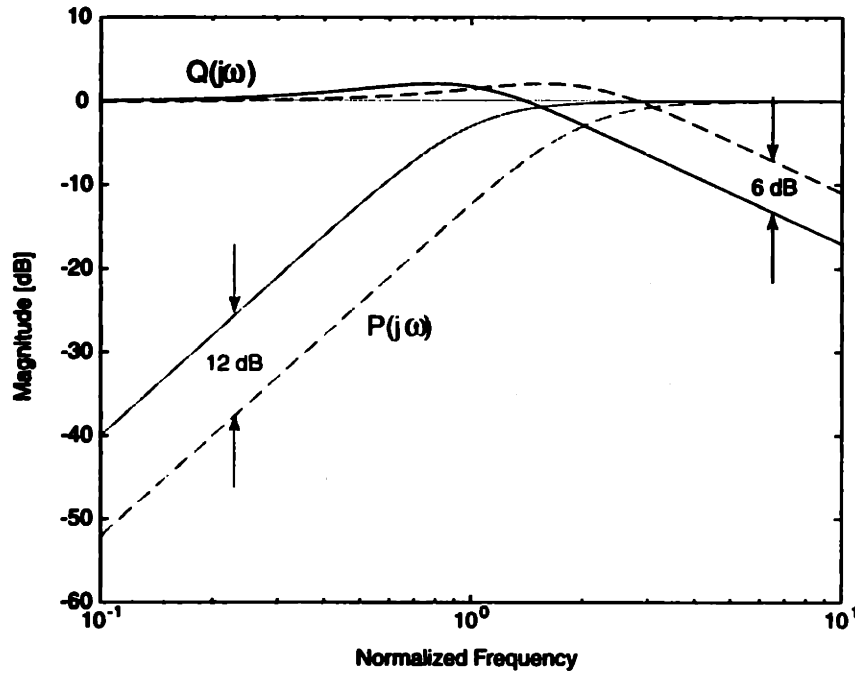


Figure 3-9: Trade-off between base and payload disturbance rejection as the natural frequency of the mount  $\bar{\omega}_n$  is changed from 1 to 2. Note that the sensitivity  $P(j\omega)$  and the complementary sensitivity  $Q(j\omega)$  follow traditional control system practice.

A dimensionless plot of (3.12) for a damping ratio of 0.707 is illustrated in Figure 3-9 as a function of normalized frequency. Improved vibration isolation comes at the expense of payload disturbance rejection and vice-versa. It can be seen that a factor of two reduction in mount natural frequency provides 6 dB more isolation above resonance. This improved isolation comes at the expense of 12 dB reduced disturbance force isolation below mount resonance. This clearly illustrates the fundamental tradeoff of passive vibration isolation.

It should be noted that besides illustrating the fundamental tradeoff in passive vibration isolation, there is one more significant practical use of the passive sensitivity and complementary sensitivity functions. In most large structures, it is difficult to obtain clear transmissibility plots due to the difficulties in exciting the ground adequately over all the frequencies of interest. In such cases, a shaker can be used to excite the structure in the required direction and the resulting acceleration recorded.

This along with the knowledge of the mass/inertia matrix  $\mathbf{M}$  can be used to determine the sensitivity function  $\mathbf{P}(s)$ . The complementary sensitivity function or transmissibility of the isolation system is then given simply by

$$\mathbf{Q}(s) = \mathbf{I} - \mathbf{P}(s) \quad (3.17)$$

The use of (3.17) is illustrated in the context of the prototype wafer stepper considered in this thesis in Chapter 6.

Next, we illustrate a novel procedure to select optimum values for the damping and stiffness of the mount. This is done by casting the mount design procedure in the form of a state estimation problem. This permits us to apply the various techniques available to us in the design of state estimators to the problem of mount selection. In particular, we discuss an  $\mathcal{H}_2$  solution to the problem, *i.e.*, that of Kalman filtering.

### **3.6 A Kalman filter approach to the synthesis of passive mounts**

In the previous section, we cast the passive vibration isolation problem in the context of a feedback control problem with the payload disturbances and seismic vibrations related to payload motions through sensitivity and complementary sensitivity functions. The next logical step is to ask if there is an easy procedure to design the optimal mount given these conflicting disturbance phenomena. To do this, we turn to established techniques of Kalman filtering. A Kalman filter is an optimal state estimator that minimizes the 2-norm of the state estimation error for a system subject to process disturbances and sensor noise. The process disturbance and sensor noise are related to the output of a system through the sensitivity and complementary sensitivity function - a fact that motivates application of the Kalman filtering technique to our problem of passive mount design. While the motivation behind a state estimation problem is to obtain an "optimal" state estimate given quantitative estimates of the sensor noise and process disturbances, the motivation behind the pas-



sive mount synthesis problem is to obtain the “optimal” stiffness and damping given a quantitative measure of the conflicting seismic and payload disturbance sources. When these external disturbance sources can be described as white noise processes, the Kalman filter provides the optimal solution to the state estimation problem. In this section, we pose the design of the passive mount parameters (*i.e.*, stiffness and damping) as a Kalman filtering problem and use established techniques to synthesize optimal passive mounts. The resulting solution is found to minimize the variance of payload motions.

### 3.6.1 The Kalman Filter

Since the Kalman filter is central to this section, we present a review of Kalman filter equations and the state estimation process. While there is a considerable amount of literature on Kalman filtering and different notations, we rely on the notation established by Athans [6]. First, we represent the plant dynamics as a finite-dimensional system whose state vector  $\mathbf{x}(t)$ ,  $\mathbf{x}(t) \in \mathfrak{R}^n$  obeys a stochastic differential equation and the measurement is a linear combination of the state variables with additive sensor noise. Accordingly,

$$\begin{aligned}\dot{\mathbf{x}}(t) &= \mathbf{A}\mathbf{x}(t) + \mathbf{L}\xi(t) \\ \mathbf{y}(t) &= \mathbf{C}\mathbf{x}(t) + \boldsymbol{\theta}(t)\end{aligned}\tag{3.18}$$

The design of a Kalman filter requires two other assumptions on the plant equations. They are that

- $[\mathbf{A}, \mathbf{L}]$  is stabilizable (or controllable)
- $[\mathbf{A}, \mathbf{C}]$  is detectable (or observable)

Both  $\xi(t) \in \mathfrak{R}^q$  and  $\theta(t) \in \mathfrak{R}^p$  are assumed to be independent, Gaussian, zero-mean, white noise processes.

$$\begin{aligned}
 E\{\xi(t)\} &= \mathbf{0}, & \forall t \\
 E\{\xi(t)\xi'(t)\} &= \Xi\delta(t-\tau), & \Xi = \Xi' > \mathbf{0} \\
 E\{\theta(t)\} &= \mathbf{0}, & \forall t \\
 E\{\theta(t)\theta'(t)\} &= \Theta\delta(t-\tau), & \Theta = \Theta' > \mathbf{0} \\
 E\{\xi(t)\theta'(t)\} &= \mathbf{0} & 
 \end{aligned} \tag{3.19}$$

The process disturbance intensity matrix  $\Xi$  along with the Dirac delta function  $\delta(t-\tau)$  gives the covariance of the process disturbances  $\xi(t)$  while the sensor noise intensity matrix  $\Theta$  along with the Dirac delta function  $\delta(t-\tau)$  gives the covariance of the sensor noise  $\theta(t)$ .

The state estimation problem is now posed as follows, given the control input  $u(t)$  (which is set to zero in our case since we this is a pure estimation/filtering problem) and the measurement  $y(t)$  over all time  $t$ , find a vector  $\hat{x}$  at any time  $t$  which is an optimal estimate of the true state  $x(t)$  of the system defined by (3.30). This generally optimal estimate which is given by the conditional mean [6] can be generated using various algorithms. One popular method is to demand that the state estimate be generated by a linear transformation on past data such that the state estimation error  $\tilde{x}(t)$

$$\tilde{x}(t) = x(t) - \hat{x}(t) \tag{3.20}$$

has zero mean, *i.e.*,

$$E\{\tilde{x}(t)\} = \mathbf{0}$$

and the cost functional

$$\begin{aligned} J &= \mathbf{E} \left\{ \sum_{i=1}^n \tilde{x}_i^2(t) \right\} \\ &= \mathbf{E} \{ \tilde{\mathbf{x}}'(t) \tilde{\mathbf{x}}(t) \} = \text{tr} [\mathbf{E} \{ \tilde{\mathbf{x}}(t) \tilde{\mathbf{x}}'(t) \}] \end{aligned} \quad (3.21)$$

is minimized.

The cost functional  $J$  has the physical interpretation that it is the sum of the error variances  $\mathbf{E} \{ \tilde{x}_i^2(t) \}$  for each state variable. If we let  $\Sigma$  denote the (stationary) covariance matrix of the state estimation error

$$\Sigma = \mathbf{E} \{ \tilde{\mathbf{x}}(t) \tilde{\mathbf{x}}'(t) \} \quad (3.22)$$

the cost  $J$  from (3.21) can be written as

$$J = \text{tr} [\Sigma] \quad (3.23)$$

The Kalman filter is an optimal filter which minimizes the 2-norm of the state prediction error given the process and sensor noise covariance. It generates the state estimate  $\hat{\mathbf{x}}(t)$  and the output estimate  $\hat{\mathbf{y}}(t)$  in real time.

The Kalman filter equations in the absence of a control vector are given by [6].

$$\begin{aligned} \dot{\hat{\mathbf{x}}}(t) &= \mathbf{A}\hat{\mathbf{x}}(t) + \mathbf{H}[\mathbf{y}(t) - \mathbf{C}\hat{\mathbf{x}}(t)] \\ \hat{\mathbf{y}}(t) &= \mathbf{C}\hat{\mathbf{x}}(t) \end{aligned} \quad (3.24)$$

A block diagram representation of the dynamics of the plant and the Kalman filter for the isolation problem is illustrated in Figure 3-10.

After some algebraic manipulation of the plant and filter equations given in (3.18) and (3.24), we obtain the following stochastic vector differential equation for the state estimation error  $\tilde{\mathbf{x}}(t)$ .

$$\dot{\tilde{\mathbf{x}}}(t) = (\mathbf{A} - \mathbf{H}\mathbf{C})\tilde{\mathbf{x}}(t) + \mathbf{L}\xi(t) - \mathbf{H}\theta(t) \quad (3.25)$$

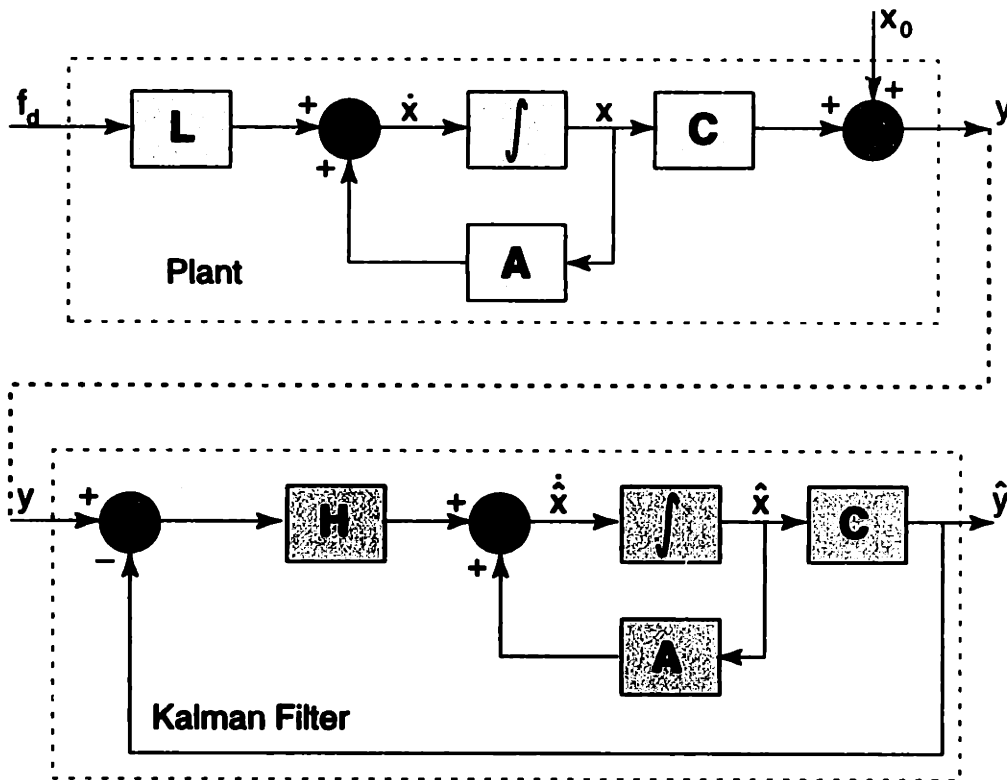


Figure 3-10: Illustration of the stochastic dynamics of the plant and its Kalman filter for the passive isolation problem.

Using elementary facts from stochastic linear system theory [13], one can compute the error covariance matrix  $\Sigma$  of the state estimation error  $\tilde{\mathbf{x}}(t)$

$$\Sigma = \text{cov} [\tilde{\mathbf{x}}(t); \tilde{\mathbf{x}}(t)] = \mathbf{E} \{ \tilde{\mathbf{x}}(t) \tilde{\mathbf{x}}'(t) \}$$

The covariance matrix  $\Sigma$  is the solution of the so-called *Lyapunov matrix equation*

$$(\mathbf{A} - \mathbf{H}\mathbf{C}) \Sigma + \Sigma (\mathbf{A} - \mathbf{H}\mathbf{C})' + \mathbf{L}\Xi\mathbf{L}' + \mathbf{H}\Theta\mathbf{H}' = \mathbf{0} \quad (3.26)$$

with,

$$\Sigma = \Sigma'$$

The trace of the error covariance matrix  $\Sigma$  then gives the quality (or cost) of the state estimator according to (3.23).

The Kalman filter minimizes this cost. The specific way the Kalman filter gain is computed is by solving a constrained static optimization problem the details of which are available in many optimal control textbooks [40]. We give only the end results here. The Kalman gain  $\mathbf{H}$  is given by

$$\mathbf{H} = \Sigma \mathbf{C}' \Theta^{-1} \quad (3.27)$$

where,  $\Sigma$  is the unique, symmetric and at least positive semi-definite solution to the so-called Filter Algebraic Riccati Equation (FARE).

$$\mathbf{A}\Sigma + \Sigma\mathbf{A}' + \mathbf{L}\Xi\mathbf{L}' - \Sigma\mathbf{C}'\Theta^{-1}\mathbf{C}\Sigma = \mathbf{0} \quad (3.28)$$

with,

$$\Sigma = \Sigma' \geq \mathbf{0}$$

Having discussed the Kalman filter and its application to the state estimation problem, we now proceed to its application to the passive mount synthesis problem.

### 3.6.2 Optimal Passive mount synthesis

The optimal passive mount synthesis problem is cast into the form of the generic Kalman filtering problem described above as follows. We consider payload disturbance forces to be the process disturbance and the seismic vibrations to be sensor noise. Accordingly, we make the following definitions.

$$\begin{aligned}\boldsymbol{\xi}(t) &= \mathbf{f}_d(t), & \boldsymbol{\xi}(t) \in \mathfrak{R}^n \\ \boldsymbol{\theta}(t) &= \mathbf{x}_0(t), & \boldsymbol{\theta}(t) \in \mathfrak{R}^n\end{aligned}\tag{3.29}$$

The plant is just a double integrator as discussed in the previous section. Accordingly (3.18) when specialized to the vibration isolation problem, takes on the following form.

$$\begin{aligned}\begin{Bmatrix} \dot{\mathbf{x}}(t) \\ \ddot{\mathbf{x}}(t) \end{Bmatrix} &= \begin{pmatrix} \mathbf{0} & \mathbf{I} \\ \mathbf{0} & \mathbf{0} \end{pmatrix} \begin{Bmatrix} \mathbf{x}(t) \\ \dot{\mathbf{x}}(t) \end{Bmatrix} + \begin{Bmatrix} \mathbf{0} \\ \mathbf{M}^{-1} \end{Bmatrix} \mathbf{f}_d(t) \\ \mathbf{y}(t) &= \begin{pmatrix} \mathbf{I} & \mathbf{0} \end{pmatrix} \begin{Bmatrix} \mathbf{x}(t) \\ \dot{\mathbf{x}}(t) \end{Bmatrix} + \mathbf{x}_0(t)\end{aligned}\tag{3.30}$$

where  $\mathbf{M}$  is the inertia matrix of the payload mass and we have chosen the state variables to be the absolute displacement and velocity of the payload mass. The requirements that  $[\mathbf{A}, \mathbf{L}]$  be controllable and  $[\mathbf{A}, \mathbf{C}]$  be observable are readily met by the plant equations in (3.30).

The Kalman filter minimizes the covariance of the state estimation error, and in our passive mount synthesis problem we wish to minimize payload motions. With our formulation, the state estimation error in the generic Kalman filtering problem is replaced by the state of the payload motions (displacement and velocity of the payload mass). Corresponding to the parameterization of the plant equations in (3.30) we can parameterize the Kalman gain as follows,

$$\mathbf{H} = \begin{pmatrix} \mathbf{M}^{-1}\mathbf{C} \\ \mathbf{M}^{-1}\mathbf{K} \end{pmatrix}\tag{3.31}$$

where  $\mathbf{C}$  and  $\mathbf{K}$  are the optimum mount damping and stiffness matrices.

We finally demonstrate that the Kalman filter formulation is representative of the sensitivity and complementary sensitivity transfer functions in (3.15). We demonstrate this by taking the Laplace transform of (3.25) and performing a few algebraic manipulations.

$$\begin{aligned}\bar{\mathbf{x}}(s) &= (s\mathbf{I} - \mathbf{A} + \mathbf{HC})^{-1} \mathbf{L}\xi(s) - (s\mathbf{I} - \mathbf{A} + \mathbf{HC})^{-1} \mathbf{H}\theta(s) \\ \bar{\mathbf{y}}(s) &= \mathbf{C}(s\mathbf{I} - \mathbf{A} + \mathbf{HC})^{-1} \mathbf{L}\xi(s) - \mathbf{C}(s\mathbf{I} - \mathbf{A} + \mathbf{HC})^{-1} \mathbf{H}\theta(s)\end{aligned}\quad (3.32)$$

We obtain the inverse of the matrix  $(s\mathbf{I} - \mathbf{A} + \mathbf{HC})$  using the matrix inversion rule for partitioned matrices from Horn *et al.* [30]. Specifically,

$$\mathbf{C}(s\mathbf{I} - \mathbf{A} + \mathbf{HC})^{-1} = (s^2\mathbf{I} + \mathbf{M}^{-1}\mathbf{C}s + \mathbf{M}^{-1}\mathbf{K})^{-1} \begin{pmatrix} s\mathbf{I} & \mathbf{I} \end{pmatrix}\quad (3.33)$$

Substituting (3.33) in (3.32), we get

$$\begin{aligned}\bar{\mathbf{y}}(s) &= \\ & (s^2\mathbf{I} + \mathbf{M}^{-1}\mathbf{C}s + \mathbf{M}^{-1}\mathbf{K})^{-1} \begin{pmatrix} s\mathbf{I} & \mathbf{I} \end{pmatrix} \left( \begin{Bmatrix} \mathbf{0} \\ \mathbf{M}^{-1} \end{Bmatrix} \mathbf{f}_d(s) - \begin{Bmatrix} \mathbf{M}^{-1}\mathbf{C} \\ \mathbf{M}^{-1}\mathbf{K} \end{Bmatrix} \mathbf{x}_0(s) \right)\end{aligned}\quad (3.34)$$

Except for a sign change which denotes the direction of the seismic vibrations, we recover (3.15) from the above. This verifies our Kalman filter formulation. Hence, established Kalman filter techniques can be used to determine the optimum filter gain. The mount stiffness and damping parameters can then be recovered from the filter gain matrix using (3.31).

### 3.7 Summary of Chapter 3

The objective of this chapter is to review passive vibration isolation techniques. Specifically, we discuss low frequency vibration isolation. Low frequency passive isolation is currently achieved by the use of either pneumatic mounts or negative

stiffness mechanisms. A review of both these mechanisms is presented. Fundamental relations governing pneumatic isolation are also presented - this is because pneumatic isolation has excellent properties that make it a highly suitable candidate for active/passive isolation mounts. We then present an analytical derivation of the fundamental tradeoff in passive vibration isolation. We pose this tradeoff in terms of passive sensitivity and complementary sensitivity functions along the lines of similar quantities in control literature. These functions while illustrating the fundamental tradeoff are also of practical interest in both system identification and experimental isolation performance studies.

The identification of the fact that the two conflicting disturbances in an isolation system affect the performance through the sensitivity and complementary sensitivity functions leads us to pose the passive mount design problem as a state estimation problem. Specifically, minimization of the payload motion variance is demonstrated by casting the isolation mount design problem in the form of a Kalman filtering problem.



# Chapter 4

## Active Isolation Design

### 4.1 Introduction

Payload and seismic disturbances impose conflicting requirements on the isolation system calling for hard and soft mounts respectively. These conflicting requirements cannot be met by the simple constitutive relations of a passive device due to the tradeoff established by (3.16). Indeed, the biggest contributor of error motions in a photolithographic stepper is due to inertial reaction forces on the frame of the stepper caused by stage motions. This is illustrated later through an example in Chapter 5. Attenuation of error motions due to these conflicting disturbances requires the use of active control.

As mentioned in Chapter 3, vibration isolation becomes truly important only in the presence of flexible modes of the equipment being isolated. However, traditional approaches to vibration isolation have been to treat both the payload being isolated and the substructure supporting the payload as rigid bodies. Unfortunately, the rigid body assumption can lead to poor performance as well as instability in active schemes. This has lately led to considerable activity in modeling and compensation for the flexibility in the substructure and the payload especially in the aerospace industry. The theses of Blackwood [14] and Hyde [31] represent significant efforts in this direction. We consider the stepper in Figure 3-1 to be a rigid body for the purposes of isolation systems design described in Chapter 5 and in the initial controller

design described in Chapter 4. This assumption is relaxed in Chapter 7 to include flexibility effects and hence improve the performance of the stepper.

In this chapter, we first review the literature to compare and contrast the designs proposed by various researchers. Specifically, we study certain designs that are commercially available and investigate their pros and cons. We then study active isolation architectures and the influence of the architecture on the selection of actuators. Following this, we illustrate how active systems are not subject to the same fundamental tradeoff of passive mounts and hence the obvious choice for machinery mounts where the effects of both payload disturbance and seismic vibration need to be attenuated. We derive the performance improvement afforded by active control over passive mounts. This permits us to draw up guidelines for the design of active control systems. Following this, we formulate the controller design problem as a linear quadratic design problem. A single degree of freedom example is worked out to illustrate the effect of control and to illustrate loopshaping. Finally, we summarize the advantages and limitations of active isolation.

## 4.2 Relevant Literature

Ruzicka [67] presents a good review of the historical development of active isolation in applications such as marine vessels, jet aircraft pilot seats, and inertial guidance platforms for missiles. Karnopp [34] presents a good review of optimal control techniques for a single degree of freedom system subject to white noise disturbances. A significant amount of work on active vibration isolation has been performed in the aerospace industry due to the stringent requirements on pointing and inertial guidance of payloads. Both Blackwood [14] and Hyde [31] present good reviews of the work done in the aerospace industry. Grodsinsky *et al.* [28] have performed considerable work towards low frequency vibration isolation technology for microgravity space experiments. Spanos *et al.* [73] present an interesting 6-axis active vibration isolator using 6 active struts arranged in an orthogonal Stewart platform configuration.

Isolation in the aerospace industry is characterized by the presence of flexible

substructures and broadband disturbances due to personnel, firing of thrusters and the angular momentum of reaction wheels. Active isolation also finds application in the automobile industry. Thompson [77] presents the application of optimal control techniques to the problem of automobile isolation. The road profile is modeled to be continuous and random and simulations are performed to show improvement in a quadratic index as compared with passive isolation. We consider the isolation of precision machine tools which presents a very different problem from the aerospace industry because of the nature of the masses involved and the presence of gravity. In this area, von Flotow [82] presents an expository overview of active machinery mounts. He discusses various architectures, and raises some issues about sensors, actuators and control schemes. Vibration isolation of a machine from the environment is dual to the problem of force isolation of the environment from the machine. Tanaka *et al.* [75] discuss this problem using a rigid support, a reaction mass and force feedback. Debra [21] presents a good overview of active and passive isolation for precision instruments and machines.

#### 4.2.1 Commercial Devices

Barry controls<sup>1</sup> pioneered commercial application of active isolation for precision motion applications. Not surprisingly, commercial applications of active isolation for precision machines target the semiconductor industry - primarily photolithography. Schubert [69] presents the first active damper developed by Barry controls for precision motion applications. The "active softmount"<sup>2</sup> system described by Schubert is based on conventional pneumatic air springs that provide a (passive) vertical natural frequency of 4 Hz, and a (passive) lateral natural frequency of 2.5 Hz due to a pendulum arrangement. Four such isolators are used to support the payload. Geophones are used to sense inertial velocities of the payload in all six degrees of freedom and the control signal is computed to be proportional to the velocity. This form of active

---

<sup>1</sup>Brighton, MA

<sup>2</sup>Literature refers to a parallel arrangement as an active softmount and a series arrangement as an active hardmount for reasons that will be obvious later.

isolation is called “skyhook damping”, since the damping is enhanced and it appears that the active damper is connected between the payload and free space due to the inertial measurements provided by the geophones. Six voice coil actuators are used to apply control forces onto the payload. The result is a corner frequency of 0.5 Hz with very little resonance. A review of literature suggests that this is the first description of a commercially developed isolation system specifically meant for the semiconductor industry. However, it does not appear that this system was very successful. From later Barry publications, it appears that payload dynamics (flexibility of the stepper) caused stability problems with this active softmount.

Barry controls then developed the Stacis 2000<sup>3</sup> system [12] [36]. This is a so-called active hardmount where an elastomeric mount is used to provide passive isolation of the payload above 20 Hz. The single axis mount illustrated in Figure 4-1 offers both

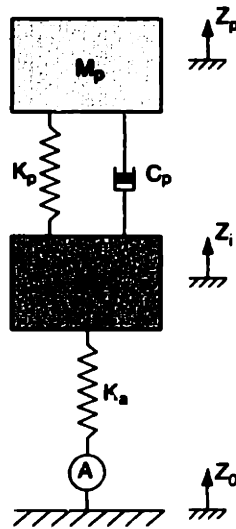


Figure 4-1: Schematic representation of a single axis hardmount reproduced from Beard *et al.* [12].  $M_P$  is the payload to be isolated,  $M_i$  the intermediate mass,  $K_p$  the stiffness of the elastomeric mount and  $K_a$  the finite stiffness of the piezoelectric actuator.

performance and stability advantages over a soft mount. This is because the payload modes are only weakly coupled to the intermediate mass  $M_i$ . This permits controller design that does not need to be tuned to specific payloads and thus better stability over all operating conditions. Use of the hardmount (with a natural frequency of

<sup>3</sup>Currently marketed by Technical Manufacturing Corporation (TMC), Peabody, MA

20 Hz and above) enhances payload disturbance rejection also. The Stacis system uses absolute velocity sensors (geophones) to measure seismic and payload vibrations with piezoelectric stacks used to apply control forces to the intermediate mass. Barry controls has commercialized this design by incorporating three degrees of freedom in a leg and selling three legs as one complete isolation systems design. Each degree of freedom is mechanically decoupled from the other and SISO control techniques are used to compute the control forces. Increased payload acceleration requirements cause payload disturbances to be large enough to cause settling problems with the Stacis 2000 system. Hence, this system has not found widespread commercial application in lithography applications. However, this represents a clever approach to the design of a general purpose active mount to be independent of payload dynamics.

Integrated Dynamics Engineering Inc.<sup>4</sup> seeks to resolve the problems involved in commercial application of active vibration isolation by recognizing that the key to better isolation of payload reaction forces is using feedforward techniques. This resulted in the introduction of their “FF Series isolation systems” which look very similar to the system described by Schubert [69]. Voice coil actuators are used along with pneumatic mounts as described by Schubert. Their “MaxAktiv” family uses linear motors rather than voice coil actuators. Linear motors are capable of generating larger control forces than voice coil actuators with considerable size and packaging improvements. Though there is no comment on the passive isolation used in these isolators, from the size of the active mounts, it would appear that elastomeric mounts are used to provide passive isolation. While these active mounts are of the “parallel softmount architecture”, IDE also markets their PTC series of isolation mounts which seem to be built along similar lines to the Stacis 2000 system (“series hardmount architecture”). Their “top-of-the-line” ATC isolation modules provide isolation down to about 10 mHz and use pneumatic rather than elastomeric isolators. This design also seems to be an active softmount.

IDE emphasizes feedforward control in all its active control designs, but it is not clear how the effect of payload dynamics is handled. This can be a significant

---

<sup>4</sup>Woburn, MA

limiting factor unless the isolation system is correctly integrated into the payload being controlled. Besides, in most cases, one is not interested in vibration isolation of the payload itself as in controlling error motions between specified parts of the machine (*i.e.* Lens and stage for the wafer stepper). A very different design and control philosophy is needed in such a case for optimal performance. This thesis aims to fill in this gap, and differs from commercial designs in this aspect.

### 4.3 Active Isolation Architecture

Active isolation can be classified according to the interaction between the passive and active components of the mount. Blackwood [14] reviews four different configurations and classifies them to be series actuation, parallel actuation, momentum compensation and force compensation. Momentum and force compensation use a reaction mass to modify the passive transmissibility and are not considered in this thesis. We consider series and parallel actuation in this section. Actuators may be piezoelectric, hydraulic, pneumatic or electromechanical and will have a finite output impedance which governs the load carrying capacity at zero power and determines whether the actuator may be considered to command force or displacement. The parallel and series configurations are shown in Figure 4-2. A parallel configuration is

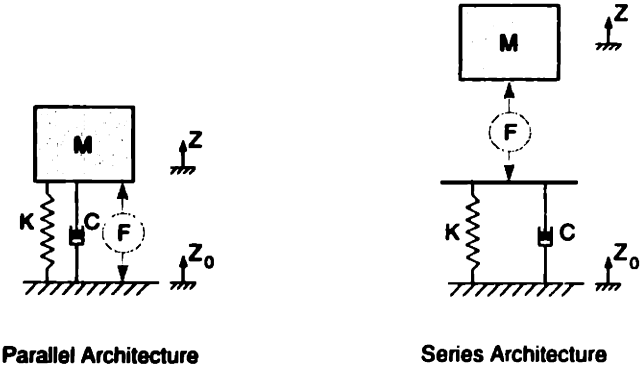


Figure 4-2: Comparison of Parallel and Series Isolation Architectures

one where the actuator applies control forces in parallel with the forces due to the spring and damper. In a series configuration, the actuator is in series with the spring and damper. Both have their advantages and disadvantages.

In a parallel configuration, the passive mount (spring/damper) carries the static weight of the machine. The actuator provides dynamic forces for control and hence can be sized accordingly. Actuators used in such a configuration need to have low internal impedance<sup>5</sup> since the overall spring constant of the mount  $K$  is determined by the passive isolator stiffness plus any internal stiffness of the physical force actuator. For this reason, low impedance actuators are usually force actuators as opposed to displacement actuators. Most actuators used in parallel configurations are large displacement, low force actuators which are usually electromagnetic. Voice-coil actuators based on Lorentz forces and more recently brushless motors are typically used in such a configuration. A significant advantage of this configuration is that the actuators can be removed for maintenance without having to lift the machine off the mounts. The “FF-series” and the “ATC-series” of isolation mounts from IDE are both of this kind. This type of mount is also referred to as an active soft mount. TMC’s “Electrodamp II” architecture is also based on a parallel configuration and is similar to the “MaxAktiv” series of isolation mounts from IDE.

In a series configuration, the passive mount and the actuator are constrained to carry the same amount of force. Hence, these actuators need to have high internal impedance to permit them to carry the weight of the machine. As such, these actuators are stiff and are mostly displacement-type actuators. That is, most actuators used in series configurations are small displacement, high force actuators such as piezoelectric crystals or stacks. A commercial implementation of this configuration is the Stacis system from Newport [50] [12] [36]. IDE also markets their “PTC-series” of isolators which are based on the series architecture and use piezoelectric stacks as the active element.

In the work of this thesis, we have chosen a parallel configuration over a series configuration because of the need to service the actuators without having to remove the mount. Our choice of parallel architecture also constrains us to use low impedance actuators. The selection of the actuators is discussed in Chapter 5 after a review of the mechanical design of the wafer stepper and the isolation system.

---

<sup>5</sup>Impedance is the force per unit velocity.

## 4.4 The Active Isolation Design Paradigm

Payload and seismic disturbances impose conflicting requirements on the isolation system calling for hard and soft mounts respectively. Chapter 3 established the fundamental tradeoff of a passive mount by casting the passive mount design problem into the form of a feedback design problem. We repeat the key results from Chapter 3 here for completeness. Considering a rigid body (with all six degrees of freedom) subject to seismic vibrations and supported by discrete isolators, we have the following :

$$\begin{aligned}
 \ddot{\mathbf{X}}(s) &= (\mathbf{M}s^2 + \mathbf{C}s + \mathbf{K})^{-1} \mathbf{M}s^2 (\mathbf{M}^{-1}\mathbf{F}_d(s)) + \\
 &\quad (\mathbf{M}s^2 + \mathbf{C}s + \mathbf{K})^{-1} (\mathbf{C}s + \mathbf{K}) \ddot{\mathbf{X}}_0(s) \\
 &= \mathbf{P}(s) (\mathbf{M}^{-1}\mathbf{F}_d(s)) + \mathbf{Q}(s)\ddot{\mathbf{X}}_0(s)
 \end{aligned} \tag{4.1}$$

where  $\mathbf{X}(s)$  is a six dimensional vector comprising the Laplace transforms of the six rigid body degrees of freedom,  $\mathbf{M}$  the mass/inertia matrix,  $\mathbf{C}$  the damping matrix and  $\mathbf{K}$  the stiffness matrix.  $\mathbf{X}_0$  is a six dimensional vector of seismic vibrations and  $\mathbf{f}_d$  is a six dimensional vector of payload disturbance forces. Equations (4.1) illustrate the sensitivity and complementary sensitivity functions for a multi-degree of freedom system. We observe from (4.1) that

$$\mathbf{P}(s) + \mathbf{Q}(s) = \mathbf{I} \tag{4.2}$$

This establishes the fundamental tradeoff for a passive device in analytical terms. Payload accelerations are related to payload disturbance forces through the sensitivity function and to seismic disturbances through the complementary sensitivity function.

Hence, good attenuation of these conflicting disturbance mechanisms cannot be provided by the simple constitutive relations of a passive device. Attenuation of error motions due to these conflicting disturbances requires the use of active control. It is shortly shown that an active system is not constrained by the constitutive relations of a passive mount. Active control can be used to enhance the transmissibility provided by a passive mount, or to provide a level of isolation when the passive mount is stiff.



In an active system, sensor measurements (usually inertial velocity or acceleration)

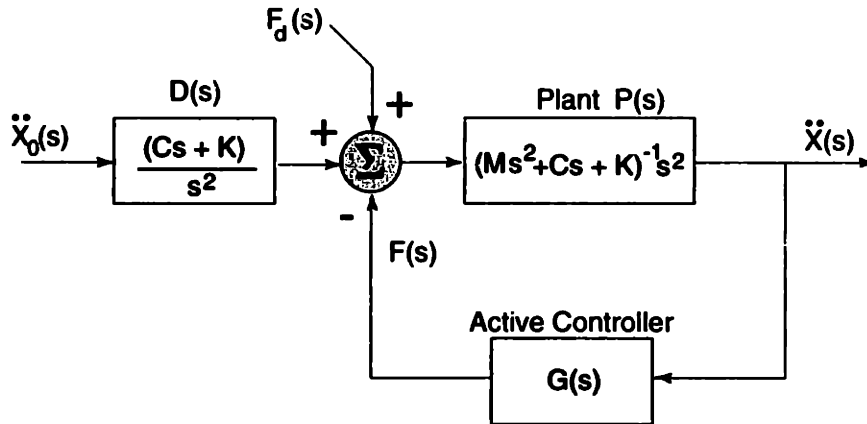


Figure 4-3: Influence of active control on a passive mount. Active isolation design paradigm.

are used to command an actuator in order to reject disturbances. This is illustrated in Figure 4-3 where in addition to the payload and seismic disturbances, we have a control force determined by the feedback compensation law  $G(s)$ .

The addition of the controller into the loop changes things significantly. Denoting the compensator to be  $G(s)$  and making the definitions indicated in Figure 4-3, *i.e.*,

$$D(s) = \frac{Cs + K}{s^2}$$

$$P(s) = (M^{-1}s^2 + Cs + K)^{-1}s^2$$

we find that active control has a beneficial effect on both the conflicting disturbance sources. To observe this, let us first define the sensitivity function of the loop. This is given by

$$S(s) = (I + PG)^{-1} \quad (4.3)$$

By manipulation of the block diagram in Figure 4-3, we obtain the results in Table 4.4. We see that the sensitivity function of the loop has the same effect on both the conflicting disturbance sources. Hence, we obtain performance improvement over the passive case when the sensitivity function is less than unity. There are two

Disturbance	Passive	Active
Seismic	$\mathbf{PD}\ddot{\mathbf{x}}_0$	$\mathbf{SPD}\ddot{\mathbf{x}}_0$
Payload	$\mathbf{P}\mathbf{f}_d$	$\mathbf{SP}\mathbf{f}_d$

Table 4.1: Comparison of the performance of active and passive isolation. Note that the transmissibility of the passive mount is the sensitivity function times the passive transmissibility for both disturbance mechanisms.

key observations to be made here. First, we are not limited in performance by the constitutive law given in (3.16). Second, there is a lot more freedom in shaping the sensitivity function and thus both the seismic vibration transmissibility and the payload disturbance force rejection through proper design of the compensator  $\mathbf{G}(s)$ .

Our approach to the design of an active isolation system for a machine tool is outlined below :

- **Design of the passive mounts :** The passive mounts are first designed according to the procedure outlined in Chapter 3. An optimal mount can be designed by casting the problem in the context of a Kalman filter given an adequate knowledge of the statistics of the two disturbance mechanisms and the inertial parameters of the machine.
- **Design of the compensator :** Since the sensitivity function of the loop plays the key role in determining the amount of performance improvement over passive isolation, our approach to active isolation of machine tools is to shape the sensitivity function. We take an  $\mathcal{H}_2$  approach to the design of the compensator since most performance specifications are given in terms of RMS values and further it is desired to minimize the energy of the payload mass.

We discuss compensator design in more detail in the next section.

## 4.5 Feedback Control Design for Active Isolation

In this section, we illustrate how the transmissibility of a passive mount can be further shaped by an active compensator. To do this, we follow the approach of Hyde [31]

to describe the active vibration isolation problem by the modern control paradigm as illustrated in Figure 4-4. A generalized state variable representation of the plant  $P$

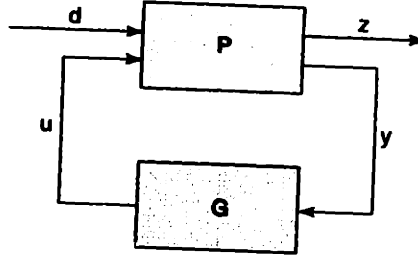


Figure 4-4: The general feedback system description.

is given by

$$\begin{aligned}\dot{\mathbf{x}}(t) &= \mathbf{A}\mathbf{x}(t) + \mathbf{B}_d\mathbf{d}(t) + \mathbf{B}_u\mathbf{u}(t) \\ \mathbf{z}(t) &= \mathbf{C}_z\mathbf{x}(t) + \mathbf{D}_{zd}\mathbf{d}(t) + \mathbf{D}_{zu}\mathbf{u}(t) \\ \mathbf{y}(t) &= \mathbf{C}_y\mathbf{x}(t) + \mathbf{D}_{yd}\mathbf{d}(t) + \mathbf{D}_{yu}\mathbf{u}(t)\end{aligned}\tag{4.4}$$

where  $\mathbf{x}(t)$  is the state vector,  $\mathbf{z}(t)$  the performance metric,  $\mathbf{y}(t)$  the sensor measurements,  $\mathbf{d}(t)$  the disturbances and  $\mathbf{u}(t)$  the control inputs.

Next, we transform the equations of motion (3.14) to the generalized state variable representation in (4.4). To do this, we first define the relative displacement  $\mathbf{q} = \mathbf{x} - \mathbf{x}_0$ . Substituting this into (3.14) and following a few algebraic manipulations, we obtain,

$$\mathbf{M}\ddot{\mathbf{q}} + \mathbf{C}\dot{\mathbf{q}} + \mathbf{K}\mathbf{q} = \mathbf{f}_d - \mathbf{M}\ddot{\mathbf{x}}_0 + \mathbf{f}$$

where we have also introduced the control force vector  $\mathbf{f}$ . Defining  $\{\mathbf{q} \dot{\mathbf{q}}\}^T$  to be the state vector,  $\ddot{\mathbf{x}}_0$  to be the disturbance  $\mathbf{d}$ ,  $\mathbf{M}^{-1}\mathbf{f}$  to be the control input and the payload acceleration  $\ddot{\mathbf{x}}$  to be the measurement as well as the performance (except for the addition of sensor noise to the measurement), we obtain a state variable

representation for the plant,

$$\begin{aligned} \begin{Bmatrix} \dot{\mathbf{q}} \\ \ddot{\mathbf{q}} \end{Bmatrix} &= \begin{pmatrix} \mathbf{0} & \mathbf{I} \\ -\mathbf{M}^{-1}\mathbf{K} & -\mathbf{M}^{-1}\mathbf{C} \end{pmatrix} \begin{Bmatrix} \mathbf{q} \\ \dot{\mathbf{q}} \end{Bmatrix} + \begin{Bmatrix} \mathbf{0} \\ -\mathbf{I} \end{Bmatrix} \mathbf{d} + \begin{Bmatrix} \mathbf{0} \\ \mathbf{I} \end{Bmatrix} \mathbf{u} \\ \mathbf{y} &= \begin{pmatrix} -\mathbf{M}^{-1}\mathbf{K} & -\mathbf{M}^{-1}\mathbf{C} \end{pmatrix} \begin{Bmatrix} \mathbf{q} \\ \dot{\mathbf{q}} \end{Bmatrix} + \begin{pmatrix} \mathbf{I} \end{pmatrix} \mathbf{u} \end{aligned} \quad (4.5)$$

Following Hydes' approach, we have scaled the control such that it has units of acceleration. This is to make transfer functions non-dimensional and also to ensure that the mass falls out of the design and everything scales with mount resonance. LQG methodology is then used to design the compensator  $\mathbf{G}(s)$ . This comprises designing a full state linear quadratic regulator (LQR) and a Kalman filter as an estimator and using the separation principle to form the controller. This procedure is best illustrated through a single degree of freedom example.

## 4.6 Single Degree of Freedom Example

We consider the single degree of freedom example illustrated in Figure 4-5. Using the

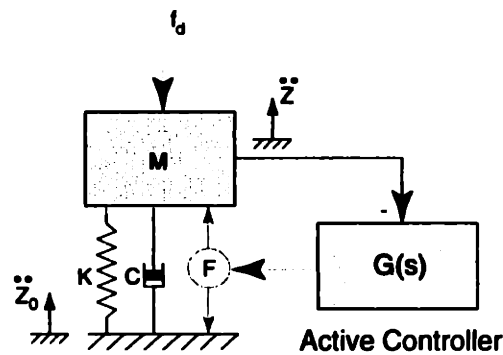


Figure 4-5: Single degree of freedom system retrofitted with an actuator, a sensor and an active controller. Note the explicit negative feedback employed.

LQG methodology, a full state regulator is first designed to minimize the cost  $z^T z + \rho u^T u$ . For decreasing  $\rho$ , the closed-loop poles are first damped to the characteristic Butterworth pattern of 0.707 damping ratio (60 degrees phase margin) and then go asymptotically towards zero frequency. To select the active mount resonant frequency

and thus shape the transmissibility, choose

$$\sqrt{\rho} = \left( \frac{\omega_{cl}}{\omega_{ol}} \right)^2 \quad (4.6)$$

The squared frequency ratio is due to the fact that the control to performance transfer function rolls up from zero to the second order mount resonance proportional to  $\omega^2$ . The regulator design balances the weighted control effort with the performance; as the mount resonance is lowered in frequency additional control effort is required.

Next, a Kalman filter is designed to provide estimates  $\hat{\mathbf{x}}$  of the states  $\mathbf{x}$  for feedback using sensor measurement. This ensures that the state estimation error is minimized in the presence of white sensor noise  $\theta(t)$  with intensity  $\Theta$  and white noise process disturbance  $d(t)$  with intensity  $\Xi$ . In the formation for the estimator, the ratio of measurement noise to the process noise sets the dynamics of the estimator. For simplicity, the process noise is assumed to be of unity intensity and the sensor noise intensity  $\Theta$  is used as the design parameter. For decreasing  $\Theta$ , the estimator poles are first damped as in the regulator, then asymptotically increase in frequency. The closed-loop estimator poles are set by choosing

$$\sqrt{\Theta} = \left( \frac{\omega_{ol}}{\omega_{est}} \right)^2 \quad (4.7)$$

The squared frequency ratio in this case is due to the fact that the disturbance to sensor transfer function rolls off after the second order mount resonance proportional to  $1/\omega^2$ . By choosing  $\sqrt{\rho} = \sqrt{\Theta} = \left(\frac{1}{10}\right)^2$  for example, one has a closed loop system with a pair of poles a decade below and above the open-loop resonance.

The LQG compensator is then formed using the regulator ( $\mathbf{K}$ ) and estimator ( $\mathbf{L}$ ) gains resulting in a dynamic compensator  $\mathbf{G}(s)$  with the same number of states as the plant.

$$\mathbf{G}(s) = \mathbf{K} (s\mathbf{I} - \mathbf{A} + \mathbf{B}_u\mathbf{K} + \mathbf{L}\mathbf{C}_y)^{-1} \mathbf{L} \quad (4.8)$$

The compensator transfer function is plotted in Figure 4-6. At low frequencies, the

control force acts on the payload mass in proportion to sensed acceleration. This is equivalent to enhancing the mass of the payload. To reduce the mount resonance by a factor of 10 (which is how the LQ regulator was designed), requires enhancing the mass by a factor of 100. This is the low frequency gain (40 dB) of the compensator as illustrated in Figure 4-6. At intermediate frequencies the compensator transfer

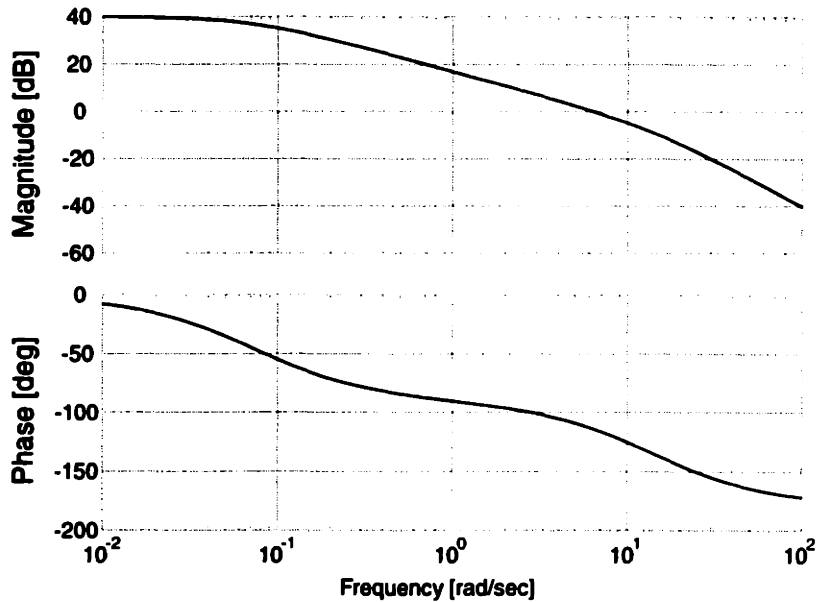


Figure 4-6: LQG compensator transfer function that provides isolation over two decades.

function rolls off at -20 dB/decade. This is akin to inertial velocity feedback and thus damps the open-loop resonance. The control goes to zero at high frequencies and thus the isolation mechanism at high frequencies is that due to the passive mounts.

We study the effect of the controller further by observing the loop transmission. To do this, we first define the plant transfer function to be

$$\mathbf{P}_{yu}(s) = \mathbf{C}_y (s\mathbf{I} - \mathbf{A})^{-1} \mathbf{B}_u + \mathbf{D}_{yu} \quad (4.9)$$

We can now obtain the LQG loop gain  $\mathbf{P}_{yu}(s)\mathbf{G}(s)$  (illustrated in Figure 4-7). The active control region is the region in which the loop transmission is greater than unity (0 dB). The loop gain is the greatest at the open-loop resonance and rolls off to cross over unity gain at the desired bandwidth one decade above and one decade

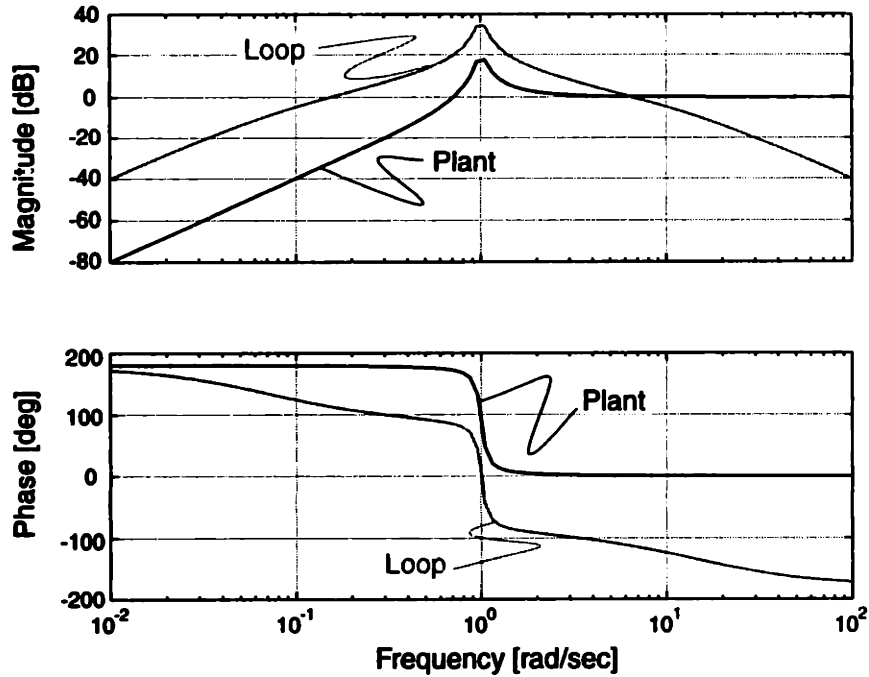


Figure 4-7: Plant and LQG loop transfer functions with  $\rho$  and  $\Theta$  chosen to set bandwidth to a decade above and below mount resonance.

below the open-loop resonance. The phase margin at both the cross-over points is approximately 60 degrees and corresponds to critical damping of the transmissibility. The loop transmission demonstrates yet another factor unique to active vibration isolation, *i.e.*, there are two crossover frequencies and it is important to have good phase margin at both these frequencies to have good robustness properties. A Nyquist plot of the loop gain illustrated in Figure 4-8 along with the unit circle demonstrates the robustness properties of the LQG compensator.

As stated earlier, a good measure of the effectiveness of the control is the ratio of the closed-loop to open-loop transmissibility and is the performance metric improvement due to active control. It is the same as the loop sensitivity given in (4.3) and is repeated here,

$$\mathbf{S}(s) = (\mathbf{I} + \mathbf{P}_{yu}(s)\mathbf{G}(s))^{-1} = \frac{\mathbf{P}_{zd}^d(s)}{\mathbf{P}_{zd}^{ol}(s)} \quad (4.10)$$

The loop sensitivity is plotted in Figure 4-9. In our example, LQG control has resulted in sensitivity less than one over one decade above and one decade below the mount

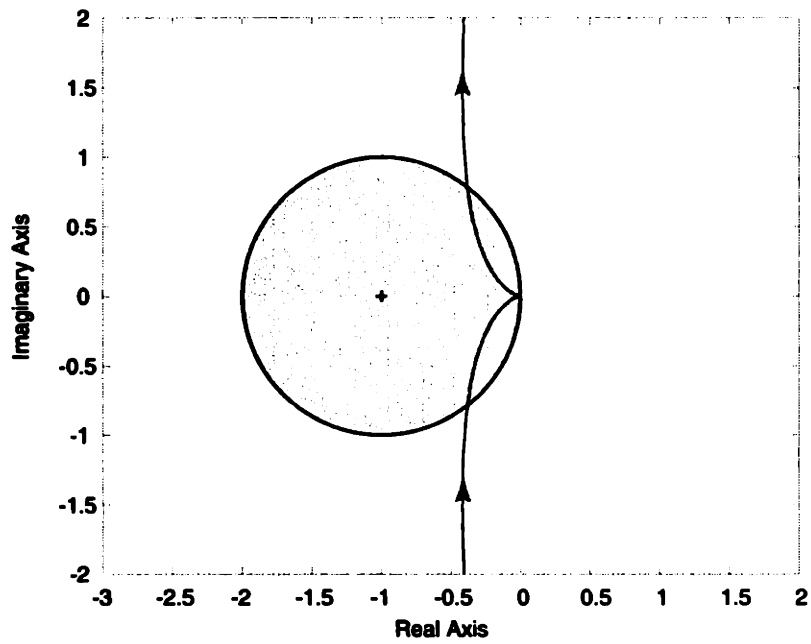


Figure 4-8: Nyquist plot of the LQG loop transfer functions illustrated in Figure 4-7 along with the unit circle. Note the 60 degree phase margin at both crossover points.

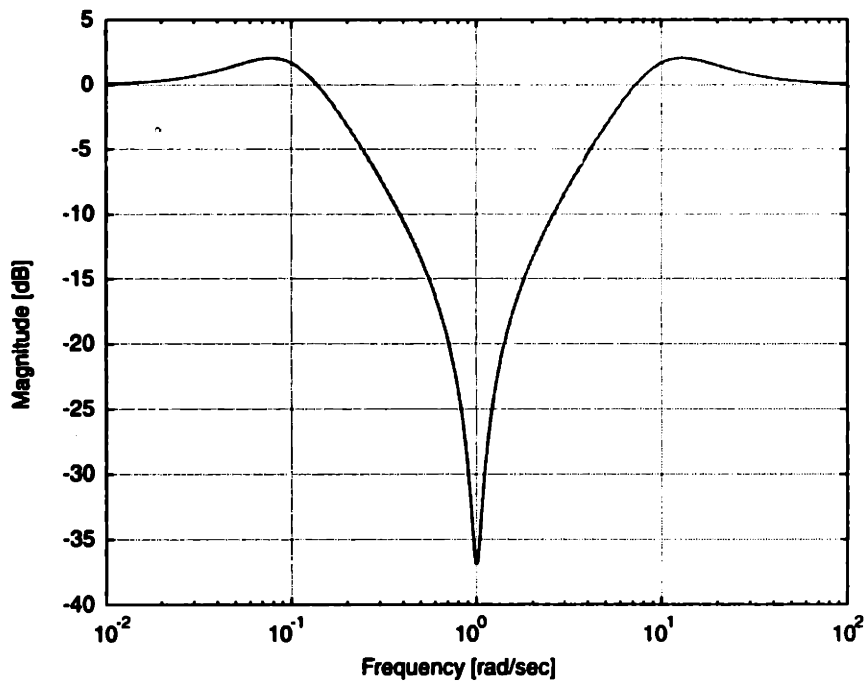


Figure 4-9: Sensitivity plot for the active mount. Note active isolation provides isolation over a decade above and a decade below the open-loop resonance.



resonance. The transmissibility of the active mount is compared with that of the passive mount in Figure 4-10. This shows the effect of suppressing the resonance of the passive system in addition to attenuating disturbances over the control bandwidth. According to Hyde [31], the high frequency roll-off is usually limited by the need to

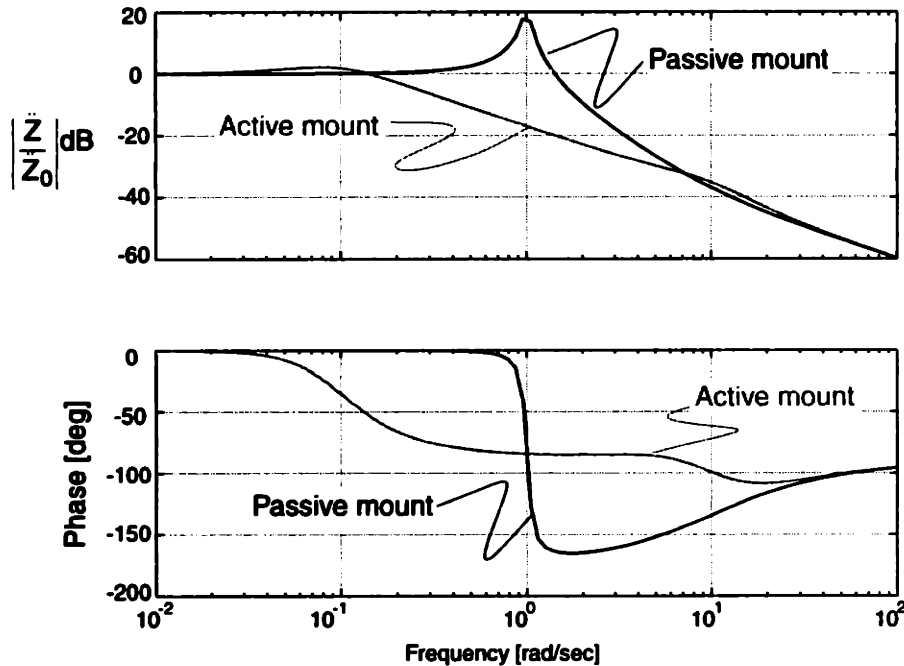


Figure 4-10: Transmissibility plot for active (closed-loop) and passive (open-loop) mounts. Note active isolation provides isolation over a decade above and a decade below the open-loop resonance.

stabilize unmodelled high frequency modes or to retain phase margin with actuator lags and computer time delay, while the low-frequency roll-up is limited by the high gain required on the compensator and the resulting large control effort and stroke. The shape of the loop gain is fixed in our example thus far with the parameters  $\rho$  and  $\Theta$  serving as control knobs to set the roll-up and roll-off crossover points of the control loop. Before discussing further ways to shape the loop, we illustrate the effect of active control on the payload disturbance force rejection in Figure 4-11. It can be clearly seen that improved payload disturbance rejection is obtained with the active mount since we are no longer governed by the fundamental tradeoff of (3.16).

The simple LQG compensator developed in this section demonstrates the application of linear quadratic techniques to the problem of compensator design for active

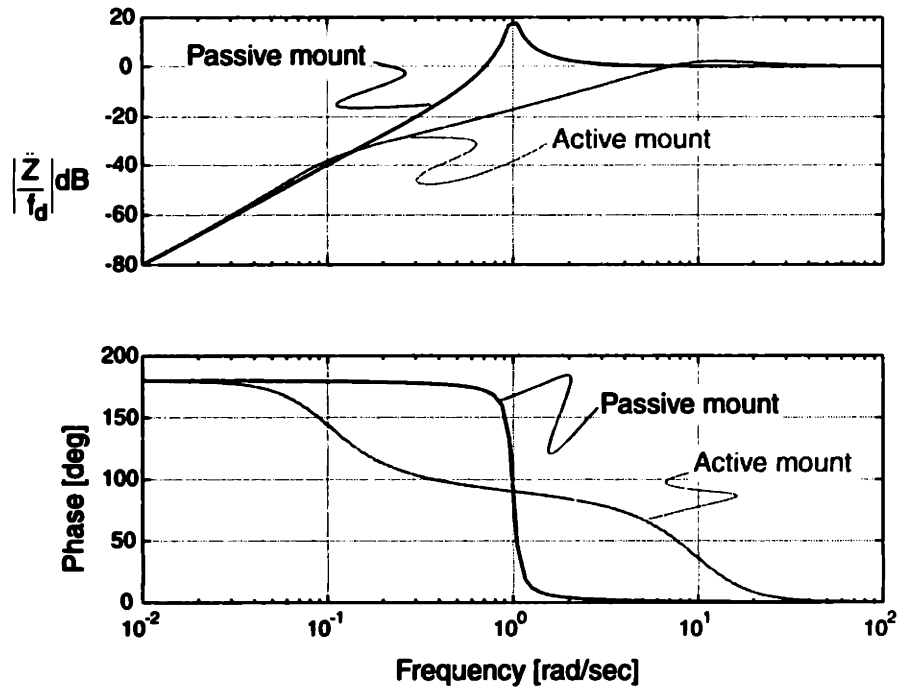


Figure 4-11: Payload disturbance rejection for the active and passive mounts. Note the improved rejection of the active mount one decade above and one decade below the open-loop resonance. We are no longer governed by the fundamental tradeoff of (3.16).

vibration isolation and its effects on the two conflicting disturbance phenomena. The compensator essentially comprises two poles, one to provide enough phase lead at the lower cross-over frequency and the other to provide phase lead at the upper cross-over frequency. Active control provides better attenuation of both seismic and payload disturbances between these two cross-over frequencies. However, in the presence of colorful seismic vibrations or to obtain better isolation, it might be advantageous to design higher order compensators. This can be done easily using frequency shaping of cost functionals [29] as illustrated in the next section.

## 4.7 Frequency Weighting

This is accomplished by frequency weighting of the performance metric and the control in the formulation of the LQ regulator. Similar frequency weights can also be applied to the sensor and process noise noise in our design of the Kalman filter. We follow

Hydes' example and set them to unity however. This notion of frequency shaping of cost-functionals is attributed to Gupta [29] and is accomplished through a simple application of Parseval's relationship. To understand this, we repeat the cost function for the LQ regulator.

$$\begin{aligned}
 J &= \int_0^{\infty} (\mathbf{z}^T(t)\mathbf{z}(t) + \mathbf{u}^T(t)\mathbf{u}(t)) dt \\
 &= \frac{1}{2\pi} \int_{-\infty}^{\infty} (\mathbf{Z}^H(j\omega)\mathbf{Z}(j\omega) + \mathbf{U}^H(j\omega)\mathbf{U}(j\omega)) d\omega
 \end{aligned} \tag{4.11}$$

where we have used Parseval's relationship to transform the time domain to the frequency domain. We can now propose weighting matrices for the performance measure  $\mathbf{z}$  and the controls  $\mathbf{u}$  in the frequency domain just as we did so in the time domain. Accordingly,

$$\begin{aligned}
 J &= \frac{1}{2\pi} \int_{-\infty}^{\infty} (\mathbf{Z}^H(j\omega)\mathbf{W}_z^H(j\omega)\mathbf{W}_z(j\omega)\mathbf{Z}(j\omega) + \mathbf{U}^H(j\omega)\mathbf{W}_u^H(j\omega)\mathbf{W}_u(j\omega)\mathbf{U}(j\omega)) d\omega \\
 &= \frac{1}{2\pi} \int_{-\infty}^{\infty} (\mathbf{Z}_a^H(j\omega)\mathbf{Z}_a(j\omega) + \mathbf{U}_a^H(j\omega)\mathbf{U}_a(j\omega)) d\omega
 \end{aligned} \tag{4.12}$$

where  $\mathbf{W}_z(s)$  and  $\mathbf{W}_u(s)$  are shaping filters for the performance measure and control respectively and we have defined the augmented performance measure and controls as

$$\begin{aligned}
 \mathbf{Z}_a(j\omega) &= \mathbf{W}_z(j\omega)\mathbf{Z}(j\omega) \\
 \mathbf{U}_a(j\omega) &= \mathbf{W}_u(j\omega)\mathbf{U}(j\omega)
 \end{aligned} \tag{4.13}$$

State variable models of the shaping filters that describe the performance metric and control are given by

$$\begin{aligned}
 \mathbf{W}_z(s) &= \mathbf{C}_z (s\mathbf{I} - \mathbf{A}_z)^{-1} \mathbf{B}_z + \mathbf{D}_z \\
 \mathbf{W}_u(s) &= \mathbf{C}_u (s\mathbf{I} - \mathbf{A}_u)^{-1} \mathbf{B}_u + \mathbf{D}_u
 \end{aligned} \tag{4.14}$$

Accordingly, the state and output equations of the shaping filters in the time domain are given by,

$$\begin{aligned}
 \dot{\mathbf{x}}_z &= \mathbf{A}_z \mathbf{x}_z + \mathbf{B}_z \mathbf{z} \\
 \mathbf{z}_a &= \mathbf{C}_z \mathbf{x}_z + \mathbf{D}_z \mathbf{z} \\
 \dot{\mathbf{x}}_u &= \mathbf{A}_u \mathbf{x}_u + \mathbf{B}_u \mathbf{u} \\
 \mathbf{u}_a &= \mathbf{C}_u \mathbf{x}_u + \mathbf{D}_u \mathbf{u}
 \end{aligned} \tag{4.15}$$

The shaping filters are augmented to the plant model and the resulting system is used for normal regulator design. The augmented plant is given by the equations :

$$\begin{aligned}
 \begin{Bmatrix} \dot{\mathbf{x}} \\ \dot{\mathbf{x}}_z \\ \dot{\mathbf{x}}_u \end{Bmatrix} &= \begin{pmatrix} \mathbf{A} & \mathbf{0} & \mathbf{0} \\ \mathbf{B}_z \mathbf{C} & \mathbf{A}_z & \mathbf{0} \\ \mathbf{0} & \mathbf{0} & \mathbf{A}_u \end{pmatrix} \begin{Bmatrix} \mathbf{x} \\ \mathbf{x}_z \\ \mathbf{x}_u \end{Bmatrix} + \begin{Bmatrix} \mathbf{B} \\ \mathbf{0} \\ \mathbf{B}_u \end{Bmatrix} \mathbf{u} \\
 \begin{Bmatrix} \mathbf{z}_a \\ \mathbf{u}_a \end{Bmatrix} &= \begin{pmatrix} \mathbf{D}_z \mathbf{C} & \mathbf{C}_z & \mathbf{0} \\ \mathbf{0} & \mathbf{0} & \mathbf{C}_u \end{pmatrix} \begin{Bmatrix} \mathbf{x} \\ \mathbf{x}_z \\ \mathbf{x}_u \end{Bmatrix} + \begin{Bmatrix} \mathbf{0} \\ \mathbf{D}_u \end{Bmatrix} \mathbf{u}
 \end{aligned} \tag{4.16}$$

The cost function in terms of the augmented measures is now given by,

$$\begin{aligned}
 J &= \int_0^{\infty} (\mathbf{z}_a^T(t) \mathbf{z}_a(t) + \mathbf{u}_a^T(t) \mathbf{u}_a(t)) dt \\
 &= \int_0^{\infty} (\mathbf{x}_a^T \mathbf{C}_a^T \mathbf{C}_a \mathbf{x}_a + 2 \mathbf{x}_a^T \mathbf{C}_a^T \mathbf{D}_a \mathbf{u} + \mathbf{u}^T \mathbf{D}_a^T \mathbf{D}_a \mathbf{u}) dt
 \end{aligned} \tag{4.17}$$

where  $\mathbf{x}_a$  is the augmented state vector. The augmented state gains from the solution of the augmented LQR problem is given by,

$$\bar{\mathbf{K}} = \begin{pmatrix} \mathbf{K}_x & \mathbf{K}_z & \mathbf{K}_u \end{pmatrix} \tag{4.18}$$

We now form a Kalman filter for just the plant using the techniques discussed earlier to get the estimator gains  $\mathbf{L}$ . The resulting LQG compensator is given by the state

equations :

$$\begin{aligned} \begin{Bmatrix} \dot{\hat{\mathbf{x}}} \\ \dot{\hat{\mathbf{x}}}_z \\ \dot{\hat{\mathbf{x}}}_u \end{Bmatrix} &= \begin{pmatrix} \mathbf{A} - \mathbf{BK}_x - \mathbf{LC} & -\mathbf{BK}_z & -\mathbf{BK}_u \\ \mathbf{0} & \mathbf{A}_z & \mathbf{0} \\ -\mathbf{B}_u\mathbf{K}_x & -\mathbf{B}_u\mathbf{K}_z & \mathbf{A}_u - \mathbf{B}_u\mathbf{K}_u \end{pmatrix} \begin{Bmatrix} \hat{\mathbf{x}} \\ \mathbf{x}_z \\ \mathbf{x}_u \end{Bmatrix} + \begin{Bmatrix} \mathbf{L} \\ \mathbf{B}_z \\ \mathbf{0} \end{Bmatrix} \mathbf{y} \\ \mathbf{u} &= -\begin{pmatrix} \mathbf{K}_x & \mathbf{K}_z & \mathbf{K}_u \end{pmatrix} \begin{Bmatrix} \mathbf{x} \\ \mathbf{x}_z \\ \mathbf{x}_u \end{Bmatrix} \end{aligned} \quad (4.19)$$

A good review of the frequency-shaping procedure can be found in Athans [5].

As an illustration, we desire to obtain a further improvement in isolation around the passive mount resonant frequency. This is obtained by applying the shaping filters  $W_z(j\omega)$  and  $W_u(j\omega)$  illustrated in Figure 4-12 to the design of the regulator and using the Kalman filter from before to complete the compensator design. Applying the

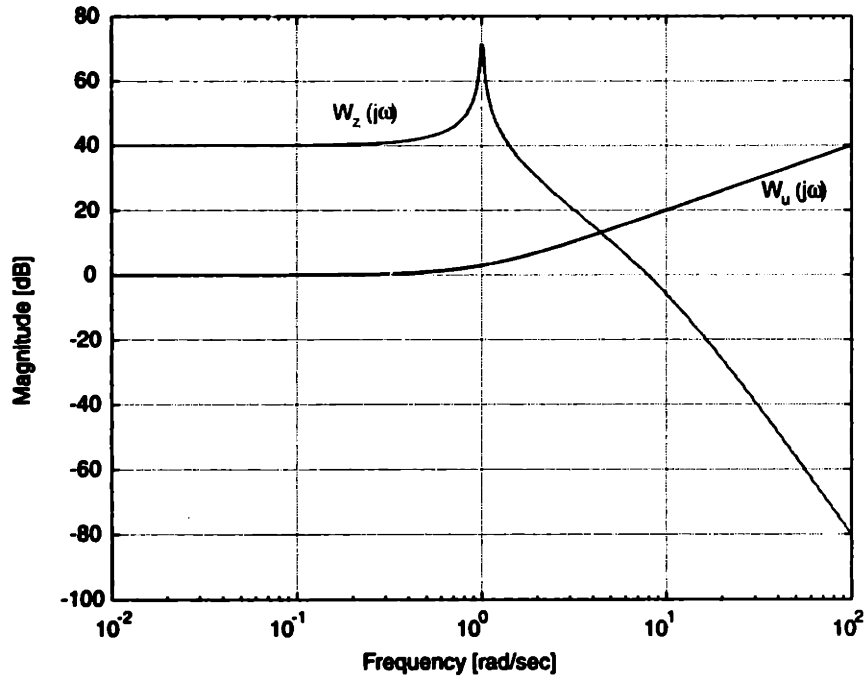


Figure 4-12: Frequency shaping cost functions  $W_z(j\omega)$  and  $W_u(j\omega)$  to obtain narrow-band and broadband improvement in isolation performance.

demonstrated procedure to give us a notch around the resonant frequency, we get the sensitivity function in Figure 4-13. Comparing Figure 4-13 with Figure 4-9 we note the further reduction in sensitivity at the passive mount resonance. This results in the

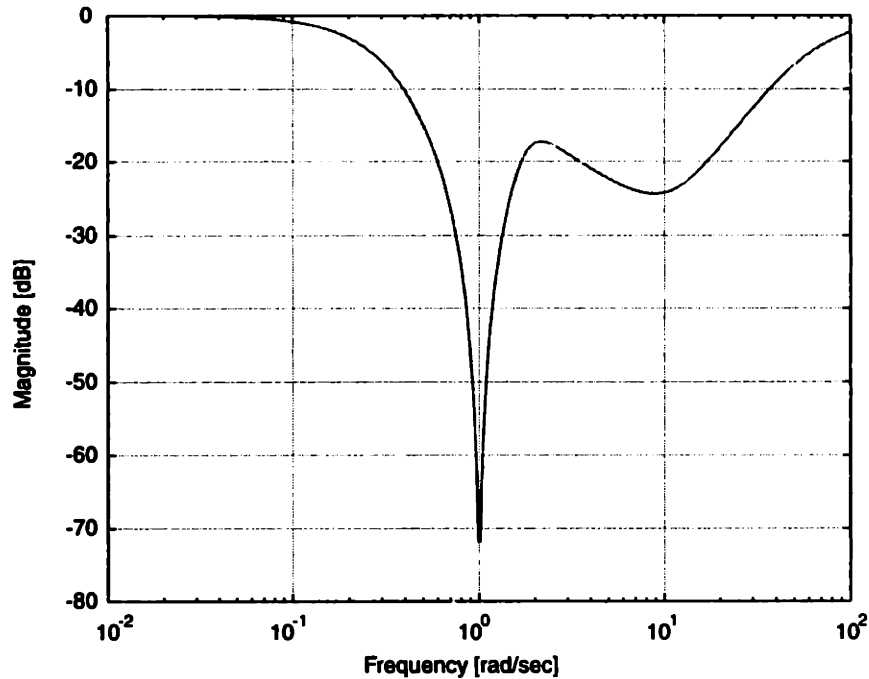


Figure 4-13: Frequency shaping of the sensitivity function to obtain a notch in the transmissibility around the passive mount resonance. Note the decreased magnitude of the sensitivity function at the mount resonance as compared to 4-9.

seismic vibration transmissibility and payload force rejection in Figure 4-14. Further examples on shaping transmissibility for broadband and narrowband improvement can also be found in Hyde [31]. We now summarize the performance of active and passive mounts following the developments in Chapters 3 and 4 in the following section.

## 4.8 Passive *vs.* Active Isolation

To summarize, the advantages of active mounts over passive mounts are as follows :

- Active isolation effectively decouples the isolator natural frequency from static deflection and active mounts are not bound by the constitutive law given in (3.4).
- There is more flexibility in shaping the transmissibility by suitable modification of the control law as shown in Figure 4-14. This applies both to broadband as well as narrowband isolation. The *rule of thumb* in typical six axis broadband isolation systems is : a) the active isolation corner frequency can be moved down by a decade and is usually limited by actuator stroke, cross-axis stiffness,

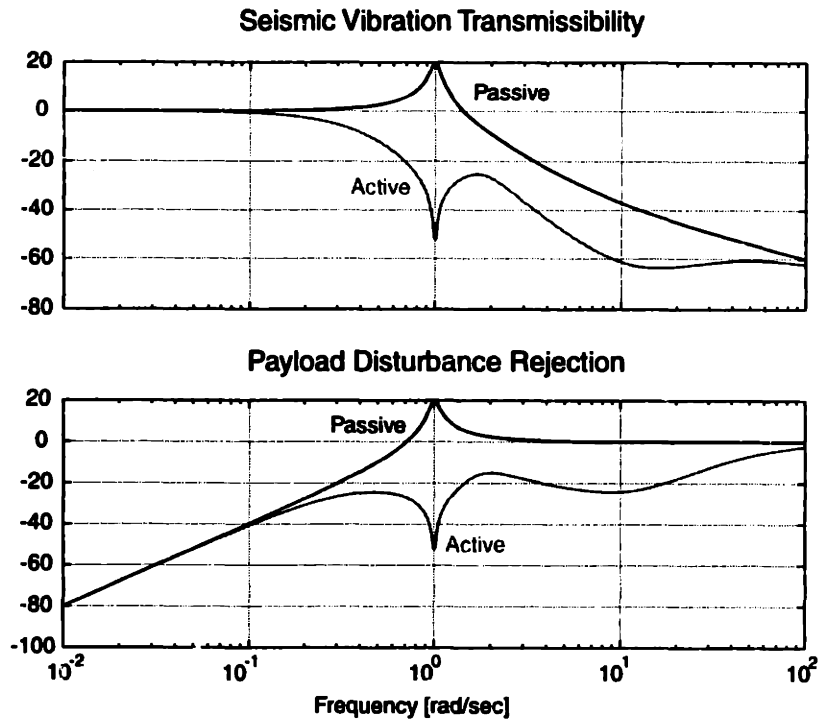


Figure 4-14: Frequency shaping of the sensitivity function to illustrate a notch in the transmissibility around the passive mount resonance.

and sensor noise, and b) narrowband isolation notches are about -30 dB and usually limited by sensor noise. Hyde [31] presents a good review of real-world limitations to the low and high frequency limits of active isolation.

- Active isolation permits good payload disturbance force rejection and is not limited by the constitutive relation of passive mounts described by (3.15) and as illustrated in Figure 3-9. This is by far the most important advantage of active mounts over passive mounts in lithography applications.
- There are possible size and weight and packaging improvements. This is very important given the huge costs of building and maintaining clean room space.

However, active mounts are not without disadvantages. They are as follows :

- Active mounts are complex and relatively more expensive than passive mounts.
- They require sensors, actuators and are less reliable than purely passive springs and dampers.
- Unstable behavior becomes a possibility whereas purely passive mounts are guaranteed to be stable. Note that pneumatic mounts with leveling valves can

exhibit unstable behavior due to orifice damping, but for the purpose of this thesis, we consider the addition of leveling valves to render the system active in the first place.

- They require additional power for their operation.

Fortunately, there have however been rapid improvements in actuator and sensor technologies and their associated reliability. A good understanding of the disturbance mechanisms and good modeling of the machine can also help design stable and robust controllers. Finally, for an expensive machine such as a wafer stepper, the incremental cost disadvantage of an active isolation system is far outweighed by the performance improvement that can be realized.

## 4.9 Summary of Chapter 4

An analytical treatment of active vibration isolation and the performance improvement yielded by the application of active isolation to machine tools is provided. The sensitivity function of the loop is shown to play a key role in the transmissibility of the two conflicting disturbance phenomena. An  $\mathcal{H}_2$  procedure to shape the loop is presented. Frequency weighting is presented as a way to obtain further narrow-band and broad-band improvement in transmissibility. The application of the procedure to a wafer stepper is presented and is shown to have about 50 dB better attenuation.

We then demonstrate that active control is not subject to the same tradeoff of passive isolation and pose the active vibration isolation problem as a new paradigm. We follow this with a discussion on active isolation architectures and review commercially available active isolation systems. We examine the difference in between our approach and existing designs. Throughout our discussions in this chapter, we assume the payload requiring to be isolated is a rigid body. This assumption is relaxed later in Chapter 7. However, we first outline the mechanical design of the isolation system and rigid body control in the next two chapters.



# Chapter 5

## Mechanical Design and Kinematics of the Isolation System

### 5.1 Introduction

We now specialize our discussions on seismic/payload disturbances and isolation systems to the design and implementation of an active/passive isolation system for the prototype stepper considered in this thesis. A schematic of the stepper is illustrated again in Figure 5-1. We first describe the mechanical design of the testbed stepper and its stages for position control. The inertial parameters of the stepper are tabulated and will be used in the development of the equations of motion and subsequent controller design.

We follow this description with a discussion on the design and selection of the various components of the active/passive isolation system. These include the mounts, actuators, sensors, amplifiers and signal conditioning filters. The use of our control paradigm in the analysis of passive mounts is demonstrated. This is followed by a discussion on the placement of the actuators, sensors and mounts in the Cartesian coordinate frame illustrated in Figure 5-1 and the resulting kinematics problem. As a prelude to deriving the rigid-body kinematics, various coordinate frames are established. Linear transformations are derived to relate these coordinate frames and the inverse/direct rigid-body kinematics problem for the stepper is posed in terms of these

coordinate transformations. These coordinate transformations lay the framework for the rigid-body modeling and control of the stepper which is discussed in Chapter 6.

## 5.2 Mechanical Design

This section outlines the mechanical design of the isolation system for the prototype wafer stepper illustrated in Figure 5-1. The stepper utilizes two coarse motion stages

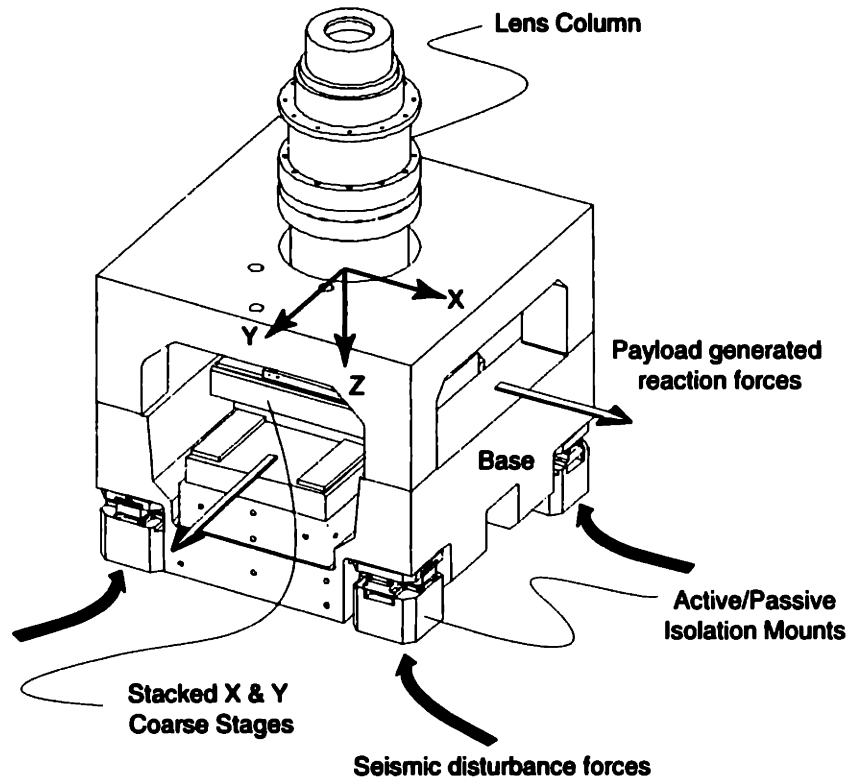


Figure 5-1: Schematic of prototype stepper showing disturbance mechanisms and Cartesian coordinate frame fixed to the center of gravity

in a stacked configuration to provide coarse X and Y motions and a six degree of freedom Maglev fine motion stage to position the wafer under the lens column. The Maglev fine stage is constrained to move in a  $400 \mu\text{m}$  cube. This stage is transported on a series of stacked air bearings which provide the long travel necessary to cover the surface of the wafer. These air bearing stages (X and Y coarse stages) are driven by two 3-phase linear motors. Williams [83] provides a good description of the stages.

The base is made of polymer concrete and is constructed like a cradle to receive

the stacked stages. An aluminum bridge on top of the base supports the lens column. The illuminator, reticle and wafer handling systems are absent in this prototype unit. These systems do not directly affect the motion control problem of the stepper and their absence allows us to concentrate more on the problem at hand.

The position of the center of gravity and the inertial parameters of the prototype stepper when the X and Y coarse stages are positioned at the center of their stroke are obtained from a solid model using a CAD program and tabulated in Table 5.1. It

Parameter	Symbol	Value	Units
Mass	$M$	1260.80	Kg
Moment of Inertia	$I_{xx}$	220.40	Kgm <sup>2</sup>
Moment of Inertia	$I_{yy}$	219.53	Kgm <sup>2</sup>
Moment of Inertia	$I_{zz}$	146.05	Kgm <sup>2</sup>
Product of Inertia	$I_{xy}$	0.0833	Kgm <sup>2</sup>
Product of Inertia	$I_{yz}$	-0.9885	Kgm <sup>2</sup>
Product of Inertia	$I_{xz}$	-2.9861	Kgm <sup>2</sup>

Table 5.1: Inertial Parameters of Prototype Wafer Stepper with the coarse stages positioned at the center of their stroke. Note negligible Products of Inertia

is of interest to note the negligible products of inertia. This means that the principal axes of the stepper are closely aligned with the Cartesian axes. This fact allows us to obtain a much simpler and less coupled set of equations in the development of the rigid-body dynamics in Chapter 6.

There exist a total of 14 degrees of freedom that need to be controlled. The X and Y coarse stages account for two degrees of freedom and are driven by linear motors; their other degrees of freedom are constrained by air bearings. The fine stage is magnetically levitated and has motion control in all six rigid-body degrees of freedom. The inertial parameters of the stages are also obtained similarly from a CAD program and tabulated in Table 5.2. Finally, the stepper itself has six (rigid body) degrees of freedom controlled by the isolation system.

Feedback of the stage position relative to the stage base is provided by 5 axes of laser interferometry and 6 capacitance probes. Position feedback for the fine stage is provided by six capacitance probes that are fixed in the fine stage frame and sense

Parameter	Symbol	Value	Units
Y Coarse stage Mass	$M$	90.90	Kg
X Coarse stage Mass	$M$	28.20	Kg
Fine stage Mass	$M$	11.63	Kg
Fine stage Moment of Inertia	$I_{xx}$	0.1039	Kgm <sup>2</sup>
Fine stage Moment of Inertia	$I_{yy}$	0.1025	Kgm <sup>2</sup>
Fine stage Moment of Inertia	$I_{zz}$	0.1719	Kgm <sup>2</sup>

Table 5.2: Inertial Parameters of the coarse and fine motion stages. Products of Inertia of the fine stage are negligible and not mentioned

flat ground surfaces on the levitated platen. This feedback is used to determine the location of the suspended platen relative to its frame. A one-piece Zerodur mirror is kinematically mounted (via three balls and grooves) onto the platen. Laser interferometry is used to measure the  $x$ ,  $y$ ,  $\theta_x$ ,  $\theta_y$  and  $\theta_z$  coordinates of the Zerodur mirror on top of the fine stage with respect to reference mirrors on the lens column. Thus, laser interferometry directly measures five of the six performance measures we intend to control. The  $z$  coordinate of the Zerodur mirror is measured by an auto-focus<sup>1</sup> mechanism which is absent from the prototype stepper. The six capacitance probes measure the six rigid-body degrees of freedom of the fine stage with respect to the coarse X stage. The X and Y coarse stages also have glass scale position encoders to measure their positions relative to the base of the stepper. In the control scheme used in this thesis, the encoders and the laser feedback are used to servo the coarse X, coarse Y and fine stages, while the six capacitance probes are used only for feedback linearization of the variable reluctance actuators used on the fine stage.

The isolation system uses six accelerometers to determine inertial rigid-body acceleration of the stepper. Six additional capacitance probes are used to determine the relative displacements of the base of the stepper with respect to the ground and thereby determine the air gaps of the variable reluctance actuators. These measurements are used in the feedback linearization of the variable reluctance actuators used

---

<sup>1</sup>Auto-focus is a system that uses grazing incidence light to determine the distance from the lens to the wafer surface.

on the isolation system.

The mechanical design of the legs for active vibration control was carried out at ISI<sup>2</sup> in collaboration with Dr. Mark Williams. The isolation system comprises four active/passive legs in a parallel configuration. A truly kinematic arrangement would comprise only three legs, but that would require significant redesign of the stepper base. The use of four legs creates over-constraint and redundancy, but by continuing to use four legs, we have avoided significant redesign of the stepper and allowed easy integration.

A cutaway view of one of the legs detailing the various components is shown in Figure 5-2. The parallel arrangement of the actuators and the passive elastomeric mount can be clearly seen. Each leg also comprises two seismic accelerometers to measure inertial acceleration. One of them can be seen assembled into the leg and is used to measure vertical acceleration while the other accelerometer is used to measure horizontal acceleration and is not shown in the figure. A photograph of the various

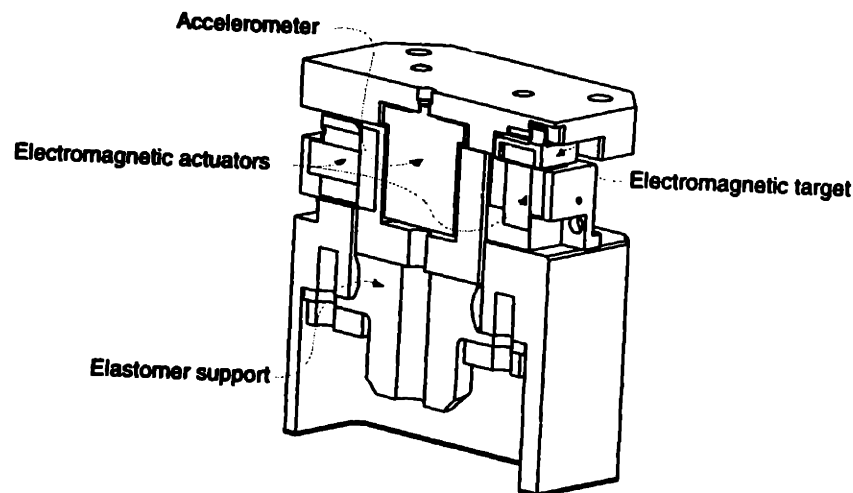
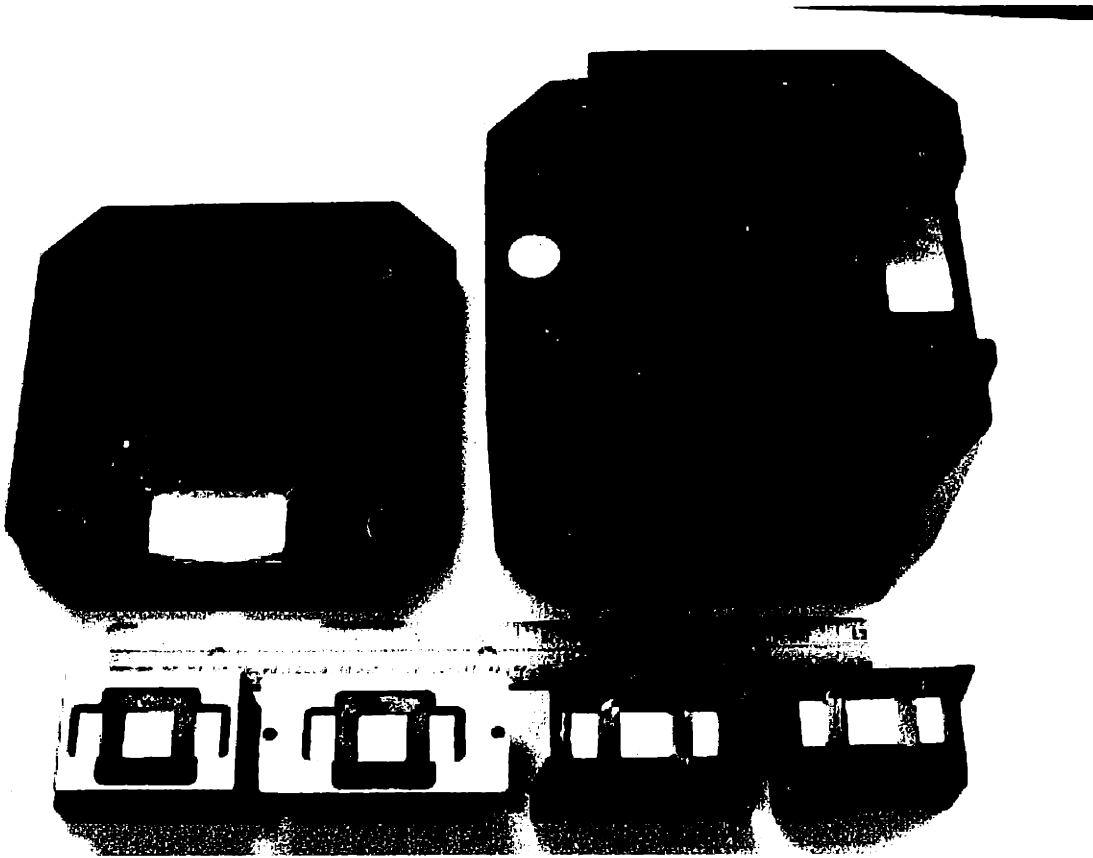


Figure 5-2: Cutaway view of one leg of the system

components of the legs taken during assembly is illustrated in Figure 5-3. We now discuss the key individual components, *i.e.*, the passive mount, actuators and sensors of the isolation system in detail.

---

<sup>2</sup>Integrated Solutions Inc., Tewksbury, MA (now Ultratech Stepper)



**Figure 5-3: Picture of the passive components and actuators of a single leg. A 12-inch ruler and a nickel are also shown to give a sense of scale.**

## 5.3 Passive Mount Selection

In this section, we first illustrate the analysis of passive mounts for a machine *subject to the conflicting demands of payload disturbance rejection and seismic vibration isolation*. The performance of the passive mount under the action of the two disturbances is predicted using the methods developed in Chapter 2. This is done under assumed spectral profiles for the disturbances and under the framework established in Chapter 3. We consider the prototype stepper illustrated in Figure 5-1 as an example.

### 5.3.1 Analysis of passive mounts

In this section we consider the stepper in the X-direction. The stepper is modeled as a single degree of freedom rigid-body as illustrated in Figure 3-7. The disturbance force  $f_d$  is caused by the motion of the X-coarse stage. The free acceleration of the stepper without mounts is given by  $f_d/M$  and is essentially the acceleration profile of the X-coarse stage times the mass ratio  $(0.0224)^3$ . This acceleration profile is plotted in Figure 5-4. The X-coarse stage is assumed to have a triangular velocity profile with a step motion of 20 mm and a peak acceleration of 0.2 g. The actual acceleration profile for the coarse stages is triangular but with a smooth taper at the end to have zero jerk at the end of the motion profile. The motion profile is discussed in more detail later in Chapter 6.

Figure 5-4 illustrates both the time-domain plot of the acceleration profile as well as a frequency-domain plot. The latter is generated through a 1024-point FFT and illustrates the fundamental disturbance at 5 Hz as well as the higher order harmonics of the square wave. We model seismic vibration as a first-order Markov process spectrum along the lines of Chapter 2 and as given by (2.6). We choose the same parameters for the Markov process, *i.e.*,  $\beta = 10$  Hz and  $\sigma = 25$  nm. Now, we obtain the PSD of the payload disturbance illustrated in Figure 5-4. The PSD is found to be nicely fitted by a first order Markov process with  $\beta = 5$  Hz and  $\sigma = 0.08$  m/s<sup>2</sup>.

---

<sup>3</sup>This is given by the ratio of the X-coarse stage mass to the stepper mass, refer to tables 5.2 and 5.1 for the respective values.

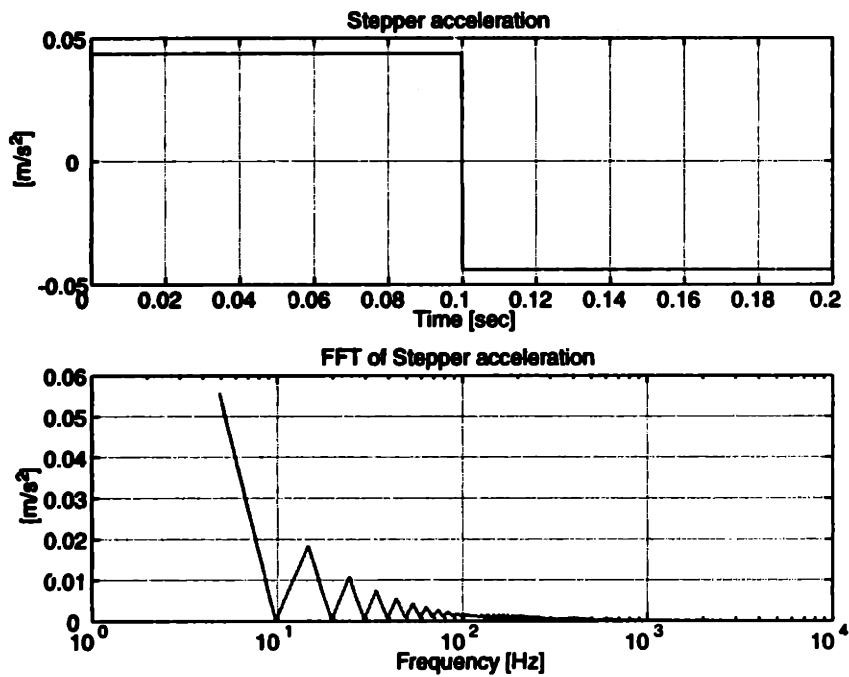


Figure 5-4: Free acceleration profile of the stepper due to a step motion of 20 mm of the X-coarse stage. The time-domain plot of the acceleration profile as well as a 1024 point FFT are illustrated. The FFT clearly shows the higher-order harmonics as well as the fundamental disturbance at 5 Hz.



The PSD of the payload disturbance as well as its fit and the PSD of the seismic vibrations are illustrated in Figure 5-5.

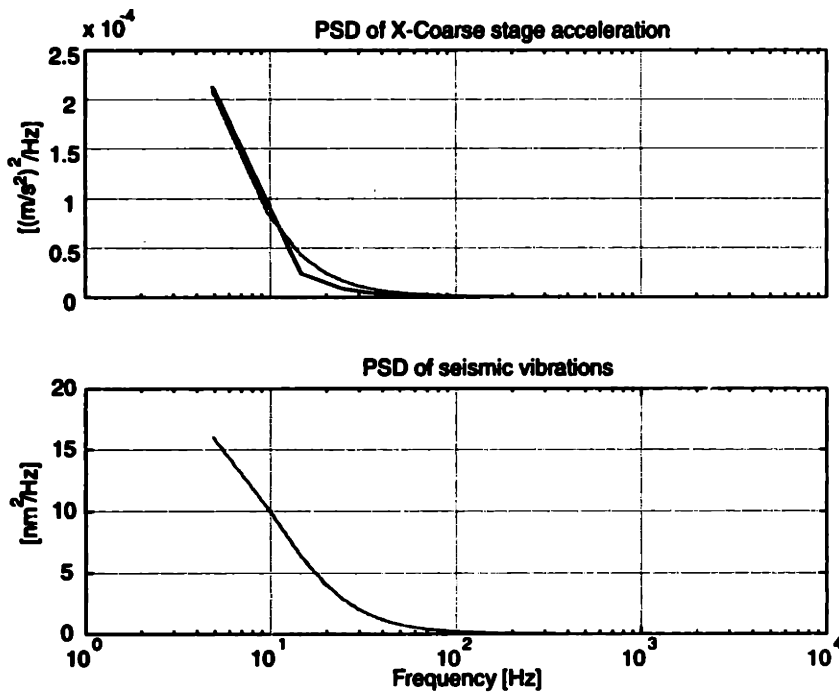
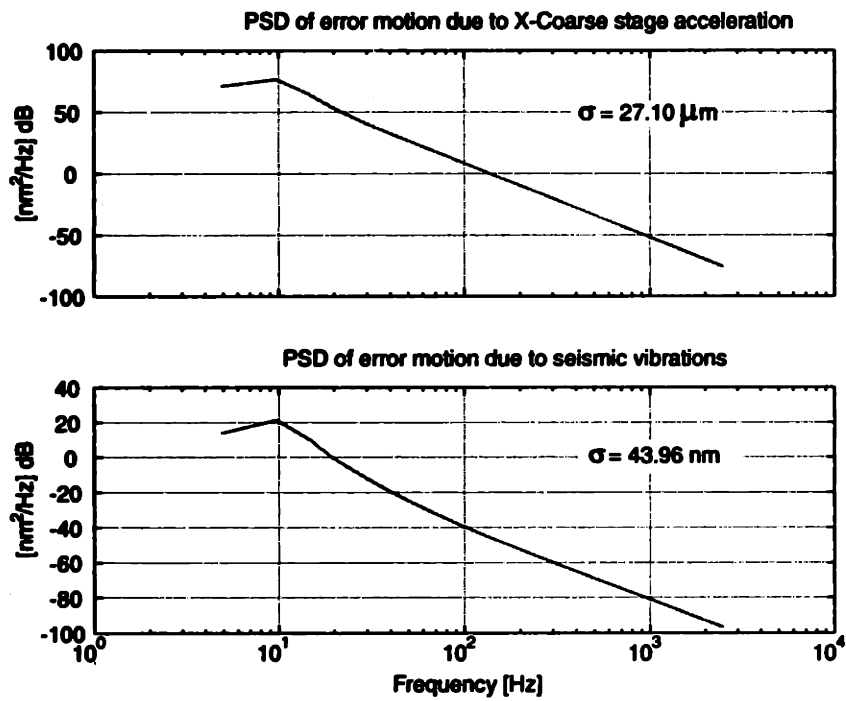


Figure 5-5: Power spectral density (PSD) plots of the payload disturbance and seismic vibrations. The payload disturbance is found to be modeled by a first-order Markov process and both the PSD and its fit are illustrated. Seismic vibrations are also modeled by a first-order Markov process along the lines of Chapter 2.

The power spectral density of the stepper motion can now be computed from the power spectral densities of disturbances, and the sensitivity and complementary sensitivity functions using (2.7). Note that the sensitivity function given by (3.12) is integrated twice to obtain the displacement of the stepper due to the payload acceleration disturbance while the complementary sensitivity function is used as in (3.12). The resulting PSDs due to these conflicting disturbances are plotted in Figure 5-6. The resonance of the mount at 11.1 Hz can be clearly observed in the plots. The variance of the stepper motion can now be obtained by integrating the PSD curves as previously demonstrated in Chapter 2. The standard deviation of the stepper motion due to seismic vibrations is found to be 43.96 nm while that due to stage motion is found to be 27.10  $\mu\text{m}$ . It is thus clearly seen for the example considered that the chief



**Figure 5-6: Power spectral density (PSD) plots of the payload error motion due to payload force disturbance and seismic vibrations. Note that the chief contributor to error motions is the payload force disturbance.**

contributor to error motions of the stepper is the payload disturbance force caused by stage motions. However, it should be noted that for the stepper considered, it is really not important to attenuate the conflicting disturbances at the same time, *i.e.*, payload reaction forces act during the stepping motion of the coarse stages while seismic isolation is really important only during the exposure of the wafer. This example however serves to illustrate the analysis of a passive mount for use in machine tools subject to these conflicting disturbances. We can also apply the Kalman filtering technique described in Chapter 3 to obtain both the variance of the stepper motions as well as optimal mount parameters. This is however not done here, since we do not have a constant excitation due to payload reaction forces *i.e.*, the stage motions are intermittent. We now discuss the mechanical characteristics of the passive mounts used in this project and their location in the Cartesian frame of the stepper.

### 5.3.2 Passive mount characteristics and location

The legs comprise a passive elastomeric mount that supports the static weight of the machine and provides isolation above a natural frequency of approximately 15 Hz. The 512-3NS<sup>4</sup> elastomeric mount from Barry controls [11] is designed to provide matched vertical and lateral stiffness. The damping mechanism in the elastomeric mounts is hysteretic.

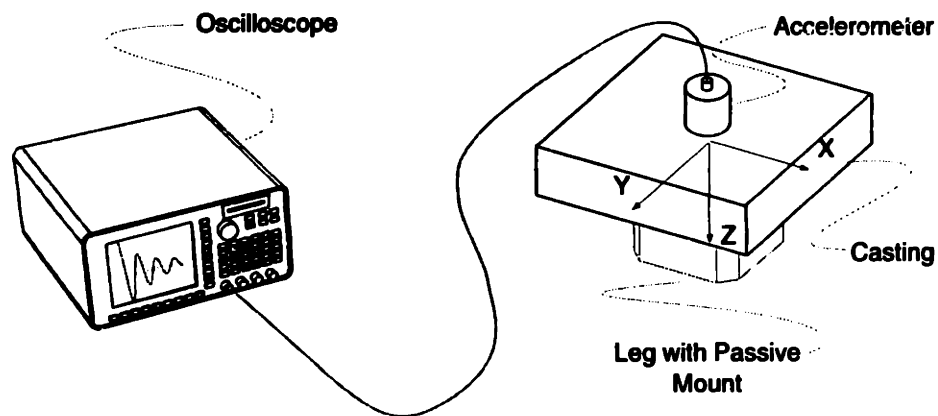


Figure 5-7: Experimental setup to determine Mount Parameters : The Mass of the casting is separately determined to be 296.8 Kg.

<sup>4</sup>Barry controls part number

A simple experiment is carried out to evaluate the stiffness (the data sheet cites a stiffness of  $1.32 \times 10^6$  N/m) and damping of the mounts using logarithmic decrement. One passive mount is fixed onto a leg and a massive casting balanced on this single mount to create a simple one degree of freedom system as shown in Figure 5-7. An

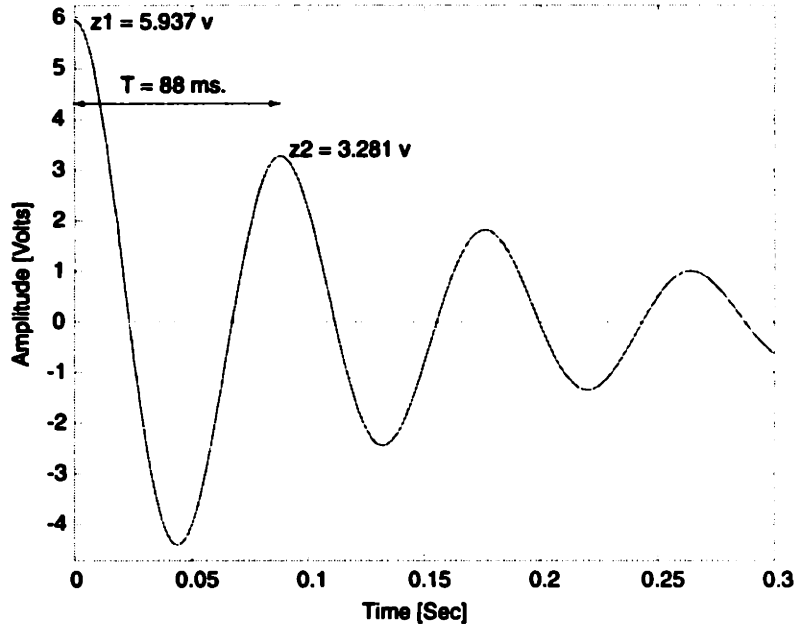


Figure 5-8: Acceleration of Base Casting in the Z direction when subjected to an impulse

impulse is applied at the center of gravity to excite the single degree of freedom system, and the resulting accelerometer signal is recorded on an oscilloscope and plotted in Figure 5-8. This signal is then used to compute the stiffness and damping using the formulas given below [46].

$$\delta = \log \left( \frac{z_1}{z_2} \right) = 0.5931$$

$$\omega_d = \frac{2\pi}{T} = 71.4 \text{ rad/s}$$

$$\zeta = \frac{\delta}{\sqrt{(2\pi)^2 + \delta^2}} = 0.094$$

$$\omega_n = \frac{\omega_d}{\sqrt{1 - \zeta^2}} = \sqrt{\frac{K}{M}} = 71.72 \text{ rad/s}$$

$$K = \omega_n^2 M = 1.53 \times 10^6 \text{ N/m}$$

$$C = 2\zeta M \omega_n = 4.0 \times 10^3 \text{ Ns/m}$$

The resulting mount parameters are tabulated in Table 5.3. Note that while the properties in the longitudinal direction are measured, those in the lateral direction are not measured, but set equal to those in the longitudinal direction. This is because static testing to determine the static stiffness on an Instron Universal testing machine<sup>5</sup> yielded similar values for stiffness in the longitudinal and lateral directions. Hence a complicated dynamic test was not performed.

Parameter	Symbol	Value	Units
Longitudinal Stiffness	$K_z$	$1.53 \times 10^6$	N/m
Longitudinal Damping	$C_z$	$4.0 \times 10^3$	Ns/m
Lateral Stiffness	$K_x$	$1.53 \times 10^6$	N/m
Lateral Damping	$C_x$	$4.0 \times 10^3$	Ns/m

Table 5.3: Passive Mount Parameters. The parameters in the vertical direction  $K_z$  and  $C_z$  are measured using the logarithmic decrement method, while the lateral stiffness and damping parameters  $K_x$  and  $C_x$  are set to equal the values in the vertical direction.

Having discussed the characteristics of a single passive mount, we now discuss the location of the various mounts. To do this, we first establish a Cartesian coordinate frame fixed to the center of gravity of the wafer stepper. This coordinate system has its axes aligned with the principal elastic axes of the isolation system. Since the products of inertia of the stepper (refer to Table 5.1) are negligible, these axes are also aligned with the principal axes of the stepper. This coordinate system is used to express the distances of the various mounts, sensors and actuators of the isolation system. The distances of the elastomeric mounts are used to derive the model presented in Chapter 6. The schematic in Figure 5-9 shows the position of the mounts with respect to the established coordinate system.

Table 5.4 tabulates the key distances for the mount locations. It should be noted that the plane of support is offset from the center of gravity of the stepper, and the axes of the mounts do not pass through the center of gravity either. Therefore, we would expect coupling between the translational and rotational motions which

---

<sup>5</sup>Courtesy of the Applied Mechanics Laboratory, MIT

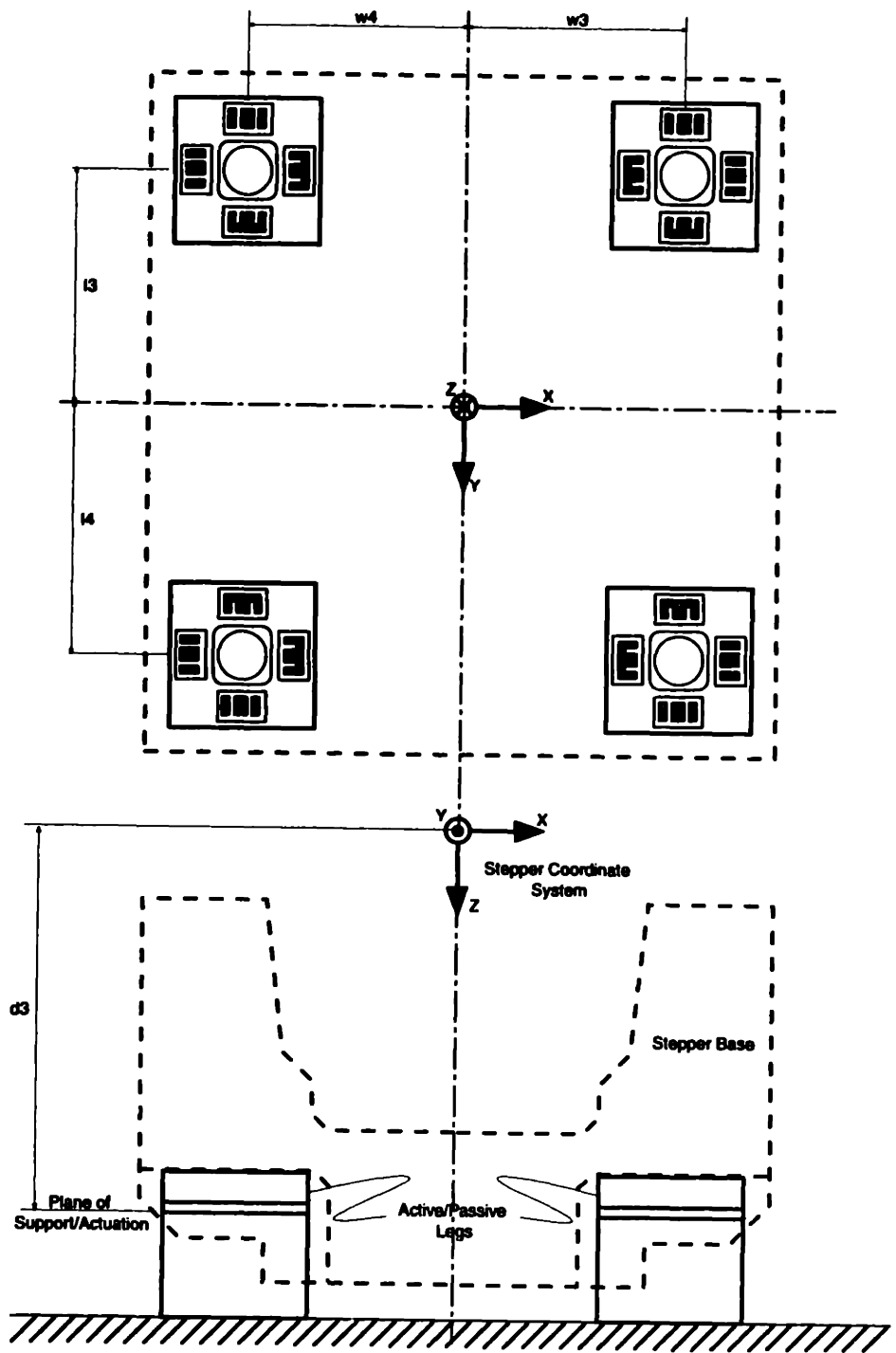


Figure 5-9: Location of Passive Mounts. The Cartesian coordinate frame is fixed to the center of gravity of the stepper.

is indeed the case. No effort has been made to optimize the mechanical design to achieve decoupling since it would involve redesign of the stepper base and it was critical to the project that the isolation system did not cause significant mechanical redesign. However, transformations in Chapter 6 are used to transform this six degree of freedom system into six decoupled single degree of freedom systems for controller design.

Parameter	Symbol	Distance [m]
Distance of Mounts in $X$ direction	$w_3 = w_4$	0.389
Distance of Mounts in $Y$ direction	$w_3 = w_4$	0.371
Distance of Mounts in $Z$ direction	$d_3$	0.368

Table 5.4: Passive Mount Location : Note that the plane of support/actuation is offset from the center of gravity of the stepper leading to coupled rotational and translational motion

## 5.4 Actuator Design

We first compute the requirements on force and displacement on the actuators. The peak requirement on force can be computed from the reaction forces that need to be impressed by the isolation actuators on the base of the stepper during stage acceleration. Assuming an acceleration of 0.5 g for the 90 Kg Y-coarse stage, this requirement on the force is approximately 450 N. However, this force is shared by at least two actuators operating in parallel (due to their arrangement on the base of the stepper). Hence, the peak force requirement on the actuators is around 250 N. The displacement requirement is computed based on a rather conservative estimate of ground motions. A peak value of 250  $\mu\text{m}$  is assumed for the ground motion resulting in a similar requirement on the displacement of the actuators of the isolation system.

As discussed earlier, we are restricted to electromagnetic actuators since we require low mechanical impedance non-contact actuators. There exist two basic mechanisms of electromagnetic actuation - Lorentz force, and reluctance force. Lorentz force actuators use the  $\mathbf{J} \times \mathbf{B}$  constitutive law and are linear. Examples in commercial use

include voice-coil actuators in the FF-series of isolators from IDE and linear motors in their MaxAktiv family of mounts. The key disadvantages with non-superconducting Lorentz force actuators include high power dissipation and bulky size. For example, the published typical power consumption of the ATC isolation modules from IDE is 0.4 KW [32] and the size of the mounts is 300 mm diameter by 230 mm height. This compares against a typical power consumption of 10 Watts for the mounts designed in this thesis and a size of 180 mm square by 230 mm height. It should be noted that the need to reduce power dissipation in the stepper stems not so much out of the cost of the power but the need to reduce thermal distortions on the structure.

Reluctance force actuators operate on the principle of minimization of co-energy. They are characterized by smaller stroke lengths than Lorentz force actuators, higher force density and smaller footprint along with a simple and robust mechanical construction. However, the key disadvantage of reluctance-type actuators is their non-linear behavior. To compensate for their nonlinear behavior, the operating gaps need to be sensed adding to the cost and complexity of the system. The compensation itself is based on a simple application of feedback linearization techniques and will be outlined later in this chapter.

We select electromagnetic, variable reluctance actuators for the purpose of this thesis. The reasons include mechanical simplicity and ease of fabrication, higher force density and smaller footprint. Variable reluctance actuators are very power-efficient for the small (250  $\mu\text{m}$ ) air-gaps used in the design. Figure 5-10 illustrates a cross-section of such an actuator. The current-force relationship for such an actuator is derived in Melcher *et al.* [86] for the case of infinite permeability of the steel core. A finite permeability is modeled simply by using an equivalent air gap given by  $g_0$  and the current-force relationship from Melcher modified as follows :

$$f = C \frac{i^2}{(g + g_0)^2} \quad (5.1)$$

where  $g$  is the air gap in between the actuator pole face and the target,  $i$  the current,



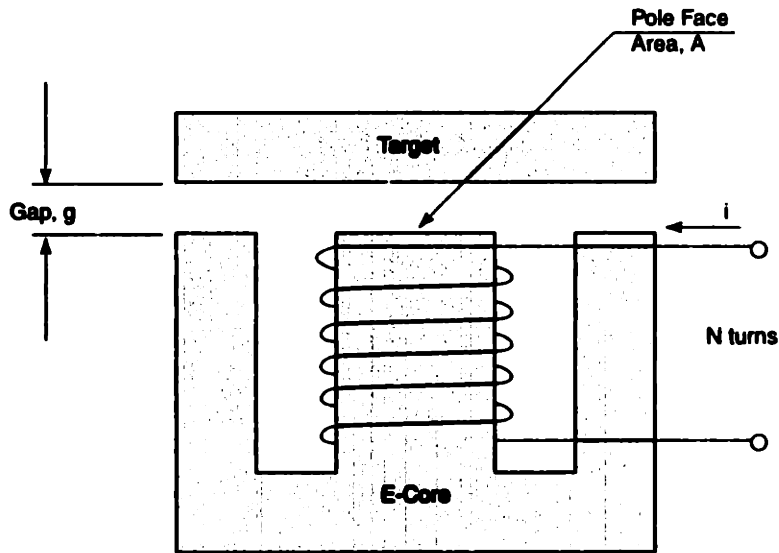


Figure 5-10: Cross section of a variable reluctance actuator

and  $C$  the actuator constant is a function of the geometry of the actuator given by :

$$C = \frac{\mu_0 N^2 A}{4} \quad (5.2)$$

$\mu_0$  is the permeability of free space and is given as  $4\pi \times 10^{-7}$  F/m,  $N$  the number of turns and  $A$  the pole face area. The design parameters  $N$  and  $A$  for the variable reluctance actuators are listed in Table 5.4. The equivalent air gap  $g_0$  is de-

Parameter	Value	Units
# Coils, $N$	558	Turns
Pole face area, $A$	$3.05 \times 10^{-4}$	$\text{m}^2$
Actuator Constant, $C$	$2.98 \times 10^{-5}$	$\text{Nm}^2/\text{A}^2$
Inductance, $L$	$\frac{5.97 \times 10^{-5}}{g}$	H

Table 5.5: Actuator Parameters

termined experimentally by obtaining experimental force/displacement/current calibration curves and performing a least-squares fit to the parabolic model given in (5.1). For this purpose, a separate actuator with the same parameters as given above but with a geometry to fit into a calibration fixture [57] in the Precision Motion Control Lab at MIT was constructed. These calibration curves are shown in Figure 5-11.

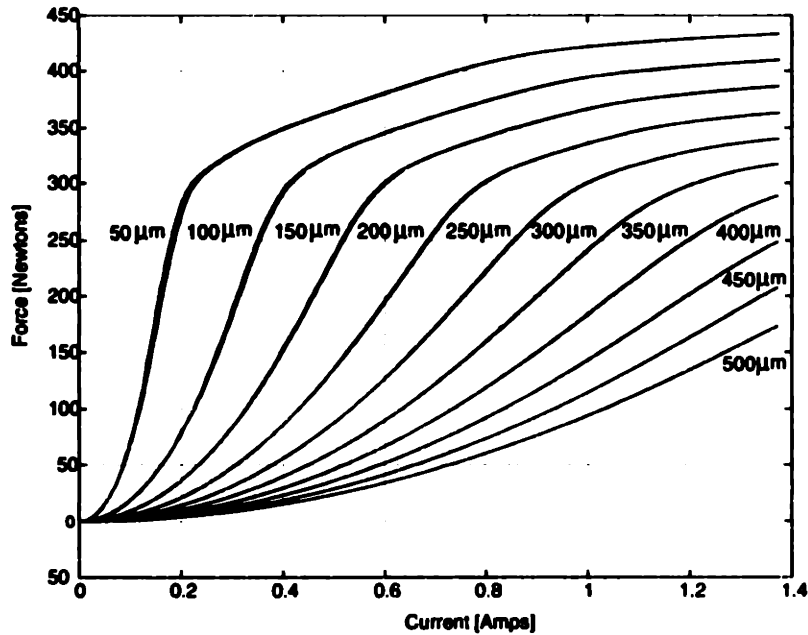


Figure 5-11: Calibration curves for the variable reluctance actuators

From the actuator calibration curves, we find that the actuators saturate at a force of about 450 N. The actuators are sized to provide a full range of motion (about 250  $\mu\text{m}$  which is the nominal air gap) before saturation. Additionally, for the purpose of determining the initial gap between the actuators and the targets accurately, we define the inductance of the actuator as

$$L = \frac{\mu_0 N^2 A}{2g} = \frac{5.97 \times 10^{-5}}{g} \quad (5.3)$$

During the assembly of the isolation system, the operating air gaps are set to 250  $\mu\text{m}$  approximately with shims. This measurement, however, is inaccurate and the actual gap  $g$  is determined by measuring the inductance of the actuator experimentally using an inductance meter at a frequency of 120 Hz<sup>6</sup> and via (5.3).

The isolation system uses sixteen variable reluctance tractive-type force actuators mounted in parallel with the passive mounts. These tractive actuators provide unidirectional attractive forces and hence lead to eight force-pairs. This again is an

---

<sup>6</sup>The inductance was also measured at a frequency of 1 KHz and found to be equal to the values measured at 120 Hz illustrating the effectiveness of the laminations used in the construction of the actuator.

over-constraint, but is used nevertheless for packaging and implementation reasons. There are four actuators on each leg, one each for X and Y motions and two in pair-wise opposition for Z motions as shown in Figure 5-12. A picture of the actuators

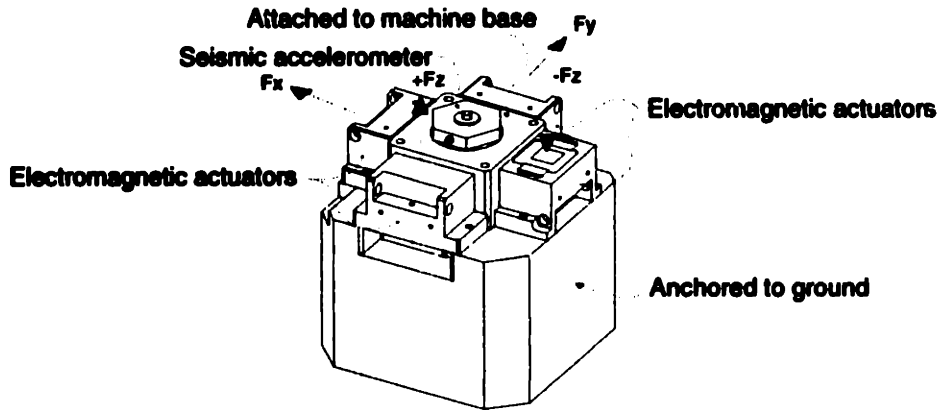


Figure 5-12: Forces provided at each leg location

assembled to the leg is given in Figure 5-13.

Next, we consider the location of the various actuators from the center of gravity of the stepper. These locations are measured in the Cartesian coordinate frame established earlier and tabulated in Table 5.6. A schematic of the location of the

Parameter	Symbol	Distance [m]
Distance of $f_{z1}, f_{z7}$ in X direction	$w_1$	0.432
Distance of $f_{z3}, f_{z5}$ in X direction	$w_2$	0.432
Distance of $f_{z2}, f_{z6}, f_{y1}, f_{y2}$ in X direction	$w_3$	0.364
Distance of $f_{z4}, f_{z8}, f_{y3}, f_{y4}$ in X direction	$w_4$	0.364
Distance of $f_{z2}, f_{z8}$ in Y direction	$l_1$	0.438
Distance of $f_{z4}, f_{z6}$ in Y direction	$l_2$	0.438
Distance of $f_{z3}, f_{z7}, f_{x2}, f_{x3}$ in Y direction	$l_3$	0.371
Distance of $f_{z5}, f_{z1}, f_{x1}, f_{x4}$ in Y direction	$l_4$	0.371
Distance of Actuator Plane in Z direction	$d_3$	0.368

Table 5.6: Actuator Locations from Center of Gravity of Stepper

various actuators along with the actuator naming convention and the direction of the forces applied is given in Figure 5-14. A photograph of the four legs, each turned

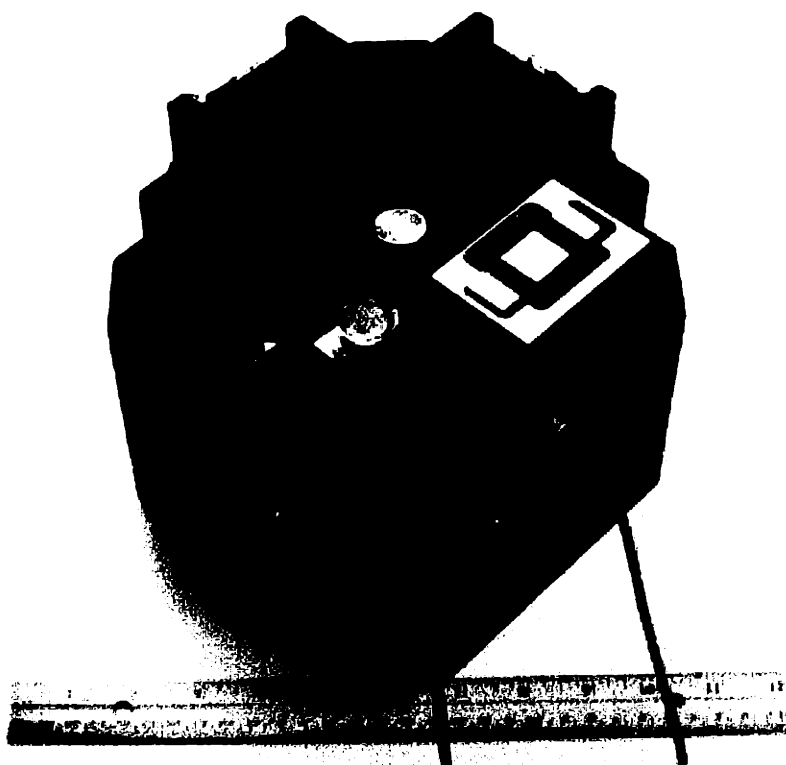


**Figure 5-13: Assembly of actuators to leg. A 12-inch ruler as well as a nickel on the top of the mount are shown for scale.**

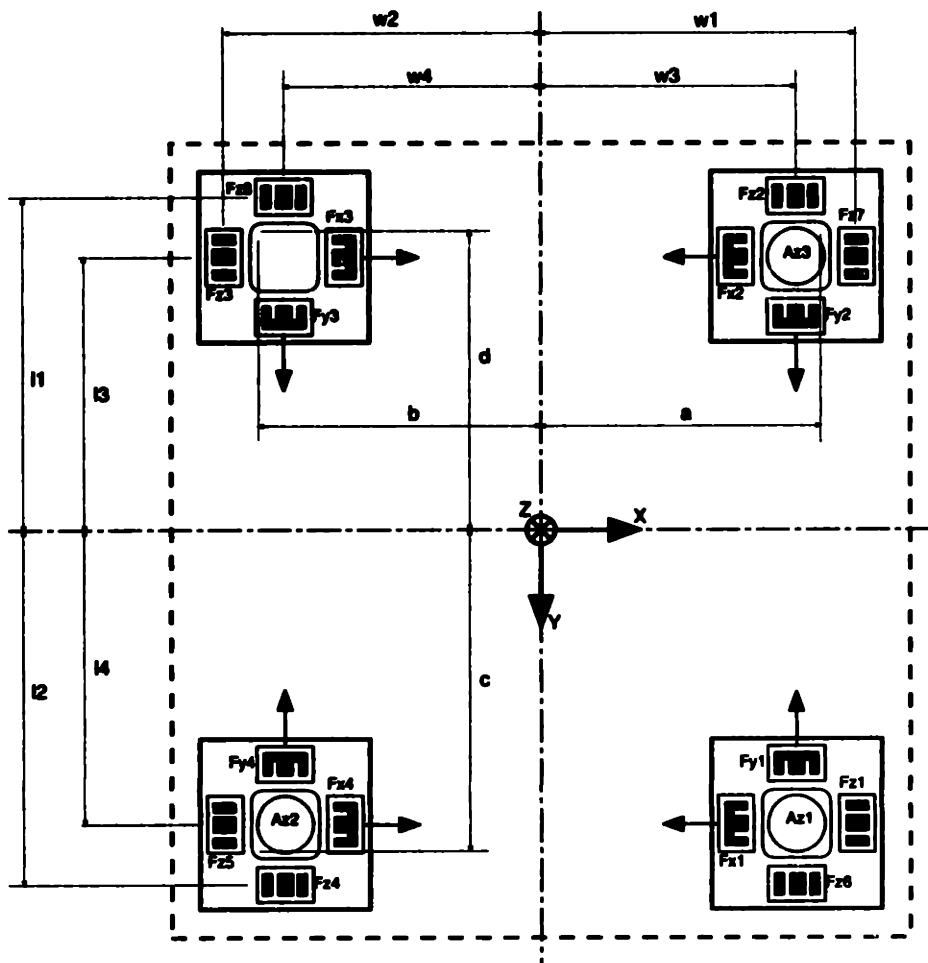
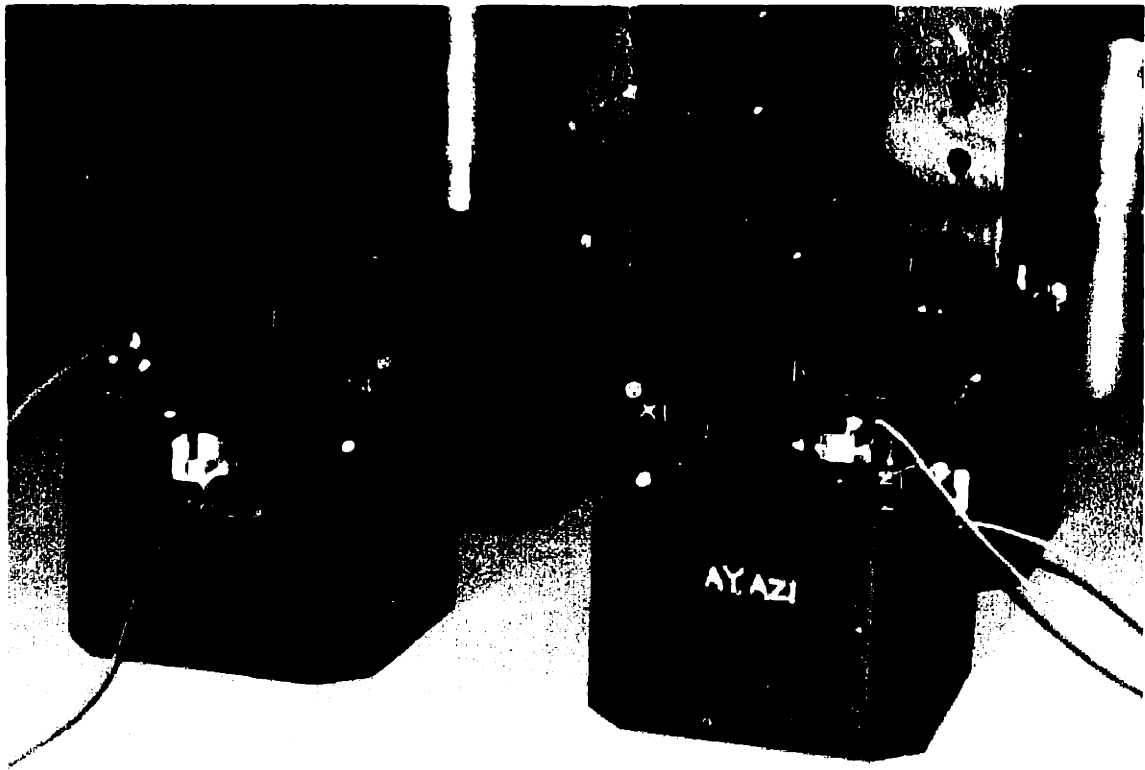


Figure 5-14: Layout of the Actuators for Active Isolation : Note that the plane of actuation (in the Z direction) coincides with the plane of support defined in Figure 5-9.



**Figure 5-15: Four legs, each turned around by 90 degrees showing the actuator locations**

around by 90 degrees is illustrated in Figure 5-15.

Since the actuators are tractive, reversing the direction of the current does not reverse the direction of force given in (5.1). Hence, it makes sense to talk of actuator pairs to provide bi-directional forces. We use a single amplifier to drive each actuator-pair. This is accomplished using a diode arrangement as shown in Figure 5-16. This

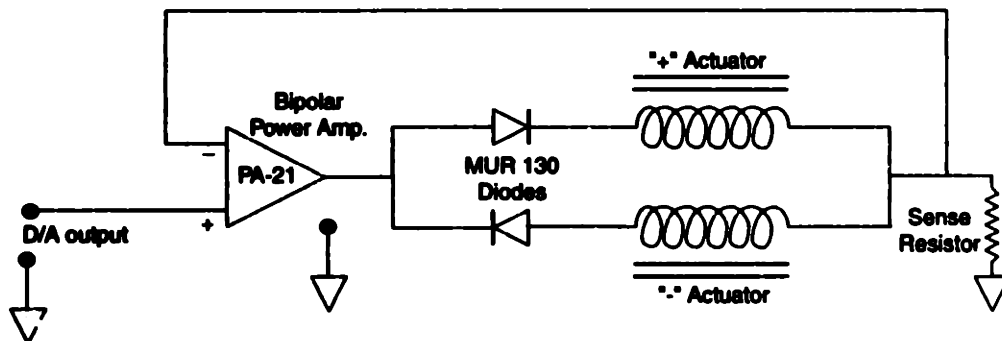


Figure 5-16: Connection of Actuator Pairs to Power Amplifier

diode arrangement saves on the number of amplifiers required to run the isolation system. A possible drawback of this configuration is that there is an uncontrollable “freewheeling” mode where the current just flows in the loop between the two actuators. Repeated experiments to measure the transfer function of the amplifier however established that this “freewheeling” mode is not a problem in our setup. The amplifier bandwidth is found to be a function of input level and at input levels of  $\pm 5$  volts corresponding to  $\pm 0.5$  amperes, the bandwidth is found to be 2 KHz which is much higher than the bandwidth of the control loop. The amplifier is hence treated as just a constant gain free of any dynamics.

Next, we need to associate the sixteen actuator forces to the six control forces and torques in the Cartesian coordinate frame. We develop linear matrix transformations for this purpose in the next section.

### 5.4.1 Transformations to Compute Actuator Forces

We have already remarked on the fact that the stepper is to be controlled as a rigid body. This means that three control forces and three control torques need to be computed as part of the control law. These control forces and torques can be applied

to the stepper only using the 16 actuators or 8 actuator force pairs described in the previous section. We need to relate the forces and torques in the Cartesian coordinate frame to the pair-wise actuator forces. This is done using the linear transformation developed below :

$$\begin{aligned}
 f_x &= -f_{14} - f_{x23} \\
 f_y &= -f_{y12} - f_{y43} \\
 f_z &= f_{z16} + f_{z45} + f_{z27} + f_{z38} \\
 \tau_x &= c(f_{z16} + f_{z45}) - d(f_{z27} + f_{z38}) + d_3(f_{y12} + f_{y43}) \\
 \tau_y &= b(f_{z45} + f_{z38}) - a(f_{z27} + f_{z16}) - d_3(f_{x14} + f_{x23}) \\
 \tau_z &= -l_3 f_{x23} + l_4 f_{x14} - w_3 f_{y12} + w_4 f_{y43}
 \end{aligned} \tag{5.4}$$

where

$$\begin{aligned}
 a &= \frac{w_1 + w_3}{2} \\
 b &= \frac{w_2 + w_4}{2} \\
 c &= \frac{l_2 + l_4}{2} \\
 d &= \frac{l_1 + l_3}{2}
 \end{aligned}$$

We can then express the above set of equations in matrix form to get

$$\mathbf{f} = \mathbf{F}_{act} \mathbf{f}_{act} \tag{5.5}$$

where  $\mathbf{f}$  is the force vector expressed in the Cartesian coordinate frame and  $\mathbf{f}_{act}$  is the force vector expressed in the actuator coordinate frame. The transformation matrix



$\mathbf{F}_{act}$  is a function of actuator location and is given below.

$$\mathbf{F}_{act} = \begin{pmatrix} -1 & -1 & 0 & 0 & 0 & 0 & 0 & 0 \\ 0 & 0 & -1 & -1 & 0 & 0 & 0 & 0 \\ 0 & 0 & 0 & 0 & 1 & 1 & 1 & 1 \\ 0 & 0 & d_3 & d_3 & c & -d & -d & c \\ -d_3 & -d_3 & 0 & 0 & -a & -a & b & b \\ l_4 & -l_3 & -w_3 & w_4 & 0 & 0 & 0 & 0 \end{pmatrix}$$

$\mathbf{F}_{act}$  can be inverted to obtain the actuator pair forces as a function of forces in the Cartesian coordinate frame. Numerical values for the elements of the inverse  $\mathbf{F}_{act}^{-1}$  are given below :

$$\mathbf{F}_{act}^{-1} = \begin{pmatrix} -0.5000 & 0 & 0 & 0 & 0 & 0.6873 \\ -0.5000 & 0 & 0 & 0 & 0 & -0.6873 \\ 0 & -0.5000 & 0 & 0 & 0 & -0.6741 \\ 0 & -0.5000 & 0 & 0 & 0 & 0.6741 \\ 0.2315 & 0.2277 & 0.2500 & 0.6183 & -0.6285 & 0 \\ 0.2315 & -0.2277 & 0.2500 & -0.6183 & -0.6285 & 0 \\ -0.2315 & -0.2277 & 0.2500 & -0.6183 & 0.6285 & 0 \\ -0.2315 & 0.2277 & 0.2500 & 0.6183 & 0.6285 & 0 \end{pmatrix} \quad (5.6)$$

## 5.5 Feedback Linearization and the Measurement of Actuator Gaps

Variable reluctance actuators have the advantages of simple and robust construction, high force density for the operating gaps considered, and permit easy design integration since they are non-contact. This last property allows easy design of the isolation system since contacting actuators would need stacked designs, and thus complicate the mechanical design. Unfortunately, variable reluctance actuators are also nonlinear and their use is complicated by the fact that the generated force is nonlinearly

dependent on both the control current and the air gap as given in (5.1). An easy technique to handle this nonlinear dependence is due to feedback linearization [78]. Using feedback linearization, the actuator currents for an actuator pair are computed according to the law :

$$\begin{aligned} i_+ &= (g_0 - g)\sqrt{\frac{f}{C}}, i_- = 0 & (f > 0) \\ i_- &= (g_0 + g)\sqrt{\frac{-f}{C}}, i_+ = 0 & (f < 0) \end{aligned} \quad (5.7)$$

where  $f$  is the force applied by an actuator pair, and the currents  $i_+$  and  $i_-$  represent the currents to the actuators in the positive and negative directions respectively in the arrangement shown in Figure 5-16.

Equations 5.7 require the measurement of the air gap  $g$  between the actuator pole face and the target. Instead of measuring the operating air gaps for each one of the sixteen actuators individually, we measure the change in position of the stepper in six degrees of freedom using six capacitance gauges. Two capacitance gauges are used in each instrumented leg. This is illustrated in Figure 5-17. These capacitance gauges are fabricated by ADE Inc. and have a range of 400  $\mu\text{m}$  with a noise floor of 10 nm RMS and a gain of 40  $\mu\text{m}/\text{v}$ . The capacitance gauges are mounted at the locations given in Table 5.7. These measurements can be used to compute the operating air gaps for the various variable reluctance actuators using another set of linear transformations described in the next section. To compute the change in position of the stepper,

Parameter	Symbol	Distance [m]
Distance of $C_x, C_{y1}, C_{y2}$ in $Z$ direction	$z_{C_x}, z_{C_y}$	0.390
Distance of $C_x$ in $Y$ direction	$y_{C_x}$	0.371
Distance of $C_{y1}, C_{y2}$ in $X$ direction	$x_{C_{y1}}, x_{C_{y2}}$	0.364
Distance of $C_{z1}$ in $X$ direction	$x_{C_{z1}}$	0.410
Distance of $C_{z2}, C_{z3}$ in $X$ direction	$x_{C_{z2}}, x_{C_{z3}}$	0.428
Distance of $C_{z1}$ in $Y$ direction	$y_{C_{z1}}$	0.435
Distance of $C_{z2}, C_{z3}$ in $Y$ direction	$y_{C_{z2}}, y_{C_{z3}}$	0.417

Table 5.7: Capacitance Gauge Locations from Center of Gravity of Stepper

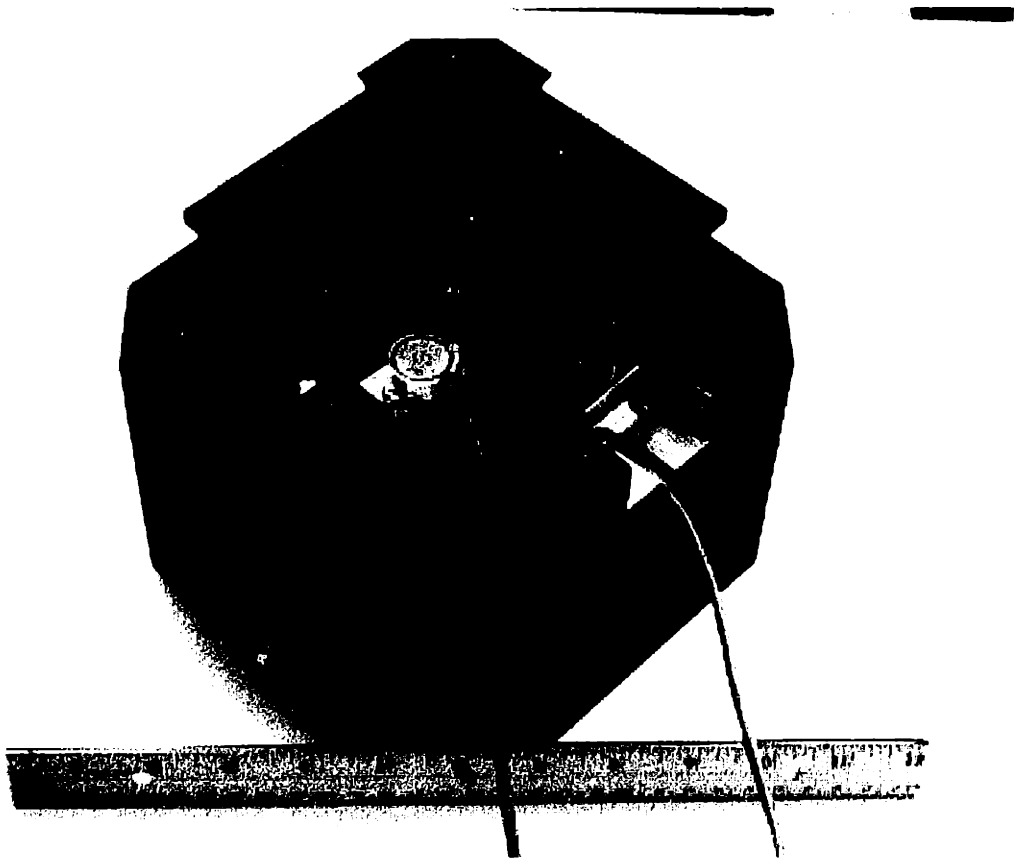


**Figure 5-17: A leg during assembly showing the capacitance gauge positions. Three legs are instrumented with capacitance probes as shown.**

we first need to establish the equilibrium position of the stepper. This is obtained by averaging the capacitance probe readings over a period of time during which the seismic disturbances are insignificant and the X-Y stages are disabled.

### 5.5.1 Transformations for Gap Computation

The capacitance probes measure the change in gap at six pointwise locations of the stepper and need to be converted to deviations from equilibrium of the stepper. Under the assumption of small motions, this is accomplished using the following transformations :

$$\begin{aligned}
\delta C_{x_1} &= -\delta x + y_{C_{x_1}}\delta\theta_z + z_{C_x}\delta\theta_y \\
\delta C_{y_1} &= -\delta y + x_{C_{y_1}}\delta\theta_z + z_{C_y}\delta\theta_x \\
\delta C_{y_2} &= \delta y + x_{C_{y_2}}\delta\theta_z - z_{C_y}\delta\theta_x \\
\delta C_{z_1} &= -\delta z - y_{C_{z_1}}\delta\theta_x + x_{C_{z_1}}\delta\theta_y \\
\delta C_{z_2} &= -\delta z - y_{C_{z_2}}\delta\theta_x - x_{C_{z_2}}\delta\theta_y \\
\delta C_{z_3} &= -\delta z + y_{C_{z_3}}\delta\theta_x + x_{C_{z_3}}\delta\theta_y
\end{aligned} \tag{5.8}$$

This linear transformation can be expressed succinctly as :

$$\delta \mathbf{x}_c = \mathbf{C}_{cap} \delta \mathbf{x} \tag{5.9}$$

where  $\delta \mathbf{x}$  is the deviation of the stepper from the equilibrium and  $\delta \mathbf{x}_c$  is the vector of deviations at the six points of measurement. The matrix  $\mathbf{C}_{cap}$  is a function of

capacitance probe location and is given by :

$$\mathbf{C}_{\text{cap}} = \begin{pmatrix} -1 & 0 & 0 & 0 & z_{Cx} & y_{Cx1} \\ 0 & -1 & 0 & z_{Cy} & 0 & x_{Cy1} \\ 0 & 1 & 0 & -z_{Cy} & 0 & x_{Cy2} \\ 0 & 0 & -1 & -y_{Cz1} & x_{Cz1} & 0 \\ 0 & 0 & -1 & -y_{Cz2} & -x_{Cz2} & 0 \\ 0 & 0 & -1 & y_{Cz3} & x_{Cz3} & 0 \end{pmatrix} \quad (5.10)$$

We can invert (5.9) to obtain  $\delta \mathbf{x}$  from  $\delta \mathbf{x}_c$ .

The deviation from the equilibrium is then used to compute the change in gaps at the individual actuators.

$$\begin{aligned} \delta g_{Fx1} &= \delta x - l_4 \delta \theta_z + d_3 \delta \theta_y & \delta g_{Fx4} &= -\delta x + l_4 \delta \theta_z - d_3 \delta \theta_y \\ \delta g_{Fx2} &= \delta x + l_3 \delta \theta_z + d_3 \delta \theta_y & \delta g_{Fx3} &= -\delta x - l_3 \delta \theta_z - d_3 \delta \theta_y \\ \\ \delta g_{Fy1} &= \delta y + w_3 \delta \theta_z - d_3 \delta \theta_x & \delta g_{Fy2} &= -\delta y - w_3 \delta \theta_z + d_3 \delta \theta_x \\ \delta g_{Fy3} &= -\delta y + w_4 \delta \theta_z + d_3 \delta \theta_x & \delta g_{Fy4} &= \delta y - w_4 \delta \theta_z - d_3 \delta \theta_x \\ \\ \delta g_{Fz1} &= -\delta z + w_1 \delta \theta_y - l_4 \delta \theta_x & \delta g_{Fz6} &= \delta z - w_3 \delta \theta_y + l_2 \delta \theta_x \\ \delta g_{Fz2} &= -\delta z + w_3 \delta \theta_y + l_1 \delta \theta_x & \delta g_{Fz7} &= \delta z - w_1 \delta \theta_y - l_3 \delta \theta_x \\ \delta g_{Fz3} &= -\delta z - w_2 \delta \theta_y + l_3 \delta \theta_x & \delta g_{Fz8} &= \delta z + w_4 \delta \theta_y - l_1 \delta \theta_x \\ \delta g_{Fz4} &= -\delta z - w_4 \delta \theta_y - l_2 \delta \theta_x & \delta g_{Fz5} &= \delta z + w_2 \delta \theta_y + l_4 \delta \theta_x \end{aligned} \quad (5.11)$$

Again, this linear transformation can be expressed succinctly as :

$$\delta \mathbf{g} = \mathbf{C}_{\text{act}} \delta \mathbf{x} \quad (5.12)$$

where  $\delta \mathbf{g}$  is the change in actuator gap and the matrix  $\mathbf{C}_{\text{act}}$  is a function of actuator

location given by

$$\mathbf{C}_{act} = \begin{pmatrix} 1 & 0 & 0 & 0 & d_3 & -l_4 \\ 1 & 0 & 0 & 0 & d_3 & l_3 \\ -1 & 0 & 0 & 0 & -d_3 & -l_3 \\ -1 & 0 & 0 & 0 & -d_3 & l_4 \\ 0 & 1 & 0 & -d_3 & 0 & w_3 \\ 0 & -1 & 0 & d_3 & 0 & -w_3 \\ 0 & -1 & 0 & d_3 & 0 & w_4 \\ 0 & 1 & 0 & -d_3 & 0 & -w_4 \\ 0 & 0 & -1 & -l_4 & w_1 & 0 \\ 0 & 0 & -1 & l_1 & w_3 & 0 \\ 0 & 0 & -1 & l_3 & -w_2 & 0 \\ 0 & 0 & -1 & -l_2 & -w_4 & 0 \\ 0 & 0 & 1 & l_4 & w_2 & 0 \\ 0 & 0 & 1 & l_2 & -w_3 & 0 \\ 0 & 0 & 1 & -l_3 & -w_1 & 0 \\ 0 & 0 & 1 & -l_1 & w_4 & 0 \end{pmatrix} \quad (5.13)$$

The transformations in (5.9) and (5.12) can be cascaded to get

$$\delta \mathbf{g} = \mathbf{C}_{pos} \delta \mathbf{x}_c \quad (5.14)$$

where,

$$\mathbf{C}_{pos} = \mathbf{C}_{act} \mathbf{C}_{cap}^{-1} \quad (5.15)$$

Numerical values for the elements of the overall transformation matrix  $\mathbf{C}_{pos}$  that converts the deviations sensed by the cap gauges to the deviations in actuator gaps

are as follows :

$$\mathbf{C}_{pos} = \begin{pmatrix}
 -1.0000 & 0.0001 & 0.0001 & 0.8867 & -0.9059 & 0.0193 \\
 -1.0000 & 1.0194 & 1.0194 & 0.8867 & -0.9059 & 0.0193 \\
 1.0000 & -1.0194 & -1.0194 & -0.8867 & 0.9059 & -0.0193 \\
 1.0000 & -0.0001 & -0.0001 & -0.8867 & 0.9059 & -0.0193 \\
 0 & 0.0348 & 1.0348 & -0.0265 & 0.0006 & 0.0259 \\
 0 & -0.0348 & -1.0348 & 0.0265 & -0.0006 & -0.0259 \\
 0 & 0.9650 & -0.0350 & 0.0265 & -0.0006 & -0.0259 \\
 0 & -0.9650 & 0.0350 & -0.0265 & 0.0006 & 0.0259 \\
 0 & 0 & 0 & 0.9791 & -0.0553 & 0.0762 \\
 0 & 0 & 0 & -0.0705 & 0.0465 & 1.0240 \\
 0 & 0 & 0 & -0.9197 & 0.9947 & 0.9251 \\
 0 & 0 & 0 & 0.1299 & 0.8928 & -0.0227 \\
 0 & 0 & 0 & 0.0302 & -0.9758 & -0.0543 \\
 0 & 0 & 0 & -0.9800 & -0.0243 & 0.0043 \\
 0 & 0 & 0 & -0.0895 & 0.0365 & -0.9470 \\
 0 & 0 & 0 & 0.9206 & -0.9151 & -1.0056
 \end{pmatrix} \quad (5.16)$$

The change in actuator gap when added with the gap at equilibrium  $\mathbf{g}_0$  gives the total operating air gap for each actuator.

$$\mathbf{g} = \mathbf{g}_0 + \delta\mathbf{g} \quad (5.17)$$

These gaps can then be used to compute the control currents using the feedback linearization algorithm given in (5.7).

## 5.6 Measurement of Acceleration

Blackwood [15] presents an illustrative trade study of sensors, actuators and configurations. Inertial sensing is required to servo the stepper to an inertially still state.

Commercial devices for inertial sensing permit sensing of either velocity (geophones) or acceleration (accelerometers). We choose to use six seismic accelerometers mounted on three legs at the locations given in Table 5.8 to measure the acceleration of the stepper. Figure 5-18 shows a photograph of all the components of a single leg assembled together. These accelerometers are piezoelectric and have a limited sensing

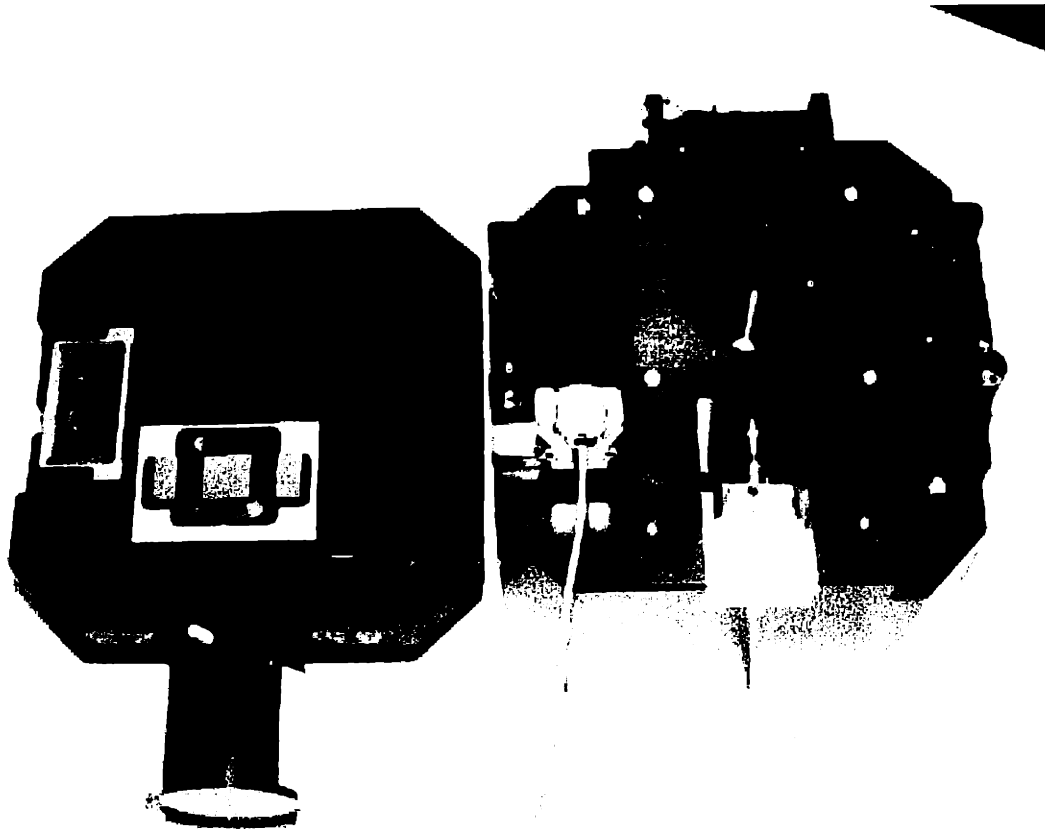


Figure 5-18: The components of a single instrumented leg showing the actuators, targets, capacitance gauges and accelerometers in place. The top plate is bolted to the post to complete the assembly.

bandwidth. McConnell [43] presents a good overview of piezoelectric accelerometers, their modeling and error sources. The lower limit is due to the charge amplification required since the accelerometer is a charge-based device and is a function of the amplifier electronics. The upper limit is due to the resonance of the proof mass inside the accelerometer. Figure 5-19 shows a generic magnitude plot of the Frequency Response Function (FRF) of a piezoelectric accelerometer. Assuming an amplifier sensitivity of 1 Volt per  $m/s^2$ , we can write the transfer function of the accelerometer



as

$$\frac{V}{A} = \left( \frac{RCs}{RCs + 1} \right) \left( \frac{\omega_n^2}{s^2 + 2\zeta\omega_n s + \omega_n^2} \right) \quad (5.18)$$

In the above equation, we have split the transfer function into the electrical and mechanical components. The electrical component is given by the amplifier input resistance R, and the sensor capacitance C while the mechanical component is given by the seismic stiffness  $\omega_n^2 = K/M$  and the corresponding damping. The working region of the accelerometer is between 0.03 Hz and 650 Hz where the sensitivity of the accelerometer can be expressed as a simple gain as can be seen from the figure. The accelerometers used in this thesis are manufactured by Vibrametrics Inc. [81]

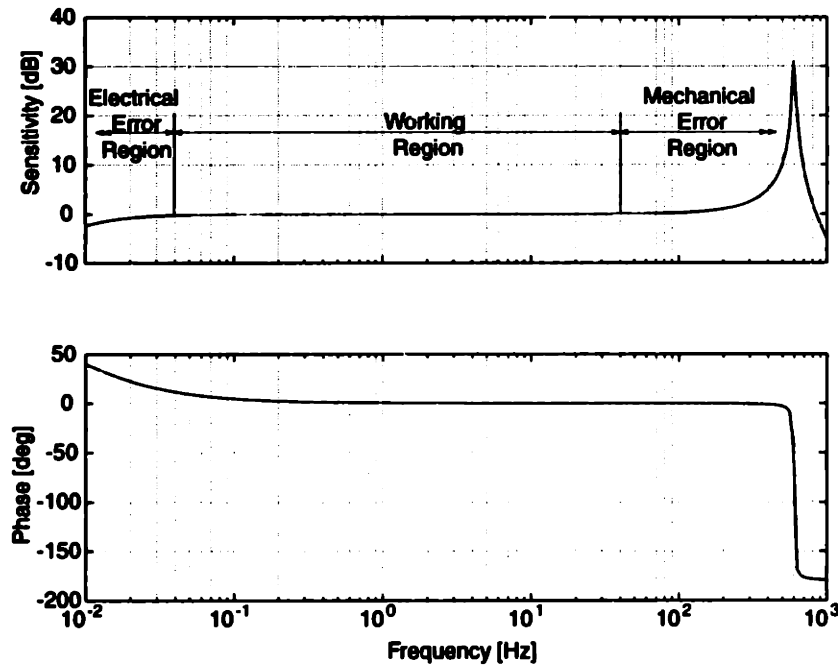


Figure 5-19: Overall accelerometer FRF showing electrical and mechanical error regions as well as working region

demonstrate a very high signal to noise ratio even at very low frequencies. The noise floor in the calibration certificates cites a typical value of  $600 \mu\text{V}/\sqrt{\text{Hz}}$  and a gain of about  $6 \text{ V/g}$ . Three of the accelerometers have a vertical orientation and sense  $\ddot{Z}$ ,  $\ddot{\theta}_x$ , and  $\ddot{\theta}_y$ . The other three are oriented horizontally and sense  $\ddot{X}$ ,  $\ddot{Y}$ , and  $\ddot{\theta}_z$ . The signals from the accelerometers are amplified by a factor of 10 and then read by 6 A/D

Parameter	Symbol	Distance [m]
Distance of $A_{x1}, A_{x2}, A_y$ in $Z$ direction	$z_{Ax}, z_{Ay}$	0.329
Distance of $A_{x1}, A_{x2}$ in $Y$ direction	$y_{Ax1}, y_{Ax2}$	0.371
Distance of $A_y$ in $X$ direction	$x_{Ay}$	0.364
Distance of $A_{z1}, A_{z2}, A_{z3}$ in $X$ direction	$x_{Az1}, x_{Az2}, x_{Az3}$	0.364
Distance of $A_{z1}, A_{z2}, A_{z3}$ in $Y$ direction	$y_{Az1}, y_{Az2}, y_{Az3}$	0.371

Table 5.8: Accelerometer Locations from Center of Gravity of Stepper

converters. The accelerometers however turned out to be one of the key limitations to the performance of the isolation system. During system identification measurements of the overall control loop, it was observed that there was an unexplained loss of phase at frequencies near and greater than 80 Hz. This phase loss was traced to the accelerometers after extensive experimentation. The calibration certificates from Vibrametrics give only the magnitude plot as a function of frequency and I assumed the phase to follow the pattern given in Figure 5-19. This however, turned out to be a wrong assumption. The FRF of one of the Vibrametrics accelerometers used in the isolation system was experimentally determined by mounting it on a shaker in series with another calibrated accelerometer (from Bruel and Kjaer) and comparing the two voltages. The ratio between the two voltages is illustrated in Figure 5-20. As can be seen from Figure 5-20, there is a loss of about 45 degrees of phase at about 100 Hz and greater losses above this frequency. This turns out to be a key limitation to achievable bandwidth of the isolation system.

### 5.6.1 Anti-Aliasing Filters

Aliasing is a concern in any discrete-time system, especially where high frequency components are involved. The accelerometers used in this project are especially sensitive even to acoustic inputs and hence the need for an anti-aliasing filter. The controller sampling rate is 5 KHz, and a passive two pole Unity gain Sallen-Key low pass filter [24] with a corner frequency of  $\approx 600$  Hz is used to prevent aliasing. The useful range of the accelerometers extends to about 350 Hz, and hence use of this

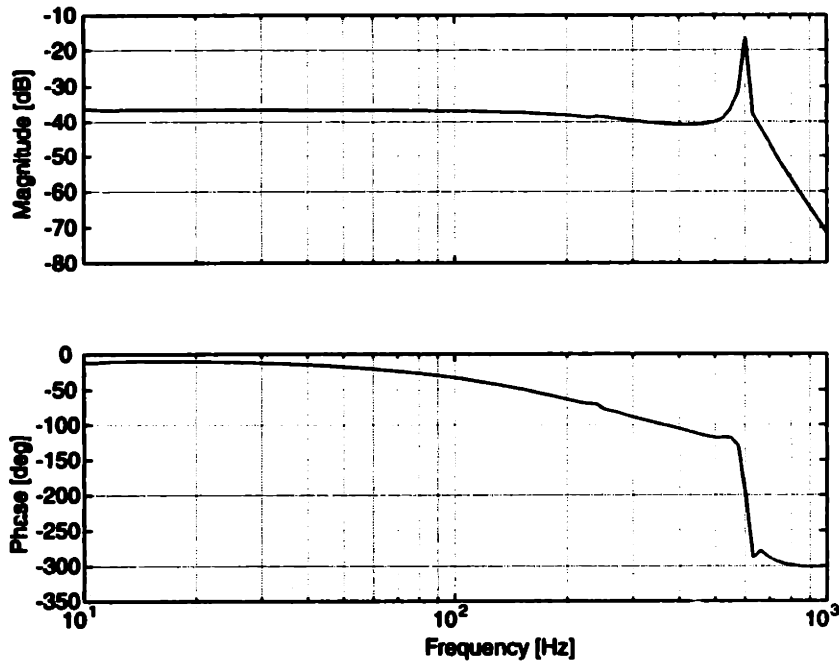


Figure 5-20: Experimentally determined FRF of Vibrametrics accelerometer (serial # 831) showing the gradual phase loss over the working region

anti-aliasing filter does not lead to loss of data. A schematic of the anti-aliasing filter is shown in Figure 5-21. The transfer function of the anti-aliasing filter is given by

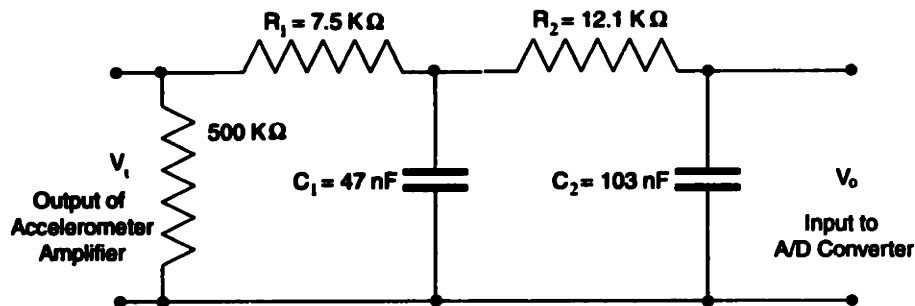


Figure 5-21: Unity-gain, low pass Sallen-Key Anti-Aliasing filter. Note the 500 KΩ impedance across the output of the accelerometer amplifier to prevent saturation.

$$\frac{V_o(s)}{V_i(s)} = \frac{1}{R_1 R_2 C_1 C_2 s^2 + (R_1(C_1 + C_2) + R_2 C_2) s + 1} \quad (5.19)$$

The frequency response of the filter is measured using a swept-sine test and found to match very well with the predicted response in Figure 5-22.

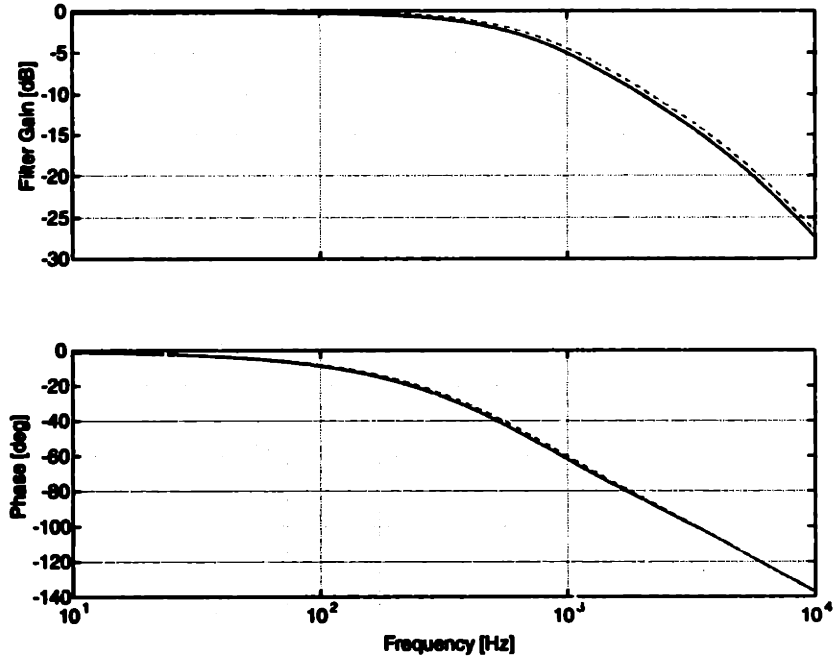


Figure 5-22: Frequency response of anti-aliasing filter. Experimental response is plotted using solid lines and predicted response using dashed lines.

## 5.6.2 Transformations for Computation of Acceleration of Stepper

The accelerometers measure pointwise acceleration at the mounting locations and are transformed to rigid body acceleration of the stepper using the transformations developed below.

$$\begin{aligned}
 Ax1 &= \ddot{x} + z_{Ax}\ddot{\theta}_y - y_{Ax1}\ddot{\theta}_z \\
 Ax2 &= -\ddot{x} - z_{Ax}\ddot{\theta}_y - y_{Ax2}\ddot{\theta}_z \\
 Ay &= -\ddot{y} + z_{Ay}\ddot{\theta}_x - x_{Ay}\ddot{\theta}_z \\
 Az1 &= -\ddot{z} - y_{Az1}\ddot{\theta}_x + x_{Az1}\ddot{\theta}_y \\
 Az2 &= -\ddot{z} - y_{Az2}\ddot{\theta}_x - x_{Az2}\ddot{\theta}_y \\
 Az3 &= -\ddot{z} + y_{Az3}\ddot{\theta}_x + x_{Az3}\ddot{\theta}_y
 \end{aligned} \tag{5.20}$$

This linear transformation in between coordinate systems can be expressed succinctly as

$$\ddot{\mathbf{x}}_{acc} = \mathbf{A}_{acc}\ddot{\mathbf{x}} \quad (5.21)$$

where  $\ddot{\mathbf{x}}$  is the acceleration vector expressed in the Cartesian coordinate frame and  $\ddot{\mathbf{x}}_{acc}$  is the acceleration vector expressed in the sensor coordinate frame. The matrix  $\mathbf{A}_{acc}$  is a function of sensor location and is given by

$$\mathbf{A}_{acc} = \begin{pmatrix} 1 & 0 & 0 & 0 & z_{Ax} & -y_{Ax1} \\ -1 & 0 & 0 & 0 & -z_{Ax} & -y_{Ax2} \\ 0 & -1 & 0 & z_{Ay} & 0 & -x_{Ay} \\ 0 & 0 & -1 & -y_{Az1} & x_{Az1} & 0 \\ 0 & 0 & -1 & -y_{Az2} & -x_{Az2} & 0 \\ 0 & 0 & -1 & y_{Az3} & x_{Az3} & 0 \end{pmatrix} \quad (5.22)$$

$\mathbf{A}_{acc}$  can be inverted to obtain the rigid body acceleration of the stepper in the Cartesian coordinate frame from the measured values. Numerical values for this inverse are given below :

$$\mathbf{A}_{acc}^{-1} = \begin{pmatrix} 0.5000 & -0.5000 & 0 & -0.4526 & 0.4526 & 0 \\ 0.4908 & 0.4908 & -1.0000 & -0.4439 & 0 & 0.4439 \\ 0 & 0 & 0 & 0 & -0.5000 & -0.5000 \\ 0 & 0 & 0 & -1.3484 & 0 & 1.3484 \\ 0 & 0 & 0 & 1.3748 & -1.3748 & 0 \\ -1.3484 & -1.3484 & 0 & 0 & 0 & 0 \end{pmatrix} \quad (5.23)$$

A layout of the active isolation system showing the location of the various sensors and actuators is shown in Figure 5-23. The capacitance probes are actually fixed to the legs, but are shown elsewhere for clarity. Figure 5-24 shows a photograph of the active isolation system assembled to the prototype wafer stepper.

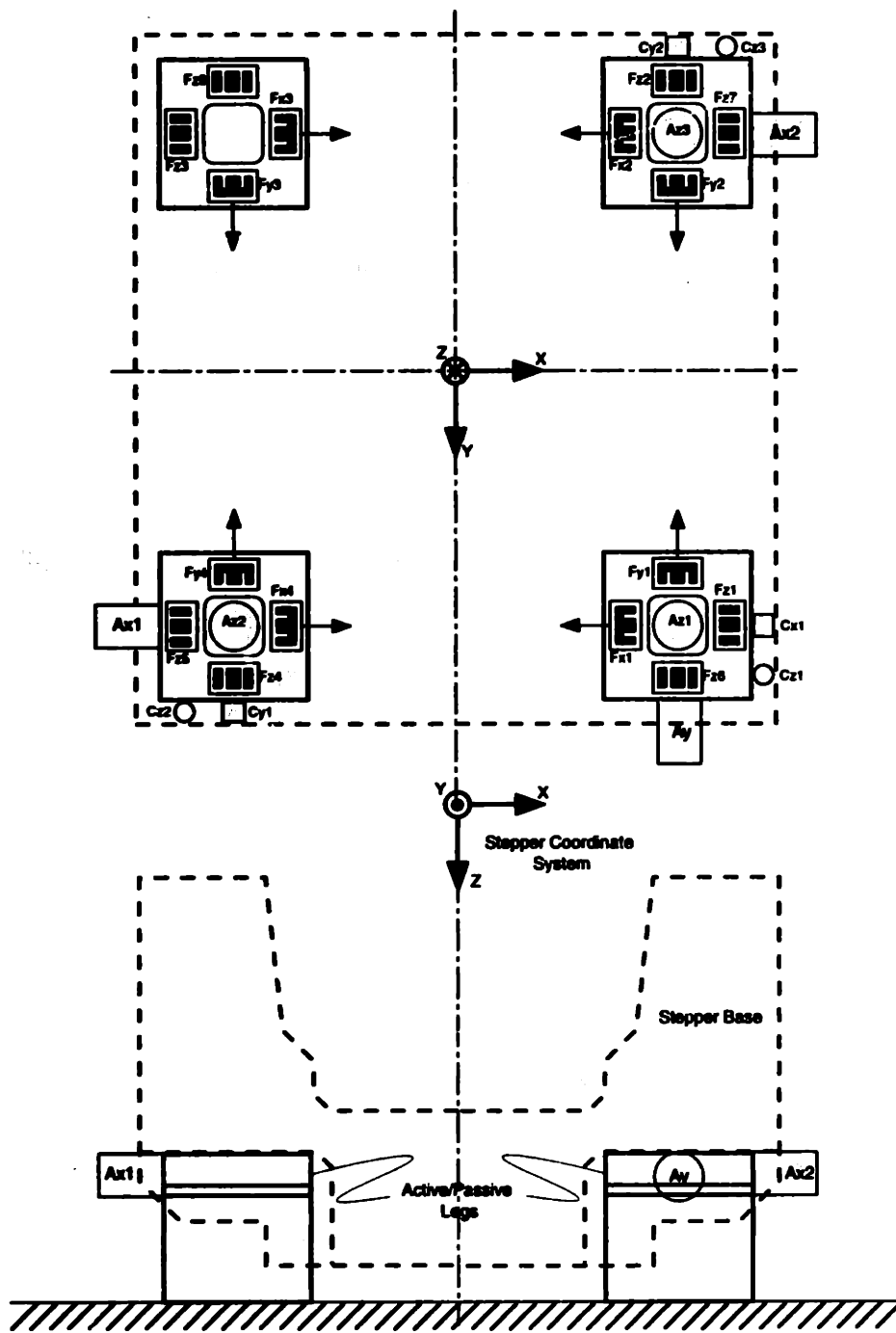
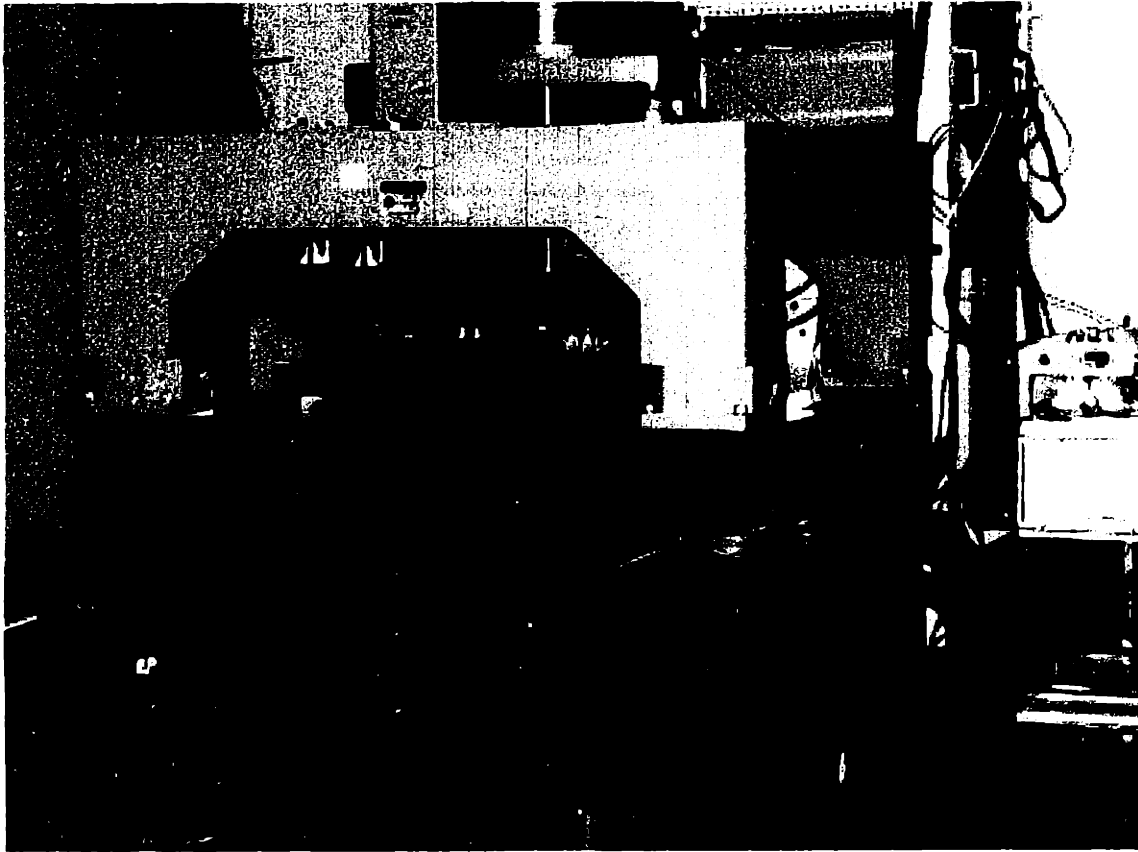


Figure 5-23: Layout of the sensors and actuators for the active isolation system. Capacitance probes are shown mounted away from legs for clarity



**Figure 5-24: Photograph of the four active legs assembled to the prototype wafer stepper**

## 5.7 Summary of Chapter 5

The objective of this chapter is to present the mechanical design of the isolation system for the prototype wafer stepper. Specifically, the passive mounts, actuators and sensors used in the isolation system are discussed in detail. An example is worked out to demonstrate the analysis of passive isolation mounts for machine tools. Locations of the mounts, actuators and sensors are tabulated and used to derive the kinematic relations for the stepper. Various coordinate frames are described and linear transformations derived to relate these. The direct and inverse kinematics problems for the stepper are then expressed in terms of these linear transformations. It should be noted that these linear transformations are derived under the assumption that the stepper is a rigid body and are key to the development of the control methodology outlined in Chapter 6. The amplifiers and filters used in the isolation system are also described.

The rigid body assumption is a false assumption albeit a good one for the frequencies of interest. We consider payload dynamics and the presence of these resonant modes of the machine to develop better control algorithms to ensure optimum isolation in Chapter 7.



# Chapter 6

## Rigid Body Modeling and Control

### 6.1 Introduction

In this chapter, we use the kinematic relations from chapter 5 to derive the rigid body equations of motion of the stepper. Due to the location of the sensors and the actuators, the rigid body degrees of freedom expressed in the Cartesian coordinate system are coupled and hence the control of the stepper turns out to be a coupled MIMO control problem. However, in this chapter, we concern ourselves only with the rigid-body dynamics and control of the stepper and hence have adequate control authority (number of degrees of freedom is equal to the number of actuators). For such a system, we can use decoupling transformations to reduce the MIMO control problem to 6 decoupled SISO control problems. The fine and coarse motion stages are modeled as double integrators.

Transfer functions resulting from the equations of motion are then compared against transfer functions determined experimentally through a system identification procedure. Our approach to compensator design for active isolation was earlier discussed in Chapter 4. Specifically, we apply the  $\mathcal{H}_2$  frequency weighting procedure for a SISO system from Chapter 4 to shape the sensitivity function of the loop. We then discuss controller design for the fine and coarse motion stages which are modeled as double integrators. The feedback control laws are derived using continuous time models and the resulting controllers are implemented using discrete-time equivalents

on a parallel DSP system comprising 8 'C40 DSPs. Figure 6-1 illustrates the sequence

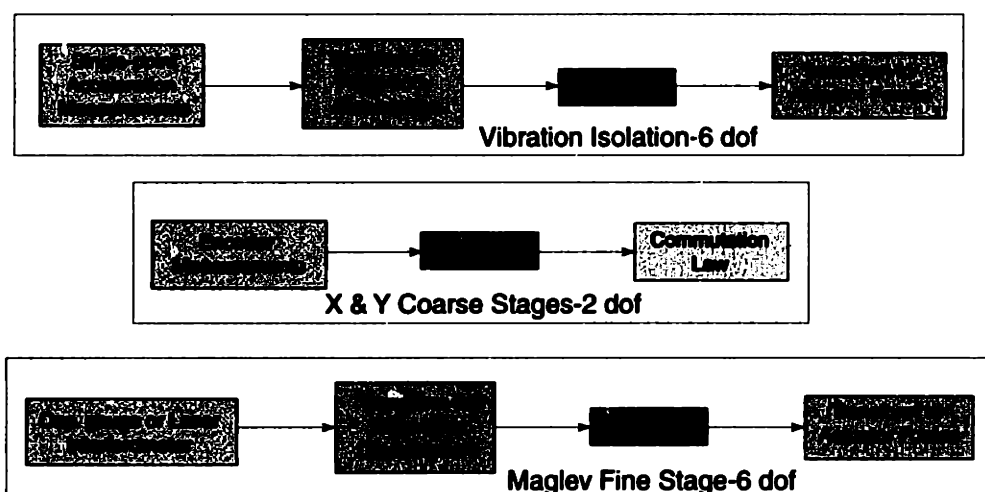


Figure 6-1: Schematic illustrating the sequence of events that take place each sample interval. All the computations illustrated are implemented on a parallel DSP system comprising 8 'C40 DSPs on a VME bus. A total of 14 degrees of freedom are controlled to position the wafer precisely under the optical column.

of events that take place during each sample interval. A total of 14 rigid body degrees of freedom are controlled to position the wafer precisely under the optical column. These are, respectively, the 6 rigid body degrees of freedom of the stepper, 1 each for the X and Y coarse stages, and the 6 rigid body degrees of freedom of the Maglev fine stage.

Key to the design and implementation of the control law is the derivation of the kinematics of the stepper in terms of linear transformations relating the sensor and actuator coordinate frames to the Cartesian coordinate frame. The use of these transformations in the implementation of the control scheme is illustrated in Figure 6-1. We refer back to these transformations as well as transformations used in the implementation of the controller for the Maglev fine stage [83] through the course of the various developments in this chapter.

## 6.2 Rigid Body Modeling

The passive isolation mounts for the isolation system are chosen to obtain natural frequencies over a range of 5-20 Hz when all the components of the stepper are mounted.

For the prototype version of the stepper under consideration, the natural frequencies range from 7-25 Hz due to the absence of components such as the illuminator, auto-focus system, wafer and reticle handling systems.

The vibration isolation project is part of the ISIS platform development effort at Integrated Solutions Inc.<sup>1</sup> The ISIS platform is based on the GCA XLS 7000 series wafer stepper. Specifically, certain key optical components like the lens column, the illuminator and the bridge have been retained from the XLS machine. The major modifications include redesign of the base, complete redesign of the coarse and fine motion stages [83] and the active vibration isolation system.

A series of structural analyzes were performed by Sandia National Labs [65] on the GCA XLS 7000 Series Lithography machine. Excerpts from the Sandia report are reproduced in table 7.1 in chapter 7 where we consider flexibility effects. For the purposes of this chapter, the key result from these analyzes is that the stepper can be safely modeled as a rigid body over frequencies under 80 Hz.

The utility of rigid body modeling is demonstrated by the following discussion. The active control bandwidth of the stepper isolation system is chosen to be between 0.1 and 80 Hz. The lower limit is due to the piezoelectric accelerometers used for feedback (refer to Figure 5-19 for a pictorial representation of the frequency response function (FRF) of the piezoelectric accelerometers used in this study) while the upper limit is due to the elastic modes of the lens column. This provides about two decades of active isolation. For example, with a mount natural frequency of about 10 Hz we can obtain 40 dB attenuation (or 99 % isolation efficiency) due to passive isolation at 100 Hz. Active control at higher bandwidths causes the performance of the isolation system to deteriorate due to increased noise sensitivity at these higher frequencies. Hence, the rigid body assumption does not limit the performance of the isolation system significantly and forms a useful study to establish various figures of merit about the mechanical system design.

The coarse and fine stages are all modeled as masses and inertias for the purpose of this chapter. Williams [83] has measured the first resonant mode for the coarse

---

<sup>1</sup>now Ultratech Stepper Inc.

stages to be around 120 Hz and the fine stage frame to be around 550 Hz. Hence, they can be modeled as rigid bodies for frequencies under 80 Hz.

### 6.2.1 Equations of Motion

Since the principal axes of inertia of the stepper are, respectively, parallel to the principal elastic axes of the elastomeric mounts we can ignore the products of inertia of the rigid body. Symmetry of the stepper and the passive mounts can be used to simplify the rigid body model. We can use symmetry arguments to decouple motions in the X-Z plane from those in the Y-Z plane. Under these conditions, the X and  $\theta_y$  degrees of freedom are coupled and so are the Y and  $\theta_x$  degrees of freedom. The Z and  $\theta_z$  degrees of freedom are largely decoupled from the other degrees of freedom due to symmetry. The stepper can then be modeled in a plane as illustrated by the three degree of freedom system in Figure 6-2. Assuming small motions, we can write

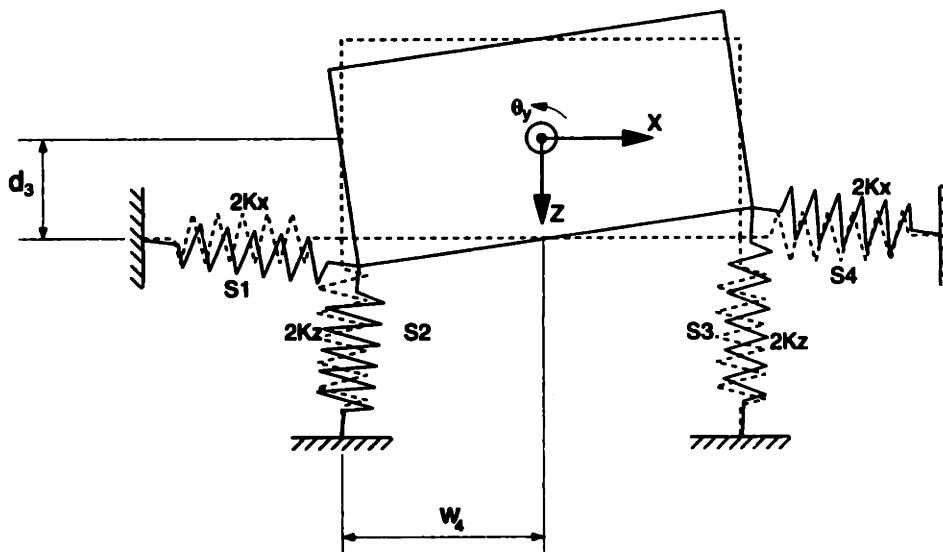


Figure 6-2: Displaced three degree of freedom rigid body model in the X-Z plane. The dampers are assumed to be in parallel with the springs and are not shown.

the equations of motion as follows :

$$\begin{aligned}
 M\ddot{x} + 4C_x\dot{x} + 4K_x x + 4d_3C_x\dot{\theta}_y + 4d_3K_x\theta_y &= F_x \\
 M\ddot{z} + 4C_z\dot{z} + 4K_z z &= F_z \\
 I_{yy}\ddot{\theta}_y + 4d_3C_x\dot{x} + 4d_3K_x x + 4(d_3^2C_x + w_4^2C_z)\dot{\theta}_y + 4(d_3^2K_x + w_4^2K_z)\theta_y &= \tau_y
 \end{aligned}$$

For the system illustrated in Figure 6-2, the rotational and lateral translation modes are coupled. This leads to two modes - one, a low frequency mode where the stepper rocks about an axis below the elastic axis and two, a high frequency mode where the stepper rocks about an axis close to its center of gravity. A similar modeling approach applied to the  $Y$ , and  $\theta_x$  degrees of freedom in the  $Y$ - $Z$  plane leads to another set of coupled equations. For the  $\theta_z$  degree of freedom, we consider the rotational system shown in Figure 6-3. Assuming small motions, we can write the  $\theta_z$  equation of motion

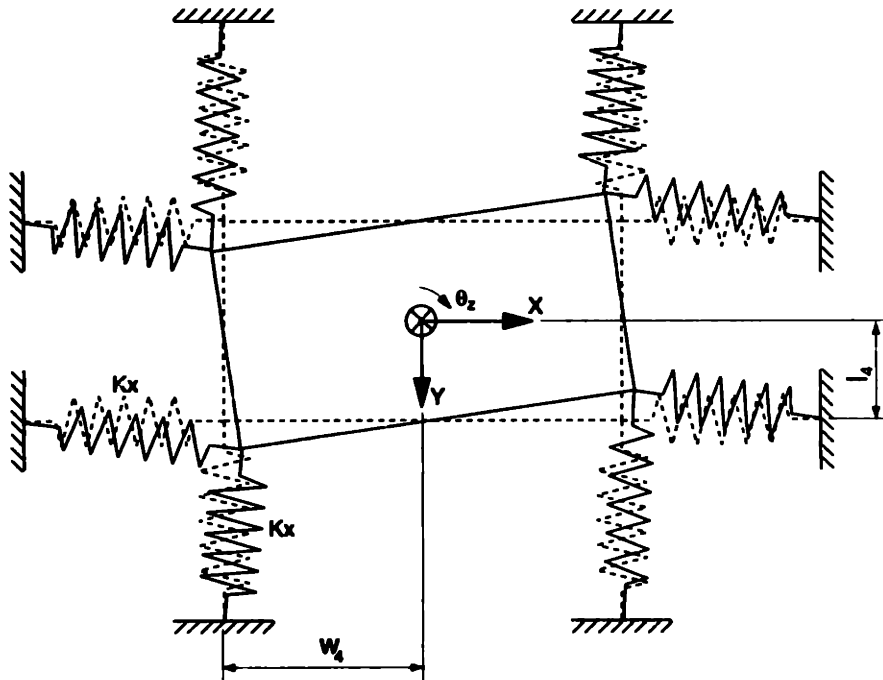


Figure 6-3: Displaced rotational system in the  $X$ - $Y$  plane. The dampers are assumed to be in parallel with the springs and are not shown.

as follows :

$$I_{zz}\ddot{\theta}_z + 4(w_4^2 + l_4^2)C_x\dot{\theta}_z + 4(w_4^2 + l_4^2)K_x\theta_z = \tau_z$$

We assemble all the six rigid body equations of motion to get the following coupled system of equations.

$$\begin{aligned}
M\ddot{x} + 4C_x\dot{x} + 4K_x x + 4d_3C_x\dot{\theta}_y + 4d_3K_x\theta_y &= F_x \\
M\ddot{y} + 4C_x\dot{y} + 4K_x y - 4d_3C_x\dot{\theta}_x - 4d_3K_x\theta_x &= F_y \\
M\ddot{z} + 4C_z\dot{z} + 4K_z z &= F_z \\
I_{xx}\ddot{\theta}_x - 4d_3C_x\dot{y} - 4d_3K_x y + 4(d_3^2C_x + l_4^2C_z)\dot{\theta}_x + 4(d_3^2K_x + l_4^2K_z)\theta_x &= \tau_x \quad (6.1) \\
I_{yy}\ddot{\theta}_y + 4d_3C_x\dot{x} + 4d_3K_x x + 4(d_3^2C_x + w_4^2C_z)\dot{\theta}_y + 4(d_3^2K_x + w_4^2K_z)\theta_y &= \tau_y \\
I_{zz}\ddot{\theta}_z + 4(w_4^2 + l_4^2)C_x\dot{\theta}_z + 4(w_4^2 + l_4^2)K_x\theta_z &= \tau_z
\end{aligned}$$

Numerical values for the inertial parameters of the stepper are tabulated in Table 5.1.  $K_z$  is the longitudinal (Z-direction) stiffness of the mount and  $K_x$  the lateral stiffness with  $C_z$  and  $C_x$  being the corresponding damping terms.  $w_4$ ,  $l_4$  and  $d_3$  are the distances of the mounts from the centroidal coordinate frame of the stepper in the X, Y and Z directions respectively. Numerical values for the mount parameters and locations are given in table 5.3 and table 5.4 respectively.

As noted in Chapter 5, there is significant coupling between the various rigid body degrees of freedom due to the offset of the mounting plane and the lack of alignment of the mount axes with the center of gravity. This coupling leads us to pursue multi-variable control design techniques. The simplest approach to multi-variable control is through decoupling transformations. This involves identifying the natural modes of the system and performing control in these modal coordinates. To preface a control implementation we first establish a set of decoupling coordinate transformations.

## 6.2.2 Modal Coordinates

The rigid body equations of motion for the stepper can be expressed in a concise matrix form as follows :

$$M\ddot{\mathbf{x}} + C\dot{\mathbf{x}} + K\mathbf{x} = \mathbf{f} \quad (6.2)$$

The control vector  $\mathbf{f}$  needs to be computed according to some feedback law. Computation of the control vector can be complicated by the coupling in the equations of motion. This computation can be significantly simplified by transforming to a modal coordinate frame where the equations of motion are decoupled to give us 6 SISO systems. To establish the modal coordinate frame, we solve the eigenvalue problem for the undamped, unforced system

$$\mathbf{M}\ddot{\mathbf{x}} + \mathbf{K}\mathbf{x} = \mathbf{0} \quad (6.3)$$

The natural frequencies,  $\lambda_i = \omega_i^2$  and mode shapes  $\mathbf{v}_i$  (the subscripts correspond to the  $i^{\text{th}}$  natural mode) are obtained from the solution of the above problem. The modal matrix  $\mathbf{V}$  is obtained by setting its columns to the modes  $\mathbf{v}_i$ . With independent modes, we can now diagonalize the equations of motion using the following transformation.

$$\begin{aligned} \mathbf{x} &= \mathbf{V}\boldsymbol{\eta} \\ \Rightarrow \boldsymbol{\eta} &= \mathbf{V}^{-1}\mathbf{x} \end{aligned} \quad (6.4)$$

Expressing the equations of motion in terms of the modal coordinates  $\boldsymbol{\eta}$  and premultiplying by  $\mathbf{V}^T$ , we obtain the modal equations of motion

$$\begin{aligned} \mathbf{V}^T\mathbf{M}\mathbf{V}\ddot{\boldsymbol{\eta}} + \mathbf{V}^T\mathbf{C}\mathbf{V}\dot{\boldsymbol{\eta}} + \mathbf{V}^T\mathbf{K}\mathbf{V}\boldsymbol{\eta} &= \mathbf{V}^T\mathbf{f} \\ \Rightarrow \mathbf{M}_m\ddot{\boldsymbol{\eta}} + \mathbf{C}_m\dot{\boldsymbol{\eta}} + \mathbf{K}_m\boldsymbol{\eta} &= \mathbf{f}_m \end{aligned} \quad (6.5)$$

where we have defined the following modal matrices :

$$\begin{aligned} \mathbf{M}_m &= \mathbf{V}^T\mathbf{M}\mathbf{V} \\ \mathbf{C}_m &= \mathbf{V}^T\mathbf{C}\mathbf{V} \\ \mathbf{K}_m &= \mathbf{V}^T\mathbf{K}\mathbf{V} \\ \mathbf{f}_m &= \mathbf{V}^T\mathbf{f} \end{aligned} \quad (6.6)$$

We further note that the mode shapes are orthogonal with respect to the mass and stiffness matrices thus making the modal mass and stiffness matrices  $\mathbf{M}_m$  and  $\mathbf{K}_m$  diagonal. However, the modal damping matrix is not diagonal since the eigenvectors are not guaranteed to be orthogonal to it except in special cases. We make one further assumption and consider only the diagonal entries of the modal damping matrix. This is similar to modal damping where a damping ratio is assigned to each mode.

Equation (6.5) is a set of six decoupled second-order equations for which SISO controllers can readily be implemented. This approach to control is termed as Independent Modal Space Control (IMSC). Meirovitch [47], [44] presents a good review of IMSC and its robustness properties. The characteristic of IMSC is that the eigenvalues of the open-loop system are modified while the eigenvectors are retained. A solution to this problem always exists when the number of actuators is equal to the number of degrees of freedom (six in our case). However, this is not guaranteed when there are more degrees of freedom than actuators as is always true in physical systems when flexibility is considered. It will be shown in chapter 7 that the open-loop eigenvectors may not be an optimal choice and that performance improvement can be obtained by requiring closed-loop eigenvectors to be different from the open-loop ones. For the purposes of this chapter where only rigid body modes are identified and controlled IMSC forms a good control technique. We discuss how the modal coordinate frame can be used along with the coordinate transformations derived in chapter 5 to lead a set of decoupling transformations.

## 6.3 Coordinate Frames

In this section, we formalize our discussion of coordinate frames before deriving the control laws. From our discussions in the previous section and chapter 5, there are four coordinate frames of interest.

- Sensor coordinate frame
- Actuator coordinate frame



- Stepper (Cartesian) coordinate frame
- Control (Modal) coordinate frame

We invert (5.5) from chapter 5 to get

$$\mathbf{f}_{act} = \mathbf{F}_{act}^{-1} \mathbf{f}$$

where  $\mathbf{F}_{act}^{-1}$  is the pseudo-inverse of  $\mathbf{F}_{act}$ . This transformation is cascaded with the transformation relating the Cartesian coordinate frame to the modal coordinate frame to express the actuator forces directly in terms of the modal forces.

$$\mathbf{f}_{act} = \mathbf{F}_m \mathbf{f}_m \quad (6.7)$$

The transformation matrix  $\mathbf{F}_m$  relating the force vector in the modal coordinate frame  $\mathbf{f}_m$  and the force vector in the actuator coordinate  $\mathbf{f}_{act}$  is given by

$$\mathbf{F}_m = \mathbf{F}_{act}^{-1} \mathbf{V}^{-T} \quad (6.8)$$

Similarly, the sensor coordinate frame can be related to the modal coordinate frame so that the feedback acceleration signals are expressed in the modal coordinate frame. This is accomplished using

$$\ddot{\boldsymbol{\eta}} = \mathbf{A}_m \ddot{\mathbf{x}}_{acc} \quad (6.9)$$

where  $\ddot{\boldsymbol{\eta}}$  is the acceleration vector expressed in the modal coordinate frame and  $\ddot{\mathbf{x}}_{acc}$  is the acceleration vector expressed in the sensor coordinate frame. The transformation matrix  $\mathbf{A}_m$  relating the two is given by

$$\mathbf{A}_m = \mathbf{V}^{-1} \mathbf{A}_{acc}^{-1} \quad (6.10)$$

We now have the six decoupled equations of motion and the means to relate the decoupled acceleration and control forces to the measured acceleration and applied

control forces. The IMSC control problem then amounts to that of isolating six single degree of freedom systems individually. We do this using dynamic compensators, however, we preface the development of the compensators by experimental verification of our model using a system identification procedure.

## 6.4 System Identification

A swept sine system identification is performed to measure the various transfer functions. From the equations of motion in (6.2), we observe that the ten transfer functions in (6.12) are of importance.

$$\begin{aligned}
\frac{\ddot{x}(s)}{F_x(s)} &= \frac{s^2[I_{yy}s^2 + C_{xr}s + K_{xr}]}{[Ms^2 + 4C_x s + 4K_x][I_{yy}s^2 + C_{xr}s + K_{xr}] - 16(d_3C_x s + d_3K_x)^2} \\
\frac{\ddot{x}(s)}{\tau_y(s)} &= -\frac{4s^2(d_3C_x s + d_3K_x)}{[Ms^2 + 4C_x s + 4K_x][I_{yy}s^2 + C_{xr}s + K_{xr}] - 16(d_3C_x s + d_3K_x)^2} \\
\frac{\ddot{y}(s)}{F_y(s)} &= \frac{s^2[I_{xx}s^2 + C_{yr}s + K_{yr}]}{[Ms^2 + 4C_x s + 4K_x][I_{xx}s^2 + C_{yr}s + K_{yr}] - 16(d_3C_x s + d_3K_x)^2} \\
\frac{\ddot{y}(s)}{\tau_x(s)} &= \frac{4s^2(d_3C_x s + d_3K_x)}{[Ms^2 + 4C_x s + 4K_x][I_{xx}s^2 + C_{yr}s + K_{yr}] - 16(d_3C_x s + d_3K_x)^2} \\
\frac{\ddot{z}(s)}{F_z(s)} &= \frac{s^2}{Ms^2 + 4C_z s + 4K_z} \\
\frac{\ddot{\theta}_x(s)}{F_y(s)} &= \frac{4s^2(d_3C_x s + d_3K_x)}{[Ms^2 + 4C_x s + 4K_x][I_{xx}s^2 + C_{yr}s + K_{yr}] - 16(d_3C_x s + d_3K_x)^2} \\
\frac{\ddot{\theta}_x(s)}{\tau_x(s)} &= \frac{s^2[Ms^2 + 4C_x s + 4K_x]}{[Ms^2 + 4C_x s + 4K_x][I_{xx}s^2 + C_{yr}s + K_{yr}] - 16(d_3C_x s + d_3K_x)^2} \\
\frac{\ddot{\theta}_y(s)}{F_x(s)} &= -\frac{4s^2(d_3C_x s + d_3K_x)}{[Ms^2 + 4C_x s + 4K_x][I_{yy}s^2 + C_{xr}s + K_{xr}] - 16(d_3C_x s + d_3K_x)^2} \\
\frac{\ddot{\theta}_y(s)}{\tau_y(s)} &= \frac{s^2[Ms^2 + 4C_x s + 4K_x]}{[Ms^2 + 4C_x s + 4K_x][I_{yy}s^2 + C_{xr}s + K_{xr}] - 16(d_3C_x s + d_3K_x)^2} \\
\frac{\ddot{\theta}_z(s)}{\tau_z(s)} &= \frac{s^2}{I_{zz}s^2 + 4(w_4^2 + l_4^2)C_x s + 4(w_4^2 + l_4^2)K_x}
\end{aligned} \tag{6.11}$$

where we have defined,

$$\begin{aligned}
 C_{xr} &= 4(d_3^2 C_x + w_4^2 C_z) \\
 K_{xr} &= 4(d_3^2 K_x + w_4^2 K_z) \\
 C_{yr} &= 4(d_3^2 C_x + l_4^2 C_z) \\
 K_{yr} &= 4(d_3^2 K_x + l_4^2 K_z)
 \end{aligned}
 \tag{6.12}$$

A swept sine test is performed on the prototype wafer stepper to obtain the transfer functions in (6.12) using the HP35670A dynamic signal analyzer as illustrated in Figure 6-4. The source signal from the spectrum analyzer is a voltage and is converted

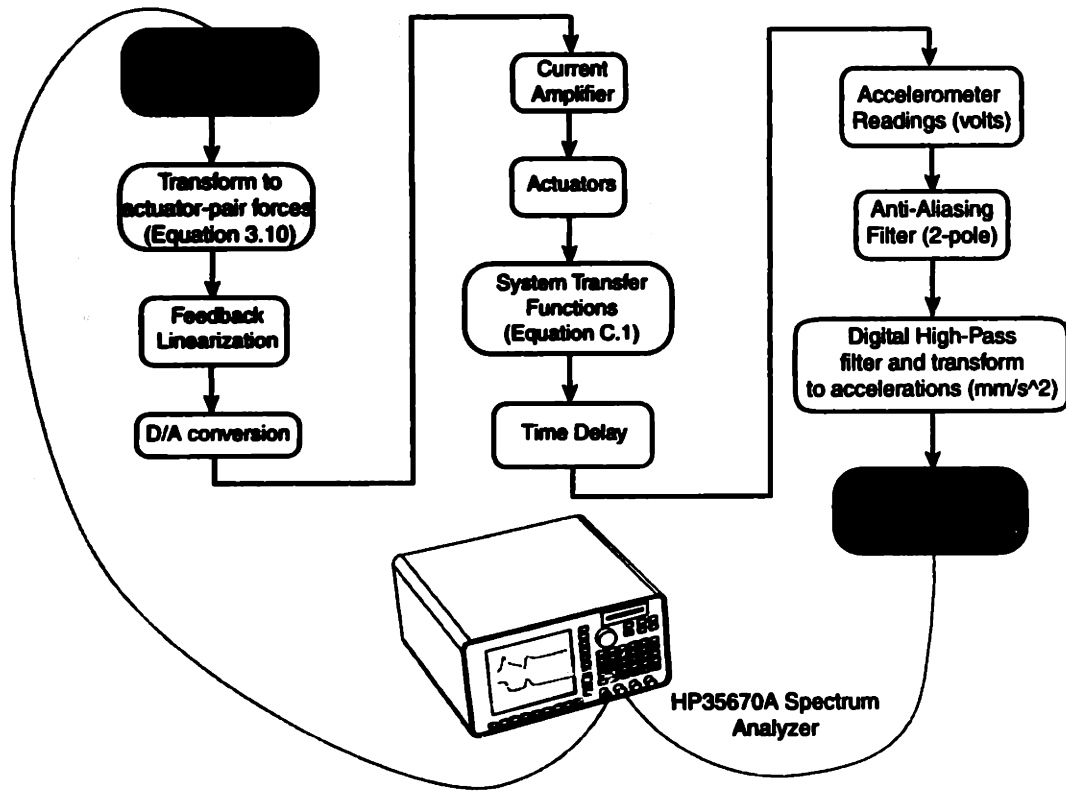


Figure 6-4: System identification setup. Both forces and acceleration are in the Cartesian coordinate frame to obtain the transfer functions listed in (6.12).

by code residing on the DSPs to a force/torque in the Cartesian coordinate system. The transformations given in (5.5) are then used to convert these rigid body forces into actuator-pair forces. Feedback linearization (5.7) is used to compute the appropriate currents for the individual actuators. These currents are applied to the various

amplifiers using the DACs to excite the system. During the next sample interval, the resulting acceleration as measured by the pointwise accelerometers is read. Note that this acceleration is passed through the two pole Sallen-Key filter illustrated in Figure 5-21. The acceleration is also passed through a digital bandpass filter implemented as an IIR filter in the DSP code. The accelerometer readings are then used to compute the rigid body acceleration of the stepper using the transformations in (5.21). This acceleration is then output as a voltage on a spare DAC channel and read back into the spectrum analyzer.

The delay of one sample interval experienced by the identification loop is modeled using a (1,1) Pade approximant [25]. For a time delay of  $T_d$  seconds, this is given by,

$$e^{-T_d s} \approx \frac{1 - (T_d s/2)}{1 + (T_d s/2)} \quad (6.13)$$

The overall transfer function of the mechanical system is computed from the equations of motion in (6.2), the sensitivity of the accelerometers and the time delay. This is compared with experimental measurements in Figures 6-5 through 6-14. The loss

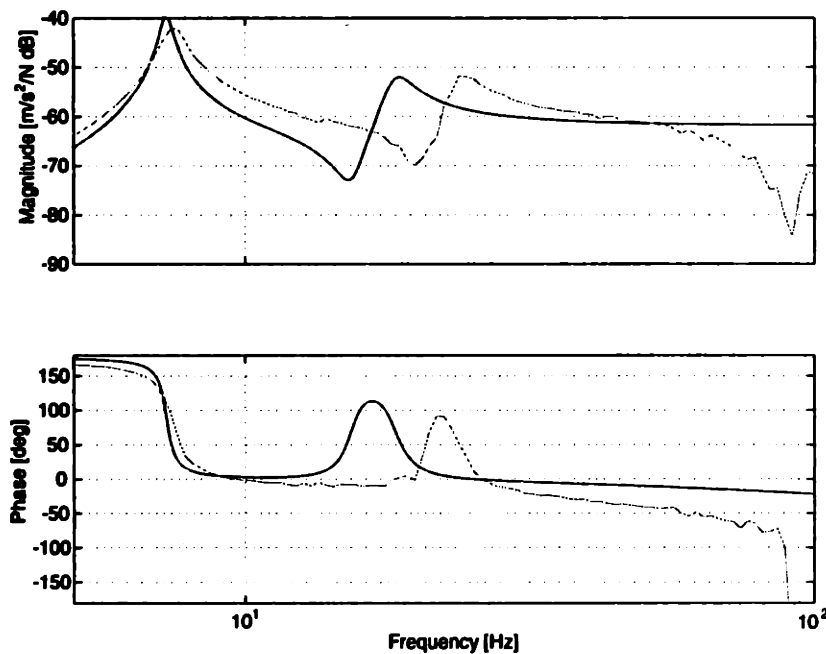


Figure 6-5: Transfer function  $\ddot{x}/F_x$

of phase in the experimental plots is clearly seen. In fact, the system identification

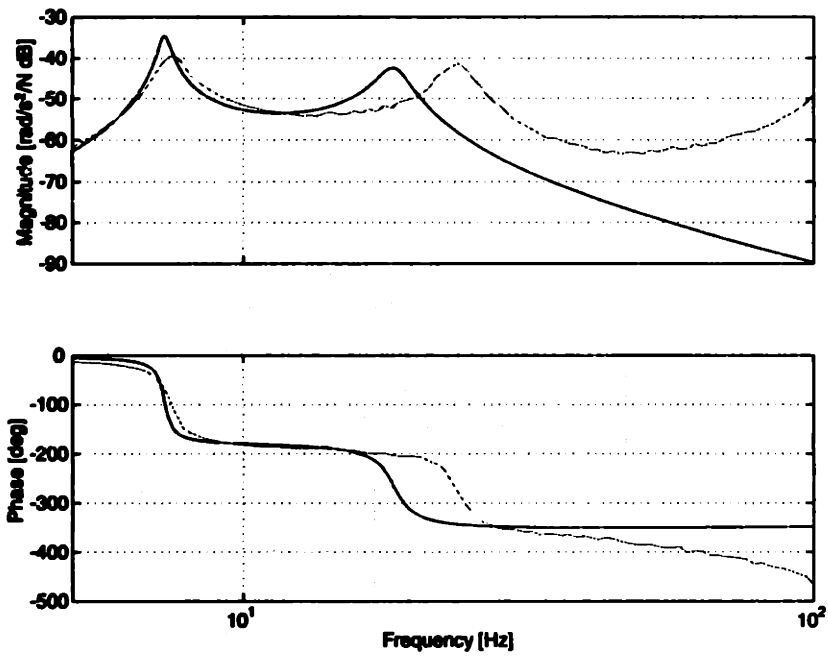


Figure 6-6: Transfer function  $\dot{\theta}_y/F_x$

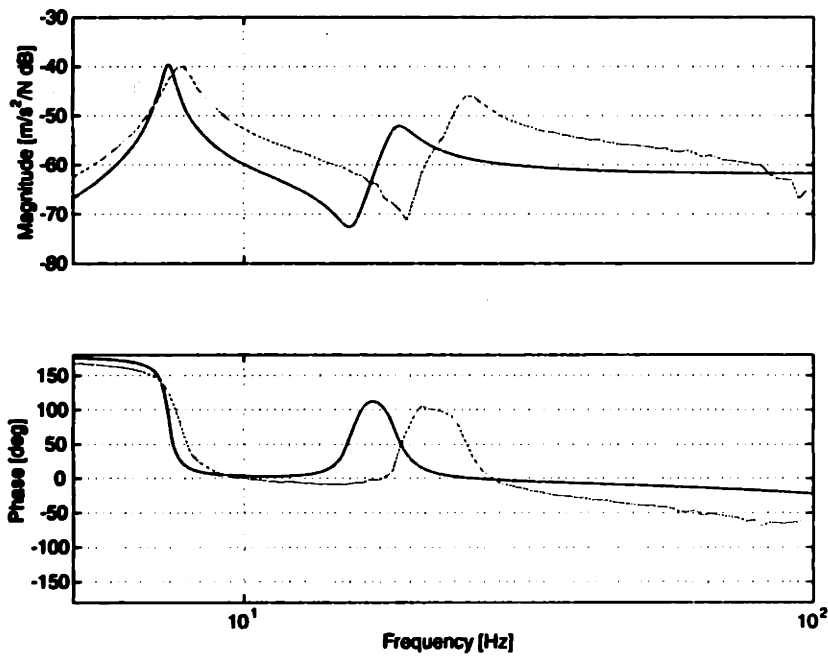


Figure 6-7: Transfer function  $\ddot{y}/F_y$

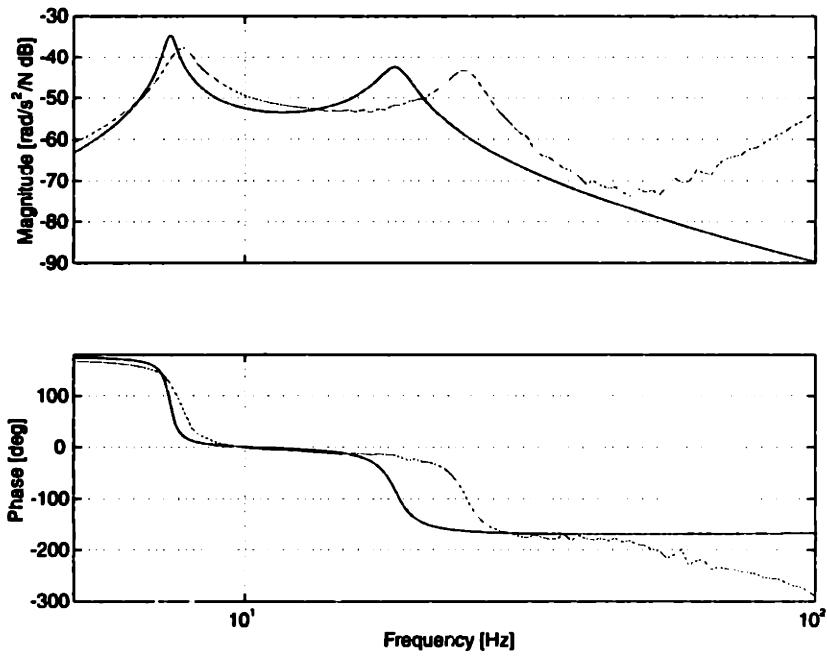


Figure 6-8: Transfer function  $\ddot{\theta}_x/F_y$

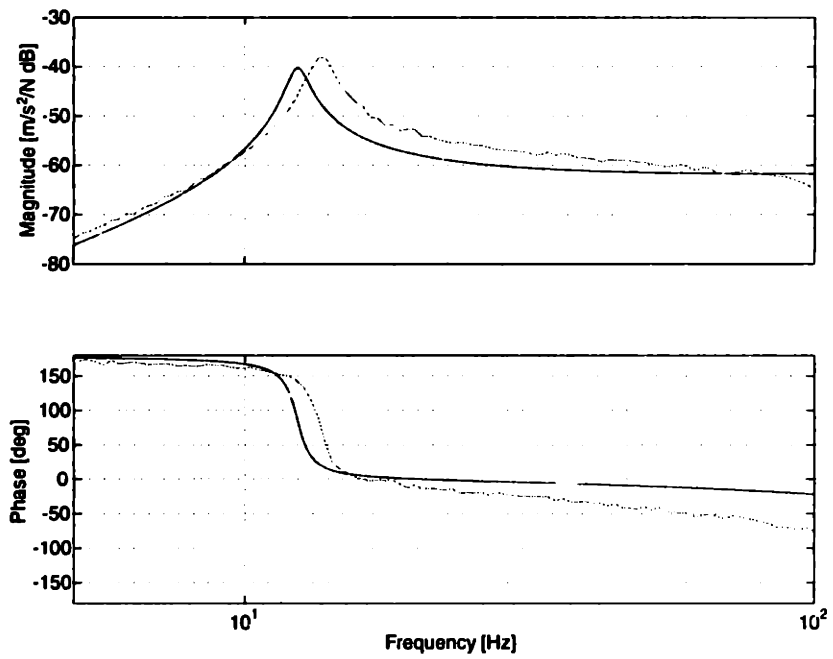


Figure 6-9: Transfer function  $\ddot{z}/F_z$

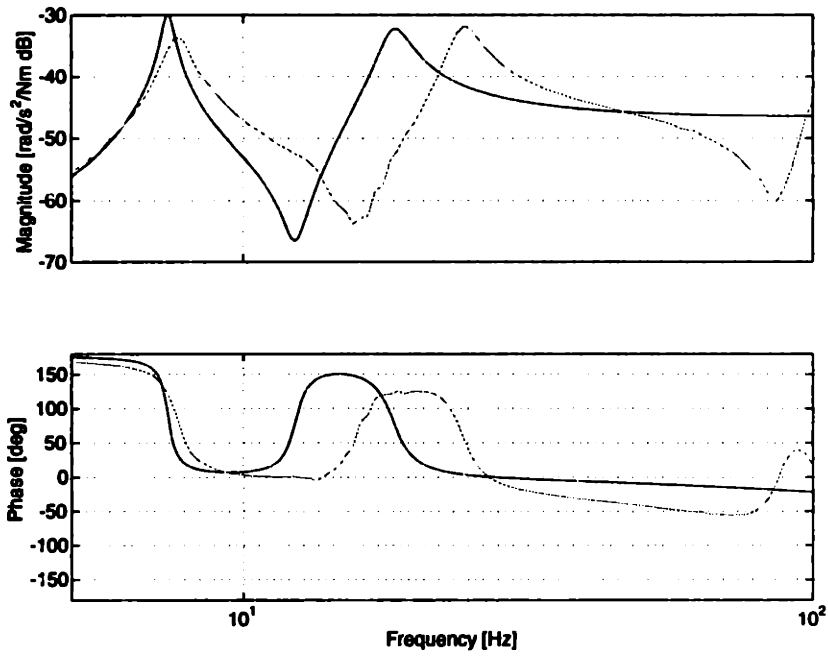


Figure 6-10: Transfer function  $\ddot{\theta}_x/\tau_x$

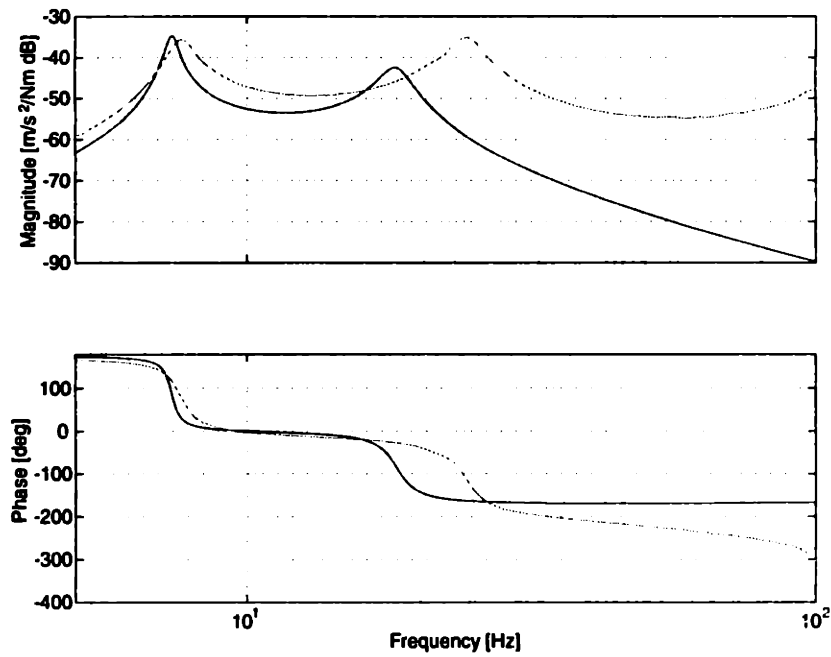


Figure 6-11: Transfer function  $\ddot{y}/\tau_x$

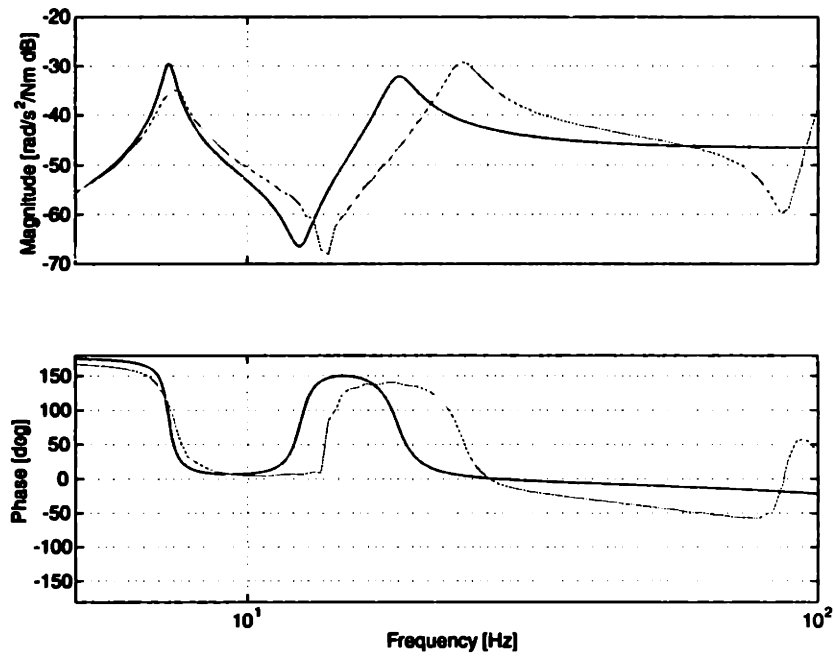


Figure 6-12: Transfer function  $\ddot{\theta}_y/\tau_y$

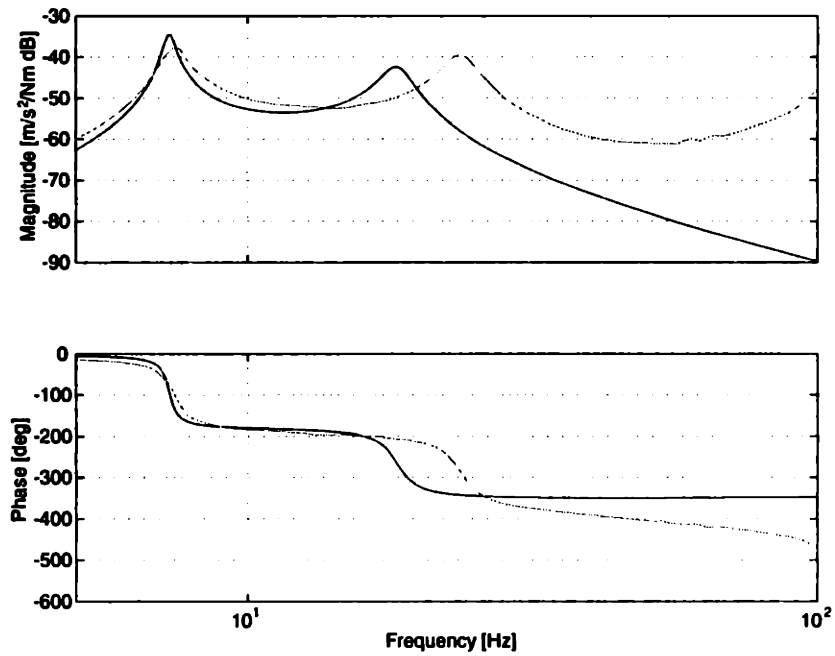


Figure 6-13: Transfer function  $\ddot{x}/\tau_y$



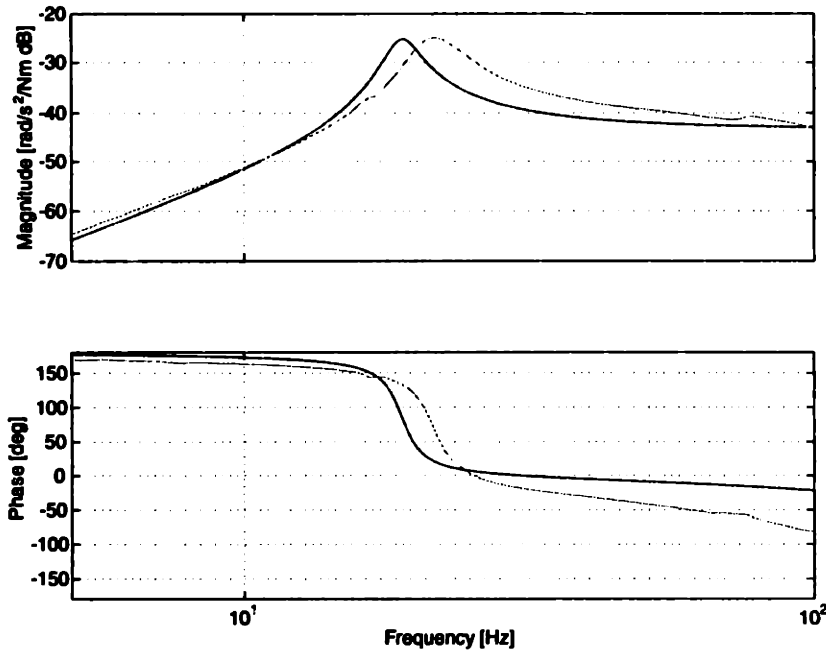


Figure 6-14: Transfer function  $\ddot{\theta}_z/\tau_z$

results led to the discovery of the problem of phase loss in the accelerometers. This phase loss along with the flexible modes of the lens column (which can be observed in the experimentally determined transfer function plots) limits the bandwidth of the closed-loop system. It is additionally seen that the model and the experimental plots compare favorably at low frequencies while the unmodeled modes lead to poor correlation at higher frequencies.

As a final check, we compare the time domain response of the stepper when the X-coarse stage is moved according to a triangular velocity profile. The resulting disturbance force on the stepper is used to simulate the first transfer function from (6.12) to obtain the  $\ddot{x}$  acceleration of the stepper. An excellent match between the simulation and the experimentally measured acceleration profile of the stepper is obtained. This confirms the fact that we have good low-frequency models of the stepper. Having obtained the models and confirmed their veracity through experiment, we are now ready to design control laws for the stepper and the stages.

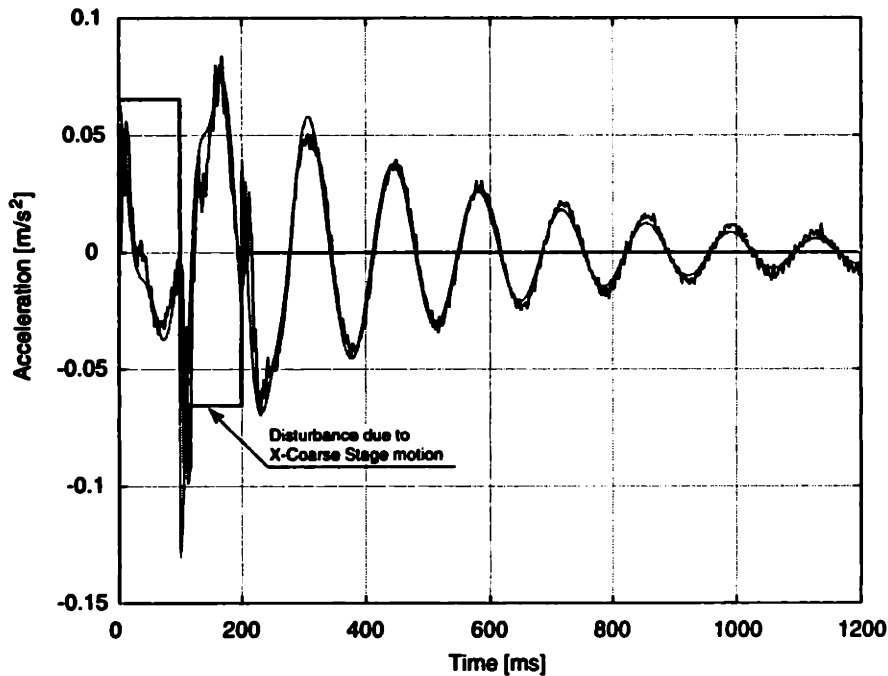


Figure 6-15: Time domain simulation of the transfer function  $\dot{x}/F_x$  compared to measured acceleration of the stepper when the X Coarse stage motion is profiled according to a triangular velocity law.

## 6.5 Control

As shown in Figure 6-1, there are three different sets of control laws, one each for the fine motion stage, the coarse motion stages, and the isolation system. We discuss the design and implementation of the control laws in this section.

### 6.5.1 Fine Motion Stage

The fine motion stage is modeled as a double integrator with the inertial properties given in Table 5.2. The products of inertia of the fine motion stage are negligible and hence the principal axes are aligned with the Cartesian frame in which the actuator forces lie. Hence, controllers are designed for 6 different SISO loops. Since we have a double integrator as the plant, a lead-lag compensation scheme is chosen to give us good phase margin ( $> 45$  degrees) and gain margin ( $> 20$  dB). A crossover frequency of 100 Hz is chosen as illustrated by Figure 6-16. This is well below the first resonant mode of 550 Hz for the fine stage. The lag compensator is a pure integrator to obtain

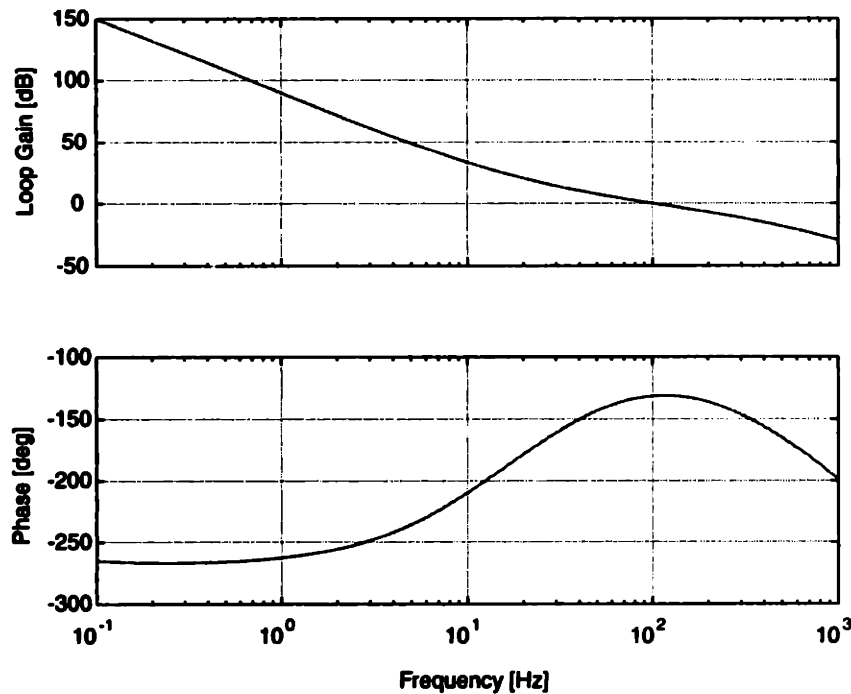


Figure 6-16: Loop transmission for the fine stage using a lead-lag compensation law. Note the crossover frequency of 100 Hz.

zero steady state error. The remainder of the poles and zeros of the lead-lag compensator are placed to maximize the phase lead at the desired crossover frequency [25]. In addition, the sensitivity or the error function of the loop is plotted in Figure 6-17. This transfer function relates the error in the loop to the reference signal. Of particular interest to us is the error around the lens column resonance of 84 Hz. It is seen that the error function has a magnitude of around -5 dB around this resonance and hence the tracking performance of the fine stage at this frequency is rather poor. Thus, the fine stage can not really track the oscillatory motions of the lens column due to its natural vibrations which could be induced by either seismic vibrations or stage motions. One could either notch the error function at this frequency or control the entire wafer stepper in such a manner that this resonant mode of the lens column does not get excited. We follow the latter approach in Chapters 7 and 8.

Finally, we compare the step response of the fine stage with the predicted value for a step motion of  $100 \mu\text{m}$  in the X-direction. Except for a small phase delay due to one sample interval, it is seen that the experimentally determined step response matches

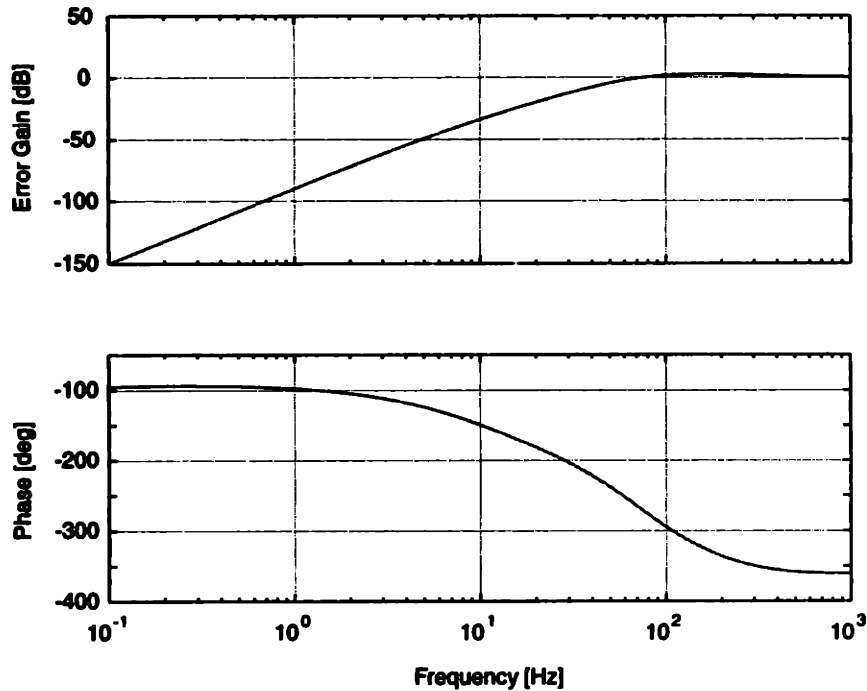


Figure 6-17: Error function for the fine motion stage.

closely with the predicted step response. There are four different controllers to be designed for the fine stage, one for the X,Y, and Z translational axes and one each for the  $\theta_x$ ,  $\theta_y$ , and  $\theta_z$  axes. It should be noted that only the gain scales with the inertia for the different axes since the crossover frequency and hence the position of the poles and zeros of the lead-lag compensators are all similar. Finally, the controllers are implemented in assembly language on the C-40 DSP as second-order sections. Given that a lead-lag compensator can be described in the frequency domain as

$$D(z) = \frac{b[0]z^2 + b[1]z + b[2]}{z^2 + a[1]z + a[2]} \quad (6.14)$$

with  $a[0]$  normalized to one, the order in which the coefficients are arranged for implementation as a second-order biquad is

$$-a[2] \quad b[2] \quad -a[1] \quad b[1] \quad b[0] \quad (6.15)$$

These coefficients are programmed into the appropriate DSP. Implementation issues are discussed in a later section.

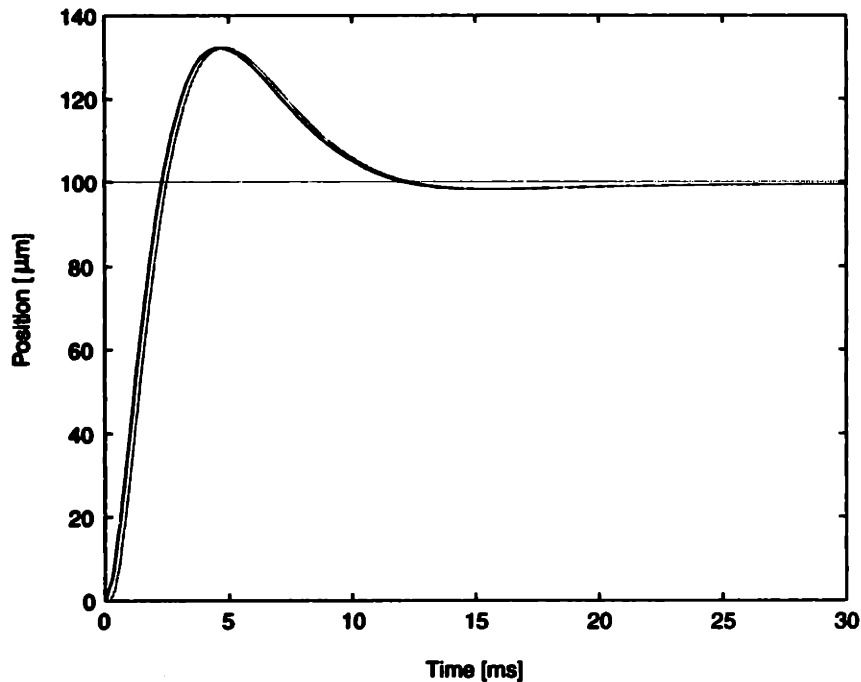


Figure 6-18: Comparison of experimental and predicted step responses. Note the close match in between the two. The small phase delay is attributed to a one sample interval delay.

### 6.5.2 Coarse Motion Stages

The X and Y coarse motion stages are also modeled as double integrators with the inertial properties given in Table 5.2. While the Y coarse stage is about three times more massive than the X coarse stage, the same linear motors and amplifiers drive both stages. To avoid problems with saturation, we choose a bandwidth of 80 Hz for the X coarse stage and 50 Hz for the Y coarse stage. Lead-lag compensators similar to those for the fine stage are designed to give us good phase margin ( $> 45$  degrees) and gain margin ( $> 20$  dB). The loop gain for the Y coarse motion stage is plotted in Figure 6-19. The crossover frequency is well below the first resonant mode of 120 Hz for the Y coarse motion stage. The lag compensator is again a pure integrator to ensure zero steady state error. The remainder of the poles and zeros of the lead-lag compensator are placed to maximize the phase lead at the desired crossover frequency [25] as before. The error function of the loop is plotted in Figure 6-20. Again, the error function illustrates the tracking capabilities of the stage. However, the tracking of the coarse stage is not of primary importance, since the fine stage

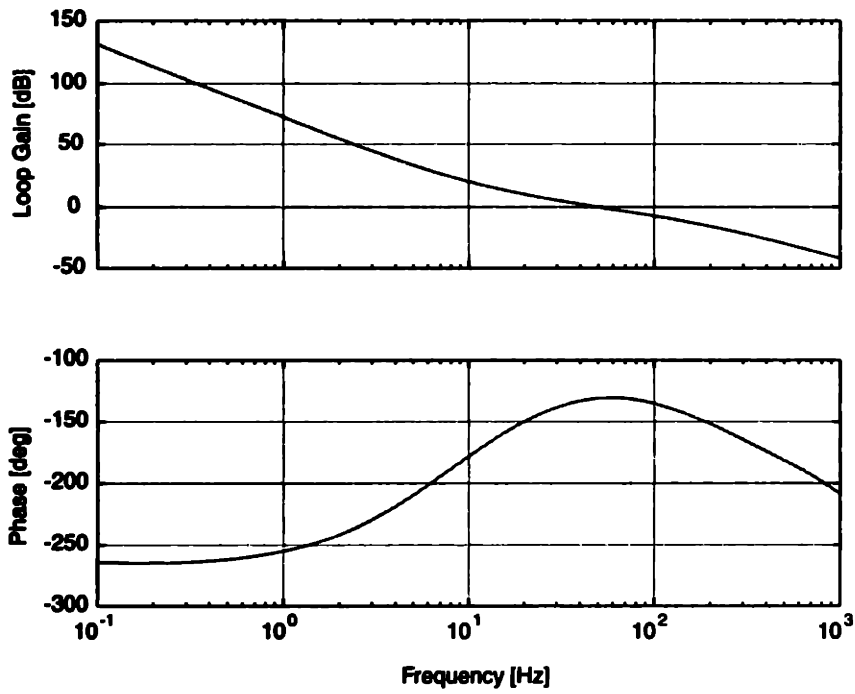


Figure 6-19: Loop transmission for the Y coarse motion stage using a lead-lag compensation law. Note the crossover frequency of 50 Hz.

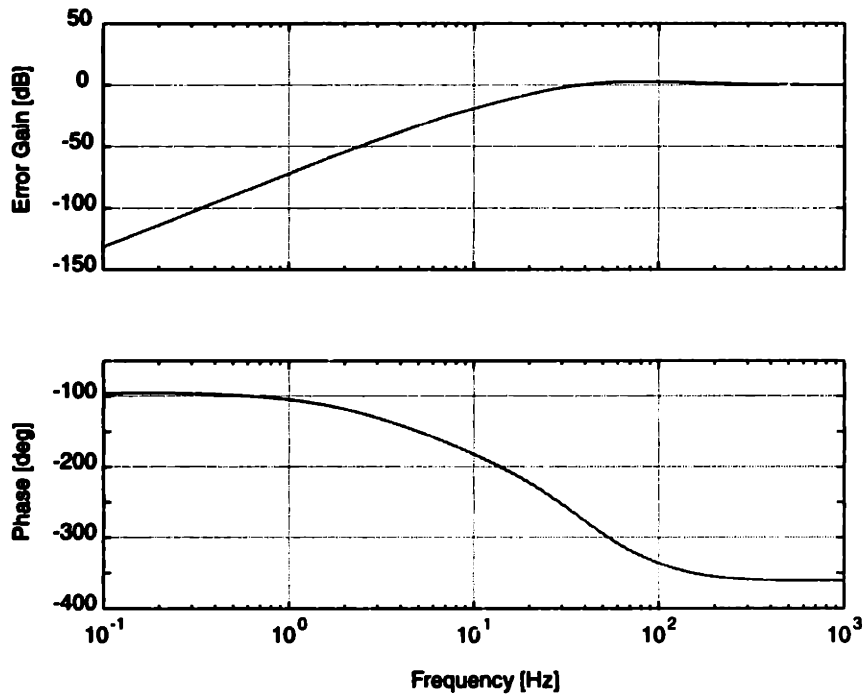


Figure 6-20: Error function for the Y coarse motion stage.

stacked on top of the coarse stage has higher bandwidth and can track better.

Finally, we compare the transient response of the Y coarse motion stage with the predicted value for a step motion of 20 mm in the Y-direction. This step motion is profiled according to a triangular velocity law. Except for a small phase delay due to one sample interval, it is again seen that the experimentally determined transient response matches closely with the predicted response. The controllers for the X and

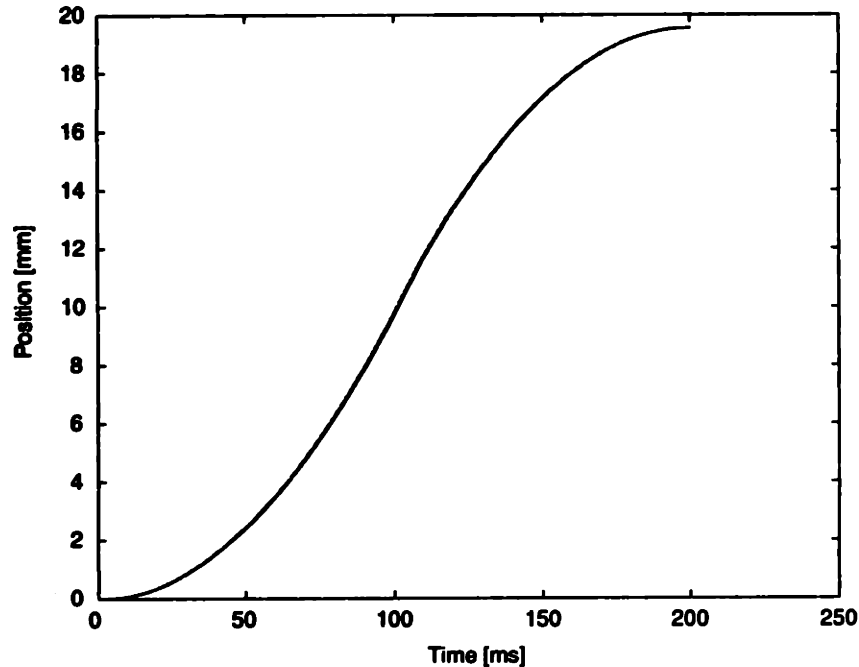


Figure 6-21: Comparison of experimental and predicted transient responses of the Y Coarse stage. The stage motion is profiled according to a triangular velocity law. Note the close match in between the simulation and experiment.

Y coarse motion stages are also implemented in assembly language on the 'C-40 DSP as second-order sections. A commutation law is used to energize the respective phases of the 3-phase linear brushless DC motor that drives the stages.

The fine stage forces are negligible and are not fed forward either to the X and Y coarse stages or to the isolation system due to problems with implementation. The X and Y coarse stage forces and position are fed forward to the isolation system controller. Feedback and feedforward control strategies for the isolation system are discussed next.

## 6.6 Feedback Control Design for Active Isolation

The equations in Chapter 4 were normalized by the mass thus scaling the design with the natural frequency. We benefit from that approach in our application of the compensator design procedure to the wafer stepper. The six modal equations of motion given in (6.5) have modal frequencies ranging from 7 Hz to 25 Hz. The one feedback loop designed in chapter 4 can now be implemented on all the 6 decoupled modal coordinates through suitable scaling of the resonant frequency. In our design law, we allow another notch to ensure low sensitivity around 12 Hz which is a significant component of the stage motions as illustrated in Figure 5-4. Accordingly, the shaping filter  $W_z(j\omega)$  has a lightly damped pair of poles around 12 Hz, a low frequency zero (around 0.05 Hz) and another set of poles to permit rapid high frequency roll-off at around 25 Hz. Figure 6-22 illustrates the vibration transmissibility obtained (in

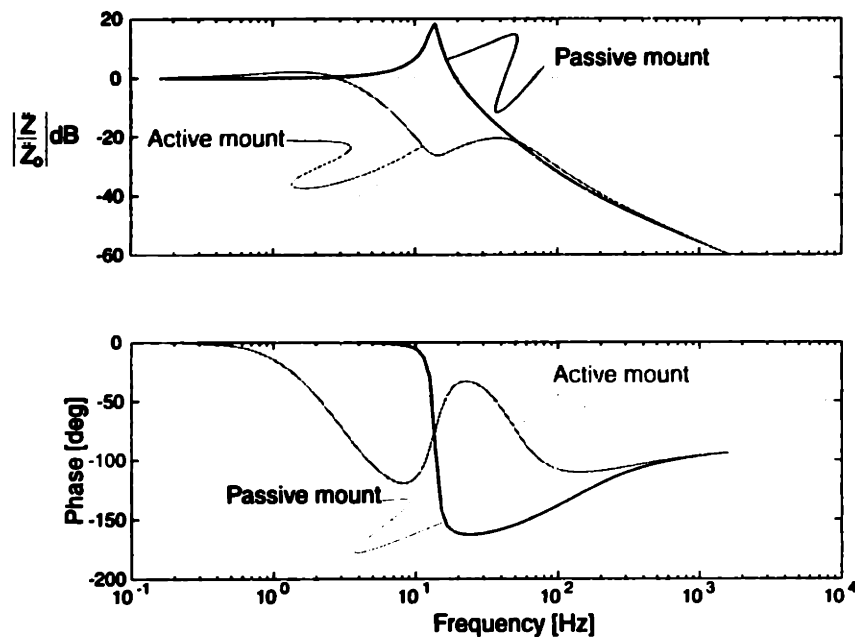


Figure 6-22: Vibration transmissibility of the active controller illustrating broadband and narrowband improvements over passive isolation.

simulation) as a result of application of the methods from Chapter 4.



### 6.6.1 Feedforward Control

The feedforward part of the control adds control forces to compensate for the reaction forces caused due to stage acceleration. The stage reaction forces are transformed into the modal coordinate system using the linear transformations given in (6.16) and added to the feedback control forces.

$$\begin{aligned}
 f_{xff} &= f_{cx} \\
 f_{yff} &= f_{cy} \\
 f_{zff} &= 0 \\
 \tau_{xff} &= -(f_{cy} \times z_{fcy}) \\
 \tau_{yff} &= f_{cx} \times z_{fcx} \\
 \tau_{zff} &= f_{cy} \times x_{fcy} - (f_{cx} \times y_{fcx})
 \end{aligned} \tag{6.16}$$

Only the X and Y coarse stage forces  $f_{rx}$  and  $f_{ry}$  are considered in this transformation. The distances of the coarse stage force vectors in the Cartesian coordinate frame are given in Table 6.1. The forces on the left hand side of (6.16) are the feedforward

Parameter	Symbol	Distance [m]
Distance of Y coarse stage in the Z direction	$z_{fcy}$	0.356
Distance of X coarse stage in the Z direction	$z_{fcx}$	0.254
Distance of Y coarse stage in the X direction	$x_{fcy}$	0.025
Distance of X coarse stage in the Y direction	$y_{fcx}$	Not fixed

Table 6.1: Coarse stage force vector stage location in the Cartesian coordinate frame. Note that  $y_{fcx}$  changes in real time with the movement of the stage.

forces/torques to be applied to the stepper. These forces/torques are in the Cartesian coordinate system and need to be transformed to the modal coordinate system before they can be added to the feedback control forces computed in the modal coordinate system. This is done by premultiplying the transformations in (6.16) by the transpose

of the modal matrix  $\mathbf{V}$ . Thus, the feedforward modal forces  $\mathbf{F}_{ffm}$  are given by

$$\mathbf{F}_{ffm} = \mathbf{V}^T \mathbf{A}_{ff} \mathbf{F}_{stage} \quad (6.17)$$

Here,  $\mathbf{F}_{stage}$  is a vector of the coarse stage forces,  $\mathbf{A}_{ff}$  is a geometric matrix which is a function of the instantaneous position of the linear motor control forces in the stepper coordinate frame,  $\mathbf{V}$  is the modal matrix, and  $\mathbf{F}_{ffm}$  is the vector of feedforward forces added to the vector of feedback forces.

Next, we discuss the implementation of the control schemes on the DSPs.

## 6.7 Implementation

The stepper is controlled by eight 'C40 Digital Signal Processors running in parallel on a VME bus. The sample rate for the whole system is 5 KHz. The arrangement of the DSP system is shown in Figure 6-23. A four processor Hydra<sup>2</sup> card forms the backbone for the filtering and control computations. Each 'C40 processor has six serial (comm) ports that can be used for inter-processor communication. The four 'C40 processors in the Hydra card have one serial port connected to each other onboard processor. The remaining three serial ports for each processor are brought out onto the front panel as illustrated in Figure 6-23. The Commio cards are primarily meant for input/output operations and each one of them has a 'C40 processor and four industry pack (IP) slots. Four of their comm ports are brought out to the front panel as shown. Communication between the Hydra card and the Commio cards is established using these comm ports.

Table 6.2 documents the function of each processor in the DSP system. The isolation system is programmed to run on a single COMM/IO board which has four Industry Pack (IP) slots. IP slots 0 and 1 are taken up by Analog to Digital converters and slots 2 and 3 are taken up by Digital to Analog converters. Figure 6-24 illustrates the algorithm implemented on the CP 4 DSP. After anti-alias filtering, the sampled

---

<sup>2</sup>Made by Ariel systems Inc.

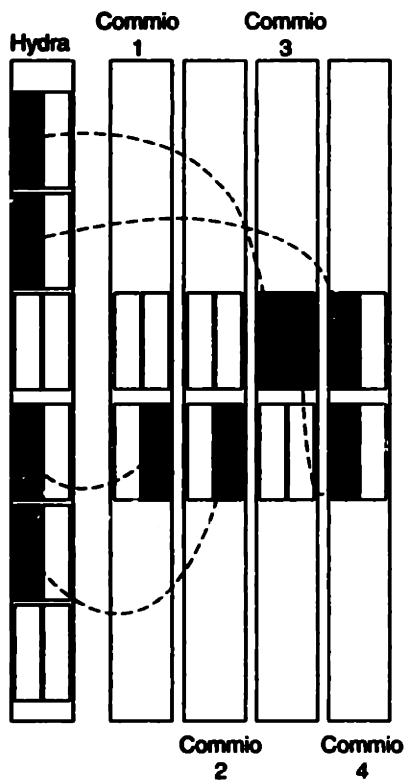


Figure 6-23: DSP Architecture used for the ISIS/Active isolation project. The dashed lines represent the fast serial port connections in between the Hydra card and the Commio cards. Note HP1-3 represents the 3<sup>rd</sup> comm port of the HP 1 'C40 processor and so on.

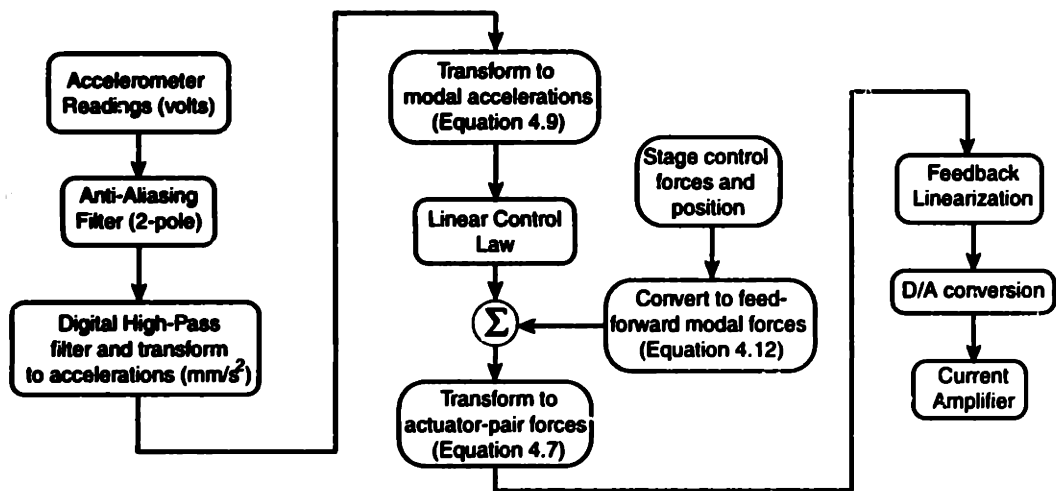


Figure 6-24: Active Isolation Control algorithm

Processor	Function
HP 1	Supervisory processor. Sends out the interrupts to the other processors. Communicates with the host processor and the VME bus. Reads in laser position from the VME bus (Six HP laser cards are connected to the VME bus). Used for data collection and routes various signals from the other Hydra processors to and from the Commio processors.
HP 2	Fine stage controller. Communicates directly with CP 1 and CP 2 to obtain the cap gauge positions for the fine stage. Computes fine stage control forces. Outputs the control currents onto the DACs on CP 1 and CP 2
HP 3	Used as a buffer for HP 1/HP 2 communication (to prevent overflow of the FIFOs on both processors).
HP 4	Not used
CP 1	A/D conversion and filtering of three cap gauge channels. Eight DACs output currents to eight amplifiers for the fine stage actuation. One spare DAC used for system identification.
CP 2	A/D conversion and filtering of three other cap gauge channels. Eight DACs output currents to eight other amplifiers for the fine stage actuation.
CP 3	X and Y Coarse stage controller. Also reads in the six cap gauges that sense change in stepper position from the legs (for the active isolation system). DACs output currents to the various phases of the X/Y linear motors.
CP 4	Active vibration isolation. Reads in accelerometer values, computes the feedback and feedforward forces and outputs the control currents onto the eight DACs for the active isolation system.

Table 6.2: Arrangement of DSPs on the VME bus and their functions

acceleration are passed through a first-order digital band-pass filter. The purpose of this filter is two-fold. The first is to remove any D.C. bias in the signals. The pole for this high-pass filtering is placed as low as possible at 0.05 Hz<sup>3</sup>. The upper limit for the band-pass filter is set to be 250 Hz. This is because the mechanical resonance of the accelerometers (refer to Figure 5-19) is found to vary in between 400 Hz and 600 Hz. Since the upper control bandwidth is approximately 80 Hz, this does not lead to significant attenuation of data. The experimentally measured frequency response of the band-pass filter is shown in Figure 6-25.

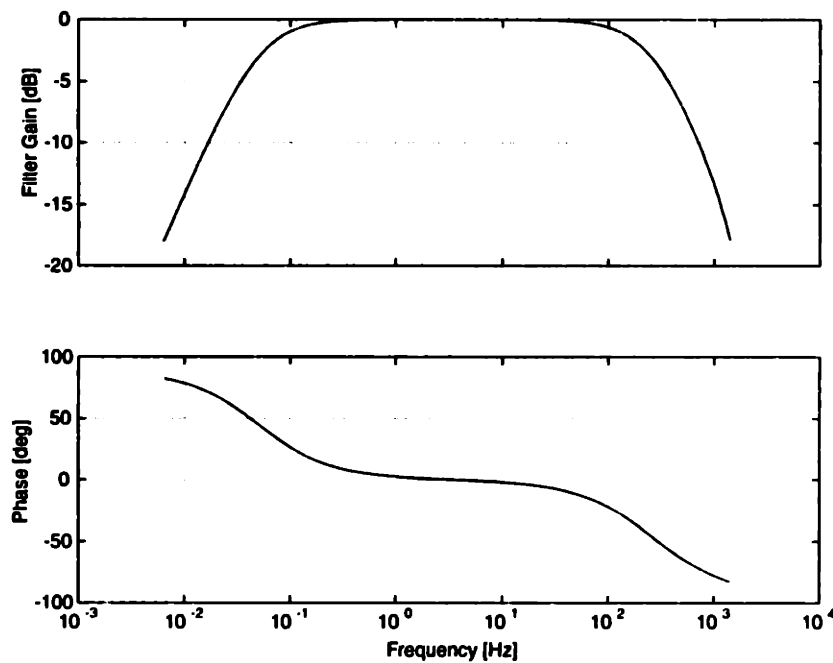


Figure 6-25: Frequency response of band-pass filter. Filter is implemented in assembly as a second order IIR Biquad.

The modal acceleration computed using the transformations given in (6.9) is used in the computation of the modal control forces according to the linear feedback control law. This law is given by a difference equation implementation of the dynamic compensator  $G(s)$ . The compensator as well as other IIR filters are implemented in assembly as second-order biquads [76]. This implementation prevents roundoff errors and allows extremely fast computation since it avails of the special features of the

<sup>3</sup>Lower frequencies were found to promote roundoff errors and lead to saturation.

'C40 processor. These features include parallel add and multiply instructions as well as circular addressing for the convolution operation.

The stage forces and position are communicated to the CP 4 DSP by the stage motion controller on the CP 3 DSP. These are transformed into modal feedforward forces using (6.17) and summed with the feedback control forces to obtain the overall control forces. Next, the overall control forces are converted to actuator-pair forces using the linear transformations in (6.7). The actuator gaps are evaluated from the capacitance probe readings (note that this is not illustrated in figure 6-24) using (5.14) and (5.17). The actuator-pair forces along with the gaps are used to compute the control currents according to the feedback linearization law given in (5.7). Control voltages corresponding to the required actuator currents are applied to the amplifiers through the DACs.

## 6.8 Experimental Results

Two sets of experiments are performed to ascertain the performance of the active vibration isolation system. The first is a seismic transmissibility test. Floor vibrations are measured using a seismic accelerometer and the vibrations of the stepper in the Cartesian coordinate frame are computed using the transformations given in equation 5.21. The transfer function in between these two accelerations is measured by the HP35670A spectrum analyzer. Figure 6-26 illustrates the experimental setup to measure this transmissibility.

The floor is excited by pounding on it - this leads to a poor signal at low frequencies. A better way to excite the floor would be to excite a large shaker with a bandwidth limited white noise signal to provide uniform excitation across all the frequencies of interest. The resulting transmissibility plots are plotted in Figure 6-27. The passive transmissibility clearly shows the resonant peak due to the passive isolation. The active system is then enabled and the transmissibility measured again. This shows a clear attenuation of about 40 dB at the resonant peak and compares favorably to our prediction from Figure 6-22.

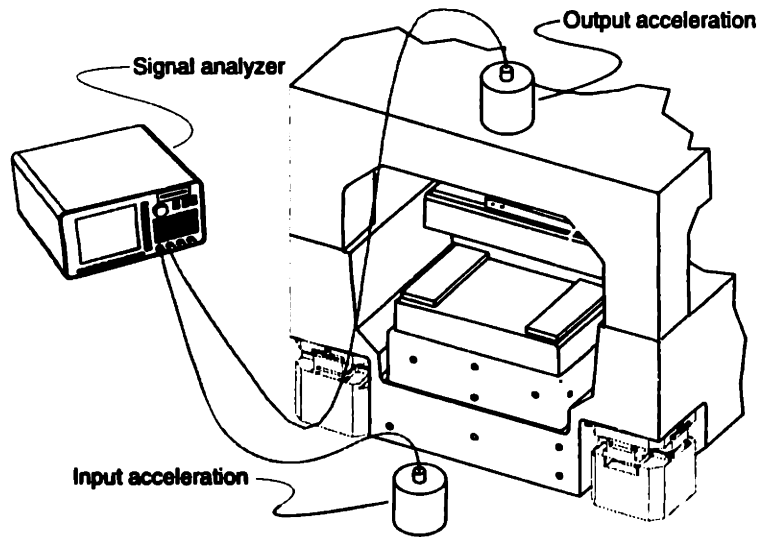


Figure 6-26: Experimental setup to measure Z-axis transmissibility. Note that the accelerometer on the bridge of the stepper represents the Z-axis acceleration computed by the DSP according to (5.21)

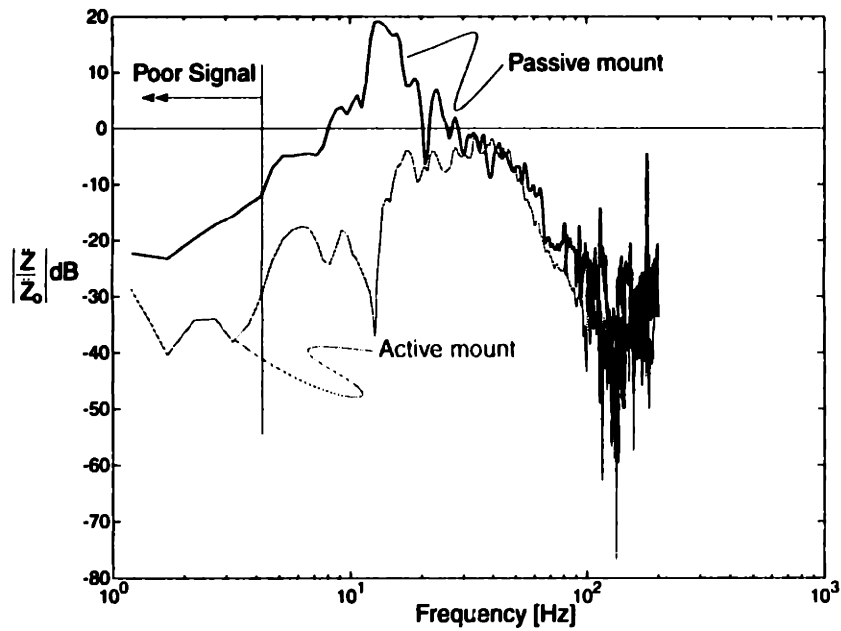


Figure 6-27: Measured Z axis Transmissibility

The second experiment is performed to quantify the transient performance of the isolation system during stage motions. In a step and repeat photolithography system such as the prototype stepper considered in this thesis, the stage steps from die site to die site. After the stepping motions are completed and the stepper as a whole reaches a settled state<sup>4</sup> exposure can proceed. We take a step of 20 mm which is typical of modern microprocessor die sites in the  $X$  direction. The peak stage acceleration is 0.3 g and the applied motion profile is triangular with a tapered acceleration profile towards the end. If the stepper were in free space, the acceleration of the stepper would be that of the stage acceleration times the mass ratio of stepper/stage. This is illustrated in Figure 6-28. The acceleration of the stepper in the  $X$ -direction is computed using (5.21) and also plotted in Figure 6-28. When the active system is turned off, the stepper is found to rock at its natural frequency due to the inertial forces of the accelerating stage. When the active system is turned on, the rocking is found to be arrested almost immediately on completion of the stage motions. Acceleration spikes corresponding to the acceleration profile of the stage are seen. This is to be expected since the effectiveness of feedforward control is a function of the accuracy of the dynamic model. We expect to see a reduction in the amplitude of these spikes with better modeling. The settling times for such a step using our settling criteria are 550 ms with active isolation turned on and about 2.5 s without.

The experimental measurements illustrate the benefits of the active isolation system. Better isolation and transient performance are observed. However, the performance measures presented in this chapter are those of rigid body acceleration of the stepper. The true performance measure is the error motions between the lens column and the fine stage and while an improvement is seen in this performance due to the shorter settling time requirement, it remains to be seen if this performance can be improved further. This requires modeling the flexibility of the stepper and using more sophisticated control algorithms to compensate for the flexural dynamics. The control procedure is derived next in chapter 8 and applied to the prototype wafer

---

<sup>4</sup>The settled state is defined using various criteria - for our prototype stepper, we assume a settled state when the position errors between the lens and the fine stage are below 50 nm peak



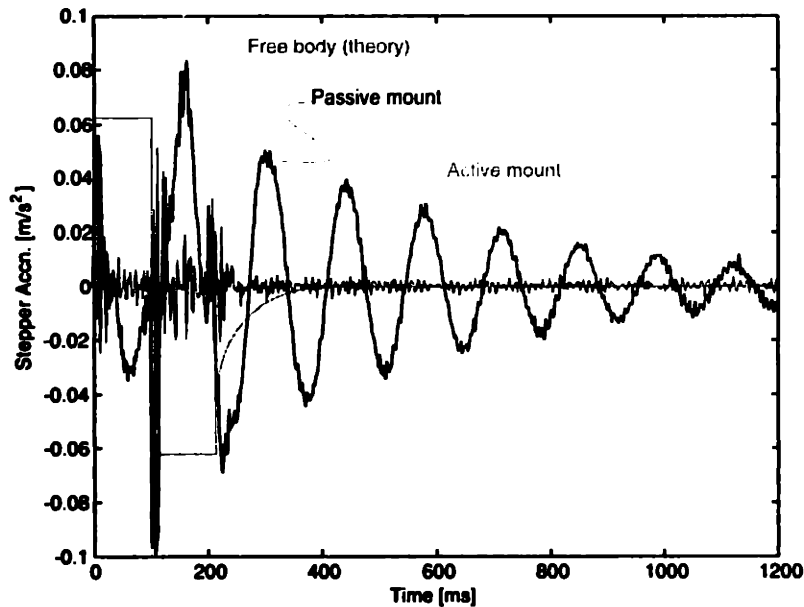


Figure 6-28: Isolation performance during stage motions

stepper in chapter 7.

## 6.9 Summary of Chapter 6

The objective of this chapter is to discuss rigid body modeling and control of the wafer stepper. An Integrated Modal Space Control technique is used and the eigenvectors of the closed-loop system are similar to those of the open-loop system. A frequency-shaped LQG controller is designed for the individual loops. The resulting controller is implemented on a parallel processing DSP system and experimental results illustrate performance improvement on the prototype stepper. Various constraints are imposed on the control system due to the rigid body assumption. The main constraint is the requirement that spillover from the unmodeled modes does not affect the stability of the closed loop system. It is shown later in chapter 7, that this is indeed a limiting constraint. Additional performance improvement can indeed be obtained by modeling and compensating for these flexible modes. It should however be noted that rigid body modeling and control is an important first step in understanding the limitations of feedback control.

# Chapter 7

## Flexibility Effects

### 7.1 Introduction

In this chapter, we consider the effects of flexibility of the mechanical system. All mechanical systems are flexible - it is the range of frequencies we consider that decides if flexibility issues are important. Mechanical systems are characterized by stiffness and mass which are functions of spatial variables. Hence, they represent distributed-parameter systems. The equations of motion are given by partial differential equations and so are the boundary conditions. The response of such a structure is usually obtained by modal analysis which involves solution of a differential eigenvalue problem and leads to an infinite set of eigenvalues and corresponding eigenfunctions. These infinite-order models are difficult to work with and closed-form solutions to these partial differential equations are invariably not feasible and in many cases not required. They are reduced to finite-order models either by truncation of modes, or by creating equivalent lumped-parameter systems. Popular techniques for discretization are the classical Rayleigh-Ritz method, the finite element method, Galerkin's method and the collocation method besides of course experimental modal analysis.

A discretized model of a precision machine is illustrated in Figure 7-1 where the flexibility of the machine is represented using a finite-order model. Here a series of lumped masses are mounted on springs and dampers, and each additional mass represents a flexible mode of the machine. Referring to the figure, it can be seen that

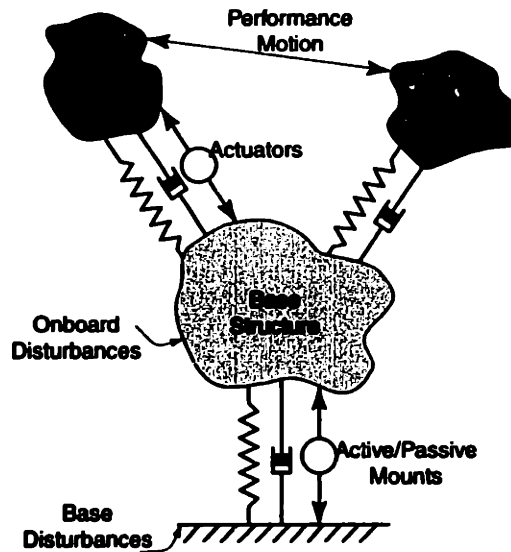


Figure 7-1: Discretized model of a precision machine. Note that the performance motion is affected by the flexibility of the machine components.

there are three essential parts to such a machine - a base structure, an assembly of moving components and an assembly of static components. The task of the machine is to position the moving components of the machine accurately with respect to the static part of the machine. This is represented in the schematic as the performance motion. The assemblies of moving and static components are lumped together as discrete masses in Figure 7-1. Additional flexible modes can be represented by adding more masses to the schematic shown. It is clearly seen from our representation that the performance motion is affected by the flexibility effects of the machine. We demonstrate this using actual data collected from the wafer stepper.

In this chapter, we consider the additional issues to be considered for systems where flexibility is a factor in determining performance and stability. Most of our analysis is performed in the modal domain, since this is the natural way to characterize mechanical systems. The reasons for this are twofold. First, creation of reduced-order models by mode truncation leads to models in the modal domain. Second, experimental model generation by experimental modal analysis techniques leads to easy synthesis of systems in the modal domain. And finally, the number of modes to be considered are often the basis for generating reduced-order models even from lumped-parameter models. We start by considering some control issues related to

flexible systems. This is followed by a discussion of the effects of mode spillover. The seminal work of Balas [8] [10] is reviewed and the results applied to the prototype wafer stepper. A higher-order model of the wafer stepper is proposed based on observations from experiments and the modal analysis on the XLS stepper performed by Sandia National Labs [65]. Spillover effects are shown to degrade the performance of the active controller designed in Chapter 6. Discussions in this chapter lead to the application of the modal controller developed in Chapter 8 to the wafer stepper.

## 7.2 Modeling Undamped Mechanical Structures

We consider undamped structures first. Most mechanical structures have very little damping and analysis of the structure can usually be done by neglecting damping and later performing a perturbation analysis. Neglecting damping also simplifies the analysis problem considerably since the modes have special orthogonality properties with the mass and stiffness operators. They usually do not exhibit such orthogonality properties with the damping operator unless it acquires some special forms (proportional damping *etc.*). Besides, damping is a dissipative mechanism which is not readily modeled in the first place.

Most structures can be modeled by the following boundary value problem [47]

$$\mathcal{L}\mathbf{u}(\mathbf{x}, t) + \mathbf{M}(\mathbf{x})\ddot{\mathbf{u}}(\mathbf{x}, t) = \mathbf{F}(\mathbf{x}, t) \quad (7.1)$$

Here,  $\mathbf{x} \in \mathcal{D}$  where  $\mathcal{D}$  represents the domain of the structure and  $\mathcal{L}$  is a self-adjoint, linear homogeneous, symmetric, differential stiffness operator of order  $2p$ . The control force distribution is usually provided by  $m$  point force actuators such that

$$\mathbf{F}(\mathbf{x}, t) = \sum_{i=1}^m b_i(\mathbf{x})\mathbf{f}_i(t) \quad (7.2)$$

where the actuator force amplitudes are given by  $|\mathbf{f}_i(t)|$  and the influence functions  $b_i(\mathbf{x})$  are approximate Dirac delta functions  $\delta(\mathbf{x} - \mathbf{x}_i)$ .

The boundary conditions are given by

$$\mathcal{B}_i \mathbf{u}(\mathbf{x}, t) = 0 \quad i = 1, 2, \dots, p \quad (7.3)$$

where  $\mathbf{x} \in \partial\mathcal{D}$  and  $\partial\mathcal{D}$  represents the boundary of the domain.  $\mathcal{B}_i$  are linear, homogeneous differential operators of maximum order  $2p - 1$ . The complete solution to the boundary value problem is dependent on the initial conditions also, but we concern ourselves primarily with the forced response of the system and assume that the system is stable so that the transients due to arbitrary initial conditions are attenuated.

We consider the free vibration problem, and assume a solution of the form

$$\mathbf{u}(\mathbf{x}, t) = \Phi(\mathbf{x})\eta(t) \quad (7.4)$$

Separating the spatial and time variables leads to the differential eigenvalue problem

$$\mathcal{L}\Phi(\mathbf{x}) = \lambda\mathbf{M}(\mathbf{x})\Phi(\mathbf{x}) \quad \mathbf{x} \in \mathcal{D} \quad (7.5)$$

subject to the boundary conditions given in (7.3).

Substitution of the boundary conditions (7.3) in (7.5) leads to the *characteristic equation* which is usually transcendental. The solution of the characteristic equation leads to an infinite set of real eigenvalues  $\lambda_j = \omega_j^2$  (due to symmetric positive operators) and associated eigenfunctions  $\phi_j$ . The eigenfunctions are unique, except for the amplitude which is consistent with the fact that for homogeneous problems, the solutions are unique to a multiplicative constant. We can now use the expansion theorem to write

$$\mathbf{u}(\mathbf{x}, t) = \sum_{j=1}^{\infty} \phi_j(\mathbf{x})\eta_j(t) \quad (7.6)$$

where  $\eta_j(t)$  are the natural coordinates and the eigenfunctions have been normalized

to satisfy

$$\int_{\mathcal{D}} \phi_j' \mathbf{M} \phi_k dx = \mathbf{I}$$

$$\int_{\mathcal{D}} \phi_j' \mathcal{L} \phi_k dx = \Lambda$$

We can use the orthogonality of mode shapes to decouple the equations. This leads to the modal equations

$$\ddot{\eta}_k(t) + \omega_k^2 \eta_k(t) = F_k(t) \quad k = 1, 2, \dots, \infty \quad (7.7)$$

where

$$F_k(t) = \int_{\mathcal{D}} \phi_k'(\mathbf{x}) \mathbf{f}(\mathbf{x}, t) dx \quad k = 1, 2, \dots, \infty \quad (7.8)$$

are the modal forces. Equations (7.7) represent an infinite set of independent second-order ordinary differential equations. If the differential eigenvalue problem permits a closed-form solution, the above solutions can be used and the modes of interest can be used to create a finite-order model based on mode truncation.

A more commonly used approach is the assumed-modes method (very similar to the Rayleigh-Ritz method) where a set of  $n$  comparison functions  $\rho_k(\mathbf{x})$  ( $k = 1, 2, \dots, n$ ) are chosen to approximate the solution. Thus, we write

$$\mathbf{u}(\mathbf{x}, t) = \sum_{k=1}^n \rho_k(\mathbf{x}) \mathbf{q}_k(t) \quad (7.9)$$

where  $\mathbf{q}_k(t)$  are generalized coordinates. Inserting (7.9) into (7.1) and premultiplying the result by  $\rho_j(\mathbf{x})$  ( $j = 1, 2, \dots, n$ ) and integrating over the domain, we get

$$\sum_{k=1}^n m_{jk} \ddot{q}_k(t) + \sum_{k=1}^n k_{jk} q_k(t) = F_j(t) \quad j = 1, 2, \dots, n \quad (7.10)$$

where

$$\begin{aligned}
 m_{jk} &= \int_{\mathcal{D}} \rho'_j m \rho_k dx & j, k = 1, 2, \dots, n \\
 k_{jk} &= \int_{\mathcal{D}} \rho'_j \mathcal{L} \rho_k dx & j, k = 1, 2, \dots, n \\
 F_j &= \int_{\mathcal{D}} \rho'_j f(\mathbf{x}, t) dx & j = 1, 2, \dots, n
 \end{aligned} \tag{7.11}$$

Equations (7.10) can be written in matrix form as

$$\mathbf{M}\ddot{\mathbf{q}}(t) + \mathbf{K}\mathbf{q}(t) = \mathbf{f}_q(t) \tag{7.12}$$

where  $\mathbf{M}$  and  $\mathbf{K}$  are the symmetric mass and stiffness matrices,  $\mathbf{q}(t)$  is a generalized displacement vector, and  $\mathbf{f}_q(t)$  is the generalized force vector given by

$$\begin{aligned}
 \mathbf{f}_q(t) &= \begin{pmatrix} \int_{\mathcal{D}} \rho'_1 b_1(\mathbf{x}) dx & \dots & \int_{\mathcal{D}} \rho'_1 b_m(\mathbf{x}) dx \\ \vdots & \ddots & \vdots \\ \int_{\mathcal{D}} \rho'_n b_1(\mathbf{x}) dx & \dots & \int_{\mathcal{D}} \rho'_n b_m(\mathbf{x}) dx \end{pmatrix} \begin{Bmatrix} f_1 \\ \vdots \\ f_m \end{Bmatrix} \\
 &= \mathbf{B}_n^c \mathbf{f}
 \end{aligned} \tag{7.13}$$

Here, the generalized force vector is given by a linear transformation  $\mathbf{B}_n^c$  on the discrete force vector  $\mathbf{f}$ . Equation (7.12) represents a set of  $n$  simultaneous second-order ordinary differential equations replacing the partial differential equations (7.1) and the boundary conditions (7.3). This represents a discretization in space of the boundary value problem. This discretization procedure is called the assumed-modes procedure and we shall rely on it heavily to obtain finite-order models for the machine tool structures we are interested in. It is in essence an application of the Rayleigh-Ritz method or the finite element method.

The equations of motion in (7.12) are usually coupled. We can decouple them according to the methods of Chapter 6 by solving an algebraic eigenvalue problem.

Accordingly, defining,

$$\begin{aligned} \mathbf{q} &= \Phi \boldsymbol{\eta} \\ \Rightarrow \mathbf{q} &= \sum_{i=1}^n \phi_i \eta_i \end{aligned} \quad (7.14)$$

we get a finite set of decoupled equations

$$\ddot{\eta}_k(t) + \omega_k^2 \eta_k(t) = f_k^m(t) \quad k = 1, 2, \dots, n \quad (7.15)$$

where  $n$  is usually large to obtain high fidelity models. This can be expressed in matrix form as

$$\begin{aligned} \ddot{\boldsymbol{\eta}}(t) + \Lambda \boldsymbol{\eta}(t) &= \mathbf{f}^m(t) \\ \Rightarrow \ddot{\boldsymbol{\eta}}(t) + \Lambda \boldsymbol{\eta}(t) &= \mathbf{B}_n \mathbf{f}(t) \end{aligned} \quad (7.16)$$

Note that (7.16) could also have been obtained from (7.7) through a mode truncation scheme. However, for complex structures, it is inevitably impossible to solve the partial differential equations (7.1) with their complex boundary conditions (7.3). A finite element scheme or an assumed modes scheme is usually used to obtain the finite-dimensional form of the equations in (7.16).

For the feedback control of the finite-dimensional equations of motion in (7.16), let us assume velocity and displacement measurements given by  $p$  point sensors. These point sensors measure linear combinations of the generalized displacements and velocities as given by

$$\begin{aligned} \mathbf{y}(t) &= \mathbf{C} \mathbf{q}(t) + \mathbf{D} \dot{\mathbf{q}}(t) \\ \Rightarrow \mathbf{y}(t) &= \mathbf{C} \Phi \boldsymbol{\eta}(t) + \mathbf{D} \Phi \dot{\boldsymbol{\eta}}(t) \end{aligned} \quad (7.17)$$

Before proceeding to the control of large-dimensional systems described by (7.16), we study the control of systems described by the infinite-dimensional equations (7.7) in the following section. This is presented for the sake of completeness only.



## 7.3 Distributed Feedback Control

We first consider the feedback control of the distributed structure without any approximation. This consists of determining the modal controls  $f_k(t)$  in (7.7). We consider linear control in the form of proportional and rate feedback control

$$\mathbf{f}(\mathbf{x}, t) = -\mathcal{G}(\mathbf{x})\mathbf{u}(\mathbf{x}, t) - \mathcal{H}(\mathbf{x})\dot{\mathbf{u}}(\mathbf{x}, t) \quad (7.18)$$

where  $\mathcal{G}$  and  $\mathcal{H}$  are control gain operators. Substituting (7.18) in (7.7) we get

$$\ddot{\eta}_k(t) + \sum_{j=1}^{\infty} h_{jk} \dot{\eta}_k(t) + \sum_{j=1}^{\infty} (\omega_k^2 \delta_{jk} + g_{jk}) \eta_k(t) = 0 \quad k = 1, 2, \dots, \infty \quad (7.19)$$

where

$$g_{jk} = \langle \phi_j, \mathcal{G}\phi_k \rangle = \int_{\mathcal{D}} \phi_j' \mathcal{G}\phi_k dx \quad j, k = 1, 2, \dots, \infty$$

$$h_{jk} = \langle \phi_j, \mathcal{H}\phi_k \rangle = \int_{\mathcal{D}} \phi_j' \mathcal{H}\phi_k dx \quad j, k = 1, 2, \dots, \infty$$

Because feedback control characterized by  $g_{jk} \neq 0$  and  $h_{jk} \neq 0$  for  $j \neq k$  destroys the independence of the open-loop modal equations, we refer to this as *coupled control*. However, there are no algorithms to generate the infinite order matrices  $\mathbf{G}$  or  $\mathbf{H}$  associated with the control gain operators  $\mathcal{G}$  or  $\mathcal{H}$ . Hence, distributed feedback control realized through coupled control is not feasible.

### 7.3.1 Independent Modal Space Control (IMSC)

There is one special case in which distributed feedback control is possible. Here, the operators  $\mathcal{G}$  and  $\mathcal{H}$  satisfy the eigenvalue problems

$$\mathcal{G}\phi_k(\mathbf{x}) = g_k \mathbf{M}(\mathbf{x})\phi_k(\mathbf{x}) \quad k = 1, 2, \dots, \infty$$

$$\mathcal{H}\phi_k(\mathbf{x}) = h_k \mathbf{M}(\mathbf{x})\phi_k(\mathbf{x}) \quad k = 1, 2, \dots, \infty$$

which imply that  $\mathcal{G}$  and  $\mathcal{H}$  are such that

$$\begin{aligned}\langle \phi_j, \mathcal{G}\phi_k \rangle &= g_k \delta_{jk} \quad j, k = 1, 2, \dots, \infty \\ \langle \phi_j, \mathcal{H}\phi_k \rangle &= h_k \delta_{jk} \quad j, k = 1, 2, \dots, \infty\end{aligned}$$

In such a case, the closed-loop modal equations 7.19 reduce to the independent set

$$\ddot{\eta}_k(t) + h_k \dot{\eta}_k(t) + (\omega_k^2 + g_k) \eta_k(t) = 0 \quad k = 1, 2, \dots, \infty \quad (7.20)$$

The closed-loop modal equations are thus independent of one another, and this type of control is called *Independent Modal-Space Control* (IMSC). This implies that the open-loop eigenfunctions  $\phi_k$  are the closed-loop eigenfunctions as well. The control effort in IMSC is then directed entirely to altering the eigenvalues leaving the eigenfunctions unaltered. Two techniques used in determining the modal gains  $g_k$  and  $h_k$ , ( $k = 1, 2, \dots, \infty$ ) are pole placement and linear quadratic methods of optimal control. Kwakernaak and Sivan's classic text [39] is a good reference for a discussion of these methods.

### 7.3.2 Approximations to Distributed Feedback Control

There are two shortcomings to the control techniques discussed in the previous section. Although theoretically feasible, IMSC is hard to implement because of problems in developing distributed actuators and sensors. Invariably, actuators and sensors are discrete and there is only a finite number of them. This is one of the key limitations to structural control - control of a very high order system with very few control inputs. The actuators and sensors have finite bandwidths and it becomes impossible to control modes beyond their bandwidth. Secondly, control of the entirety of modes is neither feasible nor necessary. There is very little participation of the higher modes in the overall systems response and structural damping associated with the higher modes is much higher than that of the lower modes. Also, various assumptions made in deriving the equations of motion limit the validity of the theory to lower modes only.

Hence, we propose to model only a limited number of modes  $n$ . To obtain this finite-order model, we can use either the mode truncation procedure when the differential eigenvalue problem permits a closed-form solution or a discretization procedure such as the assumed-modes approach. Either approach leads to the discrete equations as given in (7.12). The development of our theory can be applied to more general lumped-parameter systems with gyroscopic and circulatory terms as given in (8.16) but our chief concern will be with equations of the form given in (7.12).

Meirovitch *et al.* [44] [45] have shown that the Independent Modal Space Controller provides robustness advantages when you have full actuation authority, *i.e.*, the number of actuators is equal to the number of modeled/controlled modes. However, in practice it is impossible to have enough control authority and we control only a limited number ( $r$ ) of lower modes. This leads to problems with *spillover* that we discuss in the next section.

## 7.4 Control and Observation Spillover

In theory, mechanically flexible systems require an infinite number of elastic modes as shown in (7.7) to completely describe their behavior, and in practice, they are usually modeled by large finite-dimensional systems (7.16). A finite-dimensional model is further justified by the fact that actuators and sensors can not excite or respond to the higher frequency modes. The fundamental problem of feedback control of such flexible systems is to precisely control a large dimensional system with a much smaller dimensional controller because computational limitations and modeling error would restrict the control to a few critical modes. These critical modes are chosen by the system performance requirements and excitation sources and need not necessarily be the first few low frequency modes in the system spectrum.

Since the number of modeled modes  $n$  is usually large, it might not be reasonable to expect to control all  $n$  modes, instead  $r$  controlled modes are selected with  $r < n$

and the displacement is partitioned into a controlled and residual part. Accordingly,

$$\mathbf{q}(t) = \mathbf{q}_r(t) + \mathbf{q}_s(t) \quad (7.21)$$

where the controlled part is given by

$$\mathbf{q}_r(t) = \sum_{k=1}^r \phi_k \eta_k(t) \quad (7.22)$$

The modes can be reordered such that any subset of the  $n$  modes can be the controlled part of (7.21). We can now express the equations of motion in standard state variable notation using the modal coordinates  $\mathbf{v}^T = (\boldsymbol{\eta} \ \dot{\boldsymbol{\eta}})$ . Accordingly,

$$\begin{aligned} \begin{Bmatrix} \dot{\boldsymbol{\eta}}_r \\ \ddot{\boldsymbol{\eta}}_r \end{Bmatrix} &= \begin{pmatrix} \mathbf{0} & \mathbf{I} \\ -\boldsymbol{\Lambda}_r & \mathbf{0} \end{pmatrix} \begin{Bmatrix} \boldsymbol{\eta}_r \\ \dot{\boldsymbol{\eta}}_r \end{Bmatrix} + \begin{Bmatrix} \mathbf{0} \\ \mathbf{B}_r \end{Bmatrix} \mathbf{f} \\ &= \mathbf{A}_R \mathbf{v}_R + \mathbf{B}_R \mathbf{f} \end{aligned} \quad (7.23)$$

$$\begin{aligned} \begin{Bmatrix} \dot{\boldsymbol{\eta}}_s \\ \ddot{\boldsymbol{\eta}}_s \end{Bmatrix} &= \begin{pmatrix} \mathbf{0} & \mathbf{I} \\ -\boldsymbol{\Lambda}_s & \mathbf{0} \end{pmatrix} \begin{Bmatrix} \boldsymbol{\eta}_s \\ \dot{\boldsymbol{\eta}}_s \end{Bmatrix} + \begin{Bmatrix} \mathbf{0} \\ \mathbf{B}_s \end{Bmatrix} \mathbf{f} \\ &= \mathbf{A}_S \mathbf{v}_S + \mathbf{B}_S \mathbf{f} \end{aligned} \quad (7.24)$$

$$\begin{aligned} \mathbf{y} &= (\mathbf{C}\boldsymbol{\Phi}_r \ \mathbf{D}\boldsymbol{\Phi}_r) \begin{Bmatrix} \boldsymbol{\eta}_r \\ \dot{\boldsymbol{\eta}}_r \end{Bmatrix} + (\mathbf{C}\boldsymbol{\Phi}_s \ \mathbf{D}\boldsymbol{\Phi}_s) \begin{Bmatrix} \boldsymbol{\eta}_s \\ \dot{\boldsymbol{\eta}}_s \end{Bmatrix} \\ &= \mathbf{C}_R \mathbf{v}_R + \mathbf{C}_S \mathbf{v}_S \end{aligned} \quad (7.25)$$

where we have the appropriate partitions

$$\Lambda = \begin{pmatrix} \Lambda_r & \mathbf{0} \\ \mathbf{0} & \Lambda_s \end{pmatrix}$$

$$\mathbf{B}_n = \begin{pmatrix} \mathbf{B}_r \\ \mathbf{B}_s \end{pmatrix}$$

$$\Phi = \begin{pmatrix} \Phi_r & \Phi_s \end{pmatrix}$$

### 7.4.1 Modal Control

The feedback control law to compute the force vector  $\mathbf{f}(t)$  is developed using standard state feedback along with an estimator for the controlled subsystem given in (7.23). The estimator can be either a Kalman filter or a Luenberger observer. In either case, the estimator has the form

$$\begin{aligned} \dot{\hat{\mathbf{v}}}_R &= \mathbf{A}_R \hat{\mathbf{v}}_R + \mathbf{B}_R \mathbf{f} + \mathbf{L}_R (\mathbf{y} - \hat{\mathbf{y}}) \\ \hat{\mathbf{y}} &= \mathbf{C}_R \hat{\mathbf{v}}_R \end{aligned} \quad (7.26)$$

Defining the estimator error  $\tilde{\mathbf{v}}_R = \hat{\mathbf{v}}_R - \mathbf{v}_R$  we obtain the estimator dynamics

$$\dot{\tilde{\mathbf{v}}}_R = (\mathbf{A}_R - \mathbf{L}_R \mathbf{C}_R) \tilde{\mathbf{v}}_R + \mathbf{L}_R \mathbf{C}_S \mathbf{v}_S \quad (7.27)$$

The control law is now given by standard state feedback

$$\mathbf{f} = -\mathbf{K}_R \hat{\mathbf{v}} \quad (7.28)$$

The composite closed-loop system now becomes

$$\begin{Bmatrix} \dot{\mathbf{v}}_R \\ \dot{\tilde{\mathbf{v}}}_R \\ \dot{\mathbf{v}}_S \end{Bmatrix} = \begin{pmatrix} \mathbf{A}_R - \mathbf{B}_R \mathbf{K}_R & -\mathbf{B}_R \mathbf{K}_R & \mathbf{0} \\ \mathbf{0} & \mathbf{A}_R - \mathbf{L}_R \mathbf{C}_R & \mathbf{L}_R \mathbf{C}_S \\ -\mathbf{B}_S \mathbf{K}_R & -\mathbf{B}_S \mathbf{K}_R & \mathbf{A}_S \end{pmatrix} \begin{Bmatrix} \mathbf{v}_R \\ \tilde{\mathbf{v}}_R \\ \mathbf{v}_S \end{Bmatrix} \quad (7.29)$$

Equation (7.29) clearly demonstrates the effects of spillover [8]. The sensor outputs are contaminated by the residual modes through the term  $C_S v_S$  which is termed as the *observation spillover* and the feedback control excites the residual modes through the term  $B_S f$  which is termed *control spillover*. The effects of spillover are best illustrated in Figure 7-2.

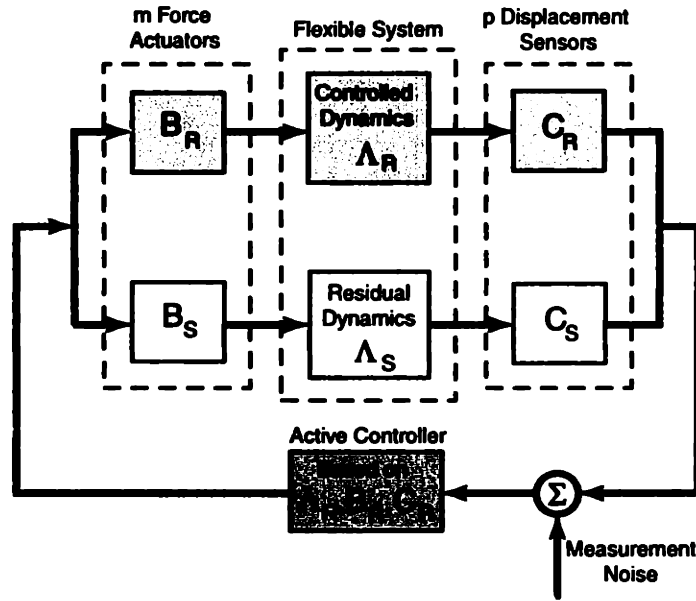


Figure 7-2: Control and Observation Spillover [8].

We concern ourselves with the case when observation spillover is zero, *i.e.*,  $C_S = 0$ . In this case, the eigenvalues of the composite system in (7.29) are the eigenvalues of  $A_R - B_R K_R$ ,  $A_R - L_R C_R$ , and  $A_S$  due to block triangularity of the equations. The residual mode system is now given by

$$\dot{v}_S = A_S v_S - B_S K_R (v_R + \tilde{v}_R) \quad (7.30)$$

or equivalently

$$\ddot{\eta}_s + \Lambda_s \eta_s = -B_S K_R (v_R + \tilde{v}_R) \quad (7.31)$$

This is nothing but a system of undamped oscillators being driven by  $v_R$  and  $\tilde{v}_R$ .

Any control spillover  $\mathbf{B}_S \neq \mathbf{0}$  causes detrimental excitation of the residual modes, but it can not shift the residual mode frequencies. Since the total response of the system depends on both the controlled and residual modes, this excitation of the residual modes can degrade the system response, but can not destabilize the system [9][7][8].

Observation spillover on the other hand can be destabilizing [8]. Balas treats the problem of observation spillover as a perturbation and the reader is referred to his work [9][7][8] for details. He suggests location of the actuators and sensors of the system near the zeros of the mode shapes of the residual modes as one way to attenuate the influence of spillover. Also, a comb filter is suggested as a means to eliminating the destabilizing influence of observation spillover. In our work, we find that observation spillover does not perturb the system in (7.29) enough to cause instability. However, the performance is affected significantly due to the effects of control spillover as demonstrated by (7.31). As a prelude to creating higher order models for the wafer stepper, we discuss the modal analysis of the GCA XLS 7000 wafer stepper by Sandia National Labs [65].

## **7.5 Modal analysis of the GCA XLS 7000 series stepper**

As mentioned in Chapter 6, the ISIS platform of steppers is based on the GCA XLS 7000 series of steppers. Key components such as the lens column, the illuminator and the bridge have been retained from the XLS machine while the motion control hardware has been completely modified. In this section, we present details of a modal analysis carried out by Sandia National Labs on the XLS series of wafer steppers. Some of the results from the Sandia report [65] can be applied to the modeling of the ISIS stepper, especially those pertaining to the optics of the machine.

In the modal analysis performed by Sandia, forty eight nodes are used to construct a modal model of the stepper; they include the main structure and all of the critical components (*i.e.* wafer and reticle handling systems are not part of the analysis).

The stepper is mounted on four elastomeric (passive) vibration isolation mounts. The rigid body modes of the stepper due to these mounts are identified and found to be below 30 Hz. In addition, 19 elastic modes are identified and found to be interspersed with the rigid body modes besides being tightly coupled. Table 7.1 is reproduced from the Sandia report and lists the rigid body and elastic modes of the XLS machine. According to the Sandia report, the elastic modes are found to lead to relative motion between the lens and the wafer chuck and have a direct bearing on the operating speed and accuracy of the machine.

Mode	Frequency [Hz]	Damping [%]	Description
1	8.7	20.0	Mainframe rigid body torsion
2	10.8	22.4	X rigid body translation
3	28.2	23.1	Mainframe rigid body rocking in XZ plane
4	13.0	2.4	Y stage bending - XY plane
5	18.4	9.2	Illuminator mount bending - XY plane
6	24.8	9.0	Lens mount bending - YZ plane
7	26.1	13.5	Lens mount axial - Z lens translation
8	31.9	4.1	Lens cell bending - YZ plane
9	32.2	1.3	Upper frame axial; stage bending
10	36.7	1.9	Lens cell second bending - YZ plane
11	43.5	1.8	Lens cell torsion - XZ plane
12	74.4	3.1	Lens column axial - Z direction
13	78.6	4.7	Lens mount 2 <sup>nd</sup> bending - YZ plane
14	84.3	3.1	Frame & lens column bending - XZ plane
15	86.4	3.5	Fine stage torsion mode - XY plane
16	90.3	4.9	Reticle platen axial mode - Z direction
17	93.1	2.2	Lens column & fine stage bending - YZ
18	100.2	4.0	Lens cell axial mode - Z direction
19	108.1	1.7	Lens/frame bend; lens cell torsion
20	113.4	4.3	Wafer chuck bending & Y translation
21	132.6	0.5	Auto focus component bending - YZ plane
22	136.5	5.4	Lens column 2 <sup>nd</sup> bending; wafer bend - XZ

Table 7.1: GCA XLS 7000 Series machine rigid body modal parameters. Reproduced from the Sandia report [65].

The Sandia report also states that the intermixing between the elastic and rigid body modes, as well as, the degree of coupling between adjacent modes makes it



difficult to tailor the machine's vibration sources (*i.e.*, the stage motions) such that they do not excite the undesirable elastic modes. To address this problem, most of the low frequency elastic modes have been moved to higher frequency ranges in the ISIS design. This is accomplished through a complete redesign of the base and the stages. The first mode associated with the air bearings of the coarse stage is approximately at 120 Hz. From table 7.1, we find that the next most significant source of flexibility is due to the lens mount, column and the illuminator. We consider the flexibility due to the lens mount and column in the next section. However, the flexibility in the illuminator is not considered, since it is absent from the prototype stepper used as the test platform. The most significant result from the Sandia report as far as this thesis is concerned is the identification of the longitudinal and bending modes of the lens mount and the lens column. The lowest longitudinal mode of the lens mount is found to be at 26.1 Hz and the lowest bending mode at 24.8 Hz while the corresponding ones for the lens column are at 74.4 Hz and 84.3 Hz. These values are to be expected in the ISIS design also since the optical system design from the XLS system is retained without change. These modes are poorly damped and affect the performance of the stepper due to control spillover.

## **7.6 Modeling Flexibility Effects on the Prototype Stepper**

In this section, we construct a model of the stepper with the first bending mode of the lens column and the coarse and fine stages as illustrated in Figure 7-3. This model is based on the measurements of the flexural dynamics of the XLS system by Sandia national labs [65] and the rigid body modeling of the stepper presented in chapter 6. Note that this model is presented for the stepper in the XZ plane and a very similar model (with different values for the components, however), can be derived for the stepper in YZ plane. We can also model flexibility in the vertical Z axis. In fact, we present such a model later in Chapter 8. However, as mentioned in Chapter 5,

there is no way to measure relative motions in between the lens column and the fine stage of the prototype stepper in the absence of an auto-focus mechanism and hence we do not follow that further in this chapter. We have a direct laser measurement

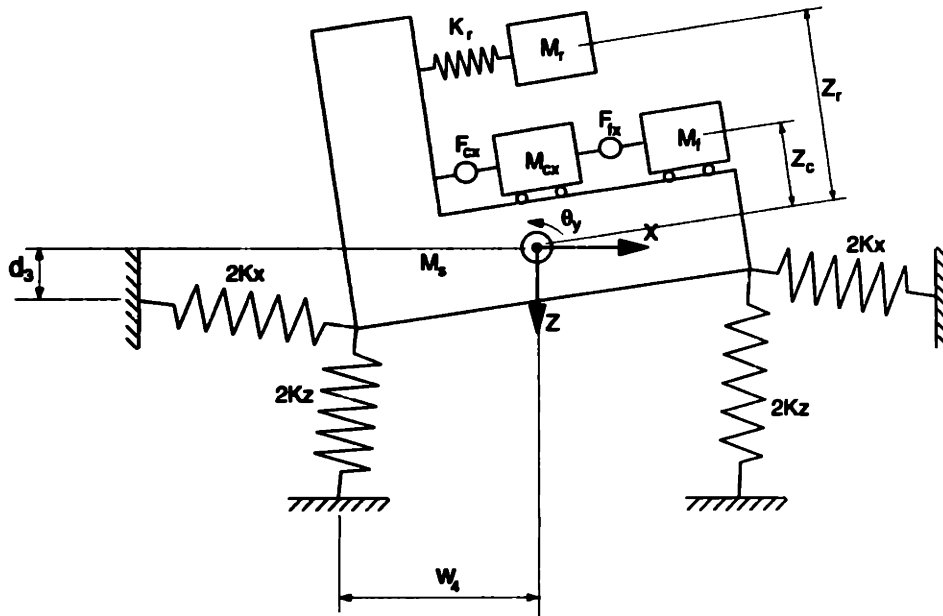


Figure 7-3: Six degree of freedom lumped parameter model of the stepper, coarse stage and fine stage in the XZ plane. Note the bending mode of the lens column at 84.3 Hz is modeled by the mass  $M_r$ .

of relative motions in between the lens column and the fine stage. In the figure, the mass of the stepper is represented by  $M_s$ . The rigid body modeling procedure presented in chapter 6 is repeated to model the isolation system. The lateral mode of the X coarse stage (mass  $M_{cx}$ ) is experimentally determined to be around 120 Hz (due to the limited stiffness of the air bearings). This is not modeled however. The fine stage is modeled by a mass  $M_f$  and the resonance by the mass  $M_r$ . The undamped

equations of motion are then given by

$$\begin{aligned}
 M_s \ddot{x}_1 + (4K_x + K_r)x_1 - K_r x_4 + (4d_3 K_x - z_r K_r)\theta_y &= F_s - F_{cx} \\
 M_{cx} \ddot{x}_2 &= F_{cx} - F_{fx} \\
 M_f \ddot{x}_3 &= F_{fx} \\
 M_r \ddot{x}_4 + K_r x_4 - K_r x_1 + z_r K_r \theta_y &= 0 \\
 I_{yy} \ddot{\theta}_y + (4d_3^2 K_x + 4w_4^2 K_z + z_r^2 K_r)\theta_y + (4d_3 K_x - z_r K_r)x_1 + z_r K_r x_4 &= \tau_y + z_c F_{cx} \\
 (M_s + M_{cx} + M_f + M_r)\ddot{z}_1 + 4K_z z_1 &= F_z
 \end{aligned}
 \tag{7.32}$$

where the generalized coordinates are illustrated in Table 7.2. The performance

Symbol	Description
$x_1$	$X$ motion of the stepper base
$x_2$	$X$ motion of the coarse stage
$x_3$	$X$ motion of the fine stage
$x_4$	$X$ motion of the lens column resonance
$\theta_y$	$\theta_y$ motion of all the inertias
$z$	$Z$ motion of all the masses

Table 7.2: Generalized coordinates for the six degree of freedom model of the prototype stepper illustrated in Figure 7-3

motion of interest is the relative motion between the lens column and the fine stage. This is directly measured by a laser interferometer. Under the controller designed for the stepper and stages in Chapter 6, a 1024-point FFT of the performance motion when the stage has just reached a settled<sup>1</sup> state is plotted in Figure 7-4. Ten averages are used to obtain this plot to attenuate the effects of measurement noise. We can see a number of peaks in the FFT of the performance motion. Based on the Sandia report we identify them in Table 7.3.

It can be seen that the low frequency mode gets the most excited because of the strong component of the coarse motion stage harmonics around 24 Hz. It is further seen that all these peaks are lightly damped. The low frequency modes are quickly

<sup>1</sup>According to our 50 nm settling criteria.

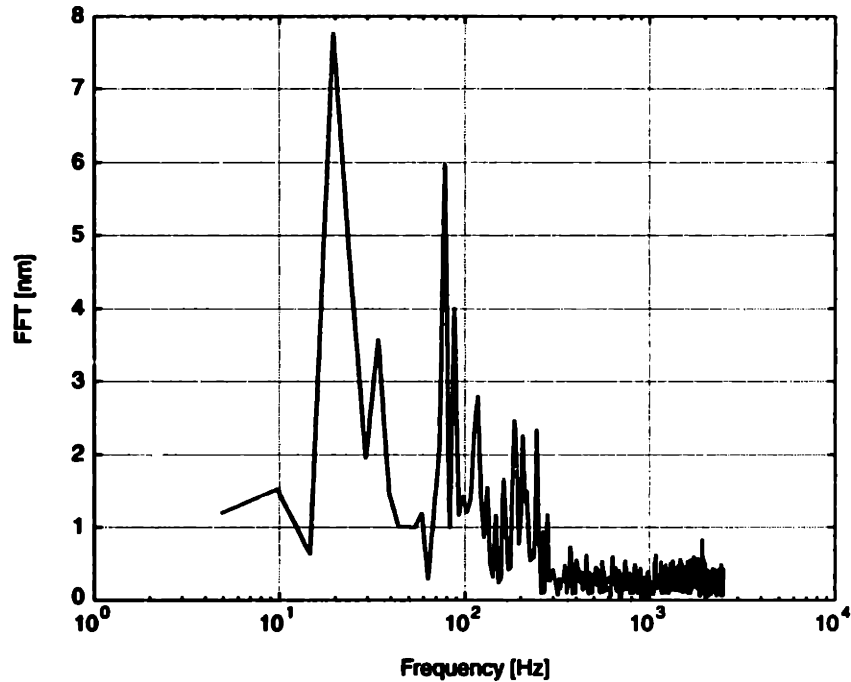


Figure 7-4: FFT of error motions in the  $X$  direction. Note the first five peaks, all below 100 Hz. These are due to control spillover which causes these modes to be continuously excited.

Frequency	Description
24.8 Hz	Lens mount bending - YZ plane
31.9 Hz	Lens cell bending - YZ plane
36.7 Hz	Lens cell second bending - YZ plane
78.6 Hz	Lens mount 2 <sup>nd</sup> bending - YZ plane
84.3 Hz	Frame & lens column bending - XZ plane

Table 7.3: Identification of flexible modes in the error motions between the fine stage and the lens.

attenuated by the rather large gain of the stage control loop at low frequencies, for example, the gain of the sensitivity function of the fine stage at 25 Hz is about -25 dB as illustrated in Figure 6-17. The fine stage can hence track such motions of the lens mount with reasonable fidelity and the error components at these frequencies get damped out. The flexural modes that cause us the most concern are the 2<sup>nd</sup> bending mode of the lens and the the first lens column bending mode at around 80 Hz. These twin peaks can be seen quite prominently in Figure 7-4. The sensitivity function for the fine stage has only an attenuation of approximately -5 dB at these frequencies as shown in Figure 6-17. This is our reasoning for creating higher-order models of the wafer stepper that include a bending mode of the lens column at 84.3 Hz as illustrated in Figure 7-3.

Even faster transient performance could in theory be obtained by modeling the flexibility of the lens mount, however, this is left for future work.

## 7.7 Summary of Chapter 7

We consider the modeling of continuous systems using partial differential equations along the lines of Balas [8]. However, for complex structures with complex boundary conditions, setting up the partial differential equations let alone their solution is an impossible task. Discretization approaches are used to approximate the behavior of such structures, the most popular being the finite-element and assumed-modes approaches. We present a tutorial review of control and observation spillover for systems whose finite-dimensional models are obtained through such procedures. Real world systems always have limited number of actuators as compared to the degrees of freedom and hence robust control techniques such as the IMSC method suggested by Meirovitch [44], [45] can not be applied due to this limited control authority.

A modal analysis of the XLS 7000 series of steppers from GCA is presented [65]. The optical components on the ISIS series of machines are similar to the XLS machine, and the flexible modes associated with these components can be identified in the performance motion of the wafer stepper. This performance motion is the error

motions in between the Zerodur mirror on the fine stage and the lens mount. The lower frequency modes can be attenuated due to the good attenuation properties of the error function of the fine stage, but the higher frequency modes are lightly damped and need to be attenuated using better controller design. For such controller design, a higher-order model of the stepper that models the lens column resonance is set up and the equations of motion derived. The derivation of the modal controller that compensates for this structural resonance will now be presented in Chapter 8.

# Chapter 8

## Eigenstructure Assignment

### 8.1 Introduction

“ but there is one system of coordinates which is especially suitable ...”

Lord Rayleigh, ‘‘Theory of Sound’’.

Lord Rayleigh’s quote is an eminently suitable introduction to this chapter. According to Porter *et al.* [58], the modal analysis of dynamical systems is, of course, one of the best known and most extensively cultivated fields of classical physics. In fact, modal analysis is the key to the development of optimal structural systems and has been extensively used by structural engineers. Our key motivation in using a modal approach to control is prompted by possible implications for the structural design of the machine. With more and more demanding requirements on precision machines, it is important to understand the controller-structure interaction and use results from the analysis of the structure to optimize the controller and vice-versa. In the words of Porter *et al.* [58], the central concept of modal control is very simple : it is that of generating the input vector of a system by linear feedback of the state vector in such a way that prescribed eigenvalues are associated with the dynamical modes of the resulting closed-loop system.

The state-feedback modal assignment problem in control system design is essentially an inverse eigenvalue problem. It should be noted that both state and output feedback have been used in the solution of the modal assignment problem with the latter presenting significantly greater challenges. In this thesis, we restrict ourselves to state feedback and concentrate on obtaining explicit relations to illustrate the controller-structure interaction. The modal control problem has resulted in a vast collection of literature on the exact assignment of eigenvalues to the closed-loop system. This technique as applied to single-input systems is better known as pole-placement. It is a well-known fact now that, apart from the case of single-input systems, specification of the closed-loop eigenvalues does not uniquely determine a closed-loop system. The source of nonuniqueness can be identified as coming from the freedom offered by state feedback beyond eigenvalue assignment, in selecting the associated eigenvectors from an admissible set [48] and leads to an infinity of solutions to the problem of determining a feedback gain matrix. This freedom has been widely used to solve gain minimization or suppression problems [58] [72], mode decoupling problems [48] [2] [62], disturbance suppression problems [87] [19] and to increase robustness [35] [71]. One of the drawbacks of such a modal assignment procedure as compared with some of the other multivariable control techniques such as  $\mathcal{H}_\infty$  and  $\mathcal{H}_2$  is that the synthesis procedure does not guarantee stability robustness with respect to even parameter variations in the plant dynamics. However, due to a significant amount of work by various researchers, a lot of desirable control requirements, for example, low eigenvalue sensitivity in the time domain and good robustness in the frequency domain [71] have been successfully incorporated into eigenstructure assignment. Eigenstructure assignment has primarily found considerable use in the aerospace industry in both civil and military applications, a notable example being the lateral motion stability augmentation system of the Airbus A320 aircraft and its successors [42].

On the other hand, it can be argued that application of  $\mathcal{H}_\infty$  and  $\mathcal{H}_2$  methods to the solution of the control problem leads to very high order and conservative controllers which pose problems with real-time implementation besides not realizing full



performance capability. Controller order reduction is used in such cases to realize lower-order controllers suitable for real-time implementation. The physical intuition into the problem is lost as a result of all these mathematical manipulations. Additionally, any hopes of integrating the mechanical or structural design with the controller design are lost.

Traditionally, the eigenstructure or modal assignment problem is carried out as a two-step procedure; either the desired eigenvalues are assigned first and then the resulting eigenvectors are accounted for, or the desired eigenvectors are selected first and then the resulting eigenvalues are accounted for. Unfortunately, prespecification of the eigenvalues has a restrictive influence on the eigenvectors and vice-versa. In order to avoid such restricted designs, robust modal assignment methods have been developed to take advantage of the fact that in practice, especially for MIMO control problems, exact pole assignment is seldom required. Instead, the closed-loop eigenvalues are allowed to vary in a small region in the complex plane [55] [84] [17]. Various optimality criteria and cost functions are established and the assignment problem is set up as a nonlinear optimization problem. Again, physical intuition into the controller-structure interaction is lost amongst the plethora of cost functions and optimality criteria.

In this chapter, we follow a similar approach in that, we allow the closed-loop eigenvalues to vary inside desired regions in the complex left-half plane. We express the errors between the attainable and desired closed-loop eigenvectors as an explicit function of the closed-loop eigenvalues. A unique parametrization of the closed-loop eigenvectors offers an interesting closed-form expression for this variation and has implications for the design of the open-loop system. Initially, we consider the general problem of modal control of linear systems with state feedback, and later specialize the concepts developed to a class of linear non-gyroscopic, conservative structural systems. These structural systems model the class of precision machines considered in this thesis and permit simplification to the solution of the problem.

We first note the following facts about the modal behavior of a system.

- **Eigenvalues** or natural frequencies of the system determine the stability of the

closed loop system (negative real parts) and the speed of response (bandwidth).

- **Eigenvectors** or mode shapes of the system determine the shape of the transient response of the closed loop system. The response of a linear system can usually be expressed as a sum of the modes weighted by the mode participation factors.

This is readily apparent from the equations (1.4) through (1.8) given in Chapter 1. We repeat them here to aid the reader in following the developments of this chapter.

$$\begin{aligned}\dot{\mathbf{x}}(t) &= \mathbf{A}_c \mathbf{x}(t) + \mathbf{B}_r \mathbf{r}(t) + \mathbf{E} \mathbf{d}(t) \\ \mathbf{z}(t) &= \mathbf{C}_p \mathbf{x}(t)\end{aligned}$$

where  $\mathbf{x}(t) \in \mathfrak{R}^n$  is the state vector,  $\mathbf{z}(t) \in \mathfrak{R}^p$  the performance measure that is required to be held small,  $\mathbf{r}(t) \in \mathfrak{R}^m$  the reference,  $\mathbf{d}(t) \in \mathfrak{R}^r$  the disturbance,  $\mathbf{A}_c$  the closed-loop state matrix,  $\mathbf{B}_r$  the reference coupling matrix,  $\mathbf{E}$  the disturbance coupling matrix and  $\mathbf{C}_p$  the performance matrix. Now, the zero state response of the performance measure is given by the integral,

$$\mathbf{z}(t) = \mathbf{C}_p \int_0^t e^{\mathbf{A}_c(t-\tau)} [\mathbf{B}_r \mathbf{r}(\tau) + \mathbf{E} \mathbf{d}(\tau)] d\tau \quad (8.1)$$

Substituting the spectral decomposition of  $\mathbf{A}_c = \mathbf{\Phi} \mathbf{\Lambda} \mathbf{\Psi}^T$  in the above,

$$\mathbf{z}(t) = \mathbf{C}_p \mathbf{\Phi} \int_0^t e^{\mathbf{\Lambda}(t-\tau)} [\mathbf{\Psi}^T \mathbf{B}_r \mathbf{r}(\tau) + \mathbf{\Psi}^T \mathbf{E} \mathbf{d}(\tau)] d\tau \quad (8.2)$$

we observe that the shape of the response to both reference signals and disturbance inputs is significantly influenced by the left  $\mathbf{\Phi}$  and right modal matrices  $\mathbf{\Psi}$ .  $\mathbf{\Lambda}$  is the matrix of eigenvalues.

We initially make the assumption that the matrix  $\mathbf{A}_c$  is diagonalizable. Under this assumption, we can rewrite the spectral decomposition of the closed loop matrix

as :

$$\mathbf{A}_c = \Phi \Lambda \Psi^T = \sum_{i=1}^n \lambda_i \phi_i \psi_i^T \quad (8.3)$$

The performance measure  $\mathbf{z}(t)$  is then given by

$$\begin{aligned} \mathbf{z}(t) &= \mathbf{C}_p \sum_{i=1}^n \mathbf{z}_i(t) \\ &= \sum_{i=1}^n \int_0^t e^{\lambda_i(t-\tau)} \mathbf{C}_p \phi_i \psi_i^T \mathbf{B}_r \mathbf{r}(\tau) d\tau + \sum_{i=1}^n \int_0^t e^{\lambda_i(t-\tau)} \mathbf{C}_p \phi_i \psi_i^T \mathbf{E} \mathbf{d}(\tau) d\tau \end{aligned} \quad (8.4)$$

Equation (8.4) shows the effects of disturbance on the performance measure. To achieve perfect disturbance attenuation, we could require that the closed-loop left eigenvectors  $\psi_i$  lie in the left null-space of the disturbance coupling matrix  $\mathbf{E}$  [19]. This null-space has dimension  $n - r$  and hence we can choose  $n - r$  closed-loop left eigenvectors to be the orthogonal basis vectors for this null space. The remaining  $r$  closed-loop eigenvectors can then be picked to be in the null space of the performance matrix  $\mathbf{C}_p$ . By picking these vectors to be as orthogonal a set as possible we obtain better closed-loop robustness to uncertainty in the model and control gains [35]. We thus see that the choice of closed-loop eigenvectors affects the closed-loop response of the system significantly and needs to be considered in the design of high- performance systems.

To put things in a mechanical context, shaping the modes of vibration is a big challenge in structural control. In our formulation of the active structural control problem, we do not require a fixed natural frequency. Rather, we explore the (explicit) change in the mode shape of the controlled structure with natural frequency and use our knowledge of this variation to choose a natural frequency which optimizes some other measure such as the least-squared error between the desired closed-loop modeshape and the attainable modeshape. At the same time, we also look for answers to the inverse problem, *i.e.*, “How could one design the mode shapes and natural frequencies of the open-loop system to achieve the desired closed-loop modes ?”

We start by describing the eigenvalue problem for linear systems. This is followed by a discussion on a class of linear non-gyroscopic, conservative structural systems. We cast the equations of motion of such systems in a form similar to that of the linear problem. The rest of the discussions in this chapter are carried out in the context of standard state-space systems, but can readily be applied to the structural problem by replacing the terms in the equations appropriately. We discuss the pole placement problem first and trace the approaches to pole placement that have evolved over the years especially as applied to MIMO problems. We then review the work done on the assignment of eigenvectors or rather a projection of the desired eigenvectors onto the attainable subspace. This has led to work on selective assignment of eigenvectors - we show this selective assignment fails in reality under certain “singular” conditions. Following this, we derive a unique eigenvector assignment procedure. For structural systems, the attainable closed-loop eigenvector is expressed explicitly in terms of the closed-loop eigenvalues and the flexible modes of the system. It is also shown that under special conditions, the desired closed-loop eigenvector can be realized exactly. We illustrate the application of the assignment procedure to specific problems in state-space and structural systems. We conclude by application of the control algorithm to the wafer stepper and demonstrating performance improvements in settling time.

## 8.2 Preliminaries and Problem Statement

Consider the system given by the state and output equations

$$\begin{aligned}\dot{\mathbf{x}} &= \mathbf{Ax} + \mathbf{Bu} \\ \mathbf{y} &= \mathbf{Cx} + \mathbf{Du}\end{aligned}\tag{8.5}$$

where  $\mathbf{A}$  is the open loop system matrix,  $\mathbf{B}$  the control influence matrix,  $\mathbf{C}$  the sensor matrix,  $\mathbf{D}$  the direct feedthrough matrix,  $\mathbf{x} \in \mathfrak{R}^n$  the state vector,  $\mathbf{u} \in \mathfrak{R}^m$  the control input vector, and  $\mathbf{y} \in \mathfrak{R}^p$  the measurement vector. We consider the state feedback regulator problem under the assumption that the system is controllable and the input

matrix  $\mathbf{B}$  has full column rank. This is always the case in a minimal realization of any physical system and does not lead to any loss of generality. The control law using state feedback is given by

$$\mathbf{u} = -\mathbf{K}\mathbf{x} \quad (8.6)$$

where  $\mathbf{K} \in \mathfrak{R}^{m \times n}$  is the control gain matrix that is to be determined. Substituting the control law given by (8.6) into the state equations (8.5) leads to the following closed loop state equations

$$\begin{aligned} \dot{\mathbf{x}} &= (\mathbf{A} - \mathbf{BK})\mathbf{x} \\ \Rightarrow \dot{\mathbf{x}} &= \mathbf{A}_c\mathbf{x} \end{aligned}$$

where

$$\mathbf{A}_c = \mathbf{A} - \mathbf{BK} \quad (8.7)$$

The problem of eigenstructure assignment is now to assign “as closely as possible” the desired eigenvalues  $\lambda_i^d$  and eigenvectors  $\phi_i^d$  to the closed loop system above. This allows us to specify both the shape and speed of response besides ensuring the stability of the closed loop system. We wish to find the control gain matrix  $\mathbf{K}$  such that the closed loop matrix  $\mathbf{A}_c$  has the desired modal properties (or comes close to having them). We start by expressing the error between the attainable eigenvalues/eigenvectors and the desired ones as follows :

$$\lambda_i = \lambda_i^d + e_i \quad (8.8)$$

$$\phi_i = \phi_i^d + \epsilon_i \quad (8.9)$$

$e_i$  and  $\epsilon_i$  are the errors between the attainable and desired eigenvalues and eigenvectors respectively, and our task is to minimize these errors. Given that we have a self-conjugate set of eigenvalues and eigenvectors, we have the familiar eigenvalue

problem

$$\begin{aligned}(\lambda_i \mathbf{I} - \mathbf{A}_c) \phi_i &= 0 \\ \Rightarrow (\lambda_i \mathbf{I} - \mathbf{A} + \mathbf{BK}) \phi_i &= 0\end{aligned}\tag{8.10}$$

Substituting  $\mathbf{K}\phi_i = \mathbf{v}_i$  into the above equations leads to

$$(\lambda_i \mathbf{I} - \mathbf{A}) \phi_i + \mathbf{B}\mathbf{v}_i = 0$$

Under the assumption of distinct eigenvalues, we can write the Jordan canonical form  $\mathbf{\Lambda}$ , the right modal matrix  $\mathbf{\Phi}$ , and the control modal matrix  $\mathbf{U}$  as follows :

$$\begin{aligned}\mathbf{\Lambda} &= \text{diag} \{ \lambda_i \} \\ \mathbf{\Phi} &= (\phi_1, \phi_2, \dots, \phi_n) \\ \mathbf{U} &= (\mathbf{v}_1, \mathbf{v}_2, \dots, \mathbf{v}_n)\end{aligned}\tag{8.11}$$

Also, by our earlier definition  $\mathbf{K}\phi_i = \mathbf{v}_i$ , the control gain is given by

$$\mathbf{K} = \mathbf{U}\mathbf{\Phi}^{-1}\tag{8.12}$$

From the above discussion, we note that the eigenvalues and the eigenvectors can not be specified arbitrarily. They need to satisfy the equation

$$(\lambda_i \mathbf{I} - \mathbf{A}) \phi_i = -\mathbf{B}\mathbf{v}_i\tag{8.13}$$

While (8.13) is the constraint equation for unique eigenvalues, we can follow a similar procedure for confluent eigenvalues using generalized eigenvector chains. Klein and Moore [37] outline the following procedure to realize “allowable” Jordan structures of the closed-loop system.

The closed-loop generalized eigenvalue problem is given by :

$$\begin{aligned}\lambda_j \phi_j &= \mathbf{A}_c \phi_j \\ \lambda_j \phi_{i+1} + \phi_i &= \mathbf{A}_c \phi_{i+1}, \quad j \leq i < k\end{aligned}\tag{8.14}$$

where  $k$  is the multiplicity of the eigenvalue  $\lambda_j$ . As in the case of distinct eigenvalues, the constraint equation can be derived as

$$\begin{aligned}(\lambda_j \mathbf{I} - \mathbf{A}) \phi_j &= -\mathbf{B} \mathbf{v}_j \\ (\lambda_j \mathbf{I} - \mathbf{A}) \phi_{i+1} &= -\mathbf{B} \mathbf{v}_{i+1} - \phi_i, \quad j \leq i < k\end{aligned}\tag{8.15}$$

In both (8.13) and (8.15) we have  $n$  equations in  $m$  unknowns, with the number of states  $n$  typically much greater than the number of control inputs  $m$ , leading to an overconstrained problem. These equations are usually inconsistent for arbitrary choices of  $\lambda_i^d$  and  $\phi_i^d$ . The whole problem of eigenstructure assignment is one that constrains the attainable eigenvalues and eigenvectors to be as close as possible to the desired values according to some (for example weighted least squares) criterion while satisfying the constraint condition given in these equations. Unless specified otherwise, we will consider only the problem of distinct eigenvalues expressed by (8.13). The developments for the problem of confluent eigenvalues in (8.15) are similar and are not shown here.

There are various methods to solve this set of overconstrained equations. Before proceeding further with the solution of (8.13), we consider reduction of the equations of motion of machine tool structures to the form above. This permits easy application of the theory developed to structural applications.

### 8.3 Structural Systems

In this section and for the remainder of the thesis, we consider lumped-parameter systems. While most systems are continuous, we assume that a lumped-parameter

model is available or may be created through the application of mode-truncation, finite-element or finite-difference methods. The general form of equations of motion for a structural system can be written as follows, see Meirovitch [47] :

$$\mathbf{M}\ddot{\mathbf{x}} + (\mathbf{C} + \mathbf{G})\dot{\mathbf{x}} + (\mathbf{K} + \mathbf{H})\mathbf{x} = \mathbf{F}\mathbf{u} \quad (8.16)$$

where  $\mathbf{M}$  is the symmetric mass matrix,  $\mathbf{C}$  the symmetric damping matrix,  $\mathbf{G}$  the skew-symmetric gyroscopic matrix,  $\mathbf{K}$  the symmetric stiffness matrix,  $\mathbf{H}$  the skew-symmetric circulatory matrix and  $\mathbf{F}$  the control influence matrix;  $\mathbf{x}$  is the vector of generalized coordinates and  $\mathbf{u}$  is a vector of control inputs. Note that the viscous damping and circulatory forces appearing in the above equations are non-conservative. Also, gyroscopic and circulatory terms appear only in structures that are spinning or possess spinning parts.

The machine tool structures that we consider in this thesis either do not have spinning parts (*e.g.*, wafer steppers, coordinate measuring machines) or in those cases that possess spinning parts (*e.g.*, diamond turning machines, hard disk drives), the gyroscopic terms are negligible. In such cases, the equations of motion can be simplified as follows :

$$\mathbf{M}\ddot{\mathbf{x}} + \mathbf{C}\dot{\mathbf{x}} + \mathbf{K}\mathbf{x} = \mathbf{F}\mathbf{u} \quad (8.17)$$

Using the generalized displacements and velocities as state variables, we can now cast the problem in a state space form :

$$\begin{Bmatrix} \dot{\mathbf{x}} \\ \ddot{\mathbf{x}} \end{Bmatrix} = \begin{pmatrix} \mathbf{0} & \mathbf{I} \\ -\mathbf{M}^{-1}\mathbf{K} & -\mathbf{M}^{-1}\mathbf{C} \end{pmatrix} \begin{Bmatrix} \mathbf{x} \\ \dot{\mathbf{x}} \end{Bmatrix} + \begin{Bmatrix} \mathbf{0} \\ \mathbf{M}^{-1}\mathbf{F} \end{Bmatrix} \mathbf{u} \quad (8.18)$$

We further observe that damping is negligible in most machine tool structures [49]. This assumption is consistent with most mechanical structures where damping is added by a controller in the absence of any significant damping in the structure itself. Sources of damping can be introduced as a perturbation for a final analysis



and usually do not affect the stability of the system although in theory performance could deteriorate due to the additional source of coupling.

We assume state feedback of the form

$$\begin{aligned} \mathbf{u} &= -\mathbf{K}\mathbf{x} \\ &= -\begin{pmatrix} \mathbf{K}_x & \mathbf{K}_v \end{pmatrix} \begin{Bmatrix} \mathbf{x} \\ \dot{\mathbf{x}} \end{Bmatrix} \end{aligned}$$

Substituting for the control law and under the assumption of zero damping in (8.18), we obtain the closed-loop equations of motion as follows

$$\begin{Bmatrix} \dot{\mathbf{x}} \\ \ddot{\mathbf{x}} \end{Bmatrix} = \begin{pmatrix} \mathbf{0} & \mathbf{I} \\ -\mathbf{M}^{-1}\mathbf{K} - \mathbf{M}^{-1}\mathbf{F}\mathbf{K}_x & -\mathbf{M}^{-1}\mathbf{F}\mathbf{K}_v \end{pmatrix} \begin{Bmatrix} \mathbf{x} \\ \dot{\mathbf{x}} \end{Bmatrix} \quad (8.19)$$

This leads to the closed-loop eigenvalue problem

$$\lambda_i \begin{Bmatrix} \phi_{x_i} \\ \phi_{v_i} \end{Bmatrix} = \begin{pmatrix} \mathbf{0} & \mathbf{I} \\ -\mathbf{M}^{-1}\mathbf{K} - \mathbf{M}^{-1}\mathbf{F}\mathbf{K}_x & -\mathbf{M}^{-1}\mathbf{F}\mathbf{K}_v \end{pmatrix} \begin{Bmatrix} \phi_{x_i} \\ \phi_{v_i} \end{Bmatrix} \quad (8.20)$$

With our choice of state variables, the partitioned form of the eigenvectors reflects the mode shapes of the structure. In fact, the vector  $\phi_{x_i}$  is exactly the mode shape of the vibrating structure. The matrix equations can now be expanded to get

$$\begin{aligned} \lambda_i \phi_{x_i} &= \phi_{v_i} \\ \lambda_i \phi_{v_i} &= -(\mathbf{M}^{-1}\mathbf{K} - \mathbf{M}^{-1}\mathbf{F}\mathbf{K}_x) \phi_{x_i} - \mathbf{M}^{-1}\mathbf{F}\mathbf{K}_v \phi_{v_i} \end{aligned}$$

Carrying out a few substitutions and simplifying, we obtain the constraint equation for structural problems :

$$\lambda_i^2 \phi_{x_i} = -\mathbf{M}^{-1}\mathbf{K}\phi_{x_i} - \mathbf{M}^{-1}\mathbf{F}\mathbf{v}_{x_i} - \mathbf{M}^{-1}\mathbf{F}\mathbf{v}_{v_i} \quad (8.21)$$

where we have defined the control modal vectors

$$\mathbf{K}_x \phi_{x_i} = \mathbf{v}_{x_i}$$

$$\mathbf{K}_v \phi_{v_i} = \mathbf{v}_{v_i}$$

To cast the structural problem in the same form as the state variable problem discussed in section 8.2, we define the following matrices :

$$\mathbf{A}_x = -\mathbf{M}^{-1}\mathbf{K}$$

$$\mathbf{B}_x = \mathbf{M}^{-1}\mathbf{F}$$

$$\mathbf{v}_i = \mathbf{v}_{x_i} + \mathbf{v}_{v_i}$$

Substituting in (8.21) we obtain an equation very similar to (8.13).

$$(\lambda_i^2 \mathbf{I} - \mathbf{A}_x) \phi_{x_i} = -\mathbf{B}_x \mathbf{v}_i \quad (8.22)$$

We note that these constraint equations are very similar to the ones given in (8.13) if we replace  $\lambda_i$  with  $\lambda_i^2$ ,  $\mathbf{A}$  with  $\mathbf{A}_x$ ,  $\mathbf{B}$  with  $\mathbf{B}_x$  and  $\phi_i$  with  $\phi_{x_i}$ . In the sections to follow, we will consider the solution to (8.13). It is understood that for undamped, non-gyroscopic structural systems, the solution to (8.22) is similar to the one for (8.13) with the appropriate substitutions given above. There are some special characteristics of (8.22) which we point out and exploit in subsequent sections.

## 8.4 Review of Literature

An excellent review of literature on eigenstructure can be found in the recent text written by Liu and Patton [42]. In this section, we trace the key results that are applicable to eigenstructure assignment for machine tool structures. Wonham [85] presented the fundamental result on eigenvalue assignment that the closed-loop eigenvalues of any controllable system may be arbitrarily assigned by state feedback control. Freedom offered by state feedback beyond specification of the closed-loop eigenvalues was first

identified by Moore [48] in 1976. The necessary and sufficient conditions for the existence of a state feedback controller which yields the prescribed eigenvalues and eigenvectors were derived for the case where the closed loop eigenvalues were distinct. Since then, there have been hundreds of papers concerning the problem of eigenstructure assignment and its applications. Both state and output feedback have been addressed by various authors.

The additional freedom offered by the MIMO pole assignment problem has been used by various researchers in different ways. Some researchers have used the additional degrees of freedom to specify the desired closed loop eigenvectors [2]. These eigenvectors may not be attainable since the problem of specifying both the closed loop eigenvalues and the eigenvectors makes the modal assignment problem an over-constrained one. The solution is usually obtained by minimizing the least squared error between the desired eigenvectors and the achievable eigenvectors while holding the eigenvalues fixed. We term this procedure "Eigenvalue Assignment". This has been studied by various researchers and has been applied with success in the aerospace industry [2] [61] [62]. Meirovitch *et al.* [47] compute the feedback gain to move the poles around to desired location and retain the open loop eigenvectors in an application of the Independent Modal Space Control (IMSC) technique.

By introducing a set of free parameter vectors, a parametric solution of the eigenvalue assignment problem in MIMO systems was developed by Porter and D'Azzo [59], [60]; Fahmy and O'Reilly [22], [23]; and Roppenecker [66]. Based on the parametric solution, several iterative and non-iterative algorithms have emerged to either improve the performance of the closed-loop system or minimize the control effort. Amongst the iterative schemes, the KNV algorithms (Kautsky *et al.* [35])<sup>1</sup>, the rank- $n$ -update algorithm (Burrows and Patton [16]) iteratively minimize some sensitivity measure of the closed-loop system in terms of the conditioning of the closed-loop modal matrix, through an orthogonal projection approach. Their algorithm for the MIMO pole placement problem designs the controller which is maximally robust to changes in the system matrices and the controller gain matrix. Direct non-linear programming

---

<sup>1</sup>Implemented in Matlab as the *place* algorithm.

techniques are used to minimize scalar sensitivity measures such as the closed-loop conditioning and the closed-loop normality indices. In non-iterative schemes, a projection algorithm (Juang *et al.* [33]) is used such that closed-loop eigenvectors are chosen specially to maximize their orthogonal projection to the desired closed-loop modal matrix or its closest unitary matrix; thereby minimizing the sensitivity of the closed-loop system.

In practice, modeling errors are introduced when a model is derived by linearizing the system equations and/or there is some parameter uncertainty. It is necessary that the real system be stabilized even when the control system is designed using an incorrect model. Although some eigenstructure assignment schemes are concerned with eigenvalue sensitivity such as the quadratic norm condition number of the closed-loop modal matrix [35] and the sum of the squares of the norms of the quadratic norms of the left eigenvectors, it is found that a small improvement in the sensitivity measure may result in a significant degradation in a frequency-domain measure of robustness [70]. In contrast to eigenvalue sensitivity, the standard  $\mathcal{H}_\infty$  controller guarantees closed-loop stability and ensures that the disturbance-performance transfer function is less than a given bound. But, one of the practical concerns of control design (especially in servo systems) as brought out earlier is the time-domain performance which is mainly governed by the closed-loop eigenvalues and mode shapes. While the standard  $\mathcal{H}_\infty$  control design problem is primarily concerned with closed-loop stability and frequency domain specifications, it says little about transient performance. There has been some work done of late to realize the performance afforded by eigenstructure assignment along with the robust stability of  $\mathcal{H}_\infty$  schemes. Here, a robust performance index defined to be a combination of various sensitivity functions of the closed-loop system in the frequency domain is minimized using the extra degrees of freedom in eigenstructure assignment by state feedback [41].

A review of various papers that address multi-objective eigenstructure assignment and their applications can be found in the text by Liu and Patton [42]. In this thesis, we address the problem of mode shape assignment rigorously since the transient performance (settling time) of a step and repeat wafer stepper of the kind considered

in this thesis is a key parameter.

In most MIMO control problems, specification of the desired closed loop eigenvalues is an ad-hoc process. In some cases, it might be more desirable to specify just the closed-loop eigenvectors and use an algorithm to pick a closed-loop eigenvalue that minimizes the error between the desired and attainable eigenvectors according to some defined (*e.g.* least squares) criterion. We term this procedure “Eigenvector Assignment”. There is a class of structural problems where the specification of the desired mode shapes (eigenvectors) is a more natural way to specify the control problem than that of specification of the natural frequencies (eigenvalues). Hence, the problem is more that of eigenvector assignment than eigenvalue assignment. Usually however, the problem is a combination of the two. We should however note that we are always constrained to have the closed-loop eigenvalues in the left-half plane to ensure stability of the closed loop system.

We first set up the eigenstructure assignment problem for state space systems and show how it can be specialized to the case of certain structural systems which are representative of precision machine tools.

## 8.5 Eigenvalue Assignment for State-Space Systems

**Problem 8.1** *Given a set of desired self-conjugate eigenvalues  $\lambda_i$  and a set of desired self-conjugate vectors  $\phi_i^d$ , assign the eigenvalues exactly and minimize the 2-norm of the error  $\epsilon_i$  between the desired and achievable eigenvectors.*

Consider (8.13) which is valid for the distinct eigenvalues for the closed loop system matrix  $\mathbf{A}_c$ . This implies that the attainable eigenvector  $\phi_i$  must be in the subspace spanned by the columns of  $\mathbf{L}_i$ , *i.e.*,

$$\phi_i = \mathbf{L}_i \mathbf{v}_i \tag{8.23}$$

where

$$\mathbf{L}_i = -(\lambda_i \mathbf{I} - \mathbf{A})^{-1} \mathbf{B} \quad (8.24)$$

The required inverse in (8.24) exists as long as the desired closed-loop eigenvalues are distinct from the open-loop ones, which we assume from now on. The subspace spanned by the columns of  $\mathbf{L}$  has dimension  $m$  which is equal to the rank of  $\mathbf{B}$ , *i.e.*, the number of independent control variables. We see that to obtain the desired closed loop eigenvectors  $\phi_i^d$  exactly, they must reside in the  $m$  dimensional subspace spanned by the columns of  $\mathbf{L}_i$ . We observe the following :

- The number of independent control variables determines the dimension of the subspace in which the achievable eigenvectors must reside.
- The orientation of this subspace is determined by open-loop system matrices  $\mathbf{A}$  and  $\mathbf{B}$  and by the desired closed-loop eigenvalues  $\lambda_i$ .

Equation (8.23) also illustrates the freedom offered by linear state feedback is precisely that of choosing the dynamical control modes  $\mathbf{v}_i$ . However, our interest is in the specification and design of the modes of the system  $\phi_i$ . This is an overconstrained problem as discussed in the previous section.

Next, consider the eigenvectors corresponding to the repeated eigenvalue  $\lambda_j$  as in (8.15).

$$\begin{aligned} \phi_j &= -(\lambda_j \mathbf{I} - \mathbf{A})^{-1} \mathbf{B} \mathbf{v}_j \\ \phi_{i+1} &= -(\lambda_j \mathbf{I} - \mathbf{A})^{-1} \mathbf{B} \mathbf{v}_{i+1} - (\lambda_j \mathbf{I} - \mathbf{A})^{-1} \phi_i, \quad j \leq i < k \end{aligned} \quad (8.25)$$

For deriving the assignability condition for  $\phi_{i+1}, j \leq i < k$ , the expression for  $\phi_{i+1}$  can be rewritten as

$$\phi_{i+1} + (\lambda_j \mathbf{I} - \mathbf{A})^{-1} \phi_i = -(\lambda_j \mathbf{I} - \mathbf{A})^{-1} \mathbf{B} \mathbf{v}_{i+1}, \quad j \leq i < k$$

From this equation, we can conclude that if the eigenvector  $\phi_{i+1}, j \leq i < k$  is chosen

in such a way that the vector  $\phi_{i+1} + (\lambda_j \mathbf{I} - \mathbf{A})^{-1} \phi_i$  lies precisely in the space spanned by the columns of  $\mathbf{L}_j = -(\lambda_j \mathbf{I} - \mathbf{A})^{-1} \mathbf{B}$ , it will be attained exactly.

In general, a desired eigenvector  $\phi_i^d$  may not reside in its prescribed subspace, and hence we look for a best fit to this eigenvector. This best fit in the sense of least squares (minimum 2-norm of the error  $\epsilon_i$ ) is given by projecting  $\phi_i^d$  onto the subspace spanned by the columns of  $\mathbf{L}_i$  as shown in Figure 8-1. We obtain this best fit  $\phi_i$  by

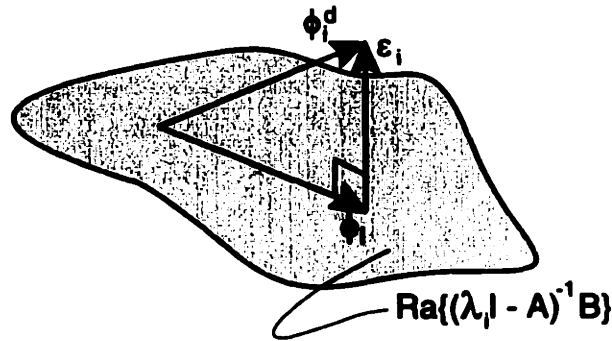


Figure 8-1: Characterization of the space of attainable eigenvectors. Projecting the desired eigenvector  $\phi_i^d$  onto this space results in minimum 2-norm of the error  $\|\epsilon_i\|_2$

solving the normal equations

$$\mathbf{v}_i = (\mathbf{L}_i' \mathbf{L}_i)^{-1} \mathbf{L}_i' \phi_i^d \quad (8.26)$$

$$\phi_i = \mathbf{L}_i \mathbf{v}_i \quad (8.27)$$

The vectors  $\mathbf{v}_i$  and  $\phi_i$  are then assembled to form the matrices  $\mathbf{U}$  and  $\Phi$  respectively as in (8.12). We can then solve for the control gain using (8.12). A different equation that leads to a similar gain matrix  $\mathbf{K}$  is derived by Pradhan *et al.* [62].

$$\mathbf{K} = (\mathbf{B}' \mathbf{B})^{-1} \mathbf{B}' (\mathbf{A} - \mathbf{A}_c) \quad (8.28)$$

Using this control gain matrix in the control law given in (8.6), we obtain a closed loop system with modal properties as close as possible to the desired values in a least squares sense. To conclude, we make a few further observations on this assignment procedure.

- If a desired eigenvector  $\phi_i^d$  is nearly orthogonal to the subspace spanned by the

columns of  $\mathbf{L}_i$ , there is little chance of affecting the system transients by  $\phi_i$  as computed above. The reverse is true when  $\phi_i^d$  lies in the subspace.

- For a single-input system,  $\mathbf{B}$  is simply a column vector, hence there is no possibility of affecting the transient response by altering the eigenvectors. This is because only one element of each eigenvector can be specified ( $m = 1$ ), which will not alter the transient response.
- If a large number of entries in the eigenvectors are to be assigned, more independent control variables are necessary. When the rank of  $\mathbf{B}$  is  $n$ , the closed loop eigenvectors can be completely specified.

The method has the advantage that the eigenvalues are known and hence a degree of stability can be built into the system by choosing the eigenvalues carefully. However, the disadvantage of this method lies in the fact that a lot of freedom in the assignment procedure is lost because the closed-loop eigenvalues are held fixed. The variation of the subspace spanned by the columns of  $\mathbf{L}_i$  with respect to changes in the closed-loop eigenvalues  $\lambda_i$  is not known. The sensitivity of this subspace with respect to the closed-loop eigenvalues is of special importance. In a typical structural control problem, it might be of more importance to obtain certain mode shapes exactly and the natural frequencies for these modes are not much of a concern as long as the closed loop system remains stable. There are other modes in which it is important that the eigenvalues be obtained exactly and the eigenvectors can be obtained according to the algorithm described in this section.

### 8.5.1 Partial Specification of Eigenvectors

We realize that we have only  $m$  degrees of freedom in specifying the eigenvector - this means that only  $m$  components of the eigenvector can be independently specified. This is usually not a significantly limiting condition since in most large-scale systems, one is interested in specifying how only certain states behave in a given mode.

We handle this by using so-called permutation or weighting matrices as follows. For any given mode, let  $r$  denote the number of terms in an eigenvector that are



desired to be specified. When  $r \leq m$ , we can specify all  $r$  arbitrary terms in the eigenvector and the eigenvalue corresponding to the desired mode also by defining weighting matrices  $\mathbf{W}_i$  for each mode. It is assumed without loss of generality that the weighting matrices have full rank  $r$ . We have

$$\begin{aligned} \mathbf{L}_i \mathbf{v}_i &= \boldsymbol{\phi}_i = \boldsymbol{\phi}_i^d + \boldsymbol{\epsilon}_i \\ \Rightarrow \mathbf{W}_i \mathbf{L}_i \mathbf{v}_i &= \mathbf{W}_i \boldsymbol{\phi}_i^d \end{aligned} \quad (8.29)$$

where we have used the fact that  $\mathbf{W}_i$  has full row rank and the assumption that  $\mathbf{W}_i \mathbf{L}_i$  to remove the error term  $\boldsymbol{\epsilon}_i$  since the above system of equations is underconstrained, at most having  $r$  equations in  $m$  unknowns. We can choose the least-squared solution (amongst many possible) to get

$$\mathbf{v}_i = (\mathbf{L}_i' \mathbf{W}_i' \mathbf{W}_i \mathbf{L}_i)^{-1} \mathbf{L}_i' \mathbf{W}_i' \mathbf{W}_i \boldsymbol{\phi}_i^d \quad (8.30)$$

$$\boldsymbol{\phi}_i = \mathbf{L}_i \mathbf{v}_i \quad (8.31)$$

The vectors  $\mathbf{v}_i$  and  $\boldsymbol{\phi}_i$  are then assembled as before to obtain the control gain as given in (8.12).

### 8.5.2 A Caveat

While the partial specification of eigenvectors has been propounded as a tool for various applications in the aerospace industry, there is one caveat that is not mentioned anywhere. This has to do with the zero dynamics and is illustrated by the following argument. We have an inconsistent set of equations if the desired closed-loop eigenvalue  $\lambda_i^d$  is a transmission zero of the system

$$\begin{pmatrix} s\mathbf{I} - \mathbf{A} & \mathbf{B} \\ \mathbf{W}_i & \mathbf{0} \end{pmatrix} \quad (8.32)$$

For the desired closed-loop eigenvalue  $\lambda_i^d$  to be a transmission zero of the above system of equations (8.32), the following will have to hold true :

$$\begin{pmatrix} \lambda_i \mathbf{I} - \mathbf{A} & \mathbf{B} \\ \mathbf{W}_i & \mathbf{0} \end{pmatrix} \begin{Bmatrix} \phi_i \\ v_i \end{Bmatrix} = \mathbf{0} \quad (8.33)$$

Equation (8.33) shows that the set of achievable eigenvectors  $\phi_i$  is spanned by the set of zero state directions and will be in the null-space of  $\mathbf{W}_i$ .

This is one case where the claim that the eigenvalue and  $m$  components of each eigenvector can be arbitrarily assigned to a linear system falls apart. A thorough literature search has not revealed the existence of this caveat. Our eigenvector assignment procedure reveals this inconsistency through a singularity as will be shown later.

### 8.5.3 Eigenvalue Assignment for Structural Systems

The procedure for structural systems is similar to that of state space systems with a few caveats. Consider (8.22) which is valid for the distinct eigenvalues of the closed loop system. This implies that the attainable eigenvector  $\phi_{xi}$  must lie in the subspace spanned by the columns of  $\mathbf{L}_{xi}$ , *i.e.*,

$$\phi_{xi} = \mathbf{L}_{xi} v_i \quad (8.34)$$

where

$$\mathbf{L}_{xi} = -(\lambda_i^2 \mathbf{I} - \mathbf{A}_x)^{-1} \mathbf{B}_x \quad (8.35)$$

We solve this set of overconstrained equations using a least squares procedure similar to the one in the previous section. We then obtain the closed loop eigenvectors by

setting

$$\phi_i = \begin{Bmatrix} \phi_{z_i} \\ \phi_{v_i} \end{Bmatrix} = \begin{Bmatrix} \phi_{z_i} \\ \lambda_i \phi_{z_i} \end{Bmatrix} \quad (8.36)$$

The eigenvectors given by (8.36) can be obtained exactly since they have already been projected down to the achievable subspace. We use these along with the control modal vectors  $v_i$  to compute the feedback gain matrix as shown in (8.12).

We now focus on the problem of “Eigenvector assignment” where we allow the closed-loop eigenvalues to vary in a small region in the complex plane. This permits us in most cases to reduce the error in the attainable eigenvector.

## 8.6 Eigenvector Assignment for State-Space Systems

Unlike eigenvalue assignment which leads to no error  $e_i$  between the attainable and desired eigenvalues, eigenvector assignment is an inexact process. We pose the eigenvector assignment problem as follows :

**Problem 8.2** *Given a set of desired self-conjugate vectors  $\phi_i^d$  minimize the 2-norm of the error  $\epsilon_i$  between the desired and achievable eigenvectors subject to the constraint given by (8.13) and the inequality constraint that  $\Re\{\lambda_i\} < 0$ .*

In the eigenvalue assignment procedure reviewed earlier, we had only  $m$  degrees of freedom in specifying the eigenvector - this means that only  $m$  components of the eigenvector can be independently specified. This is usually not a significantly limiting condition since in most large scale systems, one is only interested in specifying how certain states behave in a given mode rather than specifying the behavior of all the states. However, the weighted eigenvalue assignment can lead to an inconsistent set of equations when the desired closed-loop eigenvalue corresponds to a transmission zero of the system in (8.32). We term these modes to be *singular* modes. The weighted assignment procedure leads to a solution where, singular terms corresponding to the

non-zero entries of the state direction associated with the transmission zero could result amongst the unspecified components of the eigenvector. Normalization of the resulting eigenvector results in all the terms of the eigenvector except the singular terms being set to zero. This is due to the fact that, corresponding to a transmission zero, the only assignable closed-loop eigenvectors are the zero-state directions. Besides, the eigenvalue assignment procedure when used to assign  $m$  components of the closed-loop eigenvectors might not always result in a system that has low sensitivity to perturbations in the system matrices [35]. Besides, in certain cases, it might be desirable to assign more than  $m$  terms of the closed-loop modes. This is done through the eigenvector assignment procedure described in this section.

The shortcomings of the weighted assignment procedure for structural systems are addressed by explicitly relating the variation of the closed-loop eigenvectors to the closed-loop eigenvalues and the open-loop flexible modes. The singular modes for structural systems are those where certain masses behave as dynamic vibration absorbers. While explicitly illustrating these singularities, this procedure has advantages over the partial assignment procedure reviewed earlier in that the error  $\epsilon_i$  between the desired and achievable eigenvectors can be reduced further by using the additional degree of freedom available (since the closed-loop eigenvalue is not specified). Requirements on the achievable closed-loop eigenvalues associated with the specified modes might include a certain amount of damping besides the obvious requirement of stability.

Under the assumption that the control influence matrix  $\mathbf{B}$  has full column rank, we write the singular value decomposition of  $\mathbf{B}$  as follows :

$$\mathbf{B} = \begin{pmatrix} \vdots & \vdots & \vdots & \vdots & \vdots & \vdots & \vdots \\ \mathbf{u}_1 & \mathbf{u}_2 & \dots & \mathbf{u}_m & \mathbf{u}_{m+1} & \dots & \mathbf{u}_n \\ \vdots & \vdots & \vdots & \vdots & \vdots & \vdots & \vdots \end{pmatrix} \begin{pmatrix} \sigma_1 & \dots & 0 \\ & \ddots & \\ 0 & \dots & \sigma_m \\ 0 & \dots & 0 \\ & \ddots & \\ 0 & \dots & 0 \end{pmatrix} \begin{pmatrix} \dots & \mathbf{v}'_1 & \dots \\ & \vdots & \\ \dots & \mathbf{v}'_m & \dots \end{pmatrix}$$

or in matrix form

$$\mathbf{B}_{n \times m} = \mathbf{U}_B \boldsymbol{\Sigma}_B \mathbf{V}'_B \quad (8.37)$$

We also define the following submatrices :

$$\mathcal{R}a\{\mathbf{B}\} = \mathcal{R}a\{\mathbf{U}_{0B}\} = \mathcal{R}a\{\mathbf{u}_{Bi}\}_{1 \leq i \leq m} \quad (8.38)$$

$$\mathcal{R}a^\perp\{\mathbf{B}\} = \mathcal{R}a\{\mathbf{U}_{1B}\} = \mathcal{R}a\{\mathbf{u}_{Bi}\}_{m < i \leq n} \quad (8.39)$$

The above matrices span two of the important subspaces associated with  $\mathbf{B}$ .  $\mathbf{U}_{0B}$  forms an orthonormal basis for the range of  $\mathbf{B}$ , i.e.,  $\mathcal{R}a\{\mathbf{B}\}$  while  $\mathbf{U}_{1B}$  forms an orthonormal basis for the subspace orthogonal to the range of  $\mathbf{B}$ , i.e.,  $\mathcal{R}a^\perp\{\mathbf{B}\}$ . This allows us to rewrite the constraint equation (8.13) as follows :

$$\mathbf{U}'_{1B} (\lambda_i \mathbf{I} - \mathbf{A}) \boldsymbol{\phi}_i = \mathbf{0} \quad (8.40)$$

where we have multiplied both sides of (8.13) by  $\mathbf{U}'_{1B}$  and used orthogonality conditions to simplify the resulting expression. The results of the above developments are best seen geometrically as in Figure 8-2. From the figure, we see that the achievable

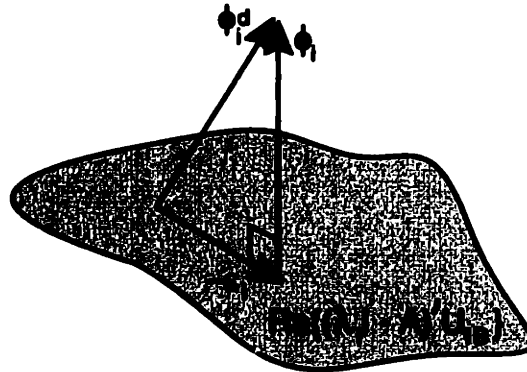


Figure 8-2: Characterization of the space of attainable eigenvectors.

eigenvectors need to be orthogonal to the range of  $(\lambda_i \mathbf{I} - \mathbf{A})' \mathbf{U}_{1B}$ . We further note that the desired eigenvectors  $\boldsymbol{\phi}_i^d$  might not be orthogonal to this subspace and the error  $\boldsymbol{\epsilon}_i$  that we seek to minimize is exactly that given by the projection of  $\boldsymbol{\phi}_i^d$  onto the

range of  $(\lambda_i \mathbf{I} - \mathbf{A})' \mathbf{U}_{1B}$ . We find that the error is then a function of the matrices  $\mathbf{A}$ ,  $\mathbf{U}_{1B}$  and the eigenvalue  $\lambda_i$ . The matrices  $\mathbf{A}$  and  $\mathbf{U}_{1B}$  are fixed based on the design of the plant and hence the only flexibility we have in reducing the error  $\epsilon_i$  is by changing the eigenvalue  $\lambda_i$ . We now derive an explicit expression for the error  $\epsilon_i$  in terms of the eigenvalue  $\lambda_i$ .

We first parametrize the achievable and desired eigenvectors into the two subspaces associated with  $\mathbf{B}$  and defined by the bases  $\mathbf{U}_{0B}$ , and  $\mathbf{U}_{1B}$ . This is done by projecting the vectors into the two subspaces using the projection matrices  $\mathbf{U}_{0B} \mathbf{U}'_{0B}$  and  $\mathbf{U}_{1B} \mathbf{U}'_{1B}$ . We have,

$$\begin{aligned}
 \phi_i &= \mathbf{U}_B \mathbf{z}_i = \begin{pmatrix} \mathbf{U}_{0B} & \mathbf{U}_{1B} \end{pmatrix} \begin{Bmatrix} \mathbf{z}_{0i} \\ \mathbf{z}_{1i} \end{Bmatrix} \\
 &= \phi_{0i} + \phi_{1i} \\
 \phi_i^d &= \phi_{0i}^d + \phi_{1i}^d \\
 \epsilon_i &= \epsilon_{0i} + \epsilon_{1i}
 \end{aligned} \tag{8.41}$$

We can now rewrite the constraint equation as follows :

$$\mathbf{U}'_{1B} (\lambda_i \mathbf{I} - \mathbf{A}) (\phi_{0i} + \phi_{1i}) = \mathbf{0} \tag{8.42}$$

Expanding the above equation, we get

$$\begin{aligned}
 \lambda_i \mathbf{U}'_{1B} \phi_{0i} + \lambda_i \mathbf{U}'_{1B} \phi_{1i} - \mathbf{U}'_{1B} \mathbf{A} \phi_{0i} - \mathbf{U}'_{1B} \mathbf{A} \phi_{1i} &= \mathbf{0} \\
 \lambda_i \underbrace{\mathbf{U}'_{1B} \mathbf{U}_{0B}}_{\mathbf{0}} \mathbf{z}_{0i} + \lambda_i \underbrace{\mathbf{U}'_{1B} \mathbf{U}_{1B}}_{\mathbf{I}} \mathbf{z}_{1i} - \mathbf{U}'_{1B} \mathbf{A} \mathbf{U}_{0B} \mathbf{z}_{0i} - \mathbf{U}'_{1B} \mathbf{A} \mathbf{U}_{1B} \mathbf{z}_{1i} &= \mathbf{0}
 \end{aligned}$$

Performing the indicated simplifications, we get

$$(\lambda_i \mathbf{I} - \mathbf{U}'_{1B} \mathbf{A} \mathbf{U}_{1B}) \mathbf{z}_{1i} = \mathbf{U}'_{1B} \mathbf{A} \mathbf{U}_{0B} \mathbf{z}_{0i} = \mathbf{U}'_{1B} \mathbf{A} \phi_{0i} \tag{8.43}$$

We now would like to minimize the 2-norm of the error  $\epsilon_i$ . This leads to a non-linear minimization problem given by,

$$\min_{\lambda_i} \|\epsilon_i\|_2^2 = \min_{\lambda_i} \|\epsilon_{0i} + \epsilon_{1i}\|_2^2 \quad (8.44)$$

subject to the constraint in (8.43). Instead of solving for the minimum value of the 2-norm of the error, we take a different approach to the solution of the problem that is specifically suited to the control of large, flexible structural systems and also leads to explicit results.

In structural systems modeled using discrete springs, masses and point forces, the control forces occur as action and reaction pairs. The control influence matrix  $\mathbf{B}$  or rather its singular value decomposition has some special properties due to its structure. The projection matrices  $\mathbf{U}_{0B}\mathbf{U}'_{0B}$  and  $\mathbf{U}_{1B}\mathbf{U}'_{1B}$  have the special structure

$$\begin{aligned} \mathbf{U}_{0B}\mathbf{U}'_{0B} &= \begin{pmatrix} \mathbf{I}_m & \mathbf{0} \\ \mathbf{0} & \mathbf{0} \end{pmatrix} \\ \mathbf{U}_{1B}\mathbf{U}'_{1B} &= \begin{pmatrix} \mathbf{0} & \mathbf{0} \\ \mathbf{0} & \mathbf{I}_{n-m} \end{pmatrix} \end{aligned} \quad (8.45)$$

In such a case, choosing  $\mathbf{z}_{0i}$  corresponds to choosing the first  $m$  elements of  $\phi_{0i}$  exactly. The error  $\epsilon_{0i}$  is zero and the contribution to the total error  $\epsilon_i$  is from  $\epsilon_{1i}$ . Setting  $\phi_{0i} = \phi_{0i}^d$  and substituting in (8.43) we get,

$$\begin{aligned} \mathbf{z}_{1i} &= (\lambda_i \mathbf{I} - \mathbf{U}'_{1B} \mathbf{A} \mathbf{U}_{1B})^{-1} \mathbf{U}'_{1B} \mathbf{A} \phi_{0i}^d \\ &= (\lambda_i \mathbf{I} - \mathbf{U}'_{1B} \mathbf{A} \mathbf{U}_{1B})^{-1} \bar{\phi}_{0i}^d \end{aligned} \quad (8.46)$$

where  $\bar{\phi}_{0i}^d = \mathbf{U}'_{1B} \mathbf{A} \phi_{0i}^d$ . We note that the expression  $\mathbf{U}'_{1B} \mathbf{A} \mathbf{U}_{1B}$  is simply the lower, right  $n-m$  dimensional submatrix of  $\mathbf{A}$  with a proper choice of coordinates<sup>2</sup> Assuming

---

<sup>2</sup>This is true especially for the class of underactuated structural systems where 8.45 holds.

that this matrix is simple, we can write its modal decomposition as

$$\mathbf{U}'_{1B}\mathbf{A}\mathbf{U}_{1B} = \sum_{j=1}^{n-m} \mu_j \mathbf{x}_j \mathbf{y}_j^T \quad (8.47)$$

Now, the resolvent  $\mathbf{F}(\lambda_i)$  may be written as,

$$\begin{aligned} \mathbf{F}(\lambda_i) &= (\lambda_i \mathbf{I} - \mathbf{U}'_{1B}\mathbf{A}\mathbf{U}_{1B})^{-1} \\ &= \sum_{j=1}^{n-m} \frac{1}{\lambda_i - \mu_j} \mathbf{x}_j \mathbf{y}_j^T \end{aligned}$$

We can now solve for  $\mathbf{z}_{1i}$  as

$$\begin{aligned} \mathbf{z}_{1i}(\lambda_i) &= \left( \sum_{j=1}^{n-m} \frac{1}{\lambda_i - \mu_j} \mathbf{x}_j \mathbf{y}_j^T \right) \mathbf{U}'_{1B}\mathbf{A}\phi_{0i}^d \\ &= \begin{pmatrix} \vdots & \vdots & \vdots & \vdots \\ \mathbf{x}_1 \mathbf{y}_1^T \bar{\phi}_{0i}^d & \mathbf{x}_2 \mathbf{y}_2^T \bar{\phi}_{0i}^d & \cdots & \mathbf{x}_{n-m} \mathbf{y}_{n-m}^T \bar{\phi}_{0i}^d \\ \vdots & \vdots & \vdots & \vdots \end{pmatrix} \left\{ \begin{array}{c} \frac{1}{\lambda_i - \mu_1} \\ \frac{1}{\lambda_i - \mu_2} \\ \vdots \\ \frac{1}{\lambda_i - \mu_{n-m}} \end{array} \right\} \\ &= \mathbf{Q}_i \mathbf{a}_i \end{aligned} \quad (8.48)$$

We now have an explicit expression for the achievable eigenvector  $\phi_i$  in terms of the eigenvalue  $\lambda_i$ .

$$\begin{aligned} \phi_i(\lambda_i) &= \phi_{0i} + \phi_{1i} \\ &= \phi_{0i}^d + \mathbf{U}_{1B} \left( \sum_{j=1}^{n-m} \frac{1}{\lambda_i - \mu_j} \mathbf{x}_j \mathbf{y}_j^T \right) \mathbf{U}'_{1B}\mathbf{A}\phi_{0i}^d \end{aligned} \quad (8.49)$$

A lot of interesting implications arise from the above parametrization of the achievable eigenvector into the two orthogonal subspaces of the control influence matrix  $\mathbf{B}$ . These are discussed in the subsequent sections and a couple of examples are worked out to demonstrate application of the above algorithm.



### 8.6.1 Selection of the Optimum Eigenvalue

We first discuss some properties that are illustrated by the parametrization of the achievable eigenvector as shown in (8.48). The rank of  $\mathbf{Q}_i$  can at most be  $n - m$ . This maximum rank is attained only if the vectors  $\bar{\phi}_{0i}^d$  excite all the modes of the system  $\mathbf{U}'_{1B}\mathbf{A}\mathbf{U}_{1B}$ . Any attainable vector  $\mathbf{z}_{1i}$  is in the range of  $\mathbf{Q}_i$  and any components of the desired vector  $\mathbf{z}_{1i}^d$  in the space orthogonal to this range can not be attained. This is the first source of error between the desired and attainable eigenvectors.

We first project the desired vector  $\mathbf{z}_{1i}^d$  onto the range of  $\mathbf{Q}_i$  and parametrize the projection  $\hat{\mathbf{z}}_{1i}^d$  as follows :

$$\hat{\mathbf{z}}_{1i}^d = \mathbf{Q}_i \hat{\mathbf{a}}_i \quad (8.50)$$

We would now like to minimize the 2-norm of the error between  $\mathbf{z}_{1i}$  and  $\hat{\mathbf{z}}_{1i}^d$ . This is done by expressing the error as follows :

$$\begin{aligned} \|\hat{\mathbf{z}}_{1i}^d - \mathbf{z}_{1i}\|_2 &= \|\mathbf{Q}_i (\hat{\mathbf{a}}_i - \mathbf{a}_i)\|_2 \\ &\leq \|\mathbf{Q}_i\|_2 \|\hat{\mathbf{a}}_i - \mathbf{a}_i\|_2 \end{aligned}$$

We now have a problem of minimizing the 2-norm of the error between  $\hat{\mathbf{a}}_i$  and  $\mathbf{a}_i$ . The problem is posed as follows :

$$\min_{\lambda_i} \|\epsilon_{ai}\|_2^2 = \min_{\lambda_i} \|\hat{\mathbf{a}}_i - \mathbf{a}_i\|_2^2 \quad (8.51)$$

Recognizing that

$$a_i^j = \frac{1}{\lambda_i - \mu_j}$$

we express,

$$\min_{\lambda_i} \|\epsilon_{ai}\|_2^2 = \min_{\lambda_i} \sum_j \left( \hat{a}_i^j - \frac{1}{\lambda_i - \mu_j} \right)' \left( \hat{a}_i^j - \frac{1}{\lambda_i - \mu_j} \right) \quad (8.52)$$

Equation (8.52) is in the form of a scalar, non-linear optimization problem and needs to be solved using numerical techniques. However, we also need to mention that in most control problems, the closed-loop eigenvalues associated with each mode are usually desired to be in a small region in the left half plane. The non-linear optimization problem given by (8.52) can be solved in that region to obtain a better fit to the desired eigenvector. As will be demonstrated using a couple of examples, depending on the plant matrices  $\mathbf{A}$  and  $\mathbf{B}$  and our choice of closed-loop modal values  $\lambda_i$  and  $\phi_i^d$ , the sensitivity of the error-norm of the eigenvector to changes in eigenvalue can be quite significant.

Our parametrization of the achievable vectors  $\mathbf{z}_{1i}$  in (8.48) also guides the choice of closed-loop eigenvalues to avoid *singularities*. To recognize the significance of these *singularities*, assume that we would like to specify the  $m$  components of the desired eigenvector in  $\mathbf{U}_{0B}$  and the associated eigenvalue. If this desired eigenvalue is chosen to be  $\mu_j$ , we see from (8.48) that the vector  $\mathbf{x}_j \mathbf{y}_j^T \mathbf{U}'_{1B} \mathbf{A} \phi_{0i}^d$  gets weighted infinitely and unless it is zero because of our choice of  $\phi_{0i}^d$ , the resulting closed-loop mode is essentially due to this vector. This corresponds to the transmission zero state direction discussed earlier. In a mechanical system, this is due to the effect of collocation. Here, the non-collocated masses act as dynamic vibration absorbers, and hence the response of any of the other masses at the natural frequency of these masses (transmission zero of system) will remain zero.

Before proceeding to a couple of illustrative examples, we illustrate a special condition under which one can obtain zero error in the assigned eigenvectors.

## 8.7 A Special Case of Eigenvector Assignment

We rewrite the constraint equation (8.13) as follows :

$$\begin{aligned} (\phi_i \quad \mathbf{B}) \begin{Bmatrix} \lambda_i \\ \mathbf{v}_i \end{Bmatrix} &= \mathbf{A}\phi_i \\ \text{or,} \\ \mathbf{T}_i \mathbf{r}_i &= \mathbf{A}\phi_i \end{aligned} \tag{8.53}$$

This system of equations is overconstrained ( $n$  equations in  $m + 1$  unknowns) and needs to be consistent to have zero error between the desired and attainable closed-loop eigenvectors. Consistency of the above set of equations forms a necessary and sufficient condition for the exact assignment of a closed-loop eigenvector. We can draw a number of interesting conclusions from this set of equations :

- All the open-loop eigenvectors are exactly attainable.
- For real system matrices  $\mathbf{A}$ ,  $\mathbf{B}$ , a self-conjugate set of eigenvectors  $\phi_i$  leads to a self-conjugate set of control vectors  $\mathbf{v}_i$  and eigenvalues  $\lambda_i$ . This leads to a real gain matrix  $\mathbf{K}$ .
- When the matrix  $\mathbf{T}_i$  has rank  $m$ ; *i.e.*, the eigenvector  $\phi_i^d$  lies in the range of  $\mathbf{B}$ , and the set of equations is consistent, there is an infinite set of choices for  $\lambda_i$ . An important corollary is that if the system has  $n$  inputs, any eigenvector/eigenvalue pair is exactly assignable.
- When the matrix  $\mathbf{T}_i$  has full rank ( $m + 1$ ), (*i.e.*,  $\phi_i^d \notin \mathcal{Ra}\{\mathbf{B}\}$ ), and the set of equations is consistent, there is exactly one unique closed-loop eigenvalue corresponding to the desired closed-loop eigenvector.

The last observation is of considerable interest. We can use the existence of a unique eigenvalue for each exactly attainable eigenvector to cast the eigenvector assignment problem in a different fashion and hence derive some interesting properties of the eigenvalue.

When there is a unique eigenvalue corresponding to an exactly attainable eigenvector, we can evaluate it using a Rayleigh quotient given by

$$\lambda_i = \frac{\phi_i^d \mathbf{U}_{1B} \mathbf{U}'_{1B} \mathbf{A} \phi_i^d}{\phi_i^{d'} \mathbf{U}_{1B} \mathbf{U}'_{1B} \phi_i^d} \quad (8.54)$$

We now solve two classical problems to illustrate the results of eigenvalue and eigenvector assignment using the procedures developed above.

## 8.8 Example of a State Space System

We consider the circuit shown in Figure 8-3. This has been studied as an example on classical eigenstructure assignment [40] and we use the same example to illustrate eigenvector assignment. The circuit has the state-variable representation

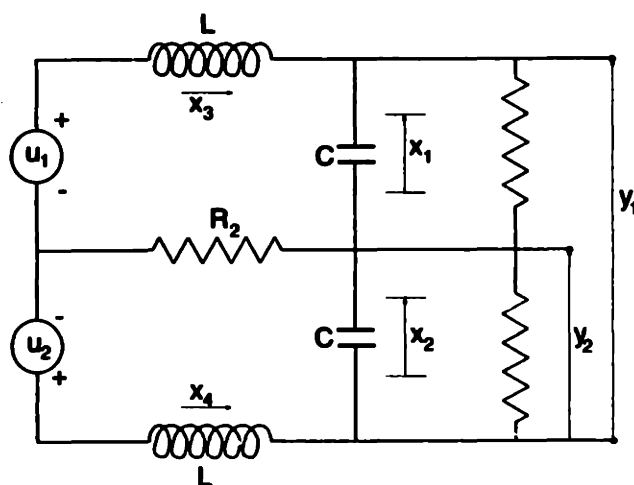


Figure 8-3: Multi-input electric circuit [40].

$$\begin{aligned} \dot{\mathbf{x}} &= \begin{pmatrix} -1/CR_1 & 0 & 1/C & 0 \\ 0 & -1/CR_1 & 0 & -1/C \\ -1/L & 0 & -R_2/L & -R_2/L \\ 0 & 1/L & -R_2/L & -R_2/L \end{pmatrix} \mathbf{x} + \begin{pmatrix} 0 & 0 \\ 0 & 0 \\ 1/L & 0 \\ 0 & 1/L \end{pmatrix} \mathbf{u} \\ \mathbf{y} &= \begin{pmatrix} 1 & 1 & 0 & 0 \\ 0 & 1 & 0 & 0 \end{pmatrix} \mathbf{x} \end{aligned} \quad (8.55)$$

We assume unit values for all the circuit components to get the numerical values for the state matrices.

### 8.8.1 Eigenvalue Assignment

We desire to place the closed loop eigenvalues at

$$\lambda_{1,2}^d = -1.5 \pm j1.5$$

$$\lambda_{3,4}^d = -1.0 \pm j0.5$$

We also select the desired eigenvectors to be

$$\phi_{1,2}^d = \begin{Bmatrix} 1 \pm j \\ 0 \\ -1 \pm j \\ 0 \end{Bmatrix} \quad \phi_{3,4}^d = \begin{Bmatrix} 0 \\ -1 \pm j \\ 0 \\ 1 \pm j \end{Bmatrix}$$

The eigenvalue assignment procedure described earlier is carried out to obtain the desired closed loop eigenvalues exactly and closed loop eigenvectors as close as possible to the desired eigenvectors. Application of the procedure leads to the following closed loop eigenvalues/vectors.

$$\lambda_{1,2} = -1.5 \pm j1.5$$

$$\lambda_{3,4} = -1.0 \pm j0.5$$

$$\phi_{1,2} = \begin{Bmatrix} 0.4286 \pm j0.2857 \\ 0 \\ -0.6429 \pm j0.5 \\ 0 \end{Bmatrix} \quad \phi_{3,4} = \begin{Bmatrix} 0 \\ -0.6 \pm j0.6 \\ 0 \\ 0.3 \pm j0.3 \end{Bmatrix}$$

The eigenvectors have been normalized to have unity Euclidean norms. We see that there is a huge error between the desired and attainable eigenvectors. The control gain matrix  $\mathbf{K}$  is given by

$$\mathbf{K} = \begin{pmatrix} 1.5 & 0 & 1 & -1 \\ 0 & 0.75 & -1 & 0 \end{pmatrix}$$

The response of the state variables to the two control inputs is shown in Figure 8-4.

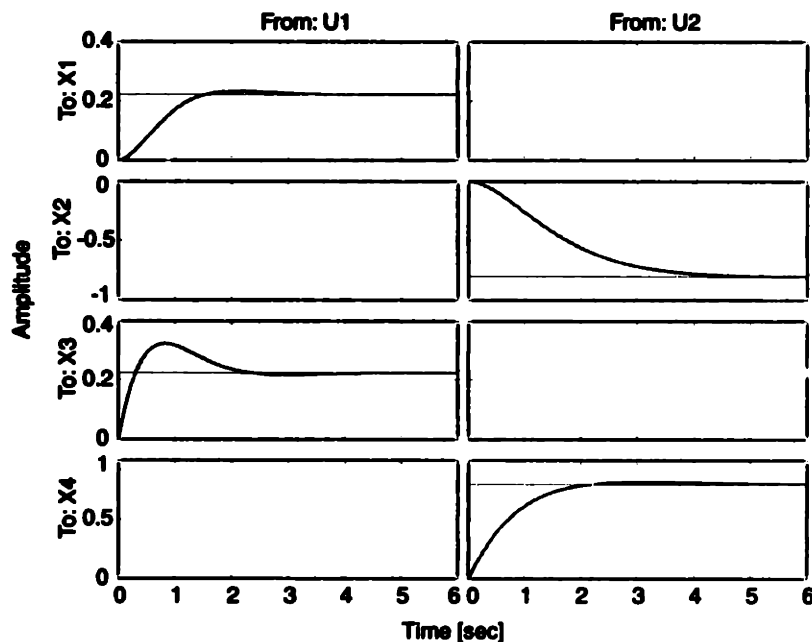


Figure 8-4: Step response from eigenvalue assignment.

### 8.8.2 Eigenvector Assignment

To reduce the error between the desired and attainable eigenvectors, we implement the eigenvector assignment procedure. Here, we specify only the desired closed-loop eigenvectors. Application of the assignment procedure leads to the closed-loop eigenvalues/vectors listed below

$$\lambda_{1,2} = -1.0 \pm j1.0$$

$$\lambda_{3,4} = -1.0 \pm j1.0$$

$$\phi_{1,2} = \begin{Bmatrix} 0.5 \pm j0.5 \\ 0 \\ -0.5 \pm j0.5 \\ 0 \end{Bmatrix} \quad \phi_{3,4} = \begin{Bmatrix} 0 \\ -0.5 \pm j0.5 \\ 0 \\ 0.5 \pm j0.5 \end{Bmatrix}$$

We observe that for a very small change in the eigenvalues, we obtain the desired eigenvectors exactly. This shows that the subspace in which the desired eigenvectors need to lie is very sensitive to perturbations in eigenvalues. A surface plot of the

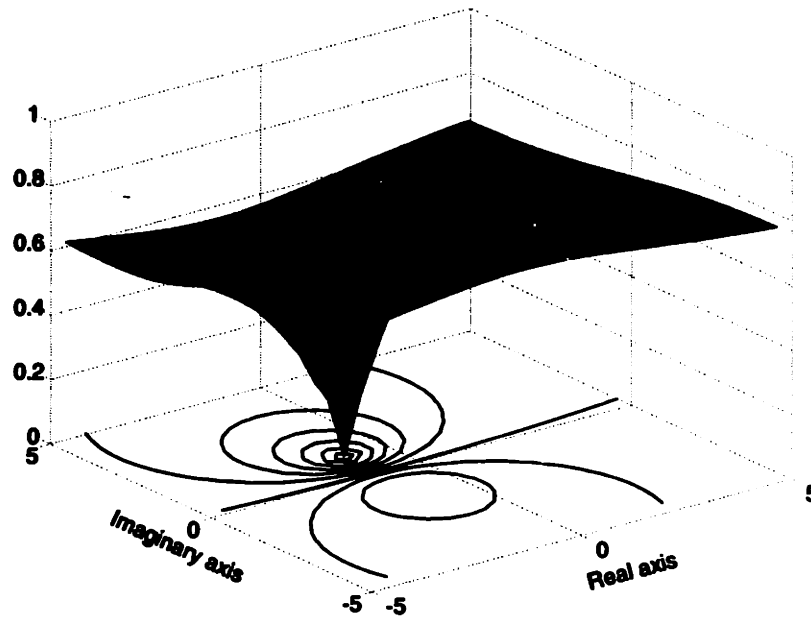


Figure 8-5: Surface plot of error norm

error norm (between the desired and attainable eigenvector) reinforces this result (see Figure 8-5). The control gain matrix  $\mathbf{K}$  is given by :

$$\mathbf{K} = \begin{pmatrix} 0 & 0 & 0 & -1 \\ 0 & 0 & -1 & 0 \end{pmatrix}$$

The response of the state variables to the two control inputs is shown in Figure 8-6. Comparing the two step responses in figures 8-4 and 8-6, we observe the symmetry of the response due to eigenvector assignment. This is to be expected since the eigenvectors control the shape of transients. We now solve a structural control problem to

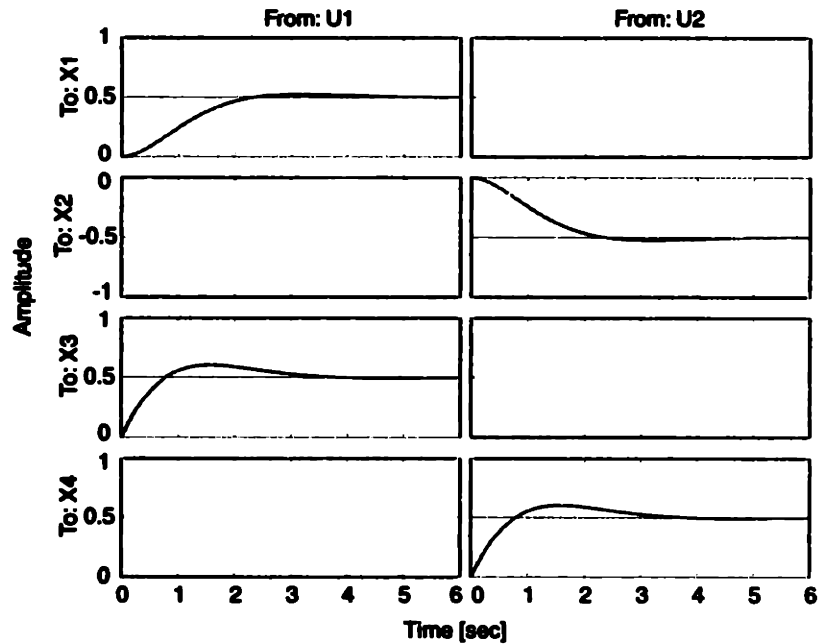


Figure 8-6: Step response from eigenvector assignment

illustrate the application of the eigenvector assignment procedure.

## 8.9 Example of a Structural Problem

In this section, we consider the mode shape assignment for a structural system that is representative of the machine tool structures we are interested in. We discuss the assignment procedure in a detailed manner. Figure 8-7 illustrates the mechanical system being considered. To put things in perspective, this typically illustrates the stage motion control problem in the  $Z$ -axis. Mass  $M_1$  corresponds to the base of the stepper,  $M_2$  corresponds to the stage itself,  $M_3$  corresponds to the first resonance of the stage - typically associated with the mounting of the interferometer mirror and  $M_4$  corresponds to the first resonance of the lens column. The system matrices are



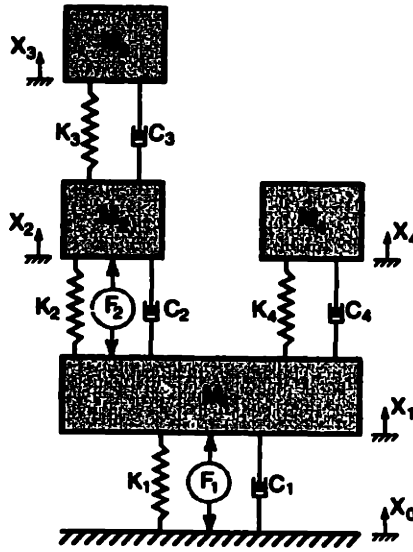


Figure 8-7: Four degree of freedom structural system

given by

$$\mathbf{A}_x = \begin{pmatrix} -\frac{K_1+K_2+K_4}{M_1} & \frac{K_2}{M_1} & 0 & \frac{K_4}{M_1} \\ \frac{K_2}{M_2} & -\frac{K_2+K_3}{M_2} & \frac{K_3}{M_2} & 0 \\ 0 & \frac{K_3}{M_3} & -\frac{K_3}{M_3} & 0 \\ \frac{K_4}{M_4} & 0 & 0 & -\frac{K_4}{M_4} \end{pmatrix} \quad \mathbf{B}_x = \begin{pmatrix} \frac{1}{M_1} & -\frac{1}{M_1} \\ 0 & \frac{1}{M_2} \\ 0 & 0 \\ 0 & 0 \end{pmatrix}$$

The transmission zeros for the system when it is desired to specify the components of the mode shape corresponding to the masses  $M_1$  and  $M_2$  are given by  $-K_4/M_4$  and  $-K_3/M_3$ . This can be verified by choosing a permutation matrix  $\mathbf{W}$  to be

$$\mathbf{W} = \begin{pmatrix} 1 & 0 & 0 & 0 \\ 0 & 1 & 0 & 0 \end{pmatrix}$$

and solving for the transmission zeros through the solution of a generalized eigenvalue problem given by (8.32). This corresponds to the fact that mass  $M_4$  is non-located with respect to the control input  $f_1$  and mass  $M_3$  is non-located with respect to the control input  $f_2$ . These masses act as dynamic vibration absorbers at the natural frequencies  $-K_4/M_4$  and  $-K_3/M_3$  respectively. This is brought out explicitly by the rest of the developments as illustrated below.

The subspace  $U_{0Bx}$  is dependent on the mass ratio  $M_2/M_1$ , but to obtain insight into the problem, let us assume that this mass ratio is one. This does not cause any loss in generality. We can now write the two subspaces of B as

$$U_{0Bx} = \begin{pmatrix} 1 & 0 \\ 0 & 1 \\ 0 & 0 \\ 0 & 0 \end{pmatrix} \quad U_{1Bx} = \begin{pmatrix} 0 & 0 \\ 0 & 0 \\ 1 & 0 \\ 0 & 1 \end{pmatrix}$$

such that we have the lower-right submatrix  $U'_{1Bx}A_xU_{1Bx}$

$$U'_{1Bx}A_xU_{1Bx} = \begin{pmatrix} -\frac{K_3}{M_3} & 0 \\ 0 & -\frac{K_4}{M_4} \end{pmatrix}$$

Solving the eigenvalue problem for  $U'_{1Bx}A_xU_{1Bx}$  we get

$$\begin{aligned} \mu_1^2 &= -\frac{K_3}{M_3} & \mathbf{x}_1\mathbf{y}_1^T &= \begin{pmatrix} 1 & 0 \\ 0 & 0 \end{pmatrix} \\ \mu_2^2 &= -\frac{K_4}{M_4} & \mathbf{x}_2\mathbf{y}_2^T &= \begin{pmatrix} 0 & 0 \\ 0 & 1 \end{pmatrix} \end{aligned}$$

Assume, we would like to assign a closed loop mode shape  $\phi_{x1}^d = \{1, 1, 1, i\}^T$ .

$$\bar{\mathbf{z}}_{01}^d = U'_{1Bx}A_x\phi_{x01}^d = \begin{pmatrix} 0 & \frac{K_3}{M_3} & -\frac{K_3}{M_3} & 0 \\ \frac{K_4}{M_4} & 0 & 0 & -\frac{K_4}{M_4} \end{pmatrix} \begin{Bmatrix} 1 \\ 1 \\ 0 \\ 0 \end{Bmatrix} = \begin{Bmatrix} \frac{K_3}{M_3} \\ \frac{K_4}{M_4} \end{Bmatrix}$$

After all our mathematical manipulations, we finally obtain

$$\mathbf{z}_{11} = \begin{pmatrix} \frac{K_3}{M_3} & 0 \\ 0 & \frac{K_4}{M_4} \end{pmatrix} \begin{Bmatrix} \frac{1}{\lambda_1^2 + K_3/M_3} \\ \frac{1}{\lambda_1^2 + K_4/M_4} \end{Bmatrix}$$

The effects of setting  $\lambda_1^2$  to either  $-K_3/M_3$  or  $-K_4/M_4$  are clearly seen. Setting  $\lambda_1^2 = -K_3/M_3$  results in a mode in which only mass  $M_3$  vibrates, and setting  $\lambda_1^2 = -K_4/M_4$  results in a mode in which only mass  $M_4$  vibrates. This is clear by looking at the structure. The transfer function from either  $f_1$  or  $f_2$  to  $x_1$  has a zero at  $\lambda_1^2 = -K_4/M_4$  and thus this mass can not be moved at that natural frequency (collocation). A similar argument holds for mass  $M_3$ . Masses  $M_3$  and  $M_4$  play the role of dynamic vibration absorbers at the respective frequencies and hence, it is impossible to obtain motion of any of the other masses in the system.

We see that our parametrization of the eigenvectors into the two subspaces associated with the  $\mathbf{B}$  matrix plays an important role in determining the set of closed-loop eigenvectors attainable as a function of closed-loop eigenvalue. Besides, for structural systems the explicit determination of the closed-loop modes in terms of the flexural modes (that are not directly actuated) plays an important role in optimizing the mechanical design for control. In most structural systems the resonant frequencies  $\mu_j^2$  are set very high or the closed-loop eigenvalues  $\lambda_i^2$  are set very low to avoid possible singular points. With the above parametrization the design of the machine tool structure can be optimized without calling for either very stiff designs or compromising on control bandwidth.

## 8.10 Application to the Wafer Stepper

In this section, we apply the eigenvector assignment procedure developed in this chapter to the higher-order model of the wafer stepper in the X-Z plane. The model is illustrated in Figure 7-3 in Chapter 7 and has the equations of motion (7.33). We observe that there are six degrees of freedom and five control forces. Thus, this problem falls under the special case described in Section 8.7 and hence the closed-loop eigenvalues can be computed using the Rayleigh quotient given by (8.54). We derive the matrices  $\mathbf{A}_x$  and  $\mathbf{B}_x$  from the equations of motion (7.33) and apply the eigenstructure assignment algorithm from Section 8.7 with the desired closed loop

modes given by

$$V = \begin{pmatrix} 0 & 0 & 1 & 0 & 0 & 0 \\ 1 & 0 & 1 & 0 & 0 & 1 \\ 1 & 1 & 1 & 0 & 0 & 1 \\ 0 & 0 & 1 & 0 & 0 & 1 \\ 0 & 0 & 0 & 0 & 1 & 0 \\ 0 & 0 & 0 & 1 & 0 & 0 \end{pmatrix}$$

The resulting state feedback gains are used along with a Kalman filter as an estimator and implemented on the prototype wafer stepper. A 1024-point FFT of the error motions in between the lens column and the fine stage is used to compare the performance of this controller with the performance illustrated in Figure 7-4. This is illustrated in Figure 8-8. Figure 8-8 illustrates the improvements due to the modal

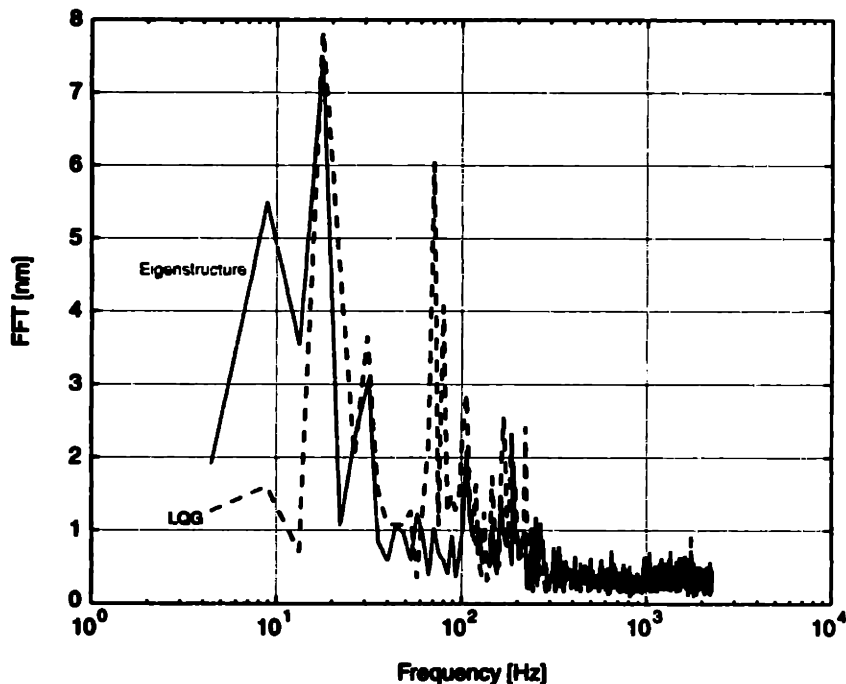


Figure 8-8: FFT of error motions in the  $X$  direction. Note the clear attenuation of the flexible bending mode at 84.3 Hz. Also due to the lack of an integrator in the fine stage control law, low frequency performance of the modal controller is worse than the LQG controller.

assignment procedure as compared to the frequency shaping LQG procedure used in

Description	Settling Time [ms]
Passive Isolation	2500
Active Isolation (LQG + IMSC)	550
Active Isolation (Modal)	350

Table 8.1: Settling times on the prototype wafer stepper for the various cases of isolation/control. Settling time in this thesis is defined as the time it takes for error motions in between the stage and the lens column to be less than 50 nm following a 20 mm step. The 20 mm step is the result of a triangular velocity profile over 250 ms.

Chapter 6. A clear attenuation of the modes around 85 Hz is demonstrated. The low frequency performance of the modal controller is however compromised due to the absence of integrating action. An integrator could however be implemented easily by augmenting the states. The lens mount modes are still excited due to spillover of controller action.

Note that possible performance improvements might be obtained by designing such an LQG shaped controller for the flexible system shown in Figure 7-3 also. Our comparison is not a true reflection on the capability of the frequency-shaped LQG controller, but indeed reflects the performance improvement obtained by modeling and compensating for the flexibility of the lens column using the eigenstructure technique.

Table 8.1 highlights the key results from this thesis while illustrating the performance benefits obtained by careful structural and control design. Three different cases are presented in Table 8.1. All three correspond to a 20 mm step motion of the X-coarse stage of the wafer stepper. This motion is profiled according to a triangular velocity profile which is tapered off at the end with a spline to produce jerk-free motion. The velocity profile is spread over a period of approximately 250 ms. The settling time is measured by the amount of time it takes for the relative motion between the lens column and the mirror on the fine stage to settle below a peak of 50 nm in all 6 axes<sup>3</sup>. The effect of compensating for the flexible modes of the stepper is clearly seen from Table 8.1. Almost an order of magnitude improvement in settling time is

---

<sup>3</sup>In its current implementation, only five axes are considered, the auto-focus mechanism for the Z-axis is not in place yet.

seen from the passive isolation case. This basically indicates that the productivity of the wafer stepper could be increased ten times the current levels.

## 8.11 Summary of Chapter 8

The modal control problem is presented. Existing techniques of modal control concentrate on the assignment of eigenvalues. While this is an important problem (the stability of the system depends on the eigenvalues), structural problems require that the assignment of eigenvectors is equally if not more important (as long as the eigenvalues are stable). We focus on the assignment of eigenvectors. The error terms, attainable and desired eigenvectors are parametrized into the two important subspaces of the control influence matrix. The orthogonality of these subspaces permits simplification of the constraint equations and allow us to derive an explicit relationship between the achievable and desired eigenvectors as a function of the closed-loop eigenvalue.

This parametrization is also important since the first step towards the control of flexible systems is the design of controllers for rigid body models that are fully actuated (complete specification of  $\phi_{0i}$ ). For structural problems, the explicit relationship between the closed-loop eigenvalues and eigenvectors also involves the flexible modes of the system. This has implications on how these flexible modes can be engineered to get good control performance rather than just stiffening the structure or compromising the control performance. A special case of eigenvector assignability where the number of actuators is one less than the number of degrees of freedom is illustrated. This is an important result since a number of studies have revealed the existence of one low frequency flexible mode in most precision machines [63]. Examples are worked out to illustrate application of the procedure - one example corresponds to the prototype wafer stepper considered in this thesis.

Finally, the modal controller derived in this chapter is implemented on the prototype wafer stepper and a further reduction in settling time demonstrated. This demonstrates the need to model and compensate for flexibility effects on the wafer

**stepper.**

# Chapter 9

## Conclusion and Future Work

### 9.1 Summary

In this thesis, the real-world limitations to precision motion as applied especially to photolithography are examined. These are due to seismic disturbances and structural resonance of the machine. Seismic disturbances are modeled and generic criteria are discussed. An overview of the vibration requirements imposed by various stepper manufacturers is presented. An analysis of a simple two degree of freedom model illustrates the need for low frequency isolation as line-widths on semiconductor devices continue to grow smaller.

An analytical treatment of passive isolation mounts is presented by posing passive isolation in the context of a feedback control problem. The conflicting disturbance sources of payload disturbances and seismic vibrations are shown to be related to the payload accelerations through the sensitivity and complementary sensitivity functions of the feedback loop. Thus passive isolators are subject to the same fundamental tradeoff that control systems are subject to - payload disturbance transmissibility and the seismic vibration transmissibility need to sum up to unity over all frequencies. Thus, the inadequacy of passive isolation for step and repeat wafer steppers (and most other precision machines) where both disturbance mechanisms are pronounced at the same low frequencies is exposed. The relationship of the two disturbance sources to the payload accelerations (which is the performance measure in a passive system) is



similar to that of sensor noise and process noise in a feedback loop. This motivates the application of state estimation techniques, more specifically Kalman filtering to the design of optimal passive mounts that minimize the RMS value of the payload motions. The two biggest contenders amongst the technologies for low-frequency passive isolation, *i.e.*, Pneumatic isolation and Negative Stiffness Mechanisms (NSMs) are discussed in detail.

Given the demands on precision positioning, passive isolation is inadequate in almost all wafer steppers. Active isolation is shown to be free of the fundamental tradeoff that passive mounts experience. In fact, active isolation is shown to attenuate both disturbance mechanisms in a similar manner. The ratio between the open-loop and closed-loop transmissibilities for both disturbance mechanisms is shown to be the sensitivity of the feedback loop. Thus the control paradigm for active isolation manifests itself as a sensitivity shaping procedure. An  $\mathcal{H}_2$  approach to sensitivity shaping is presented using the frequency-shaped cost function method along the lines of Gupta [29] and Hyde [31].

An active isolation scheme is designed and implemented on a prototype photolithographic wafer stepper. Nonlinear variable-reluctance actuators (to minimize footprint) in parallel with passive elastomeric mounts are used along with acceleration feedback in a parallel isolation architecture. Simple control laws utilizing the Independent Modal Space Control technique [47] [44] along with a frequency shaped LQG technique [29] are derived for a rigid body model. These control laws are implemented along with lead-lag compensation for the stage controllers on an 8 DSP VME platform. Experimental results illustrate almost an order of magnitude improvement in settling times. One key limitation was the unexplained phase loss in the accelerometers. This prevented further improvements in isolation by restricting the control bandwidth.

The key to obtaining even better performance is by modeling and compensating for the flexibility of the stepper. A tutorial review on the modeling and control of large flexible structures addressing observation and control spillover [8] is presented. The work of Balas [8] is reproduced with application to finite-dimensional models

resulting from an assumed-modes approach rather than the truncation scheme that is presented in literature. This is because none but the simplest dynamic systems can be modeled using partial differential equations. Discretization is a must to model large, complex systems such as a wafer stepper. Results from a modal analysis of the GCA XLS 7000 stepper [65] are used to set up a higher order model of the wafer stepper. The degrading effect of control spillover is demonstrated both analytically and through experiment on the prototype wafer stepper. This clearly demonstrates the need for modeling and compensating for the flexibility of the system.

Amongst the various control architectures available to address structural flexibility, eigenstructure assignment is chosen. This is because settling speeds and hence the shape and speed of the transients are extremely important in a wafer stepper. A caveat with existing eigenstructure assignment schemes that results in singular conditions is exposed. Following this, a modal controller is derived that explicitly relates the closed-loop eigenvectors to the closed-loop eigenvalues and the flexible modes of the machine structure. Singularities that are not immediately evident with previous assignment schemes are made explicit in this assignment procedure. This explicit relationship between the closed-loop modes and the open-loop flexible modes has interesting implications on “structural design for control”. The subject of mechanical design for control is left for future work. The modal assignment problem is also specialized to the case of systems where the number of degrees of freedom exceeds the number of control inputs by one. This is an important set of problems as made evident by the work of Rivin [63]. An example to demonstrate the application of the procedure to state-space systems is worked out. Singularities are illustrated by application of the algorithm to a structural system. In a structural system, these singularities are shown to result due to collocation in under-actuated systems which result in dynamic vibration absorbers at select frequencies.

The modal controller is then applied to the X-coarse stage, X-fine stage and the active isolation system in the X-Z plane and a further improvement in settling time over the  $\mathcal{H}_2$  procedure for vibration isolation demonstrated. However, this is not a true comparison between the  $\mathcal{H}_2$  and eigenstructure schemes since structural resonance

was not taken into account in the former. A similar performance could be expected in theory from a well-designed  $\mathcal{H}_2$  controller that takes into account the presence of structural resonance. The advantage of the modal assignment scheme lies in its intuitive appeal, the implications on structural design and the explicit illustration of the performance/tradeoff of the control scheme.

## 9.2 Recommendations for future work

The following are the recommendations for future work :

- First and foremost, the accelerometers on the wafer stepper would need to be replaced with other inertial devices that do not display such a phase loss. This loss of phase without a corresponding loss in magnitude limited the performance of the isolation system. Either geophones or accelerometers could be used for feedback, however, the phase specifications need to be obtained besides the magnitude specifications because of the use of these devices in a feedback loop.
- Second, it would be good to explore the use of pneumatic mounts for the passive isolator. While more expensive than elastomeric mounts, pneumatic mounts permit leveling of the stepper and also have lower natural frequencies. According to Hyde [31], a rule of thumb in six-axis active isolation is that the active control bandwidth could be extended by about a decade over either side of the passive mount natural frequency. It was found during controller design that sensitivity loop shaping to push the lower corner frequency of the active isolator further down resulted either in instability around the upper corner frequency (due to observation spillover of the residual modes) or high order controllers to permit a steep roll-up of the sensitivity function. With the current design (a passive mount natural frequency between 7 and 25 Hz), the full performance capability at lower frequencies ( $< 0.1$  Hz) is not utilized due to these problems. IDE seems to have realized the advantages of low natural frequency passive isolators in an active isolation scheme with their ATC isolation modules.

- A thorough modal analysis on the stepper would help with better modeling. Although the results of the modal analysis performed by Sandia [65] were used to obtain better performance in the X direction, similar models in the Y direction caused unstable behavior of the stepper. This was not investigated further for lack of time and has been left for further work.
- I inherited the 50 nm settling criteria and never questioned it. For more stringent settling criteria, the structural resonance of the lens mount could also become important. The data in Chapter 7 was gathered immediately after the stage came to a settled state. The lower frequency modes associated with the stepper around 24 Hz disappear shortly afterwards due to the good attenuation provided by the error function of the fine stage. The magnitude of these error motions is however large, around 8 nm and contribute significantly to the error budget. For more stringent settling criteria, it would be required to model and compensate for these flexible modes too.
- The modal assignment procedure derived in this thesis has interesting implications on the engineering of structural resonance. This needs to be demonstrated with real world systems. This requires the development of canonical models of flexibility as illustrated in Chapters 7 and 8. The results from the controller-structure interaction need to be compared against the work of other researchers in this area.
- The modal assignment procedure derived in this thesis has not been fully characterized in terms of robustness issues. Time-domain performance expressed through the desired natural frequencies and mode shapes has been the driving motivation. Robustness issues need to be addressed, and the effects of spillover quantified.

# Appendix A

## Hardware Interconnections for Active Isolation

In this appendix, we tabulate the connections of the various sensors and actuators to the analog input/output lines of the industry packs on the COMM-IO boards of the VME-based DSP system.

Table A gives a list of the actuator pairs and the D/As that drive them.

Actuator Pair	D/A Channel
$f_{x14}$	da0
$f_{x23}$	da1
$f_{y12}$	da2
$f_{y43}$	da3
$f_{z16}$	da4
$f_{z27}$	da5
$f_{z38}$	da6
$f_{z45}$	da7

Table A.1: Actuator Pairs, D/A Channels : The 8 actuator pairs are driven by power amplifiers which are connected to the Digital to Analog Converters on Industry Pack 2 (8 channels) on COMM/IO 3

Table A gives a list of the Capacitance gauges and the A/D channels they are read into. Table A gives a list of the accelerometers, their gains<sup>1</sup> and the A/D channels

---

<sup>1</sup>Refer to Vibrametrics Calibration certificates

Capacitance Gauge	A/D Channel
Cx	ad0
Cy1	ad1
Cy2	ad2
Cz1	ad3
Cz2	ad4
Cz3	ad5

**Table A.2: Capacitance Gauges, A/D Channels :** All the capacitance gauge signals are connected to the Analog to Digital Converters on Industry Pack 0 (8 channels) on COMM/I0 3

they are read into.

Accelerometer	Serial #	Gain (Volts/g)	A/D Channel
Az1	829	5.20	ad0
Az2	827	6.42	ad1
Az3	832	5.60	ad2
Ax1	831	5.84	ad3
Ax2	830	6.24	ad4
Ay	998	6.84	ad5

**Table A.3: Accelerometer Gains, A/D Channels :** All the accelerometer signals are connected to the Analog to Digital Converters on Industry Packs 0 (4 channels) and 1 (2 channels) on COMM/I0 4

# Bibliography

- [1] H. Amick and S.K. Bui. A review of several methods for processing vibration data. In C.G. Gordon, editor, *Vibration Control in Microelectronics, Optics and Metrology*, volume 1619, pages 253–264, San Jose, CA, 4-6 Nov. 1991. SPIE.
- [2] Jr. Andry, A.N., E.Y. Shapiro, and J.C. Chung. Eigenstructure assignment for linear systems. *IEEE Transactions on Aerospace and Electronic Systems*, AES-19(5):711–729, September 1983.
- [3] ASM Lithography. *PAS 5500/500 Site Preparation Guide*, Oct. 1997.
- [4] Semiconductor Industry Association. The national technology roadmap for semiconductors. Technical report, 1997.
- [5] M. Athans. Multivariable control systems. Lecture Notes, Department of Electrical Engineering and Computer Science, MIT, Spring 1989.
- [6] M. Athans. *The Control Handbook*, chapter 35, Kalman Filtering, pages 589–594. IEEE Press, 1996.
- [7] M.J. Balas. Active control of flexible systems. *Journal of Optimization Theory and Applications*, 25(3):415–436, 1978.
- [8] M.J. Balas. Feedback control of flexible systems. *IEEE Transactions on Automatic Control*, AC-23(4):673–679, 1978.
- [9] M.J. Balas. Modal control of certain flexible dynamic systems. *SIAM Journal on Control and Optimization*, 16(3):450–462, 1978.

- [10] M.J. Balas. Trend in large space structure control theory : Fondest hopes, wildest dreams. *IEEE Transactions on Automatic Control*, AC-27(3):522–535, June 1982.
- [11] Barry Controls, MA. *Application Selection Guide (For Selection and Application of Products to Control Vibration, Shock and Noise)*, 1992.
- [12] A.M. Beard, D.W. Schubert, and A.H. von Flotow. A practical product implementation of an active/passive vibration isolation system. In *Active Control of Vibration and Noise*, volume 75, pages 485–492. ASME, 1994.
- [13] J.S. Bendat and A.G. Piersol. *Random Data : Analysis and Measurement Procedures*. John Wiley & Sons, 2<sup>nd</sup> edition, 1986.
- [14] G.H. Blackwood. *Active Vibration Isolation for Controlled Flexible Structures*. PhD thesis, Massachusetts Institute of Technology, Dept. of Aeronautics and Astronautics, September 1993.
- [15] G.H. Blackwood and A.H. Von Flotow. Active control for vibration isolation despite resonant structural dynamics: A trade study for sensors, actuators and configurations. In *2nd Conference on Recent Advances in Active Control of Sound and Vibration*, Blacksburg, VA, April 28-30 1993.
- [16] S.P. Burrows and R.J. Patton. A comparison of some robust eigenvalue assignment techniques. *Optimal Control Application and Methods*, 11:355–362, 1990.
- [17] S.P. Burrows and R.J. Patton. Design of a low-sensitivity, minimum norm and structurally constrained control law using eigenstructure assignment. *Optimal Control Applications and Methods*, 12:131–140, 1991.
- [18] Canon Europa N.V. *FPA-3000i5 Installation Specifications*, Nov. 1995.
- [19] J.W. Choi, J.G. Lee, Y. Kim, and T. Kang. Design of an effective controller via disturbance accommodating left eigenstructure assignment. *Journal of Guidance, Control and Dynamics*, 18(2):347–354, March-April 1995.



- [20] B. DeBra, Daniel. Design of laminar flow restrictors for damping pneumatic vibration isolators. *Annals of the CIRP*, 33(1), 1984.
- [21] B. DeBra, Daniel. Vibration isolation of precision machine tools and instruments. *Annals of the CIRP*, 41(2):711-718, 1992.
- [22] M.M. Fahmy and J. O'Reilly. On eigenstructure assignment in linear multi-variable systems. *IEEE Transactions on Automatic Control*, AC-27(3):690-693, June 1982.
- [23] M.M. Fahmy and J. O'Reilly. Eigenstructure assignment in linear multivariable systems - a parametric solution. *IEEE Transactions on Automatic Control*, AC-28(10):990-994, October 1983.
- [24] S. Franco. *Design with Operational Amplifiers and Analog Integrated Circuits*. McGraw Hill, 1988.
- [25] G.E. Franklin, J.D. Powell, and A. Emami-Naeini. *Feedback Control of Dynamic Systems*. Addison Wesley, 3<sup>rd</sup> edition, 1994.
- [26] C.G. Gordon. Generic criteria for vibration-sensitive equipment. In C.G. Gordon, editor, *Vibration Control in Microelectronics, Optics and Metrology*, volume 1619, pages 71-85, San Jose, CA, 4-6 Nov. 1991. SPIE.
- [27] C.G. Gordon. Vibration control in microelectronics cleanrooms. In *Conference on Advanced Microcontamination Control and Ultrapure Manufacturing*, pages 1-24, 1996.
- [28] C.M. Grodsinsky and G.V. Brown. Low frequency vibration isolation technology for microgravity space experiments. pages 295-302, ASME Conference on Mechanical Noise and Vibration, Montreal, Sep. 17-21 1989.
- [29] N.K. Gupta. Frequency-shaped cost functionals: Extension of linear quadratic gaussian design methods. *Journal of Guidance and Control*, 3(6):529-535, Nov.-Dec. 1980.

- [30] R.A. Horn and C.R. Johnson. *Matrix Analysis*. Cambridge University Press, first edition, 1985.
- [31] T.T. Hyde. *Active Vibration Isolation for Space Structures*. PhD thesis, Massachusetts Institute of Technology, Dept. of Aeronautics and Astronautics, January 1996.
- [32] Integrated Dynamics Engineering Inc., Woburn, MA. *Active and Passive Isolation Modules*, 1998.
- [33] J.-N. Juang, K. Lim, and J.L. Junkins. Robust eigenstructure assignment for flexible structures. *Journal of Guidance, Control and Dynamics*, 12(3):381–387, May-June 1989.
- [34] D.C. Karnopp. Active and passive isolation of random vibration. In *Isolation of Mechanical Vibration, Impact and Noise*, volume 1, Cincinnati, OH, September 1973. ASME.
- [35] J. Kautsky, N.K. Nichols, and P. Van Dooren. Robust pole assignment in linear state feedback. *International Journal of Control*, 41(5):1129–1155, 1985.
- [36] J.J. Kim and H. Amick. Active vibration control in fabs. *Semiconductor International*, pages 223–228, July 1997.
- [37] G. Klein and B.C. Moore. Eigenvalue-generalized eigenvector assignment with state feedback. *IEEE transactions on Automatic Control*, AC-22:140–141, February 1977.
- [38] S. Kunica. Servo-controlled pneumatic isolators – their properties and applications. *ASME Paper 65-WA/MD-12*, 1965.
- [39] H. Kwakernaak and R. Sivan. *Linear Optimal Control Systems*. John Wiley & Sons, 1972.
- [40] F. Lewis. *Applied Optimal Control & Estimation : Digital Design & Implementation*. Prentice Hall, Englewood Cliffs, N.J., 1992.

- [41] G. P. Liu and R. J. Patton. Robust control design using eigenstructure assignment and multi-objective optimization. *International journal of systems science*, 27(9):871, 1996.
- [42] G. P. Liu and R.J. Patton. *Eigenstructure Assignment for Control System Design*. John Wiley & Sons, Chichester, 1998.
- [43] K. G. McConnell. *Vibration Testing : Theory and Practice*. John Wiley & Sons, 1995.
- [44] L. Meirovitch and H. Baruh. Robustness of the independent modal-space control method. *Journal of Guidance, Control, and Dynamics*, 6(1):20–25, 1983.
- [45] L. Meirovitch, H. Baruh, and H. Oz. A comparison of control techniques for large flexible systems. *Journal of Guidance, Control, and Dynamics*, 6(4):302–310, 1983.
- [46] L.M. Meirovitch. *Elements of Vibration Analysis*. McGraw Hill, 2<sup>nd</sup> edition, 1984.
- [47] L.M. Meirovitch. *Dynamics and Control of Structures*. John Wiley & Sons, 1990.
- [48] B.C. Moore. On the flexibility offered by state feedback in multivariable systems beyond closed loop eigenvalue assignment. *IEEE transactions on Automatic Control*, AC-21:689–692, October 1976.
- [49] S.A. Nayfeh. *Design and Application of Damped Machine Elements*. PhD thesis, Massachusetts Institute of Technology, Dept. of Mechanical Engineering, 1998.
- [50] Newport Corporation, Irvine, CA. *Vibration Control - 1998 Catalog*, 1998.
- [51] G.C. Newton, Gould L.A., and Kaiser J.F. *Analytical Design of Linear Feedback Controls*. Wiley Interscience, New York, 1957.
- [52] Nikon Corporation. *Step and Repeat Scanning System Site Preparation Guide (NSR-S203 Series)*, Sept. 1998.

- [53] Institute of Environmental Sciences. Considerations in clean room design. *IES-RP-CC012.1*, 1993.
- [54] N. Owen and R. Hale. Factors in the design and selection of vibration-sensitive equipment. In C.G. Gordon, editor, *Vibration Control in Microelectronics, Optics and Metrology*, volume 1619, pages 56–70, San Jose, CA, 4-6 Nov. 1991. SPIE.
- [55] R. J. Patton, G. P. Liu, and J. Chen. Multiobjective controller design using eigenstructure assignment and the method of inequalities. *Journal of Guidance, Control and Dynamics*, 17(4):862–864, 1994.
- [56] D.L. Platus. Negative-stiffness-mechanism vibration isolation systems. In C.G. Gordon, editor, *Vibration Control in Microelectronics, Optics and Metrology*, volume 1619, pages 44–54, San Jose, CA, 4-6 Nov. 1991. SPIE.
- [57] T. Poovey, M. Holmes, and D.L. Trumper. A kinematically coupled magnetic calibration fixture. *Precision Engineering*, 16(2):103–107, 1994.
- [58] B. Porter and T. R. Crossley. *Modal Control : Theory and Applications*. Taylor & Francis Ltd., 10-14 Macklin Street, London WC2B 5NF, 1972.
- [59] B. Porter and J.J. D'Azzo. Algorithm for closed-loop eigenstructure assignment by state feedback in multivariable linear systems. *International Journal of Control*, 27(6):943–947, 1978.
- [60] B. Porter and J.J. D'Azzo. Closed-loop eigenstructure assignment by state feedback in multivariable linear systems. *International Journal of Control*, 27(3):487–492, 1978.
- [61] S. Pradhan. Eigenstructure assignment using output feedback. *IEEE transactions on aerospace and electronic systems*, 30(4):1129, 1994.
- [62] S. Pradhan, V.J. Modi, M.S. Bhat, and A.K. Misra. Matrix method for eigenstructure assignment : The multi-input case with application. *Journal of Guidance, Control and Dynamics*, 17(5):983–989, September-October 1994.

- [63] E.I. Rivin. Vibration isolation of precision machinery. *Sound and Vibration*, 8:18-23, August 1979.
- [64] E.I. Rivin. Vibration isolation of precision equipment. *Precision Engineering*, 17(1):41-56, Jan. 1995.
- [65] D. Roach. Modal analysis of the GCA XLS 7000 series lithography machine. Technical report, Sandia National Laboratories, Albuquerque, NM, June 1991.
- [66] G. Roppenecker. On parametric state feedback design. *International Journal of Control*, 43(3):793-804, 1986.
- [67] J.E. Ruzicka. Active vibration and shock isolation. *SAE paper No. 680747*, pages 2872-2886, 1968.
- [68] J.E. Ruzicka and T.F. Derby. Influence of damping in vibration isolation. Technical report, The Shock and Vibration Information Center, Naval Research Laboratory, Washington, D.C., 1971.
- [69] D.W. Schubert. Characteristics of an active vibration isolation system using absolute velocity feedback and force actuation. In *Recent Advances in Active Control of Sound and Vibration*, pages 448-463. Virginia Polytechnic Institute and State University, 15-17 April 1991.
- [70] K. M. Sobel, E. Y. Shapiro, and Jr. Andry, A. N. Eigenstructure assignment. *International journal of control*, 59(1):13-37, 1994.
- [71] K.M. Sobel, S.S. Banda, and H.-H Yeh. Robust control for linear systems with structured state space uncertainty. *International Journal of Control*, 50:1991-2004, 1989.
- [72] K.M. Sobel, W. Yu, and F.J. Lallman. Eigenstructure assignment with gain suppression using eigenvalue and eigenvector derivatives. *Journal of Guidance, Control and Dynamics*, 13:1008-1013, 1990.

- [73] J. Spanos, Z. Rahman, and Blackwood G. A soft 6-axis active vibration isolator. In *American Control Conference*, pages 412–416, Seattle, WA, June 1995.
- [74] SVG Lithography Systems Inc. *Micrascan III Site Preparation Manual*, Mar. 1997.
- [75] N. Tanaka and Y. Kikushima. Rigid support active vibration isolation. *Journal of Sound and Vibration*, 125(3):539–553, 1988.
- [76] Texas Instruments. *TMS320C4x General-Purpose Applications User's Guide*, 1997.
- [77] A.G. Thompson. An active suspension with optimal linear state feedback. *Vehicle System Dynamics*, 5:187–203, 1976.
- [78] D.L. Trumper, S.M. Olson, and P.K. Subrahmanyam. Linearizing control of magnetic suspension systems. *IEEE Transactions on Control Systems Technology*, 5(4):427–438, July 1997.
- [79] E.E. Ungar. Designing sensitive equipment and facilities. *Mechanical Engineering*, 107(12):47–51, Dec. 1985.
- [80] E.E. Ungar, D.H. Sturz, and C.H. Amick. Vibration control design of high technology facilities. *Sound and Vibration*, 7:20–27, 1990.
- [81] Vibrametrics Inc. *User's Manual VME6U-6 Six-Channel Power Supply/Signal Conditioner*, June 1997.
- [82] A.H. von Flotow. An expository overview of active control of machinery mounts. In *27th Conference on Decision and Control*, pages 2029–2032, Austin, TX, December 1988. IEEE.
- [83] M.E. Williams. *Precision Six Degree of Freedom Magnetically-Levitated Photolithography Stage*. PhD thesis, Massachusetts Institute of Technology, Dept. of Mechanical Engineering, October 1997.

- [84] Robert F. Wilson, James R. Cloutier, and R. K. Yedavalli. Control design for robust eigenstructure assignment in linear uncertain systems. *IEEE control systems magazine*, 12(5):29–34, 1992.
- [85] W.M. Wonham. On pole assignment in multi-input, controllable linear systems. *IEEE Transactions on Automatic Control*, AC-12:660–665, 1967.
- [86] H.H. Woodson and J.R. Melcher. *Electromechanical Dynamics : Part 1, Discrete Systems*. John Wiley & Sons, 1968.
- [87] Q. Zhang, G.L. Slater, and R.J. Allemang. Suppression of undesired inputs of linear systems by eigenspace assignment. *Journal of Guidance, Control and Dynamics*, 13(3):330–336, 1990.